京都大学学術情報リポジトリ
KURENAI 紅
Kyoto University Research Information Repository

京都大学
KYOTO UNIVERSITY

Title	Coherent radar measurements of the middle atmosphere and design concepts of the MU radar(Dissertation_全文)
Author(s)	Sato, Toru
Citation	Kyoto University (京都大学)
Issue Date	1982-01-23
URL	http://dx.doi.org/10.14989/doctor.k2669
Right	
Type	Thesis or Dissertation
Textversion	author

Kyoto University

新制
工
5 24
京大附図

COHERENT RADAR MEASUREMENTS OF THE MIDDLE ATMOSPHERE AND DESIGN CONCEPTS OF THE MU RADAR

by Toru SATO

OCTOBER 1981

KYOTO UNIVERSITY

KYOTO 606, JAPAN

COHERENT RADAR MEASUREMENTS OF THE MIDDLE ATMOSPHERE AND DESIGN CONCEPTS OF THE MU RADAR

by Toru SATO

OCTOBER 1981

KYOTO UNIVERSITY

KYOTO 606, JAPAN

ACKNOWLEDGEMENTS

The author would like to express his sincere gratitude to Professor Iwane Kimura, who guided him and provided helpful suggestions in performing the present work.

He deeply acknowledges Professor Susumu Kato for many important advices and encouragements. Thanks are also due to Professor Toru Ogawa for valuable comments on the work. He appreciates continuous suggestions and constructive discussions by Dr. Shoichiro Fukao.

Special thanks are given to Dr. Ronald F. Woodman for his kind guidance and advices while the author's stay in Arecibo Observatory. He is indebted to Dr. Robert M. Harper for helpful discussions and also for kindly offering precious mesospheric data taken by the Jicamarca VHF radar.

Deep appreciations are to Dr. Shinobu Tokumaru of Keio University and Dr. Kazuaki Takao for useful suggestions and comments on antenna theory. He also appreciates suggestive discussions by Drs. Prabhat K. Rastogi, Kozo Hashimoto, Kaoru Fukuyama, and Koichiro Wakasugi.

He is grateful to Mr. Hiroshi Hojo for laborious computations of Chapter 6, to Dr. John P. Matthews for carefully reading the manuscript, and to Mr. Rei Ito for providing a fine word processor program for printing the dissertation.

Part of this work was supported by the National Aeronautical and Space Administration under NASA order W-14,569. The Arecibo observatory is operated by Cornell University under contract with the National Science Foundation.

Numerical calculations were performed by the FACOM M190 and M200 computers of the Data Processing Center of Kyoto University, and by the Harris /6 computer of the Arecibo Observatory, National Astronomy and Ionosphere Center.

ABSTRACT

The importance of the middle atmosphere research is rapidly increasing due mainly to concern over atmospheric ozone levels and to our greater interest in long term weather variability. The Middle Atmosphere Program (MAP), which will be carried out in 1982-1985, is the first international project to investigate the middle atmosphere from various aspects. The coherent radar technique is expected to play an important role in the MAP as a powerful tool of remote sensing.

The present work is motivated in two mutually related objectives: One is to establish the capability of existing large coherent radars in observing the middle atmosphere, and to study the dynamics of the middle atmosphere in detail. The other is to critically examine technical limitations and problems of these radars in order to give the basis of design concepts for the MU radar, the first large coherent radar to be constructed soon in Japan.

World's two largest coherent radars -the Jicamarca VHF radar (Peru) and the Arecibo UHF radar (Puerto Rico)- are used to investigate the mesosphere and stratosphere, respectively, in this work. Various phenomena such as the prevailing wind, waves with a wide range of periods, and the atmospheric turbulence are discussed based on continuous multi-height observations.

Considerations on technical limitations of these radars revealed that a good height resolution, a wide and fast beam steerability, and suppression of ground clutter contaminations have crucial importance in designing a radar system which can provide us a better understanding of the middle atmosphere. The design of the antenna is most important since the performance of the radar concerning most of these factors is directly determined by the capability of the

antenna.

Necessary specifications for the MU radar antenna are given based on the experiences of the observations made with the Jicamarca and Arecibo radars. Finally, a theoretical design for the MU radar antenna which satisfies the given specifications is presented.

TABLE OF CONTENTS

LIST OF TABLES

LIST OF FIGURES

CHAPTER 1
GENERAL INTRODUCTION

1.1 INTRODUCTION

Remote sensing by radio waves has been a powerful tool for investigating the earth's upper atmosphere. Among various techniques, the incoherent scatter radar is one of the most successful techniques for measuring physical parameters of the ionized plasma of this region (e.g., Evans, 1975).

Recently it was revealed that the same radar system can be used to observe the middle atmospheric heights (10-100 km) (Woodman and Guillén, 1974). Radar echoes from the middle atmosphere are thought to arise from macroscopic irregularities in the refractive index, so that it is called coherent scattering in contrast to the incoherent scattering from free electrons in ionized plasma. Several newly constructed coherent scatter radars, as well as a few incoherent scatter radars, have been devoted to the middle atmospheric study since the first experiment (see reviews by Balsley and Gage, 1980; Röttger, 1980; Harper and Gordon, 1980). The term 'coherent radar' is used for both kind of radars in this thesis to specify that it records spectral informations as well as the echo power. It is also called the Doppler radar in literatures of radar meteorology.

Concurrently, the importance of the middle atmosphere has been widely recognized both scientifically and practically since the possibility of destruction of the ozone layer by artificially released chemicals was pointed out (Molina and Rowland, 1974). In order to investigate the middle atmosphere in more detail from various aspects, the Middle Atmosphere Program (MAP) will be carried out internationally in 1982-1985. The coherent radar technique is expected to play an important role in the MAP as a powerful tool of the ground-based remote sensing. One of two main objectives of this

thesis is to clarify the characteristics of the dynamics of the middle atmosphere based on data taken by the Jicamarca VHF radar and the Arecibo UHF radar. The other is to examine capability and limitations of these radars in order to give basic design concepts to the MU radar, the first large coherent radar to be constructed soon in Japan.

In the following sections of this chapter, a general introduction to the thesis is presented. In Section 1.2, the basic structure of the middle atmosphere and characteristic parameters which dominate the atmospheric stability are discussed. In Section 1.3, scattering and reflection mechanisms which contribute to middle atmospheric echoes are discussed. Progress of coherent radar observations of the middle atmosphere is briefly reviewed in Section 1.4. Section 1.5 gives outline of the contents of the thesis.

1.2 THE MIDDLE ATMOSPHERE

The earth's atmosphere affects life on earth through various meteorological phenomena such as wind, precipitation, and storms. Measurements of atmospheric temperature, pressure, humidity, and wind velocity have been developed for use in weather forecasting. However, since most of atmospheric phenomena which directly affect human activities occur near the earth's surface, early scientific interest in the atmosphere was concentrated in the region below about 10 km or so. The lack of proper tool for measuring the higher regions was, of course, the another reason for this tendency.

The upper atmosphere above about 100 km suddenly gathered large attention when communication by radio waves started at the beginning of the 20th century. The nature of ionized plasma in this region has been extensively studied since then by means of sounding by radio waves, which are reflected there, and more recently, by rockets and satellites.

However, the region between 10 and 100 km was very poorly understood until direct measurements by meteorological rockets became available. This region is called the middle atmosphere in contrast to the lower and upper atmospheres, though boundaries between the different regions are not well defined. A better defined nomenclature of the atmosphere is the one based on the vertical structure of temperature. Fig.1-1 is a model of mid-latitude equinox temperature profile taken from the U.S. Standard Atmosphere (1976). The atmosphere is classified into 4 regions of the troposphere, stratosphere, mesosphere, and thermosphere in ascending order of height.

The troposphere is characterized by a constant decrease in temperature with height. The lapse rate of the model is 6.5 K km^{-1}. The main heat source for this region is the solar radiation absorbed by the surface of the earth. Temperature ceases to decrease at 10-15 km, at the tropopause. The height of the tropopause has a clear latitudinal variation, being highest in the equatorial region and decreasing with increasing latitude.

The stratosphere is the region in which temperature increases with height. The stable stratification of the air due to a positive temperature gradient accounts for the origin of the name of this region. Temperature reaches its maximum of about 270 K around 50 km at the stratopause height. The heat source for this maximum is the absorption of solar ultraviolet radiation by ozone.

Temperature decreases again in the mesosphere until it reaches the minimum of 180-190 K at the mesopause height of 80-90 km. The heat balance in this region is determined by the radiative heating of molecular oxygen and infrared radiative cooling of carbon dioxide.

Above 80-90 km, the temperature increases monotonically with height to the limit of 1000-2000 K due to radiative heating of atomic oxygen etc. This region is called the thermosphere in some nomenclature, but it is also called the ionosphere because ionized

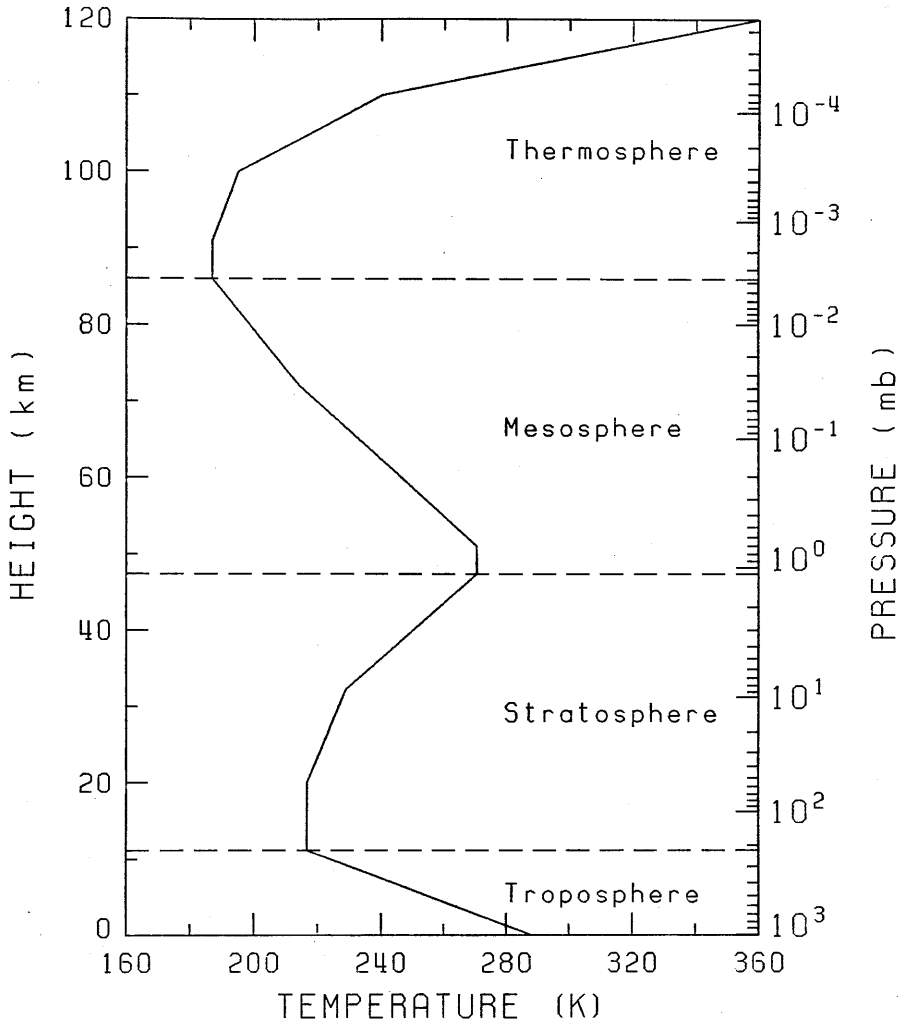

Fig.1-1 Temperature profile and nomenclature of the middle atmosphere (U.S. Standard Atmosphere 1976). The right ordinate shows the atmospheric pressure in millibars.

particles play an important role in this region.

The dynamical behavior of the middle atmosphere is well described by the following set of macroscopic equations for a perfect fluid (e.g., Kato, 1980):

The most fundamental is the equation of motion which is given by

$$\frac{D\vec{W}}{Dt} + 2(\vec{\Omega}\times\vec{W}) = -\frac{1}{\rho}\nabla p + \vec{g} + \vec{F} \tag{1.1}$$

where $D/Dt = \partial/\partial t + (\vec{W}\cdot\nabla)$ is the total derivative following the motion of the fluid, $\vec{W}$ is the velocity vector, $\vec{\Omega}$ is the angular velocity of the earth, ρ is the density, p is the pressure, $\vec{g}$ is the acceleration due to gravity, and $\vec{F}$ denotes external forces such as frictional force due to viscosity or electro-dynamic forces. The second term in the left-hand side of Eq.(1.1) is called the Coriolis force which is important in discussing long term phenomena such as the mean flow, tidal waves, and planetary waves. The density satisfies the continuity equation

$$\frac{D\rho}{Dt} + \rho\nabla\cdot\vec{W} = 0 \tag{1.2}$$

Also important is the energy conservation law

$$Q = C_v \frac{DT}{Dt} + p\frac{D}{Dt}\left(\frac{1}{\rho}\right) \tag{1.3}$$

where Q is the heat input per unit mass and time, T is temperature, and C_v is the specific heat capacity per unit mass. The pressure is related to density and temperature by the perfect gas equation

$$p = \rho RT \tag{1.4}$$

where R is the gas constant.

Eqs.(1.1)-(1.4) give a closed set for all parameters. Thus any phenomenon can be, in principle, described by solving these

equations if boundary and initial conditions are given, and external forces and heat source or sink are specified. Direct solutions for these equations are of course unobtainable for most realistic situations, even numerically, because of the complicated nature of these equations. Therefore various simplifications are made to the equations according to scale analysis, depending on the time and spatial scales of interest. Physically it is equivalent to filtering out undesired time or spatial scales (e.g., Holton, 1975). The simplest situation is the static state obtained by neglecting the time derivative, wind velocity, and external forces in Eq.(1.1). It reduces to

$$\frac{dp_o}{dz} = -\rho_o g$$
$$\frac{dp_o}{dx} = \frac{dp_o}{dy} = 0 \qquad (1.5)$$

where subscript o denotes static part, and x,y,z are coordinates taken in latitudinal, longitudinal, and vertical directions, respectively. Eq.(1.5) can be readily integrated with the aid of Eq.(1.4) to give

$$p_o = p_{oo} \exp(-\int \frac{dz}{H})$$
$$\rho_o = \rho_{oo} \frac{T_{oo}}{T_o} \exp(-\int \frac{dz}{H}) \qquad (1.6)$$

where H is the scale height defined by

$$H = RT_o/g \qquad (1.7)$$

and subscript oo denotes the value at level z = 0. This state is called the hydrostatic equilibrium and all atmospheric motions are superimposed on this state. The right ordinate of Fig.1-1 is the pressure determined by Eqs.(1.6) and (1.7) from the model

temperature profile. The hydrostatic atmosphere is dominated by the heat balance which determines the temperature profile.

If a small external force is applied in the vertical direction to an air parcel in the hydrostatic equilibrium, it oscillates at an angular frequency N given by (e.g., Gossard and Hooke, 1975)

$$N^2 = \frac{g}{T_o} (\Gamma + \frac{dT_o}{dz}) \tag{1.8}$$

where Γ is the adiabatic lapse rate for dry air, which is 9.76 K km^{-1}. This frequency is called the Brunt-Väisälä frequency. Eq.(1.8) suggests that the atmosphere becomes unstable if the right-hand side of the equation becomes negative. Thus the static stability of a stationary atmosphere can be judged simply by examining the lapse rate and by comparing it to the lapse rate of the dry air.

The stability condition becomes different when a steady flow is superimposed on the atmosphere in the hydrostatic equilibrium. The shearing stress between adjascent air parcels may produce a dynamic instability known as the Kelvin-Helmholtz instability (e.g., Dutton, 1971). A commonly used parameter to indicate the dynamic stability of the atmosphere is the ratio of the stability force due to buoyancy to the accelerating force due to shearing stress defined as (e.g., Tennekes and Lumley, 1972)

$$R_i \equiv N^2/(\frac{\partial U}{\partial z})^2 \tag{1.9}$$

where U is the horizontal mean wind velocity. This parameter is called the gradient Richardson number, or simply, the Richardson number. The atmosphere becomes turbulent if the wind shear becomes sufficiently large even if it is statically stable. However, a strict threshold for turbulence to occur depends on velocity and density structure, and is difficult to calculate for a general case since turbulence is a highly non-linear phenomenon. It is known

that a sufficient condition for the atmosphere to be stable against a small disturbance is that $R_i > 1/4$ everywhere in the flow (Miles, 1961). Observations have shown that turbulence cannot be maintained if R_i is larger than about 0.2 (Tennekes and Lumley, 1972).

1.3 SCATTERING AND REFLECTION OF RADIO WAVES BY ATMOSPHERIC IRREGULARITIES

When a radio wave is transmitted toward a target, the received echo power P_r is given by the well known radar equation (e.g., Skolnik, 1980) as

$$P_r = \frac{P_t G A_e \sigma}{(4\pi)^2 r^4} \tag{1.10}$$

where P_t is the transmitted power, G is the gain of transmitting antenna, A_e is the effective area of receiving antenna, σ is the scattering cross section of the target, and r is range of the target. According to antenna theory, the gain is related to the effective area by

$$G = \frac{4\pi A_e}{\lambda^2} \tag{1.11}$$

where λ is the radar wavelength. Thus Eq.(1.10) can be rewritten for a monostatic radar using (1.11) as

$$P_r = \frac{P_t A_e^2 \sigma}{4\pi \lambda^2 r^4} \tag{1.12}$$

In radar observations of the middle atmosphere, the target is not usually a point, but often distributed in space. The radar equation for uniformly distributed targets, observed by an antenna with a Gaussian radiation pattern, is given by (Probert-Jones, 1962)

$$P_r = \frac{P_t A_e \Delta r \eta}{9\pi r^2} \tag{1.13}$$

where Δr is the range resolution which determines the thickness of target, and η is the volume reflectivity, or the scattering cross section per unit volume.

Physically, the radar cross section of the atmosphere can be interpreted in terms of irregularities in refractive index n (Booker and Gordon, 1950). For radio waves of VHF, UHF, and SHF range, the refractive index is given approximately as (Balsley and Gage, 1980)

$$n-1 = \frac{3.73\times10^{-1}e}{T^2} + \frac{7.76\times10^{-5}p}{T} - 4.48\times10^{-16}N_e \tag{1.14}$$

where e is the water vapor pressure in millibars, and N_e is the electron number density.

The right-hand side of Eq.(1.14) contains three kinds of contributions. The first and the second terms are due to water vapor and dry air, respectively, and the last term is due to free electrons. The first term is important in the lower troposphere in which most water vapor is concentrated. The second term dominates up to around stratopause height. The last term is the major contribution in the upper atmosphere, but its importance in the middle atmosphere depends on frequency. For a frequency of 50 MHz, it exceeds the second term at 50-60 km, while it is smaller until about 70 km at 400 MHz.

Fig.1-2 illustrates these three terms versus height. The pressure and temperature are taken from the model in Fig.1-1. The saturation pressure is used for the water vapor contribution. The electron density is adopted from Mechtly et al. (1972).

Among various mechanisms which can cause inhomogeneity or fluctuations in the refractive index, turbulence is one of the most important of these phenomena for middle atmospheric observations. The volume reflectivity is expressed in terms of the three-dimensional wavenumber spectrum of turbulent fluctuations in the

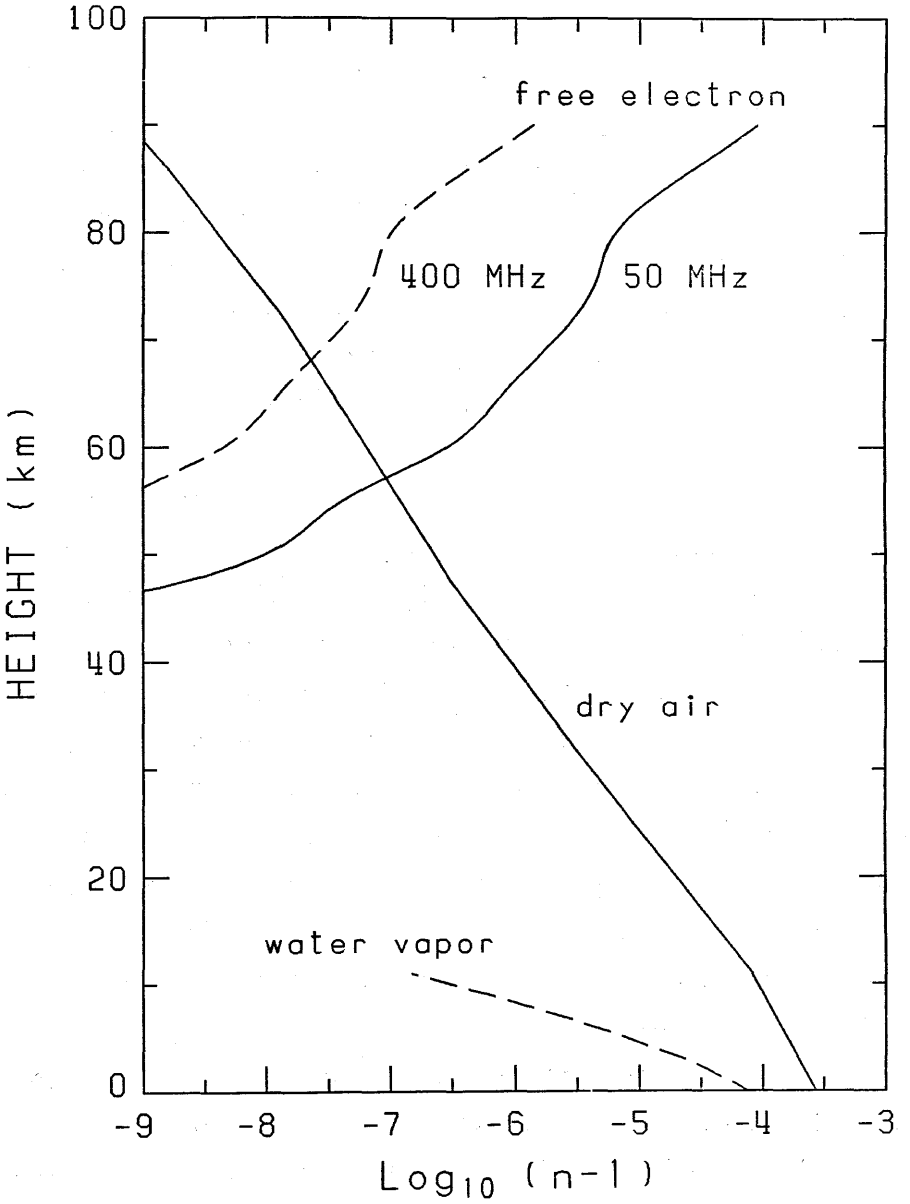

Fig.1-2 Height variation of major contributions to the refractive index.

refractive index $\Phi_n(k)$ as (Ottersten, 1969)

$$\eta = \frac{\pi^2}{2} k^4 \Phi_n(k) \tag{1.15}$$

where $k = 4\pi/\lambda$ is the Bragg wavenumber which is observed by the radar. $\Phi_n(k)$ is normalized to the mean-square fluctuation of n by

$$\int_{-\infty}^{\infty} \Phi_n(k)\, dk = \langle \Delta n^2 \rangle \tag{1.16}$$

If the turbulence is locally homogeneous and isotropic (Tatarskii, 1971)

$$\Phi_n(k) = 0.033 C_n^2 k^{-11/3} \exp(-0.0371 \alpha^3 \ell_i^2 k^2) \tag{1.17}$$

where C_n^2 is called the refractivity structure constant, α is a constant of order unity, and ℓ_i is the inner scale of turbulence. The inner scale gives the boundary between the inertial subrange and the viscous subrange of turbulence. The inertial subrange is the range of wavenumber in which kinetic energy of turbulence is transferred to smaller sizes without much loss. Viscous dissipation becomes dominant for motions with scale sizes smaller than the inner scale. By substituting (1.17) into (1.15) we obtain

$$\eta = 0.38 C_n^2 \lambda^{-1/3} \exp(-5.85 \alpha^3 \ell_o^2 \lambda^{-2}) \tag{1.18}$$

Eq.(1.18) shows that the wavelength dependence of η is small if $\lambda/2 \gg \ell_o$, i.e. the scale size probed by the radar falls in the inertial subrange of turbulence. If $\lambda/2 < \ell_o$, on the other hand, the turbulence is in viscous subrange and the reflectivity falls off very rapidly with decreasing wavelength.

Observational evidence shows that in the stratosphere, all wavelengths at VHF and UHF satisfy the innertial subrange condition, while UHF falls within the viscous subrange in the mesosphere (e.g.,

Rastogi and Bowhill, 1976c). Therefore only radars with VHF frequencies can observe turbulent scatter from the mesosphere.

Turbulence contributes to the volume reflectivity through random fluctuations in refractive index. Coherent structures of the refractive index also contributes to the radar echo, which is known as Fresnel or partial reflection. It was first utilized to investigate the lower ionosphere with frequencies of 1-5 MHz (e.g., Belrose, 1970). The same mechanism has often been observed in the middle atmosphere by VHF radars as shown later.

The radar equation must be modified for the Fresnel reflection since it is essentially a two-dimensional phenomenon characterized by a reflection coefficient ξ rather than the volume reflectivity η, which describes a three-dimensional scattering. It is expressed as (Friend, 1949)

$$P_r = \frac{P_t A_e^2}{4\lambda^2 r^2} |\xi|^2 \tag{1.19}$$

For a horizontally extended layer, the reflection coefficient is given in terms of the vertical gradient of the refractive index by (Wait, 1970)

$$\xi = \frac{1}{2\cos^2\theta} \int_{-\ell/2}^{+\ell/2} \frac{dn}{dz} \exp(-jkz \cos\theta)\, dz \tag{1.20}$$

where ℓ is the thickness of the layer, and θ is the angle of incidence.

In the upper atmosphere, thermal fluctuations in individual free electrons cause weak scattering known as incoherent scatter. It has been used as a powerful tool for measuring ionospheric parameters for the past two decades (e.g., Evans, 1975). The volume reflectivity of a collision-free plasma in thermal equilibrium probed by a wavelength much longer than the local Debye length is given by (e.g., Fejer, 1960)

$$\eta = \frac{1}{2} N_e \sigma_e \qquad (1.21)$$

where σ_e is the scattering cross section of an electron.

1.4 MIDDLE ATMOSPHERIC STUDIES BY COHERENT RADARS

VHF radar investigation of the middle atmosphere was first made at Jicamarca in 1971 (Woodman and Guillén, 1974). Since then, a remarkable progress has been made then in our understanding of this region. Here we will briefly review results of recent middle atmospheric studies by coherent radars.

a) Signal characteristics

In the first experiment, strong backscatter echoes were obtained from two separate regions : the lower stratosphere of 10-30 km, and the mesosphere of 60-85 km. Fig.1-3 shows the mean echo power versus height (Woodman and Guillén, 1974). Different heights were observed sequentially with 2 min integration. Theoretical estimates for the echo power expected from the turbulent scatter are also plotted in the figure. The magnitude of fluctuations in the refractive index was estimated as the height gradient of the index times the vertical size of the largest vortex in the turbulence, which was assumed to be 100 m. The observed levels agree well with the theoretical value both in the stratosphere and mesosphere. It is worth mentioning that the echo power in the mesosphere is much stronger than the expected incoherent scatter level plotted as a reference.

A large gap at 40-50 km roughly agrees with that of the refractive index due to transition between the dry air and free electron contributions as shown in Fig.1-2. Therefore it is concluded that the scattering from the stratosphere is due to fluctuations of the dry air component of the refractive index, while

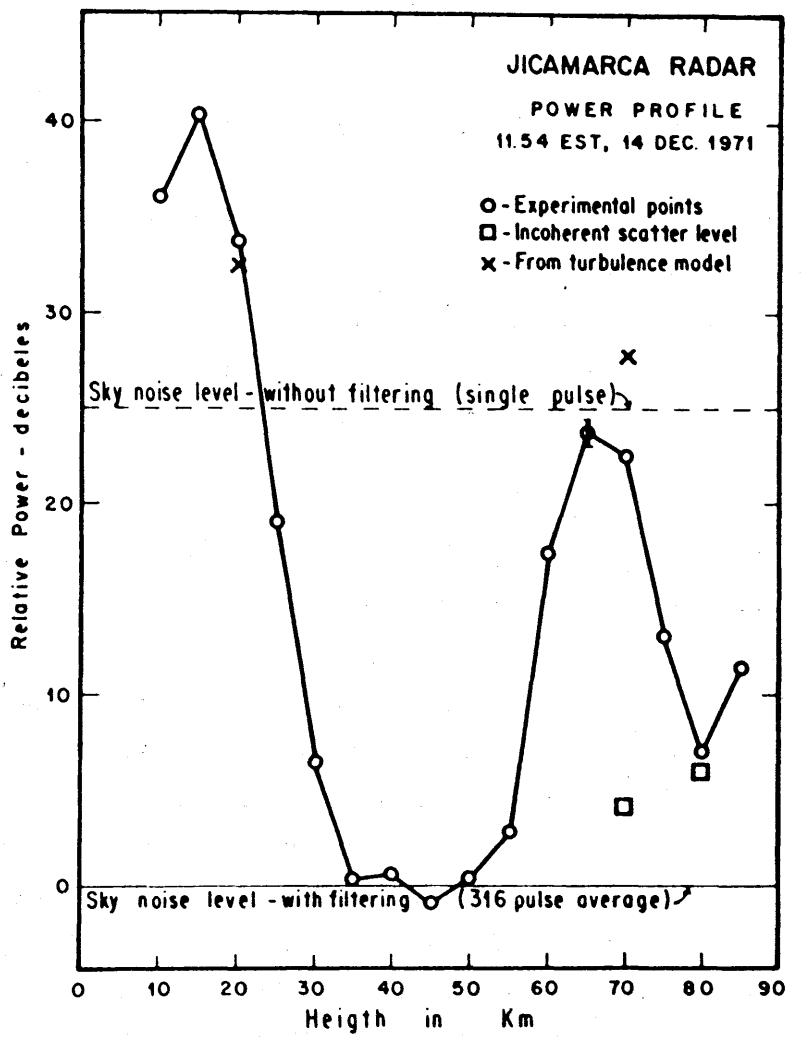

Fig.1-3 Echo power profile obtained by the Jicamarca VHF radar. Expected echo power level calculated from turbulent scatter and incoherent scatter theory are plotted for reference (after Woodman and Guillén, 1974).

irregularities in the electron density gradient is the main source of the mesospheric echoes. The mesospheric echoes disappear during nighttime, since the ionization in this region is produced mainly by solar ultraviolet (121.6 nm) radiation and has very short lifetime (e.g., Ratcliffe, 1960). Rapid decay of the mesospheric echo power above 70 km is due to the fact that the turbulence probed by the Jicamarca VHF radar falls into the viscous subrange (Rastogi and Bowhill, 1976c).

At higher frequencies in the UHF range, the transition from the inertial to viscous subranges occurs at a much lower height, so that turbulent scatter is observed only below about 30 km, where the dry air contribution dominates the refractive index. Recently, however, weak incoherent scatter from the mesosphere was detected by the French 935 MHz radar (Fukuyama, 1980), and the lower limit where incoherent scatter from free electrons can be detected was extended down to about 65 km using the Arecibo UHF radar by implementing a pulse compression technique (Harper, 1978).

b) Turbulent layers

The middle atmosphere is statically stable on average as is indicated by the temperature profile shown in Fig.1-1, but turbulence would be produced by local shear instabilities. Since the large shear required to excite an instability cannot be maintained over a large height range, the turbulence inherently appears as thin layers. This is confirmed by high resolution observations by Röttger and Schmidt (1979), Czechowsky et al., (1979), and Sato and Woodman (1980). The measured thickness of the layers as limited by equipment resolution is of the order of 100 m, and can be estimated to be even less as discussed in Chapter 5.

The abrupt change in the refractive index at nonturbulent-turbulent interfaces causes Fresnel reflections when the antenna beam is pointed toward zenith. Fig.1-4 compares vertical profiles of echo power S of vertically and obliquely incident waves observed

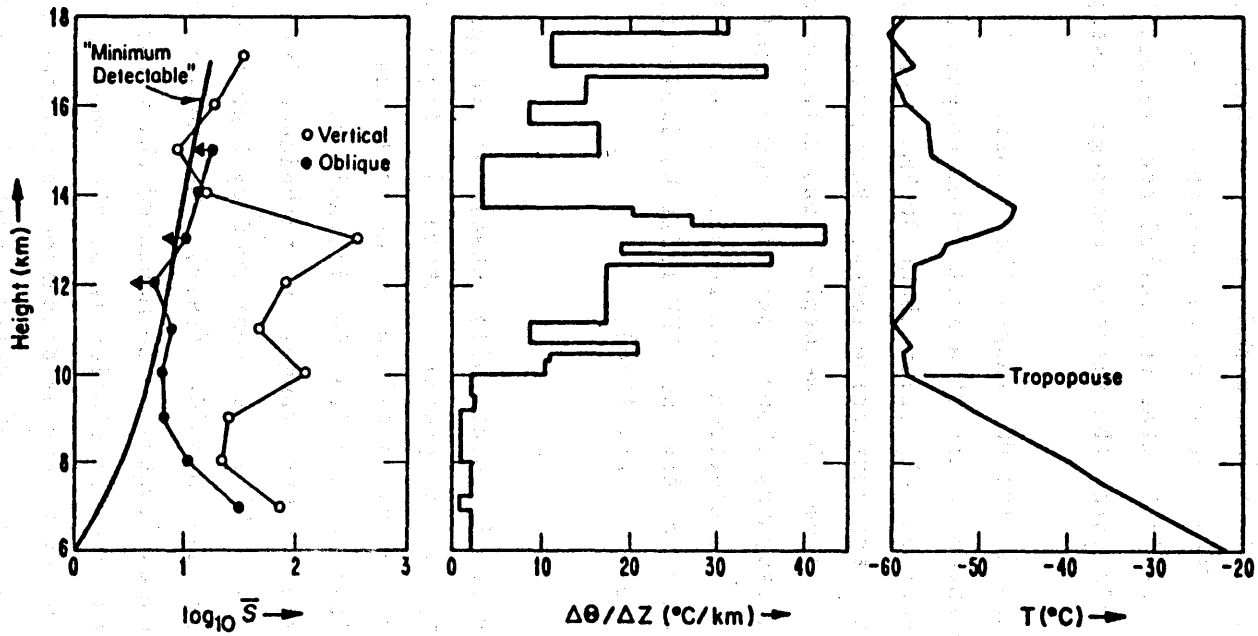

Fig.1-4 Height variation of the echo power S of vertically and obliquely incident waves observed by Sunset VHF radar on March 26, 1977. Height profiles of potential temperature gradient $\Delta\Theta/\Delta z$ and temperature T are obtained by rawinsonde flights from Denver, Colorado (after Gage and Green, 1978).

by the Sunset VHF radar (after Gage and Green, 1978). Temperature T and potential temperature gradient $\Delta\theta/\Delta z$ inferred from rawinsonde observations are also plotted in the figure. The echo power from the vertical direction is about an order of magnitude stronger than that from the oblique direction in the lower stratosphere, suggesting the existence of the Fresnel reflection. A good correlation exists between the vertical echo power and the potential temperature gradient, which is directly related to the stability of the atmosphere.

Similar evidences for the Fresnel reflection have been found by the SOUSY VHF radar in the upper troposphere (Röttger and Liu, 1978) and in the lower mesosphere by the Jicamarca VHF radar (Fukao et al., 1979). Gage and Green (1979) used this aspect sensitivity to monitor the height of the tropopause, and found a good agreement with that measured by rawinsondes.

Various attempts have been made to estimate physical parameters of turbulence such as the energy dissipation rate and the eddy diffusion coefficient. VanZandt et al. (1978) and Gage et al. (1980) used the refractivity turbulence structure constant C_n^2 derived from the echo power to obtain these parameters with the aid of temperature profiles measured by rawinsondes. Cunnold (1975) interpreted spectral width of the mesospheric echoes observed by Woodman and Guillén (1974) in terms of velocity fluctuations of turbulence.

c) Prevailing wind and long period waves

The mean Doppler frequency shift of the echo power spectra gives the radial velocity of the background flow with which the turbulent layers are drifting. Since the mean vertical velocity is much smaller (though not zero) than the horizontal components, prevailing wind and long period waves can be obtained by tilting the antenna beam from zenith.

Excellent agreements have been found between the stratospheric

wind profiles measured by rawinsondes and those obtained by the Sunset VHF radar (Green et al., 1979), the Arecibo UHF radar (Farley et al., 1979), the Poker Flat VHF radar (Ecklund et al., 1977), and the Platteville VHF radar (Ecklund et al., 1979). Fig.1-5 shows an example of these comparisons made between the Arecibo UHF radar and a rawinsonde observation from San Juan, Puerto Rico (after Farley et al., 1979)

Comparisons of the mesospheric wind profiles with meteorological rocket observations were made with the Jicamarca VHF radar (Fukao et al., 1979) as shown in Chapter 3.

Diurnal and semidiurnal oscillations associated with atmospheric tides have been detected at stratospheric heights by the Jicamarca VHF radar (Fukao et al., 1978), and by the Arecibo UHF radar (Fukao et al., 1980e). The inferred amplitude of tidal waves suggested the possibility of a local non-migrating tide superimposed on a global migrating tide predicted by classical tidal theory.

Wave phenomena with even longer period than tides have been observed in the stratosphere by the Platteville VHF radar (Ecklund et al., 1979), by the Arecibo UHF radar (Sato and Woodman, 1981a), and also in the mesosphere by the Jicamarca VHF radar (Fukao et al., 1980d), which were discussed in terms of planetary scale waves as Rossby waves and mixed Rossby-gravity waves.

d) Short period waves and oscillations

Middle atmospheric winds also contain acoustic gravity waves with periods shorter than the tidal or planetary wave periods. The Brunt-Väisälä frequency discussed before gives the high-frequency cutoff to the internal gravity wave mode (e.g., Hines, 1960). A good example to show this cutoff is given in Fig.1-6 in the fashion of time-height contours of vertical wind velocity (left), and period-height contours of power spectra of the wind velocity (right) (after Röttger, 1980). The data were taken just after a thunder storm had passed the radar site. The dotted curve in the spectra

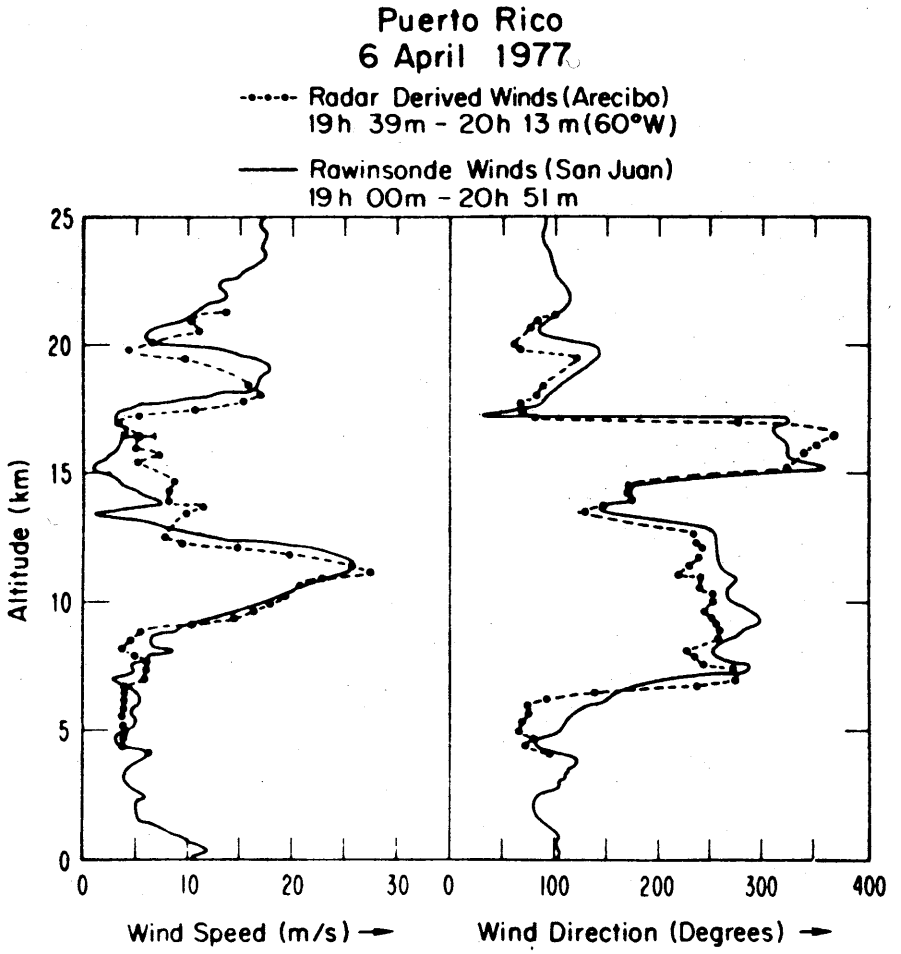

Fig.1-5 Comparison of height profiles of horizontal wind velocities observed by the Arecibo UHF radar on April 6, 1977 and rawinsonde from San Juan, Puerto Rico (after Farley et al., 1979).

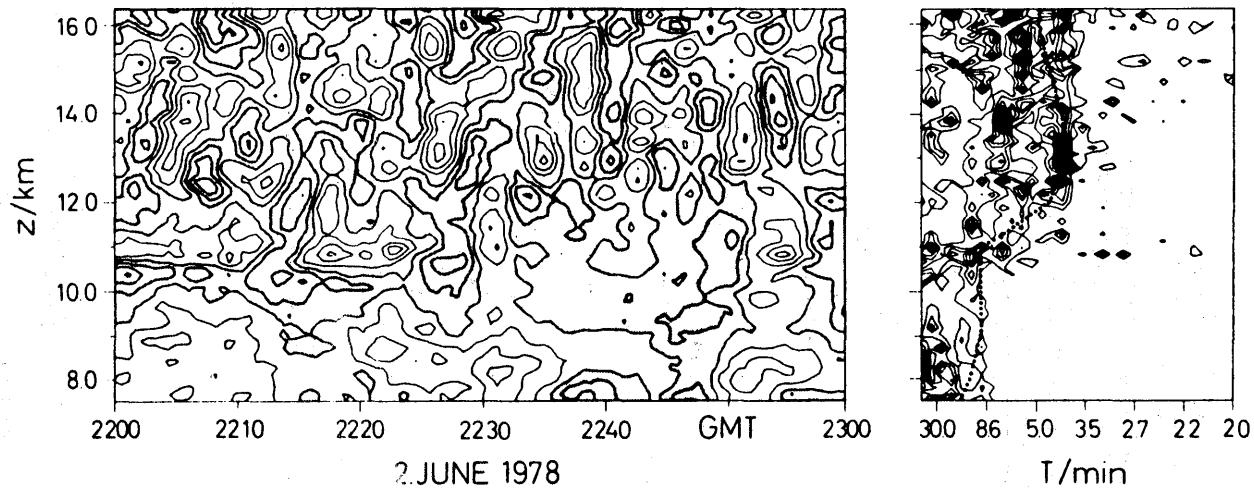

Fig.1-6 Contour plots of vertical velocity versus time and height (left) and of frequency power spectra of the velocity versus period and height (right) observed by the SOUSY VHF radar on June 2, 1978. Contours for the velocity are drawn at 0.125 m s^{-1} interval. The dotted curve shows the Brunt-Väisälä period calculated from rawinsonde data from Berlin (after Röttger, 1980).

indicates the height profile of the Brunt-Väisälä period deduced from rawinsonde data from Berlin.

Sinusoidal short period waves are often observed both in the stratosphere (VanZandt et al., 1979; Rüster and Czechowsky, 1980; Fukao et al., 1980b; Sato and Woodman, 1981a), and mesosphere (Woodman and Guillén, 1974; Rastogi and Bowhill, 1976a; Miller et al., 1978; Fukao et al., 1979). Fig.1-7 shows an example of mesospheric waves observed by the Urbana VHF radar (after Miller et al., 1978). They have been interpreted in terms of trapped and propagating gravity waves and Brunt-Väisälä oscillations, and attempts were made to estimate their wavenumbers.

1.5 CONTENTS OF THE THESIS

The present work consists of chapters with mutually related, but slightly different contents. Chapters 3 and 5 are concerned mainly with scientific aspects of the dynamics of the middle atmosphere. The objective of these chapters is to establish the capability of existing large coherent radars in observing the middle atmosphere, and to study the dynamics of the middle atmosphere in detail.

Chapters 2, 4, and 6, on the other hand, deal with technical aspects of existing and planned coherent radars for middle atmospheric observations. These chapters have a common objective of obtaining the basis of the design concepts for the MU radar. Technical limitations and problems encountered in observations with the Jicamarca and Arecibo radars are examined in Chapters 2 and 4 in order to provide scientific specifications that the MU radar should satisfy, and a solution is given by the design considerations presented in Chapter 6.

In Chapter 2, the Jicamarca VHF radar system and observational techniques for the middle atmosphere established in earlier works (e.g., Woodman and Guillén, 1974; Rastogi and Bowhill, 1975) are

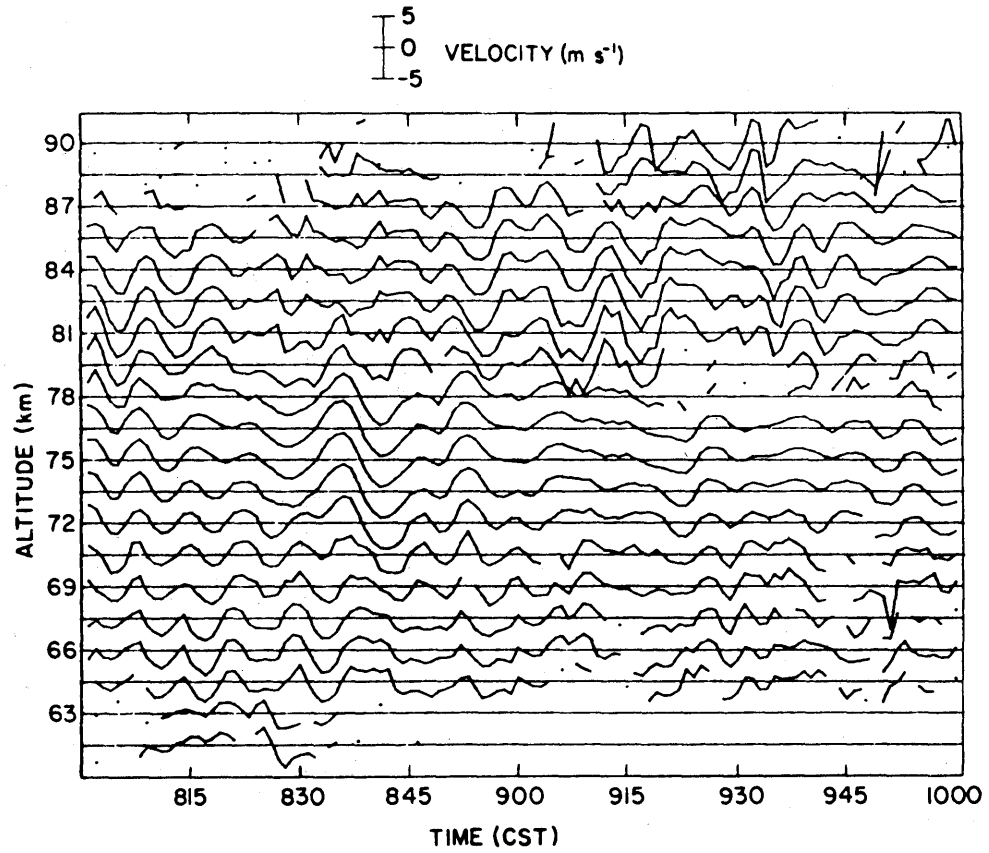

Fig.1-7 Mesospheric radial velocity versus time at different heights observed by the Urbana VHF radar on April 11, 1978. The antenna beam is tilted about 1.5° from zenith toward the southeast (after Miller et al., 1978).

described first. Next, effects of a few technical limitations such as the height resolution (Sato and Fukao, 1981) and the antenna beam steerability on observed parameters and observational capability is examined in detail. It is shown that these factors have crucial importance in a detailed study of the dynamics of the middle atmosphere.

Results of the analysis of two continuous mesospheric observations made with the Jicamarca VHF radar performed by Harper (Harper and Woodman, 1977), and by Kato et al. (Fukao et al., 1980c) are presented in Chapter 3. After the general characteristics of received signals are described, prevailing wind, long and short period waves, and mesospheric turbulence are discussed. The mean zonal wind is compared to that measured by meteorological rockets. The importance of long period waves with 2-5 day period will be demonstrated. The propagation characteristics of short period waves are examined. Mesospheric turbulent layers are discussed in terms of the aspect sensitivity in echo power and correlation between the echo power and signal correlation time.

System construction of the Arecibo UHF radar and observational and analysis techniques developed for stratospheric experiments (Woodman, 1980a; Sato and Woodman, 1980) are given in Chapter 4. Theoretical features of the complementary pulse coding scheme are compared to the observed performance. A non-linear parameter estimation procedure is applied to observed power spectra to eliminate effects of very strong fading clutter contaminations.

In Chapter 5, stratospheric dynamics are discussed based on a series of high-resolution experiments made with the Arecibo UHF radar. Planetary scale waves with a short vertical wavelength and very short period wind oscillations cannot be observed without high-resolution equipment. The thickness of stratospheric turbulent layers is estimated by a beam swinging experiment. An attempt is made to deduce physical parameters of the turbulence from the observed spectral width.

Chapter 6 concerns design concepts of the MU radar. The outline of the MU radar project (Fukao et al., 1980a) is described first. Then important requirements for the capability of the MU radar revealed by the considerations made in Chapters 2-5 are summarized. It is shown that the performance of the radar concerning these requirements is directly determined by the antenna design, which turns out to be the most important part in the whole system design.

Antenna array design is examined in terms of the beam steerability and the sidelobe suppression ratio, and an improved arrangement of antenna elements is proposed. Dimensions of Yagi antennas, which will be used as array elements, are designed based on an optimization procedure for an infinite array, taking the effects of the mutual coupling between elements into account. Lastly, the effects of a finite array is examined, and it is shown to be not serious except for the outermost elements.

The main conclusions of each chapter are summarized in Chapter 7.

CHAPTER 2

TECHNICAL CONSIDERATIONS ON THE JICAMARCA VHF RADAR OBSERVATIONS

2.1 THE JICAMARCA VHF RADAR SYSTEM

The Jicamarca VHF radar is located in a dry valley of Jicamarca (11.95°S, 76.87°W), about 30 km northeast of Lima, Peru. Its original objective was to observe the properties of the ionosphere and the exosphere by means of incoherently scattered echoes from fluctuations in the electron density of these regions. The location, which is 1° north of the geomagnetic equator, was chosen from geomagnetic considerations. It was built in 1960-1961 as a joint project of the National Bureau of Standards of U.S.A. and the Instituto Geofisico del Peru, and is operated by the latter. Details of the construction process and descriptions on the facility can be found in reports by Bowles (1961) and Ochs (1965). Fig.2-1 shows an aerial view of the Jicamarca Radio Observatory (after Rastogi and Bowhill, 1975).

The operational frequency of the Jicamarca VHF radar is 49.92 MHz. The antenna consists of two arrays of square half-wave (3 m) dipoles superimposed mutually orthogonally. Each array has the same dimensions of 288 m × 288 m, containing 9216 dipoles, and can be divided into 4 quarters. Each quarter is further subdivided into 16 square modules. A module consists of 12 parallel rows of 12 half-wave dipoles connected side-by-side. The dipoles are made of coaxial feed line, and the inner and the outer conductors are reversally connected at each junction in order to excite all dipoles in phase. The dipoles are supported by wooden posts by 1.8 m above the reflecting screen made of poultry net.

The modules are connected by equal length coaxial cables to the center of the quarters. All of these quarters are connected individually to the switchyard by equal length aluminum transmission

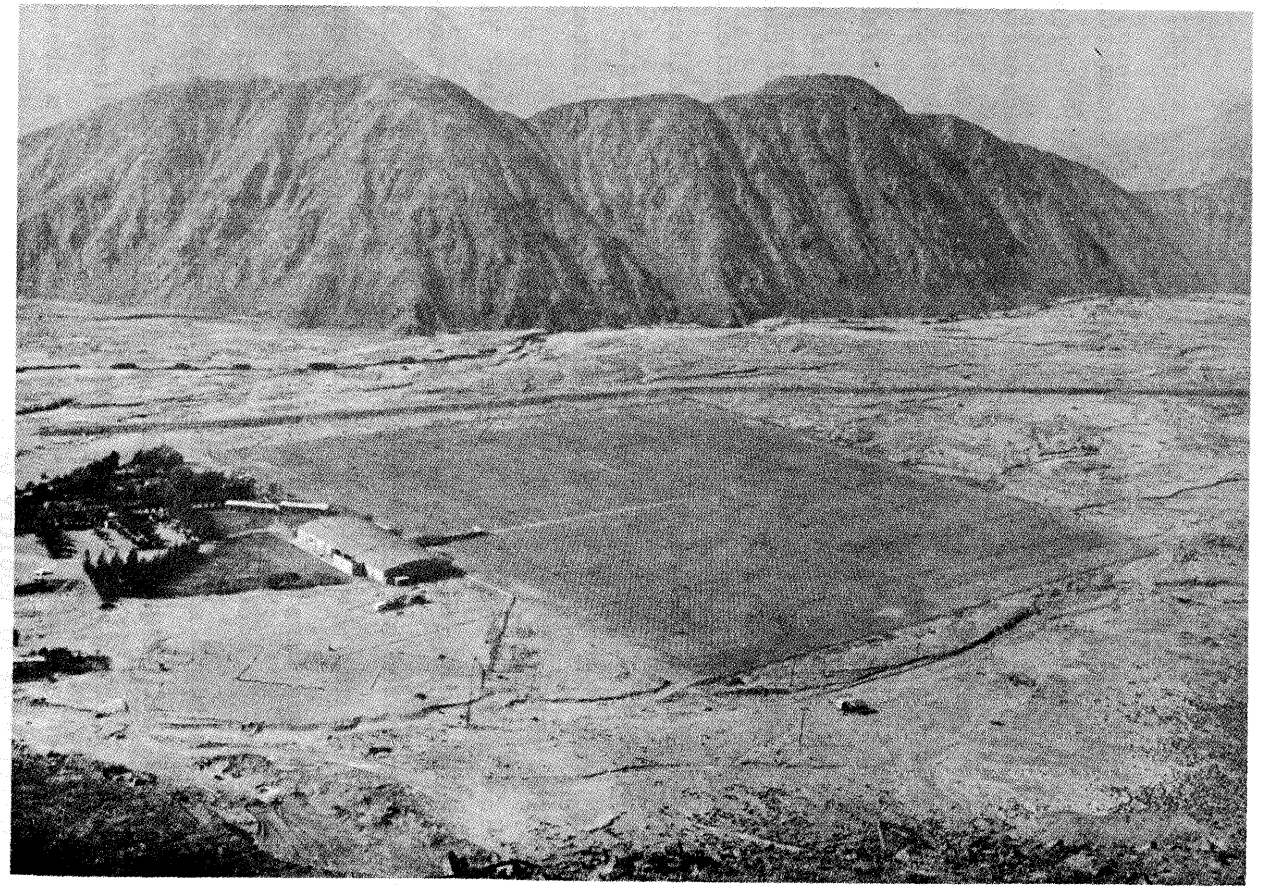

Fig.2-1 An aerial view of the Jicamarca Radio Observatory, Lima, Peru (after Rastogi and Bowhill, 1975).

lines. Therefore 8 independent quarters can be used separately at the same time, though the maximum number of partition is limited to 4 by the number of transmitters and receivers available. The half-power beam width of the full antenna and a quarter are 1.06° and 4.24°, respectively. The antenna plane is tilted about 1° in order to point the antenna beam perpendicular to the geomagnetic field line. The antenna beam can be steered manually from the on-axis direction by inserting additional cables at each module junction. Fig.2-2 illustrates the computed one-way radiation pattern of the full antenna at three different antenna beam directions. The maximum steering angle from the on-axis direction is limited to about 4° as shown later.

The switchyard is composed of the TR and ATR switches and the hybrid divider/combiner. The TR and ATR switches have functions of separating the transmitter and receiver, and connecting or disconnecting them to the antenna according to the presence of a high voltage transmitter pulse. The switches are made of tungsten spark gaps and quarter wavelength impedance transformers. The hybrid divider/combiner allows various connections between 4 transmitters and 8 quarters of two polarizations. It also keeps the isolation between individual transmitters when outputs of transmitters are combined.

A quartz basic oscillator generates the reference signal of 0.9984 MHz. It is multiplied 50 times to obtain the nominal operational frequency of 49.92 MHz. The RF signal is amplified through the exciter, the intermidiate amplifier, the driver amplifier, and the power amplifier up to the nominal peak power of 1.5 MW. Each power amplifier uses single water-cooled shielded grid triode operating at class-C mode. Control grids of each stage are turned on and off by the control pulse from the radar controller to generate pulses with a desired pulse width and the inter-pulse-period (IPP). The phase of the RF pulses are reversed alternately by the flip amplifier in order to remove dc offsets of the data

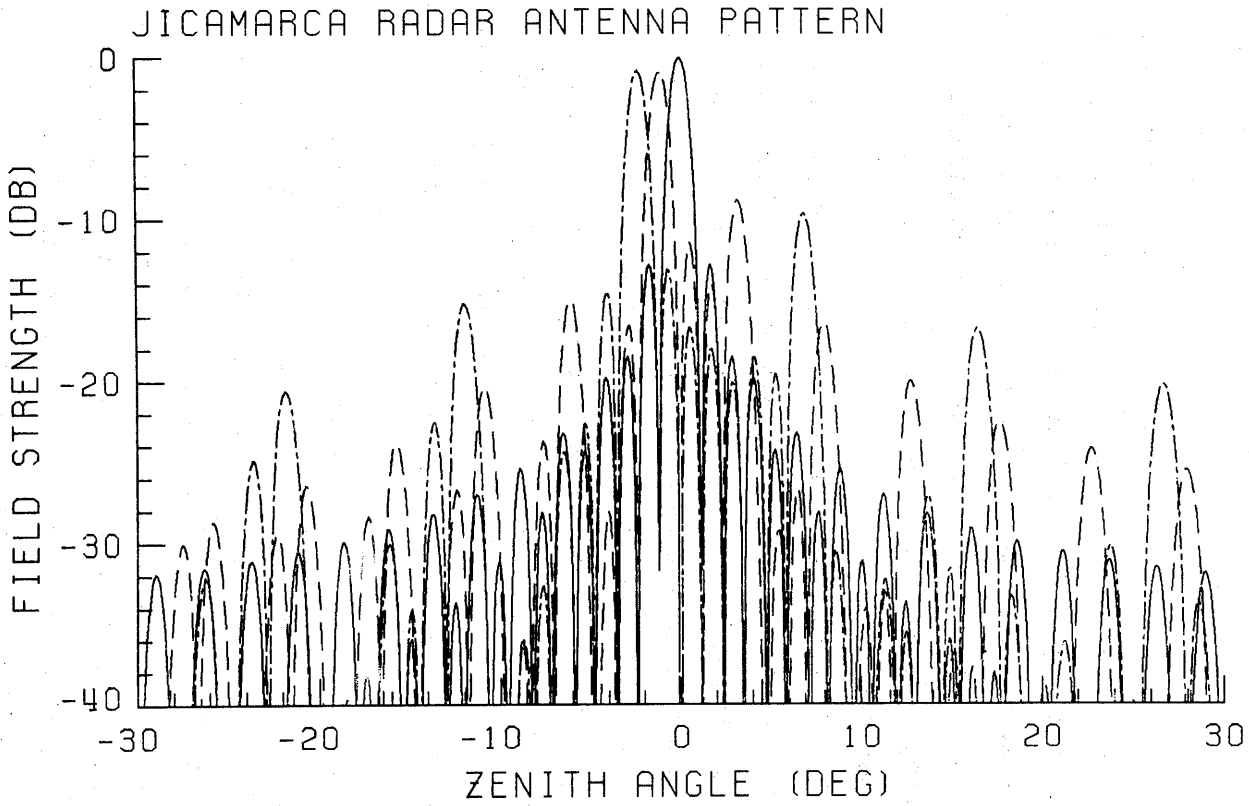

Fig.2-2 Computed one-way radiation patterns of the Jicamarca antenna. The solid, dashed curves, and chain are for the antenna beam directions of 0°, 1.2°, and 2.4° from zenith, respectively.

taking system.

The receiver utilizes a double conversion super heterodyne system with the first and the second IF of 4.75 MHz and 455 kHz, respectively. The phase detector which works on the second IF detects two orthogonal baseband signals referred to as the sine and cosine channel outputs. These output are low-pass filtered with a cutoff frequency matched to the width of the transmitter pulse. The output signals from different receivers are sampled and holded by the multiplexer, digitized, then transferred to the Datacraft DC-6024/3 computer for further processing.

Characteristics of the Jicamarca VHF radar are summarized in Table 2-1.

2.2 OBSERVATIONAL TECHNIQUES FOR THE MIDDLE ATMOSPHERIC STUDY

Coherent radar observations of the middle atmosphere consists of the measurements of the echo power, Doppler shift, and spectral shape. The method of obtaining frequency power spectra depends primarily on the relation between the signal correlation time τ_c and the IPP T, because the sampling interval of data should be shorter enough than τ_c in order to obtain un-aliased spectra. If $\tau_c < T$, multiple sampling points at the same height are required within one transmit/receive cycle. This is a fairly troublesome requirement because a different sample timing corresponds to a different observing height. This is the case for most of incoherent scatter observations of the ionosphere, for which various pulse schemes have been developed to overcome this difficulty (e.g., Farley, 1969). If $\tau_c > T$, on the other hand, the situation becomes simpler since only one sample at each height is sufficient in one transmit/receive cycle. In this case, the time delay t after the transmission of a pulse can be directly read as the observing height h by the relation $h = ct/2$, where c is the speed of light. The middle atmospheric observations using VHF or UHF radars fall in this category, and

Table 2-1 Characteristics of the Jicamarca VHF radar (after Ochs, 1965)

Location	: Jicamarca, Peru (11.95°S, 76.87°W)
Frequency	: 49.92 MHz
Antenna	
configuration	: square array of crossed half-wave dipoles
aperture	: 83000 m^2 (288 m × 288 m)
beamwidth	: 1.06°
on-axis gain	: 42.6 dB
on-axis efficiency	: 0.63
polarizations	: linear and circular
separation	: > 50 dB between linear polarizations
	: > 70 dB between adjascent quarters
beam direction	: 0-4° zenith angle (discrete points)
Transmitter	
final amplifier	: four shielded-grid triodes
peak power	: 1.5 MW × 4 (nominal)
bandwidth	: ~ 40 kHz
TR/ATR switches	: tungsten spark gaps
Receiver	
bandwidth	: ~ 40 kHz
IF	: 4.75 MHz and 455 kHz
A/D converter	: 8 bit × 8 channel
Computer	: Datacraft DC-6024/3

techniques have been developed to obtain spectral parameters from the time series of echoes received from successive pulses (e.g., Woodman and Guillén, 1974; Rastogi and Bowhill, 1975).

In the two series of mesospheric observations presented in the following chapter, IPP was chosen to be 0.866 and 1 ms. Since the signal correlation time of mesospheric echoes observed by the Jicamarca VHF radar is of the order of 1 s, the sampling interval can be as long as about 0.1 s for a reasonably good estimate of the frequency spectra. Thus the sampled data obtained every IPP were averaged over about 100 times. This process is called 'coherent integration', and the coherent integration of N points is equivalent to narrower the receiver bandwidth to 1/N, thus improving the signal-to-noise ratio by N times. The word 'coherent' refers to the fact that the phase coherency between samples is kept during the average process, since it is performed on the complex time series.

The frequency power spectra, or its Fourier transform pair, the auto-correlation function, is computed from the integrated time series. Although equivalent for infinite data points, the effect of finite length of data points appears differently on these two functions. It causes a systematic distortion on the frequency power spectra computed by the periodgram method, while estimates of the auto-correlation function is basically free from this distortion. The nature of this distortion will be examined in more detail in Section 4.3. It is enough here to mention that the distortion is not serious when the length of time series used in the computation of periodgram is sufficiently longer than the correlation time of data. The mesospheric data are free from ground clutter contaminations because of the sphericity of earth. Thus they can usually be characterized by a single correlation time, and it is not difficult to choose the length of data to satisfy this condition.

From the viewpoint of computational time, the periodgram method with FFT algorithm has an advantage over the auto-correlation function method when the number of data points becomes large.

Therefore the choice of these two methods depends on the number of points to be used in the computation, on whether the processing is done on real time or not, and on the speed of the computer.

The frequency power spectra or the auto-correlation functions thus obtained are further averaged in time to reduce the statistical fluctuations in their estimates. This averaging is called 'incoherent integration' in contrast to the coherent integration. Since the incoherent integration does not improve the signal-to-noise ratio, its role can be better understood in terms of an alternate measure of the quality of data called signal detectability (Gage and Balsley, 1978). The signal detectability is defined as the ratio of the amplitude of the largest spectral peak of the signal S to the r.m.s. fluctuation of the noise σ_N, and is expressed as

$$\frac{S}{\sigma_N} = \frac{P_S B n^{1/2}}{P_N \Delta f} \tag{2.1}$$

where P_S and P_N are the received power of signal and noise, respectively, B is the receiver bandwidth which includes the effect of the coherent integration, n is the number of spectra averaged together, and Δf is the spectral width of the signal component. When this ratio exceeds about 3, the spectral peak of the signal component is seldom misinterpreted as the statistical fluctuation of the noise component even if the signal-to-noise ratio is low. Note that the coherent integration does not improve this ratio since P_N is proportional to B, and the coherent integration simply reduces B.

Among various spectral parameters, the most important and best understood are the lowest three spectral moments as the echo power P (the zeroth moment), the mean Doppler shift ω_d (the first moment), and the spectral width σ (square root of the second moment around the first moment). They are given by

$$P = \int S(\omega) d\omega \tag{2.2}$$

$$\omega_d = \int \omega S(\omega) d\omega \; / \; \int S(\omega) d\omega \tag{2.3}$$

$$\sigma^2 = \int (\omega - \omega_d)^2 S(\omega) d\omega \; / \; \int S(\omega) d\omega \tag{2.4}$$

where $S(\omega)$ denotes the echo power spectra, and ω_d is the Doppler angular frequency shift from the center frequency. Equations (2.2)-(2.4) can be transformed into the auto-correlation domain with the aid of the Wiener-Khintchin theorem

$$\rho(\tau) = \int S(\omega) \exp(j\omega\tau) \, d\omega \tag{2.5}$$

where $\rho(\tau)$ is the auto-correlation function, and τ is the time delay. Using (2.5) we obtain

$$P = \rho(0) \tag{2.6}$$

$$\omega_d = -j\rho'(0)/\rho(0) \tag{2.7}$$

$$\sigma^2 = -\rho''(0)/\rho(0) + \{\rho'(0)/\rho(0)\}^2 \tag{2.8}$$

where primes denote derivatives. Equations (2.2)-(2.4) or (2.6)-(2.8) are used to evaluate these parameters according to whether the power spectra or the auto-correlation functions are computed. Since the actual data are given as a discrete time series, integrations and derivatives in the above equations are approximated by summations and finite differentiations, respectively.

We can obtain the relation between the signal correlation time τ_c and spectral moments by assuming the shape of the auto-correlation function. If we assume the Gaussian shape, the auto-correlation function can be expressed using the spectral moments as

$$\rho(\tau) = P \exp(-\sigma^2\tau^2/2 + j\omega_d\tau) \tag{2.9}$$

The signal correlation time is customarily defined as the time delay where $\rho(\tau)$ falls to the half of its value at the origin. Thus

$$|\rho(\tau_c)| = 0.5\rho(0) \tag{2.10}$$

By substituting (2.9) into (2.10) we obtain

$$\tau_c = (2\ell n2)^{1/2}\sigma^{-1} = 1.18\sigma^{-1} \tag{2.11}$$

Similarly, an expression for the half-power spectral width f_h can be obtained. The Fourier transform of (2.9) gives

$$S(\omega) = \frac{P}{(2\pi)^{1/2}\sigma} \exp\{-(\omega-\omega_d)^2/2\sigma^2\} \tag{2.12}$$

By definition of the half-power width, (2.12) yields

$$f_h = \frac{(2\ell n2)^{1/2}}{\pi}\sigma = 0.375\sigma \tag{2.13}$$

Combining (2.11) and (2.13), we obtain the relation between the signal correlation time and the half-power spectral width as

$$\tau_c f_h = 2\ell n2/\pi = 0.441 \tag{2.14}$$

Although the numerical coefficients in (2.11), (2.13), and (2.14) are to be changed if a different function shape is assumed, it will be justified in Sections 3.2 and 4.2 that observed shape of the echo power spectra and the auto-correlation functions are usually well approximated by a Gaussian.

The Doppler shift is usually expressed in terms of the velocity scale since it represents the line-of-sight velocity of the atmosphere. The Doppler velocity is given by

$$V = c/(4\pi f_o)\cdot\omega_d \tag{2.15}$$

where f_o is the radar frequency. In order to determine the three components of velocity vector, line-of-sight velocities of at least

three different directions are necessary. However, the horizontal component in the vertical plane which contains the antenna beam direction is often deduced assuming that the vertical component of the velocity is small. The horizontal component is given by

$$V_h = \frac{V - V_z \cos\theta}{\sin\theta} \tag{2.16}$$

where V_h and V_z are the horizontal and the vertical decompositions of V, and θ is the zenith angle. Thus if V_z is much smaller than V, V_h can be estimated from an observation of V. This is a fair assumption as justified in the following chapters, except for discussions of short period waves for which the amplitude of vertical component can be as large as the horizontal component.

2.3 EFFECTS OF THE HEIGHT RESOLUTION ON OBSERVED PARAMETERS

In the previous section, we have examined the procedure for estimating fundamental spectral parameters from received echoes. However, the situation treated there was rather ideal on the point that we did not consider the width of the transmitted pulse and its effect on the estimated parameters. In reality, a pulse of width T occupies a range of cT in space, thus a sample of the received signal contains echoes from a height range cT/2. This range is called the height resolution because it determines the accuracy in estimating the range of a target. We implicitly assumed an infinitesimal height resolution in the previous section.

The minimum value of T is usually limited by the frequency bandwidth available. As for the Jicamarca VHF radar, it is limited to about 20μs by the transmitter bandwidth. Thus the height resolution of the Jicamarca VHF radar system is about 3 km.

The apparent effect of the finite width of the transmitted pulse is to convolve the spatial distribution of scatterers with the pulse in space. Since the received signal is usually passed through a

matched filter, which maximizes the signal-to-noise ratio for the given transmitted pulse, another convolution is involved (e.g., Wakasugi, 1981). The response of the matched filter to a pulse is equivalent to auto-correlate the pulse in time (Skolnik, 1975). Thus we can take into account the effect of the convolution involved in the receiving process by convolving the height profile of the scatterers with the auto-correlation function of the pulse instead of the pulse itself.

We examine here the effect of this convolution process on deduced spectral parameters with the aid of a simple computer simulation (Sato and Fukao, 1981). We consider a case where contributions from scatterers at different heights adds incoherently. Although this may not be a valid assumption for the Fresnel reflection occurs at the vertical incidence, it is a fair approximation for the volume scattering from obliquely incident waves. We also postulate the spectral shape to be Gaussian for mathematical simplicity. Slight variation in the spectral shape may not affect any of the discussions below, because only the integral moments of spectra concern our computation.

When the spectral parameters such as the echo power, the Doppler shift, or the spectral width vary substantially in a shorter height interval than the height resolution of the observing system, height profiles of these parameters are smeared by a weighting function which represents the length and shape of the transmitted pulse. The smeared height profiles of the parameters are obtained by taking the spectral moments of the spectra convolved versus height with the weighting function. For the Gaussian spectra, they are given as

$$P_s(z) = \frac{\int W(h-z)P(h)dh}{\int W(h-z)dh} \tag{2.17}$$

$$V_s(z) = \frac{\int W(h-z)V(h)P(h)dh}{\int W(h-z)P(h)dh} \tag{2.18}$$

$$\sigma_s^2(z) = \frac{\int W(h-z)\{\sigma^2(h) + V^2(h)\}P(h)dh}{\int W(h-z)P(h)dh} - \left\{ \frac{\int W(h-z)V(h)P(h)dh}{\int W(h-z)P(h)dh} \right\}^2 \qquad (2.19)$$

where P,V, and σ are the echo power, the Doppler velocity, and the spectral width (half power width of the echo power spectrum), respectively, z is the height, W is the weighting function, and the suffix s denotes the smeared parameters. We should note here that P_s is determined by P and W only, while V_s is affected by P,V, and W, and σ_s by P,V,σ, and W.

Fig.2-3 is an example to illustrate this feature using a simple model. The solid lines in the figure shows height profiles of the echo power, the Doppler velocity, and the spectral width of the model. We use the following functional shape for W throughout this section for simplicity.

$$W(h) = \begin{cases} \frac{1+\cos\pi(h/\Delta h)}{2} & (-\Delta h \leq h \leq \Delta h) \\ 0 & (h < -\Delta h,\ h > \Delta h) \end{cases} \qquad (2.20)$$

where Δh corresponds to the height resolution. This model represents a case where two strong thin layers dominates over a weak uniform background in the presence of a constant wind shear. Dashed lines are profiles of the smeared parameters. All scales are arbitrary, and the height resolution is 20. The antenna beam is assumed to be tilted 10° from zenith. The large discrepancy between the model and smeared velocity profiles at lower and higher height ranges indicate that smeared velocity is dominated by the velocity of the height where the strong layers exist. The spectral width profile shows that when two layers with different horizontal velocity fall within a height range shorter than the height

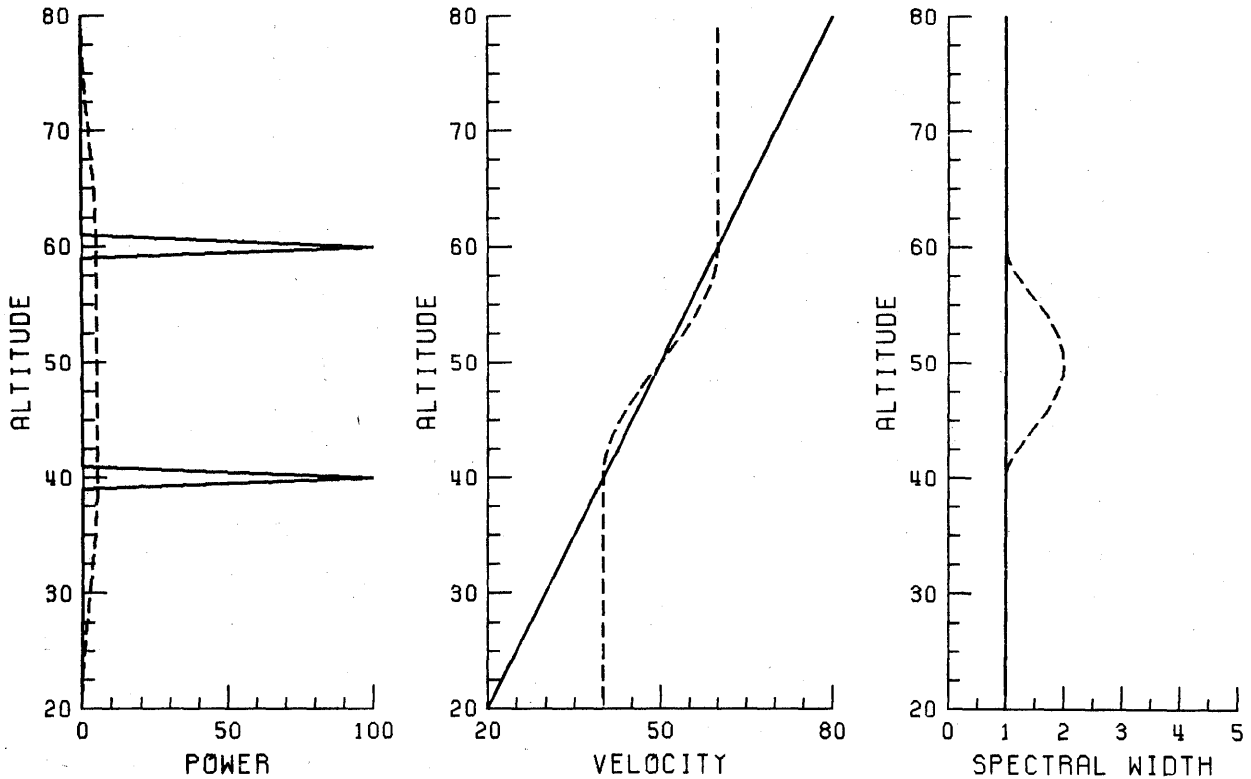

Fig.2-3 A model computation for simulating effects of a poor height resolution. The model and smeared profiles of the echo power, the Doppler velocity, and the spectral width (half power width of the echo power spectrum) are compared. The solid lines show the model, and the dashed lines show the smeared profiles with the height resolution of 20. Numbers are in arbitrary units.

resolution, estimated spectral width is broadened by the velocity difference of these layers.

Next we examine these effect for a case closer to the real situation encountered by the Jicamarca VHF radar observations. The model used here is the real stratospheric data obtained by the Arecibo UHF radar with a height resolution of 150 m. Three spectral moments are given versus height and time at the interval of 150m and 1 min, respectively. We then smear these parameters with a weighting function of 3 km height resolution to see how they would look like if they were observed by a system with 3 km height resolution, the typical value for the Jicamarca VHF radar system.

Fig.2-4 is the same as Fig.2-3 except that this case uses real data as a model. Parameters shown by the solid lines are obtained by fitting a Gaussian to the power spectra averaged for 1 min. The details of this fitting procedure is presented in Section 4.3. The antenna beam was tilted 10° from zenith toward the east, so that the velocity scale is adjusted to give the zonal wind velocity assuming that the vertical component is small. The broken lines are the result of smearing with the same manner as Fig.2-3.

The strong layer at 16 km height with a strong background shear is a good example to show the effect of smearing. This combination makes the large discrepancy between the original and the smeared wind profiles of as large as 10 m s^{-1} at 14-15 km height range. We should note that this result cannot be accounted for by a simple smoothing of the original wind profile. The spectral width profile demonstrates that the width of the smeared power spectra is determined mainly by the difference in the line-of-sight velocity at the top and bottom of the height resolution cell, rather than the original width at those heights where the background shear is large.

Fig.2-5 shows the temporal variation of the model and the smeared wind velocity at five different heights. This figure indicates that the discrepancy shown in Fig.2-4 does not smooth out in time, but continues for hours, because the strong layers which

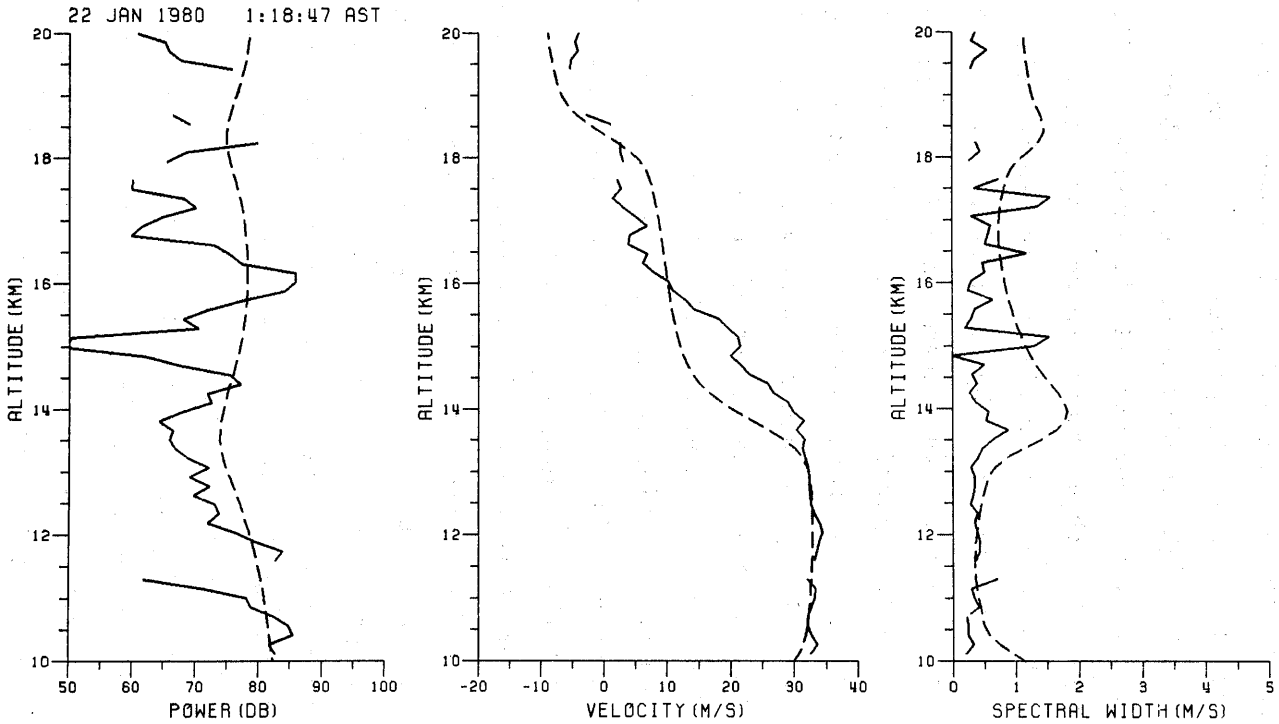

Fig.2-4 Same as Fig.2-3. The solid lines are stratospheric data taken by the Arecibo UHF radar as a model (height resolution: 150 m). The dashed lines simulate the system with a height resolution of 3 km.

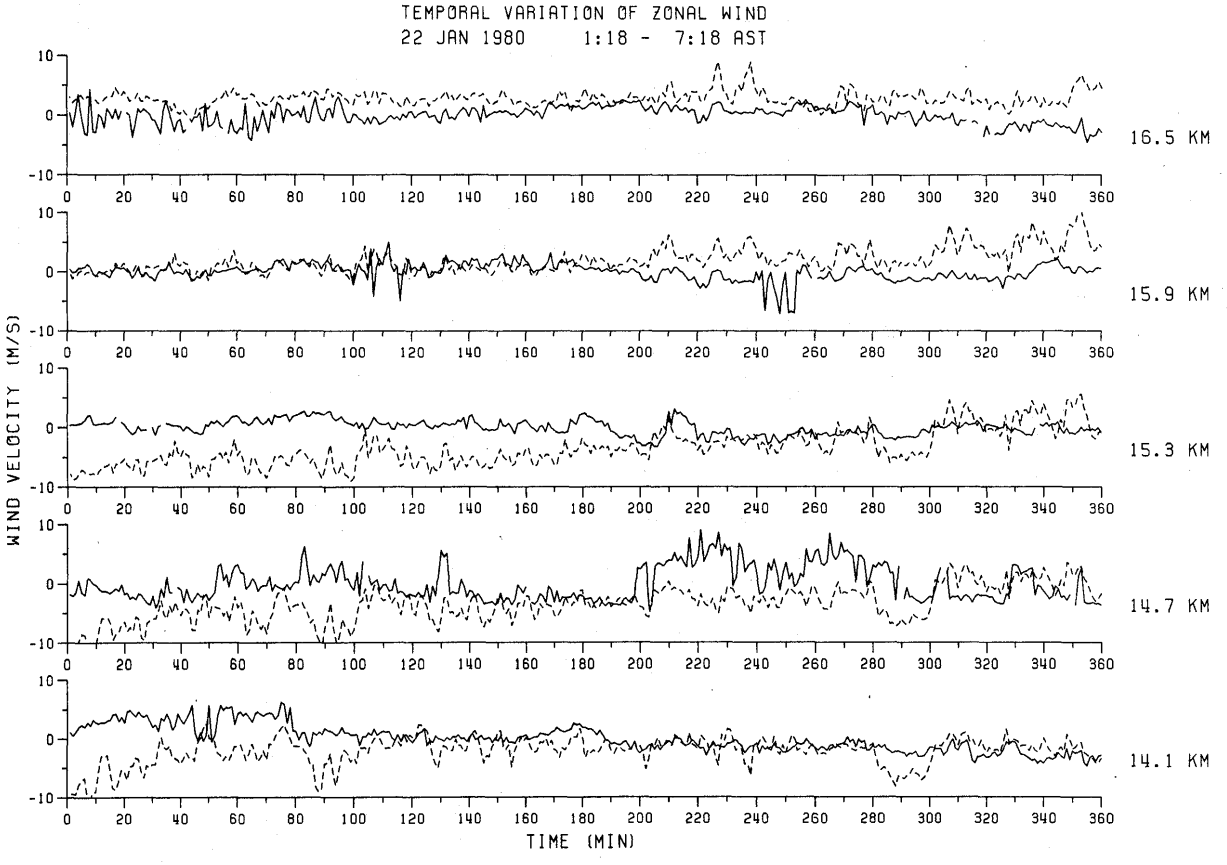

Fig.2-5 Temporal variation of the model (solid lines) and the smeared (dashed lines) wind velocity at five different heights.

dominates the smeared wind profiles usually keep their strength for a few to several hours without changing their heights largely. There also exist short period fluctuations in the smeared wind velocity which are not found in the original wind data. This suggests that we should be careful in interpreting wind velocity data taken with a poor height resolution system. We can, however, make a crude estimate of how large the contamination in wind velocity due to the height resolution is.

The largest deviation of the horizontal wind velocity at the top or bottom of the region within a height resolution Δh is given by $(\Delta h dV/dh)/2$. The largest possible wind shear dV/dh which is likely to occur can be estimated from the critical shear condition in which the Richardson number becomes 1/4, because a larger shear produces turbulence which works to smooth out the shear itself. For an isothermal atmosphere of 200 K, this shear is about 40 m $s^{-1}km^{-1}$. Thus the largest possible deviation of the observed wind velocity from the true value is of the order of 0.02 Δh, or 3 m s^{-1} for 150 m height resolution, and 60 m s^{-1} for 3 km height resolution. This is of course the extreme case, and Fig.2-5 indicates that about 1/6 of this value seems to be a more realistic estimate.

2.4 LIMITATIONS ON THE ANTENNA PERFORMANCE

The problem of the poor height resolution is one of the largest technical limitations imposed on the Jicamarca VHF radar system. This limitation arised because the system was originally designed for the ionospheric study, where a good height resolution was not an important requirement since the height variation of the physical parameters are usually much slower than in the middle atmosphere. It was realized to be a serious problem only after a new application of the radar was opened to the middle atmospheric study. A similar limitations exist in the antenna performance which also arised from the difference in requirements for ionospheric and middle

atmospheric observations.

One of them is a limited scan range of the antenna beam direction. As described in Section 2.2, the antenna array consists of 64 modules, each of which contains 144 half-wave dipoles. Since all dipoles in one module are designed to be excited in phase, scanning of the antenna beam is controlled by inserting additional length of cables at the feed point of modules. We consider the antenna pattern along the axis of one of two orthogonal sets of dipoles. The actual two-dimensional pattern is obtained by multiplying this one-dimensional pattern with the pattern along the other axis.

The one-dimensional pattern of a module is given by (e.g., Steinberg, 1975)

$$M(\theta) = D(\theta) \sum_{m=1}^{12} \exp(jm\pi\sin\theta) \tag{2.21}$$

where θ is the zenith angle and $D(\theta)$ is the pattern of a half-wave dipole given by

$$D(\theta) = \begin{cases} 1 & \text{(H-plane)} \\ \sin(\frac{\pi}{2}\sin\theta)/\cos\theta & \text{(E-plane)} \end{cases} \tag{2.22}$$

The one-dimensional pattern of the full antenna is obtained by regarding modules as elements spaced at 6 wavelength interval. Thus

$$F(\theta) = M(\theta) \sum_{n=1}^{8} \exp\{j(12n\pi\sin\theta + 2n\pi d/\lambda)\} \tag{2.23}$$

where d is the electrical length of cables inserted between adjascent modules, and λ is the radar wavelength. The second term in the parenthesis determines the steering of the antenna beam direction. The zenith angle for which the summation takes its maximum value is given by

$$\theta_m = \sin^{-1}\left(\frac{d/\lambda \pm i}{6}\right) \qquad (i = 0,1,2,\ldots) \tag{2.24}$$

This relation shows that the antenna pattern is a periodic function of d with the period λ. The solid line of Fig.2-6 illustrates the antenna pattern when $d = 0.5\lambda$, which is the condition for the ambiguity to appear. The dashed line shows the pattern of a module. Clearly, two main lobes of the same zenith angle in the opposite direction appear under this condition. Beyond this angle, the undesired lobe takes larger value than the desired lobe. This limit corresponds to the antenna zenith angle of 4.8°. The practical limit where the desired lobe is 6 dB higher than the undesired lobe is 2.8°. In the two dimensional case where the beam can be tilted along the other axis also to this limit, the maximum zenith angle becomes 4.0°.

This limitation is not so serious compared to the problem of the height resolution, because the antenna beam width of 1° is narrow enough than the maximum steering angle, so that the horizontal velocity component can be safely decomposed from the line-of-sight velocities. However, the highest sidelobe level is only about 8-9 dB below the main lobe even within the limit discussed here, as is shown in Fig.2-2. This considerably high sidelobe level becomes a problem for the higher mesospheric study when strong discrete sources as meteor trails pass through sidelobes with the same range as the desired region. Probably the most serious effect of the limited scan range for future experiments is that it precludes the possibility of studying horizontal variations of observed parameters which is required in order to discriminate the spatial and temporal variations.

The structure of the module using 6-wavelength coaxial cables as antenna elements also caused an associated problem of impedance mismatching. It was already known at the time of the design, and efforts were paid to minimize it (Ochs, 1965). Since all 12 dipoles

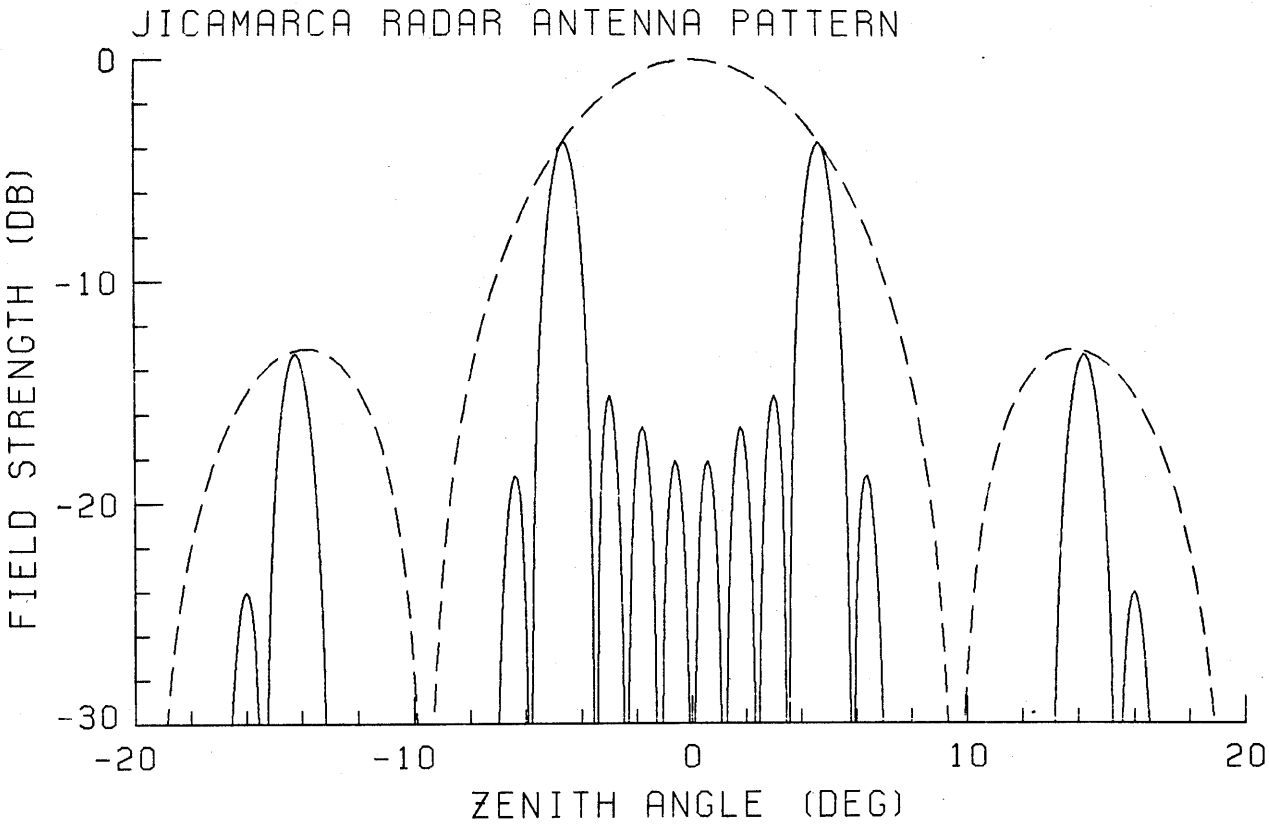

Fig.2-6 Computed one-way radiation pattern of the Jicamarca antenna when the main lobe is pointed to a direction 4.8° from zenith (solid curve). The dashed curve shows the pattern of a module.

are connected serially to the coaxial line, the load impedance seen from the line varies from 540 Ω at the end to 90 Ω at the central dipole, which makes impossible to take a precise impedance matching.

Another disadvantage in the Jicamarca antenna structure is that the phasing of the antenna beam is done by inserting coaxial cables manually at the feed point of the modules. This system apparently requires hours of effort to change the direction of the antenna beam. This disadvantage is well covered by the flexible design which allows to divide the system up to 4, and to operate them like independent systems. Also, the large aperture and the associated high gain of the Jicamarca antenna offers sufficient performance for the middle atmospheric study even when it is divided into quarters. However, it will be useful to point out that it is less efficient to divide an antenna array in order to observe different directions, than to use the full antenna in a time-divided fashion if a fast switching of the beam direction is possible.

The radar equation (1.13) for the case where scatterers fill the antenna beam shows that when the antenna area and the transmitter power are divided into N, P_r decreases to N^{-2}. The received galactic background noise power (which dominates over the receiver noise at the frequency of 50 MHz) is independent from the antenna area, because an antenna with large aperture has a higher gain than a smaller antenna but illuminates narrower area in the Galaxy. Thus the signal-to-noise ratio decreases to N^{-2}. The signal detectability, which is of our main interest, also decreases to N^{-2} as clear from (2.1).

If the full antenna is used sequentially to observe N different directions, the only effect on the signal detectability is to decrease the number of incoherent integration to N^{-1}, assuming that the time for switching the antenna beam direction can be neglected. Thus the signal detectability decreases to $N^{-1/2}$ in this case according to (2.1). This result shows that the signal detectability of the beam switching method is $N^{3/2}$ times higher than the antenna

dividing method. This difference amounts to 4.5 dB even for the minimum case of N = 2, showing the crucial importance of the ability of electronical steerability of the antenna for smaller radars than that of Jicamarca or Arecibo. The technique of dividing the antenna area should be used only for those experiments where the accurate concurrency between different directions is required, as is the case for the spaced-antenna-drift method (Briggs, 1980; Röttger, 1981) in which the phase difference between different receiving antennas is used to determine the horizontal motion of scatterers.

CHAPTER 3

MESOSPHERIC OBSERVATIONS BY THE JICAMARCA VHF RADAR

3.1 INTRODUCTION

The first middle atmospheric observation using the Jicamarca VHF radar (Woodman and Guillén, 1974) revealed two outstanding regions from which strong backscattering occurs. One is the lower stratosphere, and the other is the mesosphere. The stratospheric scattering was identified as the same kind of scattering known as the clear-air-turbulence (CAT) echoes in the tropospheric height, which occur from the fluctuations of the atmospheric refractive index due to temporal fluctuations associated with the atmospheric turbulence (Balsley and Gage, 1980; Crane, 1980).

The strong mesospheric scattering, on the other hand, suggested a clearly different mechanism from the stratospheric scattering since the latter decays exponentially with height until it becomes undetectable at about 40 km. It was also discriminated from incoherent scattering at ionospheric height because it is much stronger than the expected level of the incoherent scattering at the mesospheric height (Rastogi and Woodman, 1974). It is now believed to be the scattering from fluctuations in electron density gradient caused by the atmospheric turbulence (Rastogi and Bowhill, 1976a,b) as shown in Chapter 1, though much more is to be studied on the mechanism of scattering. Besides an interest on its mechanism itself, this strong scattering offers a powerful tool to investigate the dynamics of the mesosphere, which has been rather poorly understood due to a lack of proper measurements.

We will examine here the nature of the mesospheric scattering at the VHF frequency in more details based on two series of continuous multiheight observations carried out in 1974 (Harper and Woodman, 1977; Fukao et al., 1979) and 1977 (Fukao et al., 1980c). We begin

with inspecting the basic characteristics of the scattered echoes. Next, we use this scattering as a probe to study the dynamics of the equatorial mesosphere. Waves with various time scales are presented and discussed. Lastly the nature of the mesospheric turbulence is examined in terms of the observed anisotropy in echo power, and of the relation between the echo power and signal correlation time.

3.2 OBSERVATIONS

Two sets of data are presented in this chapter. One is taken on May 23-24, 1974 for about 24 hours, and the other is taken on November 14-16, 1977 for about 60 hours. They are referred to as the 1974 and 1977 data, respectively, for short in the followings. There are slight differences in the observational parameters and in data taking procedures between these two data sets.

1. The 1974 data : Two orthogonal antenna arrays are used separately. One was pointed to a quasi-vertical direction (about 0.36° from zenith to the southwest), while the other was tilted by 3.45° and 0.15° from zenith toward the west and the north, respectively (Fleisch, 1976). Rectangular pulses of 24 μs width are transmitted at 1 MW peak output power (nominal) with the IPP of 0.866 ms. Twelve heights spaced at 2.5 km intervals over the 62.5-90 km region were observed simultaneously in each of two antennas. Seven stratospheric heights over 10-27.5 km were also observed at the same time with the same height interval (Fukao et al., 1978). At each height the received signal was coherently integrated over 128 IPP's, or about 0.11 s. The complex auto-correlation function was calculated at 16 time delays at 0.11 s increments in real time, incoherently integrated for about 1 min, and then stored on magnetic tapes.

The signal-to-noise ratio of the mesospheric data after coherent integration is often of the order of unity, thus proper noise estimation and subtraction are important in accurate computation of

the spectral parameters. Since the sky noise can be safely regarded as the white noise within the receiver bandwidth, it contributes only to the zero time delay of the auto-correlation function. It is therefore easy to estimate the noise contribution from the observed auto-correlation function by extrapolating the values of four small time delays toward zero at lower heights where the signal correlation time is usually long. The noise power thus estimated does not vary with height, showing that the receiver recovery effect is small at the mesospheric heights. It also agrees within a difference of 1 dB with the noise power directly measured every 30 min by turning off the transmitter. The echo power, Doppler shift, and signal correlation time are obtained by applying Equations (2.6)-(2.8) to the auto-correlation function after subtracting the noise contribution.

2. The 1977 data : The arrangement of the antenna is the same as the 1974 experiment except that the vertical direction is observed instead of the quasi-vertical direction. Basic pulse width was 25 μs, and the IPP was 1 ms. Thirteen heights over 60-90 km were observed at 2.5 km intervals. Five stratospheric heights over 15-25 km were also observed for reference. Fig.3-1 illustrates a sequence of pulses consisting of 18 IPP's. In each sequence, no pulse was transmitted at the 9th and 18th IPP's. The phase of the pulses was flipped by 180° after every pulse in order to eliminate any system dc offset. At each height the sampled signal was coherently integrated over 7 sequences (or 126 ms) in the following way:

$$I = \sum_{j=1}^{7} \{(I_{1j} - I_{2j} + \cdots - I_{8j}) - (I_{10j} - I_{11j} + \cdots - I_{17j})\} \qquad (3.1)$$

where I_{ij} is the sample for the i-th pulse in the j-th sequence. The 9th and 18th samples contain only self clutter contributions, which are the echoes from the ionospheric heights due to previous pulses, so that the value

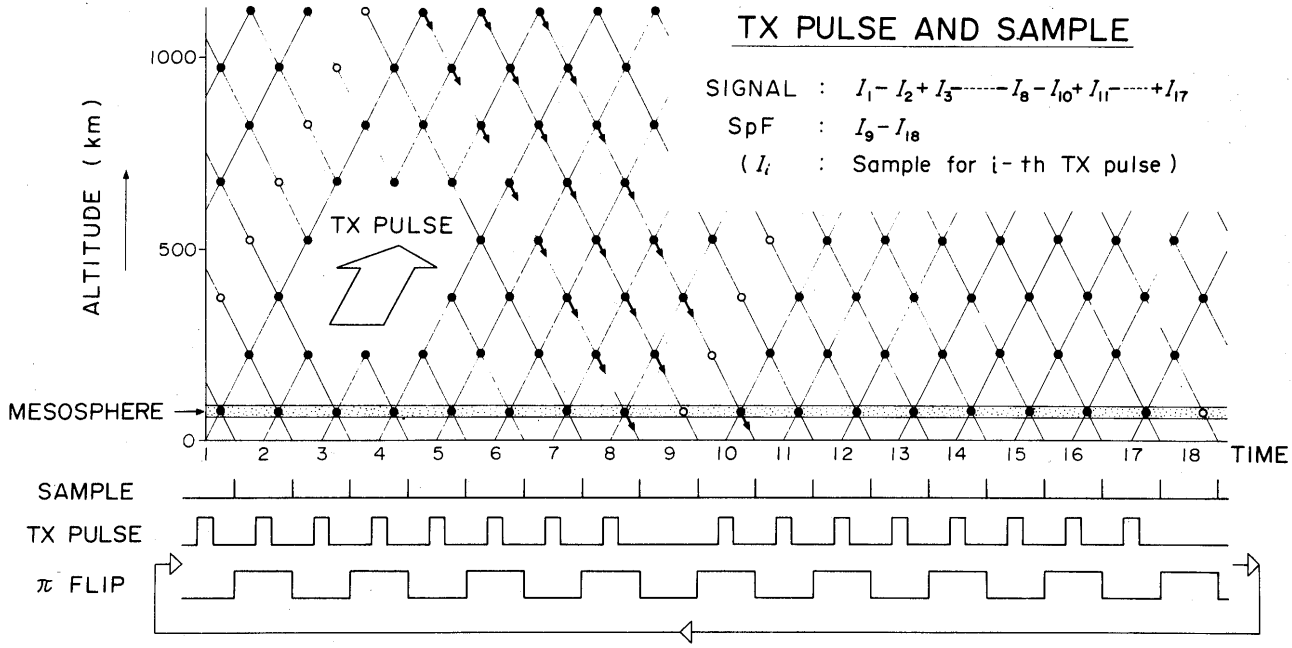

Fig.3-1 Height-time diagram for a unit sequence of transmit (TX) pulses and samples. Samples are taken at 13 levels in the mesosphere of 60-90 km. No TX pulse is transmitted at the 9th and 18th IPP's. The pulse phase is flipped by 180° after every pulse. Each dot indicates a region where radio echo arises in response to a TX pulse. The arrows show that ionospheric echoes due to preceding TX pulses may contaminate the desired mesospheric echo.

$$I_{SF} = \sum_{j=1}^{7} (I_{9j} - I_{18j}) \qquad (3.2)$$

was used to look for coherent spread F echoes that would contaminate the desired mesospheric echoes. Spread F echoes were observed only at night, when the mesospheric echoes disappear. Sky noise was measured every 7 sequences by turning off the transmitter for 18 IPP's.

The coherently integrated data were directly recorded on magnetic tapes. Frequency power spectra were computed every 7.2 s in the off-line analysis using 50-point FFT algorithm (Singleton, 1969).

Observational parameters are summarized in Table 3-1.

3.3 RADAR SIGNAL CHARACTERISTICS

Fig.3-2 shows the signal power as a function of time at the 12 mesospheric heights for the 1974 data for the quasi-vertical antenna. The height range over which samples were taken was shifted upward by 5 km near 2000 LT of May 23, 1974, thus explaining the lack of data at 87.5 and 90 km before that time. The background noise was removed by the manner described in the previous section. Below 80-82.5 km the echo power variations show features that have been reported in earlier observations (Woodman and Guillén, 1974; Rastogi and Woodman, 1974; Rastogi and Bowhill, 1976c).

1. Signal power above the noise level is observed only during daytime. The nighttime signal level shown in Fig.3-2 can be explained by the statistical fluctuations in the noise level, which is subtracted from the received echo power. In particular, the 5-7 dB increase in the echo power observed at all heights near 0300 LT is the result of a strong increase in sky noise level as the galactic center passed through the antenna beam.

Table 3-1 Observational parameters of the mesospheric experiments using the Jicamarca VHF radar

1974 data

Date	: May 23-24, 1974 (24 hours)
Antenna beam directions	: quasi-vertical (0.36° to the southwest)
	off-vertical (3.45° to the west, 0.15° to the north)
Pulse width	: 24 μs
IPP	: 0.866 ms
Observed heights	: 62.5-90.0 km (2.5 km interval)
Height resolution	: 3.6 km
Coherent integration	: 0.11 s

1977 data

Date	: November 14-16, 1977 (60 hours)
Antenna beam directions	: vertical
	: off-vertical (3.45° to the west, 0.15° to the north)
Pulse width	: 25 μs
IPP	: 1 ms
Observed heights	: 60.0-90.0 km (2.5 km interval)
Height resolution	: 3.75 km
Coherent integration	: 0.126 s

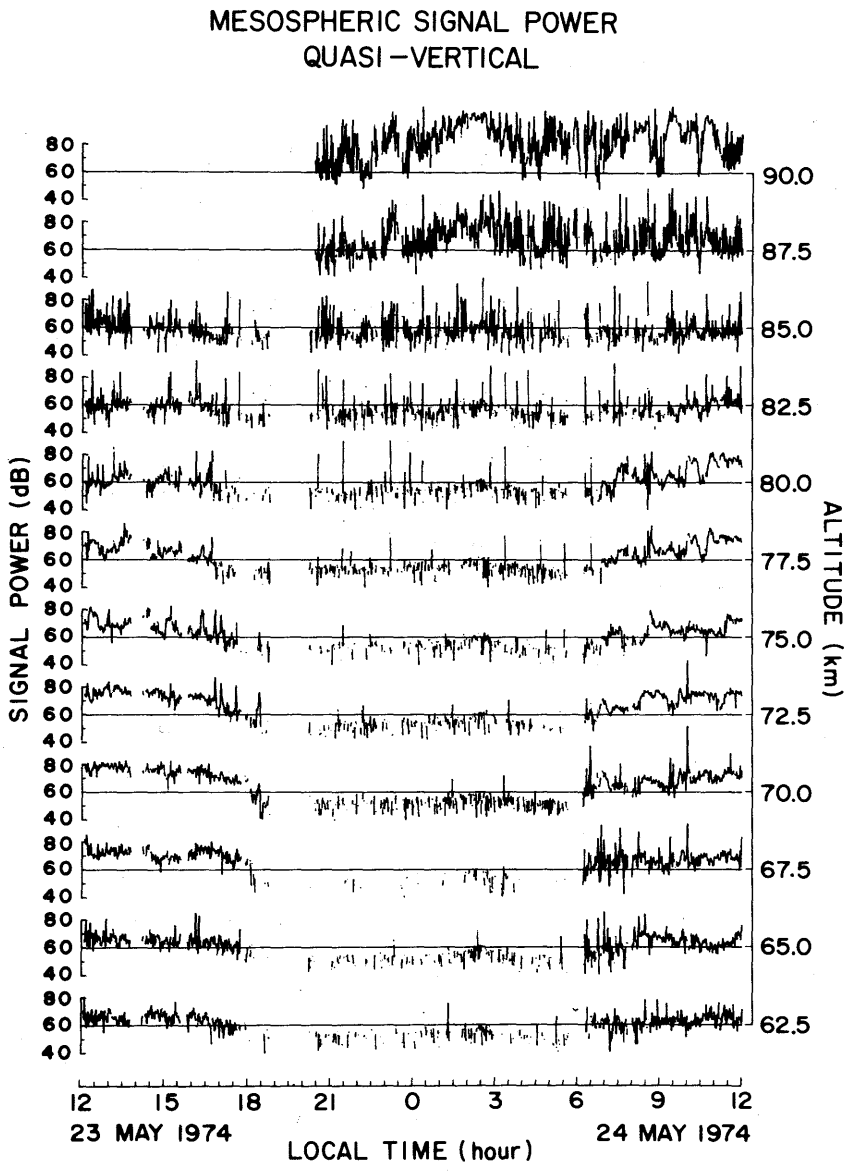

Fig.3-2 Estimate of mesospheric signal power in the quasi-vertical direction. The ordinate is relative power in decibels with an arbitrary reference level. There are no data at 87.5 km and 90 km before about 2000 LT on May 23, 1974.

2. The signal power at a given height often shows a rapid variation during daytime. However, its mean value shows a general tendency to vary in time according to the solar zenith angle.

3. Signal power usually takes its maximum value between 70 and 77.5 km height range, and shows a minimum at 80-82.5 km. Besides these continuous echoes, strong spikelike echoes are frequently observed above 80 km. These echoes appear as short bursts superimposed on the generally weak background, and last probably much shorter than the observing time resolution of 1 min, since they never continue in the next minute's data. These echoes are shown as many vertical lines in Fig.3-2, especially at 85 and 87.5 km. Contrary to the solar zenith angle dependence in the echo power at lower heights, these spikelike echoes persist throughout the night.

Fig.3-3 shows examples of complex auto-correlation functions of 1974 data in the form of the amplitude normalized to the zero time delay, and the phase; Fig.3-3 a) is a typical case for the continuous echoes observed below about 80 km, while b) is for the spikelike echoes often observed above 80 km.

The correlation time for the spikelike echoes is of the order of 0.1-0.2 s. This value seems to be too short for the coherent scattering from turbulent fluctuations in the electron density, because it requires vertical velocity fluctuations of the order of 10-15 m s^{-1}. The behavior of these spikelike echoes is, on the other hand, well explained by the echoes from ionized trails produced by meteors. Especially the correlation time of 0.1-0.2 s is consistent with the decay time of under dense meteor echoes at 50 MHz (Nowak, 1967). The occurrence frequency of meteor trails in general shows its minimum in the evening hours and a maximum in the morning hours. There is some indication of this in the data, if the apparent rise in the mean power at 90 and 87.5 km after midnight were due to very frequent arrival of meteors. Although the antenna beam width of the Jicamarca radar is very narrow compared to usual meteor radars, the scattering cross section of the meteor trails is

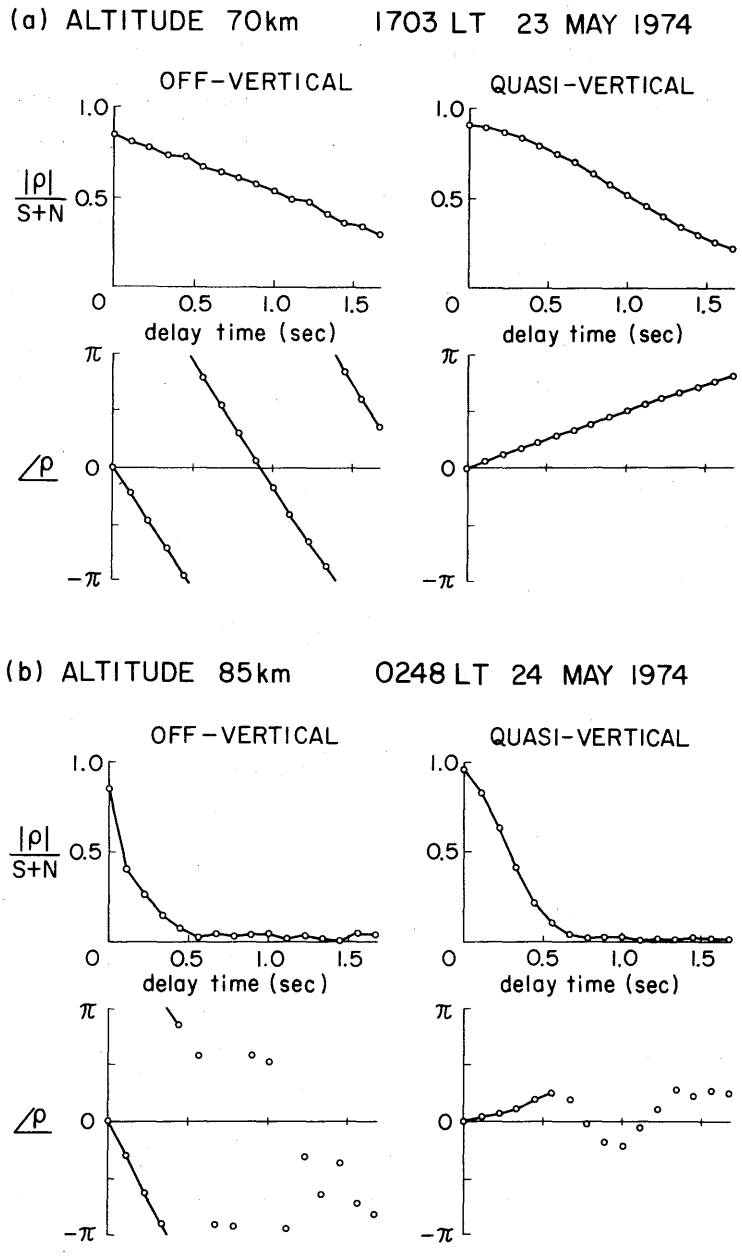

Fig.3-3 Typical complex auto-correlation functions for the off-vertical and quasi-vertical antennas that are observed at a) 70 km, and b) 85 km heights.

large enough to be observed also by sidelobes.

The equatorial electrojet (e.g., Forbes, 1981) also seems to be largely contributing to the observed echo power above 85 km. Fig.3-4 compares the echo power smoothed by a 10-min low-pass filter with the geomagnetic H component recorded at Huancayo (12.0°S, 75.3°W) for the same period. The strong correlation during 0800-1100 LT indicates that the echoes of this period are associated to the equatorial electrojet. This correlation can be seen only above 85 km. No clear correspondence exists at the broad maximum of the echo power around 0200-0500 LT. This maximum could be due to the maximum occurrence frequency of meteor trails, but could also result from an electrojet-associated irregularity which did not result in large current flows due to the low midnight electron density.

Since the background signal above 80 km is generally very weak and since we cannot distinguish whether a given spikelike echo is observed by the main lobe or a sidelobe, the data above 80 km were not used in discussions of wind velocity except in determining the hourly mean zonal wind, where the error due to this uncertainty is expected to average out.

Below 80 km the amplitude of the auto-correlation functions in general decrease monotonically with increasing time delay, with the phase changing approximately linearly with time delay while the correlation is significant. This feature corresponds to a single-peaked and symmetric power spectra in the frequency domain, which is a typical case in 1977 data. Fig.3-5 shows an example of frequency power spectra versus height in the vertical and off-vertical antenna beam directions observed at 1144-1146 LT on November 14, 1977. The ordinate is expressed in terms of relative power in decibels with an arbitrary reference level. The auto-correlation functions shown in Fig.3-3, and the power spectra in Fig.3-5 generally show that they can be safely parameterized by the power, the Doppler shift, and the signal correlation time (or the spectral width). Discussions in the following sections are based on these parameters.

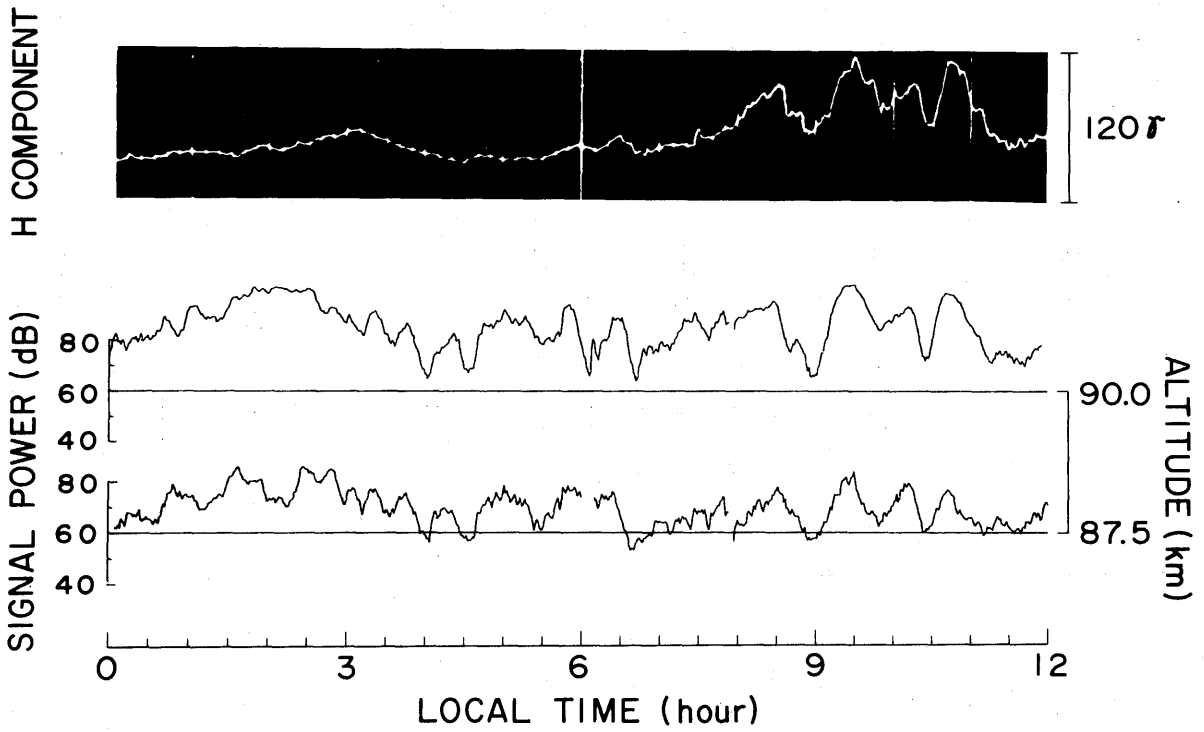

Fig.3-4 Comparison of signal power (a 10-min low-pass filter is applied to the logarithm of power) at 90 and 87.5 km and magnetic H component recorded at Huancayo (12.0°S, 75.3°W) for 0000-1200 LT on May 24, 1974.

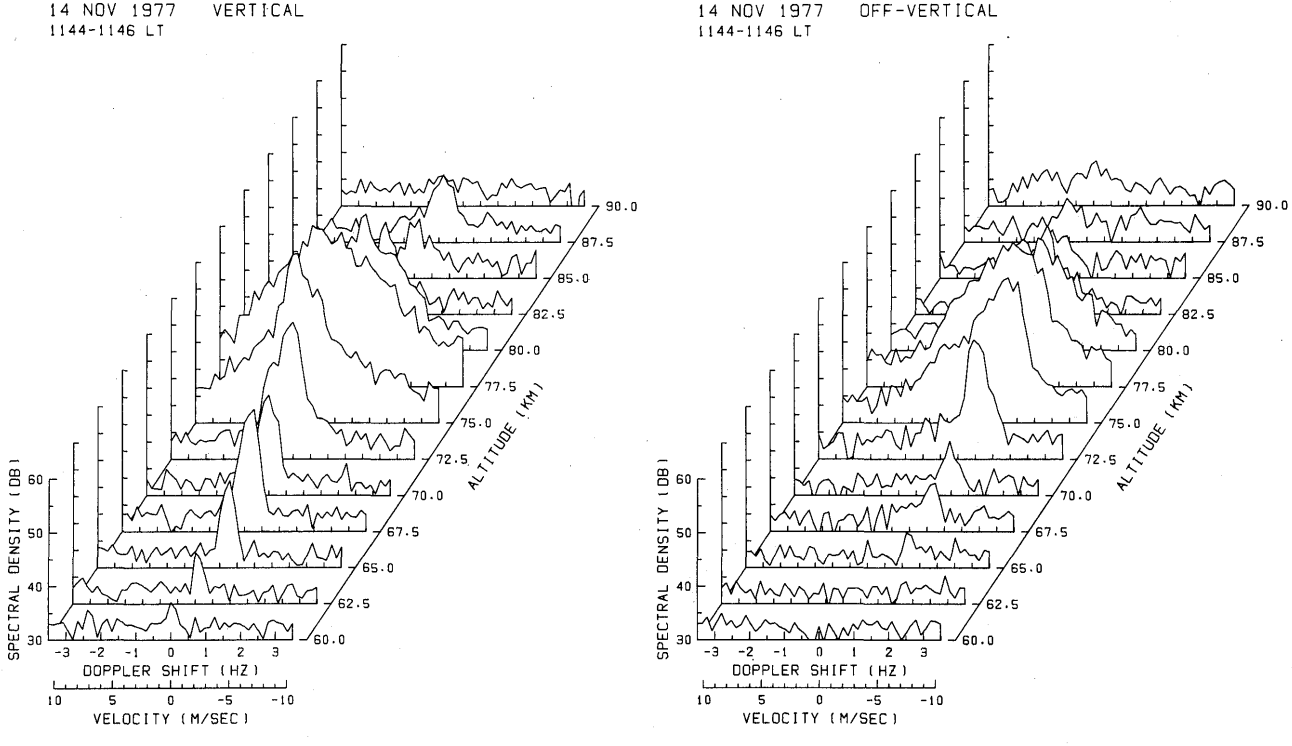

Fig.3-5 Examples of frequency power spectrum versus height in the vertical and off-vertical antenna beam directions obtained by the Jicamarca VHF radar at 1144-1146 on November 14, 1977. The ordinate is relative power in decibels with an arbitrary reference level. The abscissa is shown in terms of both the Doppler shift and the equivalent line-of-sight velocity.

3.4 PREVAILING WIND AND LONG PERIOD WAVES

Zonal wind velocity is obtained from the line-of-sight Doppler velocities at the vertical (or quasi-vertical for 1974 data) and the off-vertical antenna beam directions using Eq.(2.16), assuming that the wind velocity is uniform over the distance between scattering volumes observed by the two antenna beams. Since the distance of the scattering volumes is about 5 km at a height of 80 km, this assumption is equivalent to neglect contributions from the waves with horizontal wavelengths shorter than the order of 5 km. The classical dispersion relation for the gravity waves (e.g., Hines, 1960) shows that waves with such a short horizontal wavelength has a period of less than about 10 min under the mesospheric conditions unless the vertical wavelength of the wave is much shorter than the horizontal wavelength. Thus the above assumption is well satisfied for the mean zonal wind averaged over 1 hour or more.

Fig.3-6 shows hourly mean profiles of the zonal wind velocity versus height. Data were not included in the average when the signal-to-noise ratio fell below 0.1. Velocities could be determined only during daytime. The velocity structure below about 80 km is very stable, showing the dominance of an eastward prevailing wind of about 50 m s^{-1} around 65 km height. Since the longitudinal dependence of the prevailing zonal wind is thought to be small, we can compare it with the rocket balloon experiments at a different station with similar latitude.

Fig.3-7 compares daytime averages of zonal wind velocities of the 1974 and 1977 data with meteorological rocket observations made at Ascension Island (8.0°S, 14.4°W) in the period closest to each radar observation. The agreement of both observations in the overlapping height range for the 1974 data gives a direct confirmation that the velocity deduced from the radar observation is

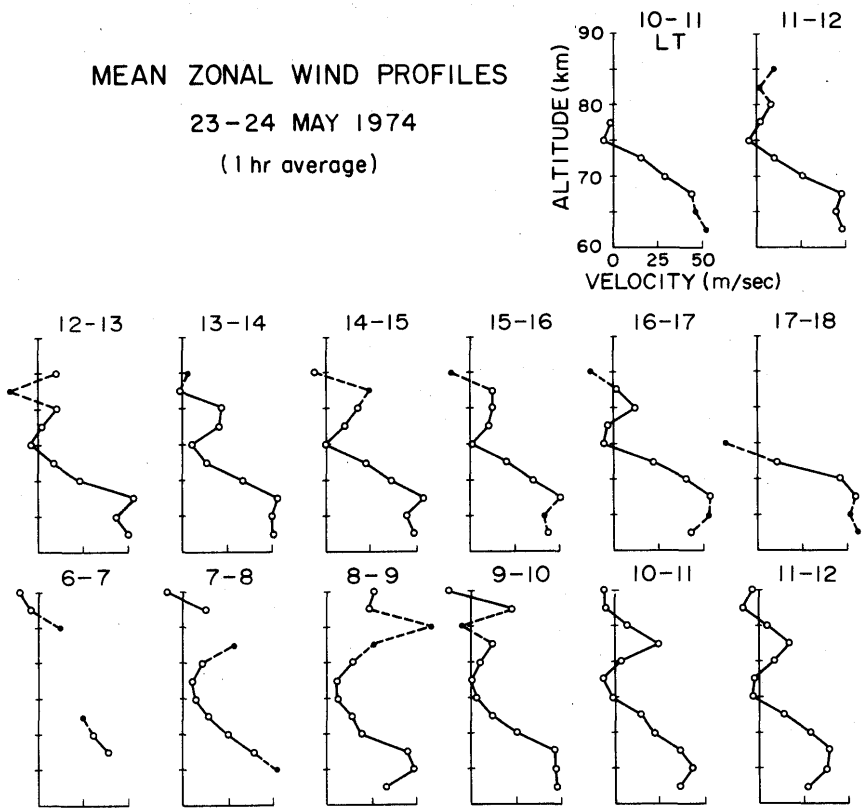

Fig.3-6 Hourly averages of the zonal velocity versus height for May 23-24, 1974. Velocities are positive eastward. Open circles indicate averages of more than 30 data points contained in a period indicated at the top of each profile, while solid ones are the averages of 10-30 data points. No average is plotted if the number of data is less than 10 within the 1-hour interval.

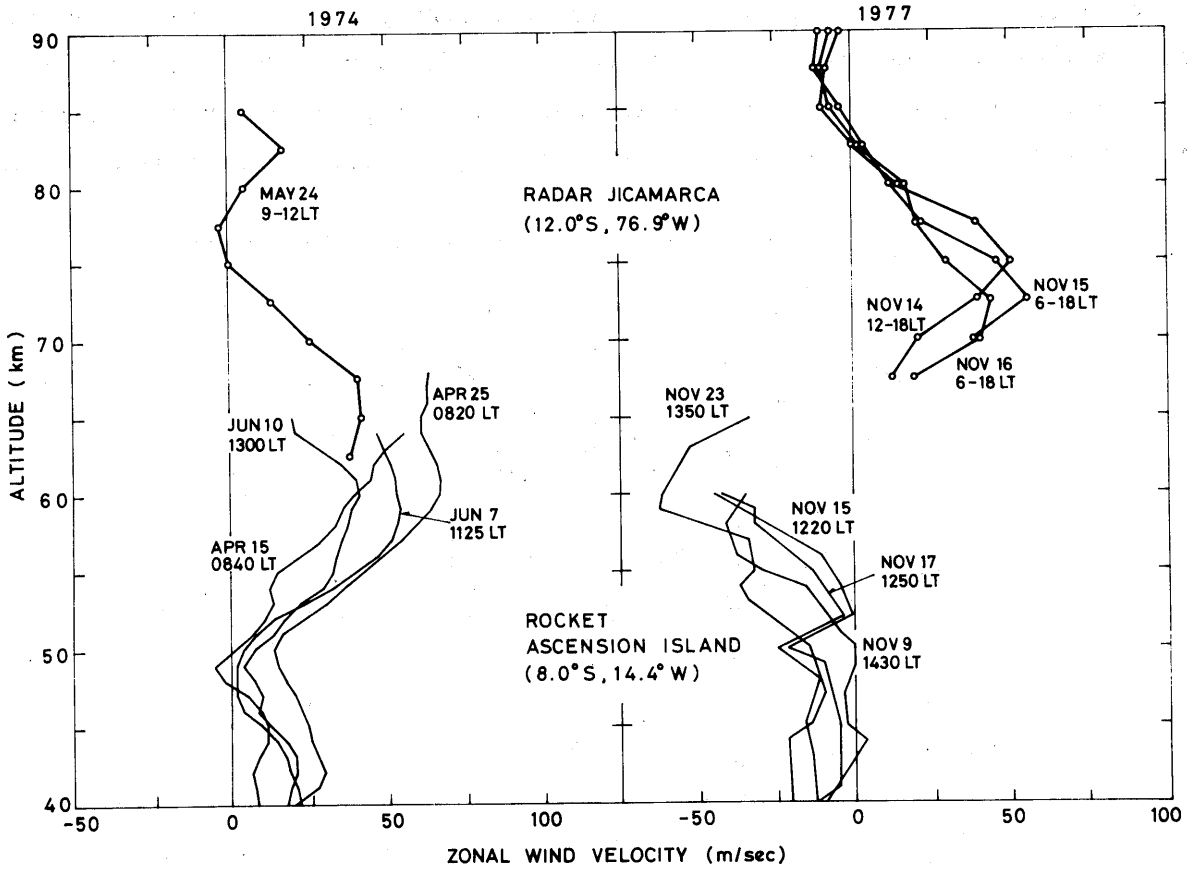

Fig.3-7 Comparison of zonal wind velocities (eastward positive) measured by the Jicamarca VHF radar (thick lines) and meteorological rockets from Ascension Island (thin lines). The radar-inferred velocities are average values of all data available on the observed daytime period.

of the same nature as that obtained by the rocket observations.

The large difference in the zonal wind profiles between 1974 and 1977 data gives a good clue for the seasonal variation of zonal prevailing wind. Since the two observations are 6 months apart in the annual cycle, the mean value between both observations is principally caused by annual mean and semiannual wind components, while major portion of deviations from the mean value is due to annual wind component. The present result seems to agree with the global mean structure of the climatrogical wind in the tropical mesosphere (Groves, 1972; Belmont et al., 1974; Hirota 1978).

Temporal variation of the 120-min means of the zonal wind for the 1977 data are plotted every 60 min in Fig.3-8. Although data points contain considerable fluctuations, the winds at each height show relatively systematic variations from hour to hour, and a clear phase change with height is also evident, especially on November 15. However, a day-to-day recurring wind pattern expected from the tidal winds does not always dominate in the height range considered. For example, the temporal variation at 75 km shows a trend with a period of the order of several days, while the wind at 82.5 km shows a variation with a period of approximately 2 days. The similar nonrecurring wind variation is also present in the 1974 data.

The dashed lines and chains in Fig.3-8 give the best fits to the data, in a least square sense, of linear combinations of a 24-hour period sinusoid and a sinusoid with a period longer than 24 hours. Because of the limited duration of the data, the long period components are represented by a monotonic oscillation with a period of 2 and 5 days. As is shown in the figure, both combinations are equally well fitted to the data, and fitting was significantly improved by introducing the long period components. It suggests that the equatorial planetary waves with periods longer than a day is playing an important role in the mesospheric dynamics. In the 1977 observation, one of the antenna beam directions was adjusted to look exactly the vertical direction, so that very small mean

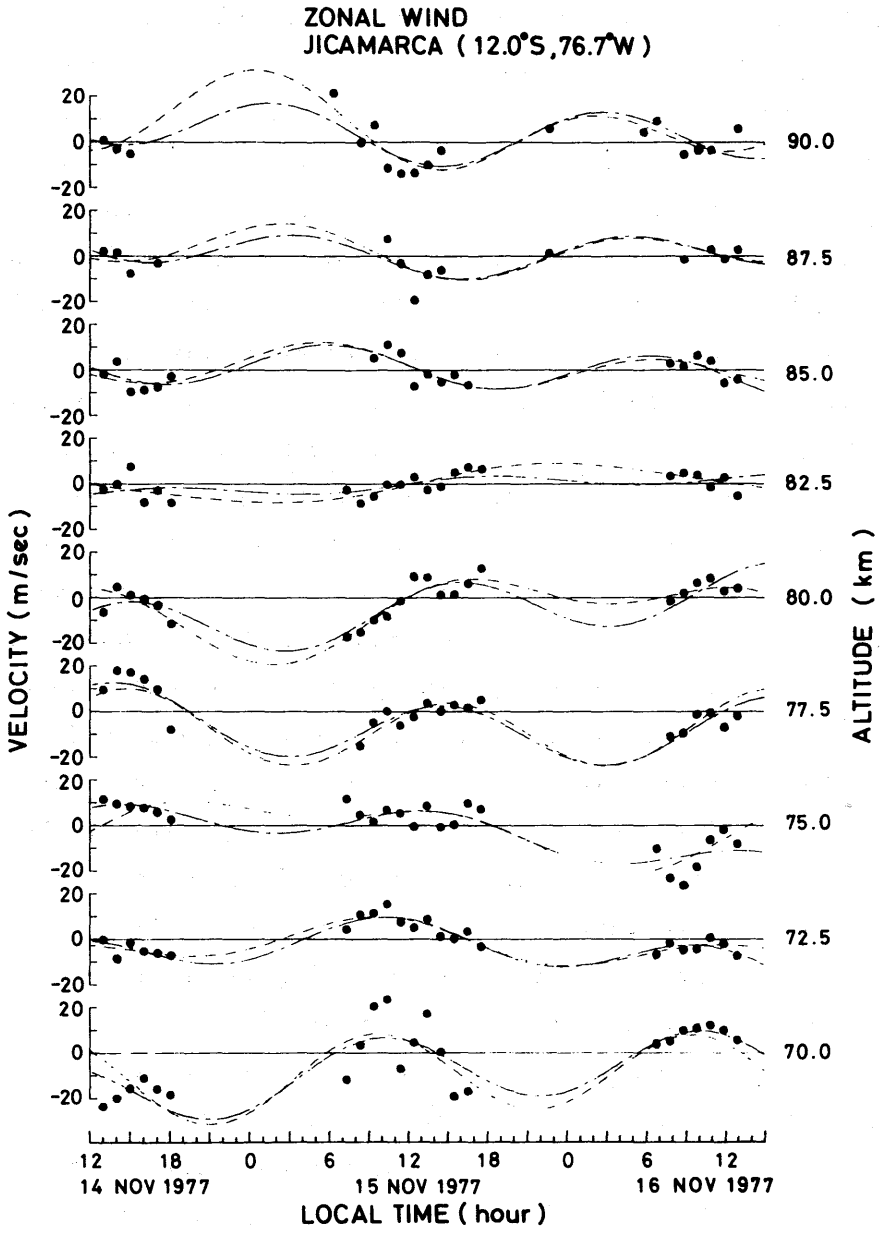

Fig.3-8 The 120-min means (dots) of the zonal wind velocities observed on November 14-16, 1977. Dashed lines and chains give the 48- and 120-hour sinusoid, respectively, which gives the best fit to data in combination with a 24-hour sinusoid.

vertical motion can be deduced without being contaminated by the large zonal wind component (Fleisch, 1976). Fig.3-9 shows daytime averages of the vertical velocity versus height. A common feature over 3 days is that the velocity is upward below about 70 km and downward above about 75 km with an amplitude of 10-20 cm s^{-1}. The velocity tends to be upward again above about 85 km. This structure also seems to suggest the existence of a long period wave with a period longer than 2 days. However, the possibility that this is the vertical component associated to the diurnal tide cannot be ruled out, since we lack the velocity data during nighttime.

3.5 SHORT PERIOD WAVES AND OSCILLATIONS

There are substantial short period oscillations in the observed temporal variation of the wind velocity, which are superimposed on the prevailing and long period waves discussed in the previous section. Fig.3-10 gives contours of isopower spectral density versus Doppler shift (or equivalently, the line-of-sight velocity) and time for the period 0800-1000 LT on May 24, 1974 for both the quasi-vertical and the off-vertical directions. The contour levels are in logarithmic scales with 2 dB interval. This form of representation shows the velocity oscillations and echo power well, but attention must be paid in interpreting the spectral width, since the strong echoes appear to be wider than weaker echoes visually due to surrounding contours. Fig.3-10 indicates that most of the echo power spectra are single peaked and continuous in time, at least to within the contour level of a factor of 1.6 (2 dB). The very broad, strong echoes which appear near minutes 35 and 40 at 77.5 and 80 km are examples of strong spikelike echoes which are often observed above 80 km.

Clear sinusoidal oscillations shown in Fig.3-10 are typical examples of the short period oscillations observed at the

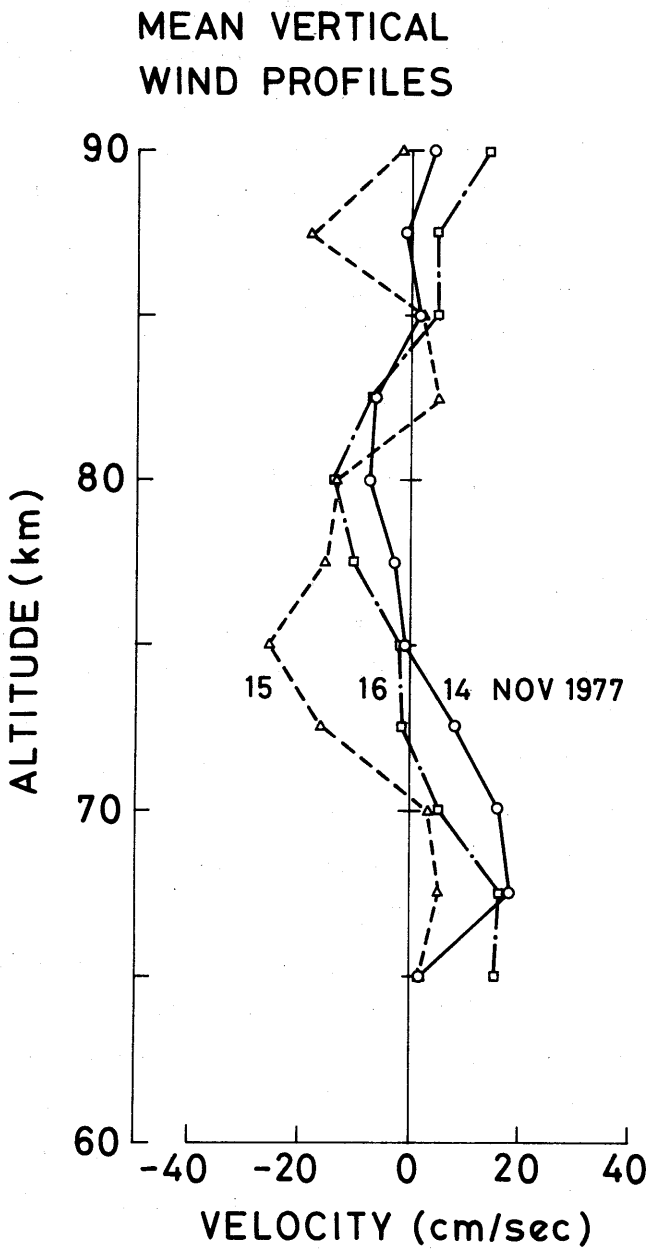

Fig.3-9 Mean vertical wind versus height on November 14-16, 1977. Each profile is an average of daytime data.

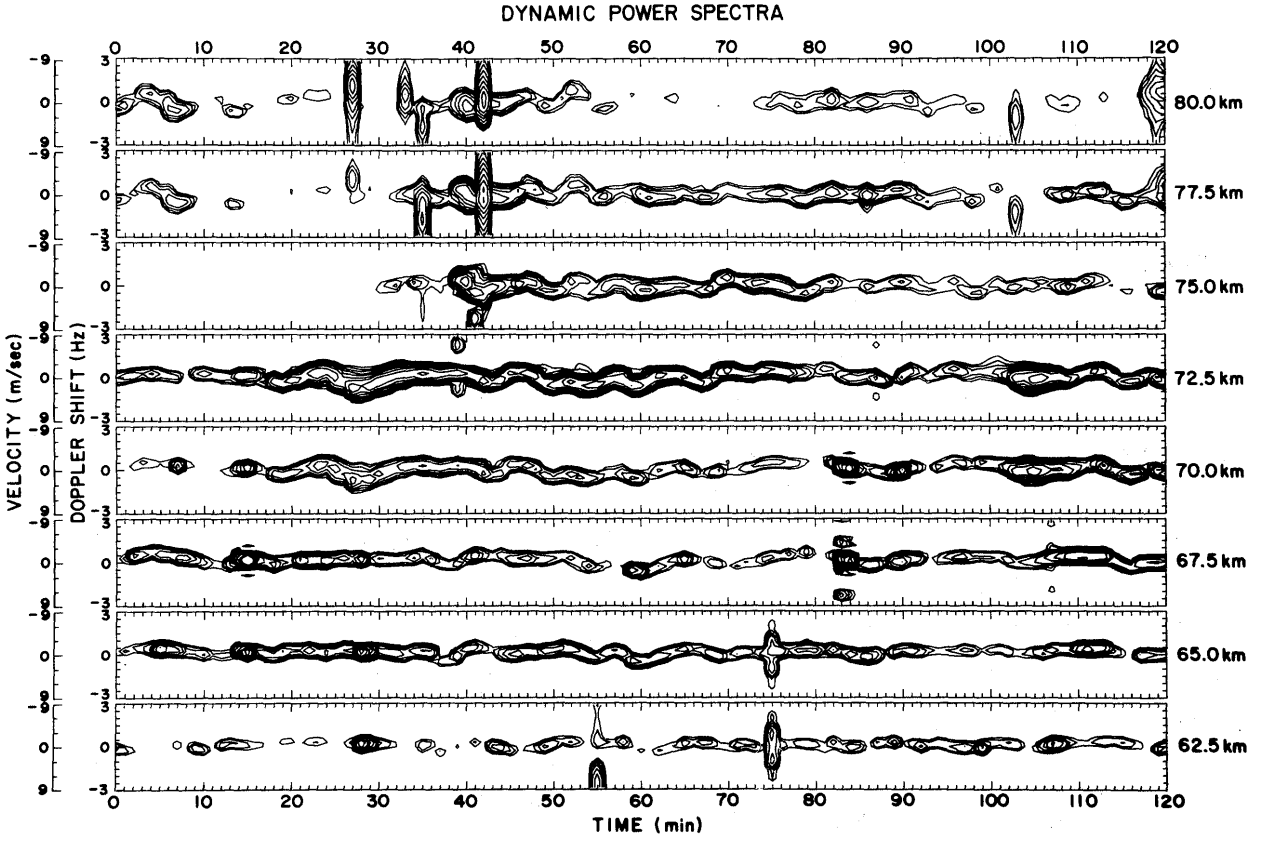

Fig.3-10 Contour plots of dynamic power spectra of scattered echoes at the a) quasi-vertical and b) off-vertical antenna beam directions for 0800-1000 LT on May 24, 1974. The ordinates are Doppler shift from center frequency and equivalent line-of-sight velocity. Contours are drawn at 2-dB intervals.

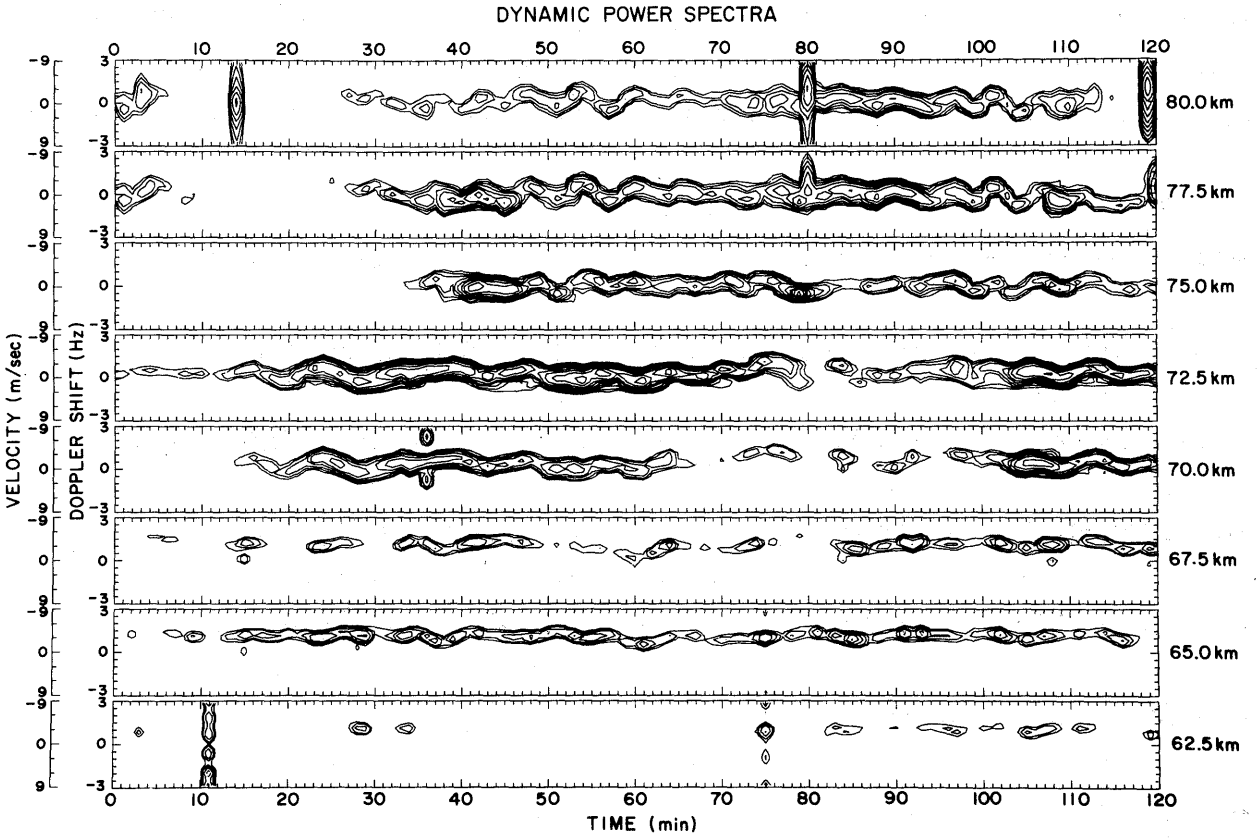

b)

Fig.3-10 (continued)

mesospheric heights by the Jicamarca VHF radar. The spectral shape does not seem to change largely even while the large amplitude oscillations exist, showing that they are the bulk motions with a spatial scale larger than the size of the scattering volume defined by the antenna beam width (1.4 km at 80 km height) and the height resolution (3.6 km). Fig.3-10 suggests that the dominant periodicity in these oscillations changes with height. It is confirmed by Fig.3-11, which shows the power spectra of the vertical wind oscillations for 0800-1200 LT on May 24, 1974. Of particular interest is the short period cutoff, which decreases with increasing height from a period of around 10 min at 70 km to about 4 min at 80 km. The 5 min periodicity which is very strong above 75 km is not observed below that height.

The general characteristics of the oscillations below 75 km agree well with earlier measurements near 70 km at Jicamarca (Rastogi and Woodman, 1974; Rastogi and Bowhill, 1976a). Except for one case found by Harper and Woodman (1977), there is no detectable phase difference between the oscillations in the two antenna beam directions below 75 km. Rastogi and Bowhill (1976a) assumed that the vertical velocities in the two antenna scattering volumes were equal and that any difference in the velocities measured in the two antennas must be due to horizontal winds; i.e., they assumed that there was no uncorrelated vertical velocity 'noise'. They then determined the mean amplitude ratio of the horizontal and vertical velocity oscillations and used this ratio in the gravity wave equations for an isothermal stationary atmosphere to derive the horizontal and vertical wavelengths of the 10-15 min period oscillations observed at 70 km. They concluded that the oscillation must be a vertically evanescent surface wave with a horizontal wavelength of the order of 200-400 km.

The oscillations observed above 75 km in the 1974 observation differ from those observed below that height; the oscillations above 75 km have shorter periods, and phase differences of 1-2 min are

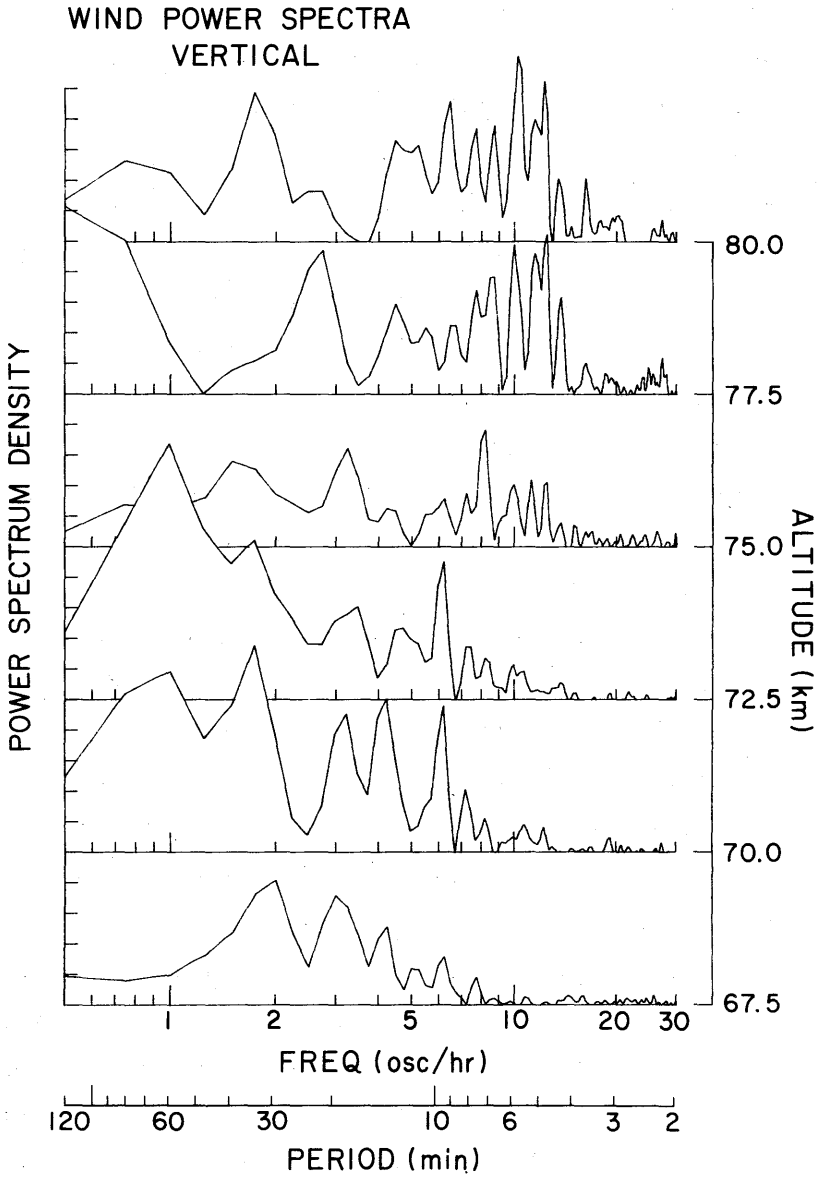

Fig.3-11 Power spectra of vertical wind velocities at 67.5-80 km for 0800-1200 LT on May 24, 1974.

frequently observed between oscillations in the two antenna directions, that are not found in oscillations below that height. This can be seen in Fig.3-12, for example, during 0800-1200 LT or 0850-0910 LT. When a clear phase difference is observed, the oscillation appear first in the vertical antenna, and then later in the antenna offset toward the west. The amplitude of the velocity oscillations are nearly equal in the two antennas. A cross-correlation analysis indicated no appreciable phase difference with height over 5 km range through which the oscillation can usually be traced.

A possible interpretation of these oscillations is that they are free buoyant oscillations with the Brunt-Väisälä period. In this case, the observed phase difference between the two directions at the same height should be due to the background flow. The velocity required to explain a phase difference of 1 min at 75 km height is about 75 m s^{-1} westward, while the maximum westward velocity observed in this period is only about 10 m s^{-1} in 70-80 km height range. It shows that these oscillations are the propagating gravity waves.

We can estimate the propagation characteristics of these waves by solving the equations of motion and continuity, and the law of heat conservation simultaneously. Since the exact solution is very hard to obtain, we consider here the simplest case of a plane wave propagating through an isothermal stationary atmosphere. This simplification seems to be reasonable for the case under consideration because the height range is close to the mesopause where vertical temperature gradient becomes zero, and the observed zonal wind velocity is indeed small. We also assume that the wave propagates in the zonal plane, which we shall examine later.

The dispersion relation for the gravity waves under these assumptions is given as (Hines, 1960)

$$\omega^4 - \omega^2 C^2 (k_x^2 + k_z^2) + (\gamma-1) g^2 k_x^2 - \gamma^2 g^2 \omega^2 / 4C^2 = 0 \qquad (3.3)$$

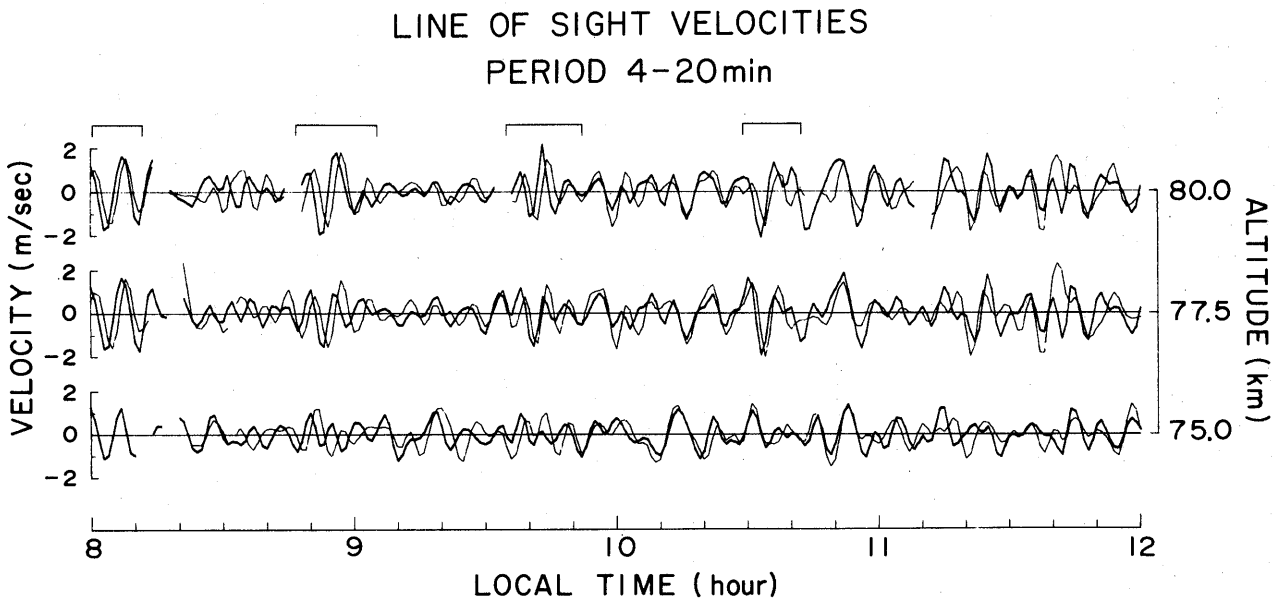

Fig.3-12 Line-of-sight velocities after 4-20 min band-pass filter. Thick lines are for quasi-vertical, and thin lines are for off-vertical antenna beam directions. Horizontal bars show periods when a clear phase difference can be seen.

where ω is the angular frequency, k_x and k_z, respectively, are the horizontal and the vertical wavenumber, C is the speed of sound, γ is the rate of specific heats (=1.4), and g is the acceleration of gravity. The polarization relation which determines the amplitude ratio of the vertical component V and the horizontal component U of the velocity oscillation becomes

$$\frac{V}{U} = \frac{\omega^2 - k_x^2 C^2}{k_x C^2 \{k_x - j(1-\gamma/2)g/C^2\}} \tag{3.4}$$

We can determine k_x and k_z from the observed value of U,V, and ω using Eq.(3.3) and (3.4). However, we should note the assumption that velocity vector is uniform over the scattering volumes observed by the two antennas, is no more valid for the short period waves under consideration. Therefore we have to restate Eq.(2.16) using the wave parameters as

$$V_{ov} = V \exp(j\omega t) + U \exp(j\omega t)\sin 3.45^\circ \tag{3.5}$$

$$V_v = V \exp\{j(\omega t - k_x d)\} \tag{3.6}$$

where V_{ov} and V_v are line-of-sight velocities in the off-vertical and quasi-vertical directions, respectively, and d is the distance between the two scattering volumes. We estimate the propagation characteristics by the following procedure:

1. Determine V_{ov}, V_v, and ω by fitting a sinusoid to the data choosing periods when clear monotonic oscillations appear. Fig.3-13 displays the amplitude ratio R and the phase difference r between V_{ov} and V_v. Numbers added to symbols denote the best fit period in minutes, and the curve attached to each symbols shows the period range within which the deduced amplitude is larger than the standard deviation in the fitting procedure.

2. Compute the dispersion relation for a given ω. The right hand side of Fig.3-13 shows the relation for periods of 5-6 min for

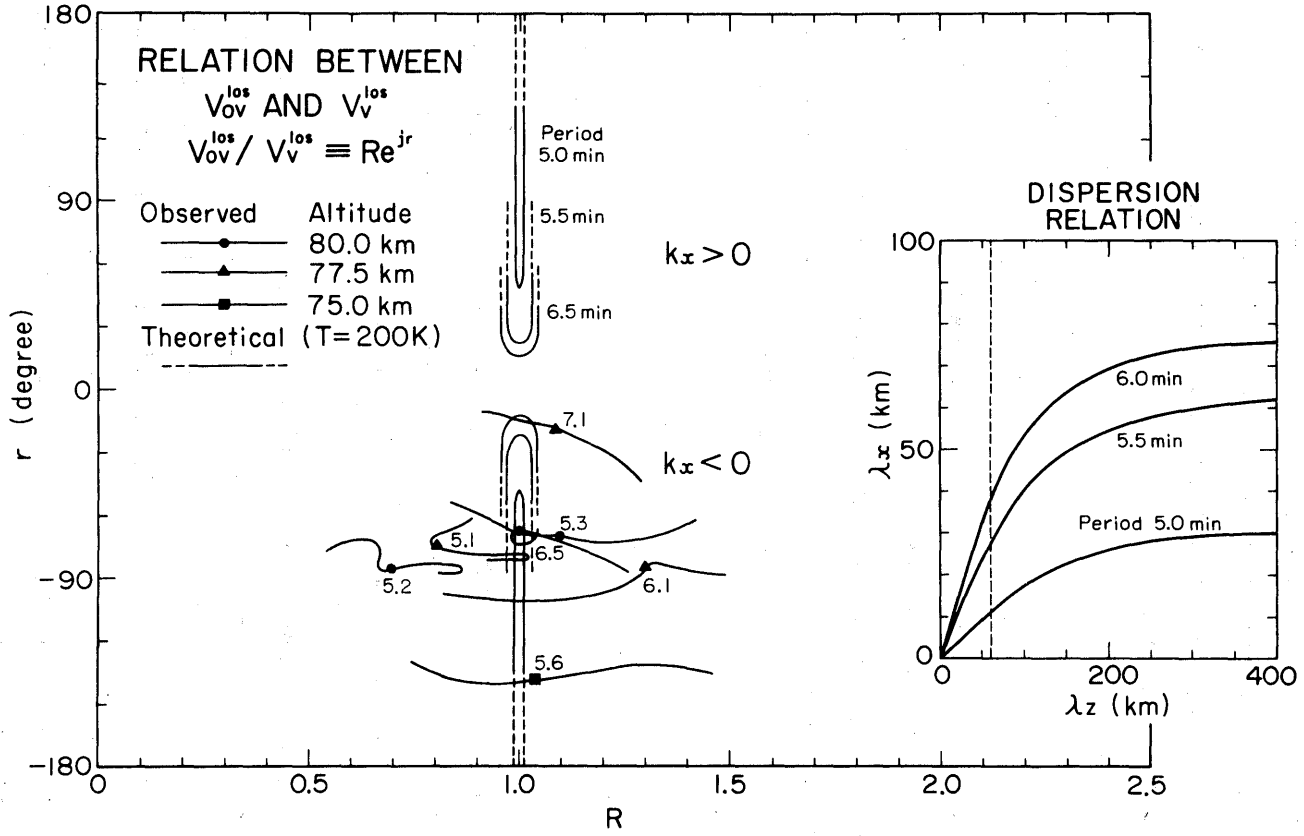

Fig.3-13 Amplitude and phase relation between quasi-vertical and off-vertical wind oscillations for the short period gravity waves. Numbers put to symbols denote the best fit period, and curves attached to the symbols indicate the range in which inferred amplitude is larger than the standard deviation. Solid and dashed parts of the theoretical curves correspond to the range $|k_z| < 10^{-4}$ m^{-1} and $10^{-4} \leq |k_z| < 1.5 \times 10^{-4}$ m^{-1}, respectively. The boundary is shown by the dashed line in the dispersion relation drawn on the right corner of the figure.

the atmosphere of 200 K. The coordinates are given in terms of wavelengths. As stated before, a cross-correlation analysis showed that the phase difference is apparently smaller than 1 min over 5-10 km height range. Thus the vertical wavelength is larger than the order of 60 km, which means that $|k_z| < 10^{-4}$ m^{-1}. The horizontal wavelength is within the range of 10-80 km.

3. Compute theoretical R and r using Eqs.(3.4)-(3.6) and compare them with R and r obtained in step 1. Solid curves in Fig.3-13 are for the range $|k_z| < 10^{-4}m^{-1}$, and dashed curves are for $10^{-4} \leq |k_z| < 1.5 \times 10^{-4}m^{-1}$. Most of the observed values fall in the region where computed values take acceptable range for k_x and k_z, showing that the observed short period oscillations can be well explained by propagating mode of internal gravity waves. However, the associated error in determining the period of oscillations precludes an accurate specification of the vertical or horizontal wavelength.

If the wave is propagating with an azimuth angle θ from the zonal plane, k_x in the above computation should be replaced by $k_x/\cos\theta$. When θ becomes large, k_x and thus k_z also becomes large, which does not agree with the fact that no appreciable phase propagation is found in the vertical direction. Therefore the direction of the propagation in the horizontal plane is at least not close to the north-south direction.

3.6 MESOSPHERIC TURBULENCE

As we have seen in some details, the Doppler shift of received echoes gives a tool to observe the dynamics of the middle atmosphere. The echo power and the signal correlation time, or the spectral width, offers a way to study the nature of the mesospheric turbulence.

Fig.3-14 shows average height variation of the echo power

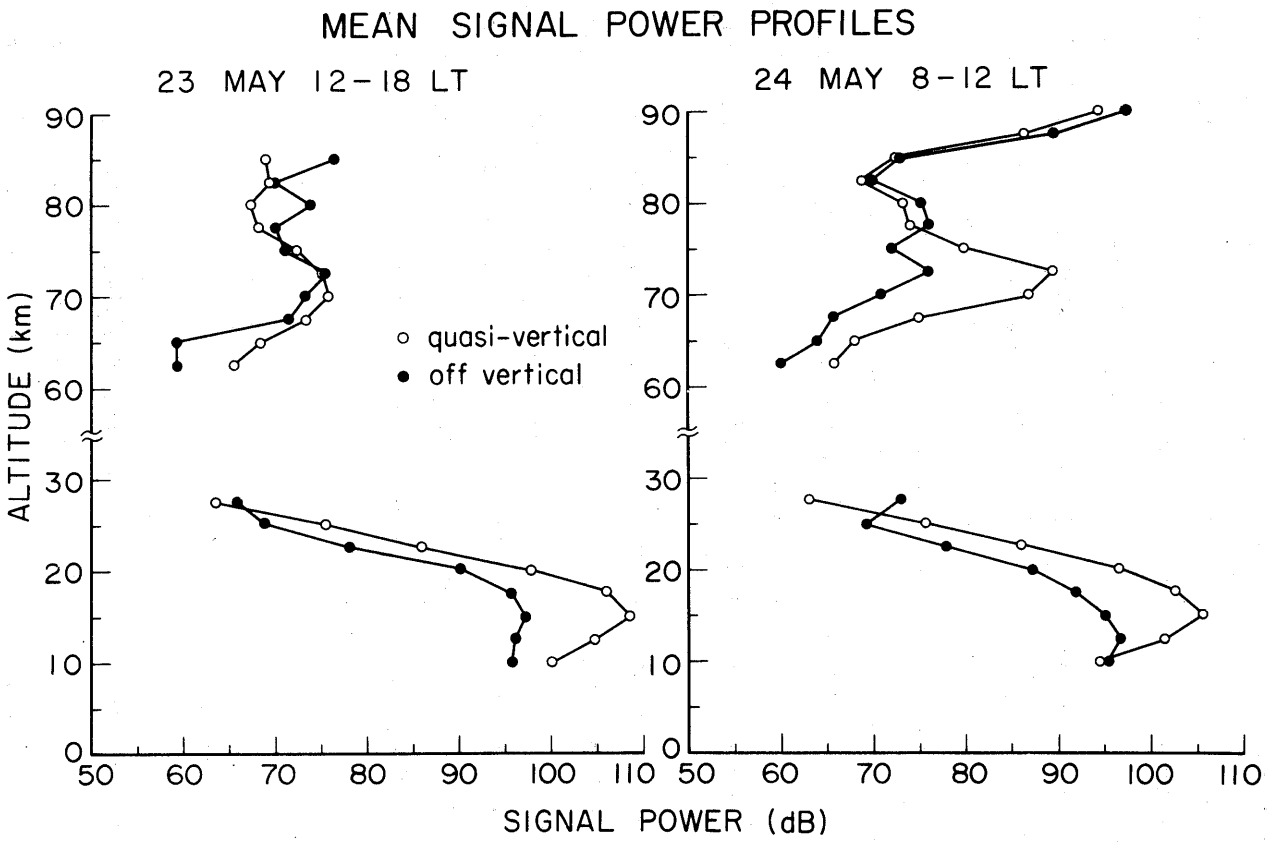

Fig.3-14 Mean signal power versus height in the quasi-vertical and off-vertical antennas for 1200-1800 LT on May 23, and 0800-1200 LT on May 24, 1974.

received by the quasi-vertical and off-vertical antenna for 1200-1800 LT on May 23, and 0800-1200 LT on May 24, 1974. The observed background noise level in the two antennas were 65.1 and 64.1 dB, respectively, indicating approximately equal system sensitivities. Although the output power of the two transmitters were not monitored, it is hard to think of a case where the difference between two transmitters amounts to a factor of 2. It is clear that about a factor of 10 times more power is received in the quasi-vertical antenna than in the off-vertical antenna at stratospheric heights, supporting the Fresnel reflection hypothesis. However, the separation of the two antenna beams at Jicamarca, only 3.45°, is much smaller than that used in the previous experiments of Gage and Green (1978) and Röttger and Liu (1978). In fact, both of the Jicamarca antenna beams fall within the 'vertical' antenna beam width used in the earlier experiments. It suggests that the Fresnel reflection is very highly aspect sensitive, and that most of the power received by a relatively broad antenna pointing approximately vertical comes from a narrow range near the vertical direction.

The quasi-vertical antenna receives 2-10 times more power than the off-vertical antenna in the lower mesosphere. The power in the two antennas becomes approximately equal by 75 km, with the possibility that the off-vertical antenna receives slightly more power above 75 km.

Fig.3-15 shows similar height profiles of the echo power observed in the vertical and off-vertical antennas in the daytime of November 14-16, 1977. The background noise levels are also shown by the vertical lines at the bottom of the figure. As is shown in the figure, a slight drift of the noise level occurred during the experiment. This drift seems to be caused by a temporal gain change of the receivers connected to each antenna. The difference of the noise levels between antenna beam directions should be considered when the echo powers are compared.

The vertical structure of the echo power shown in Fig.3-15

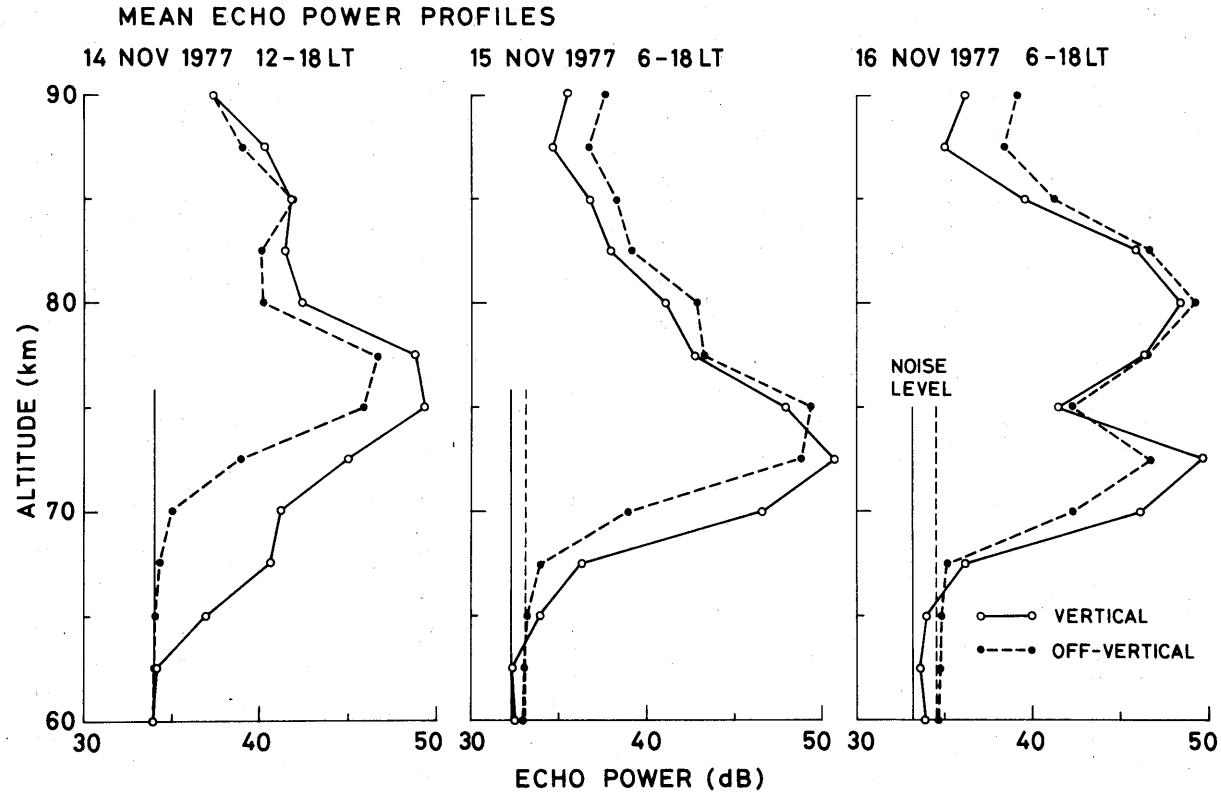

Fig.3-15 Mean signal power versus height obtained in each daytime period on November 14-16, 1977. The solid and broken curves are for the vertical and off-vertical antenna beam directions, respectively. The corresponding noise levels are given by the vertical lines.

indicates a marked day-to-day variation over 3 days. A maximum of the echo power observed at 75-77.5 km on November 14 descends to 72.5 km on November 16. On the third day, another peak appears around 80 km. It is unlikely that any large scale dynamical instability was responsible for the second peak, since the mean zonal wind shows a fairly stable profiles over the 3 days.

The echo power in the vertical antenna is consistently larger than in the off-vertical antenna in the region below about 75 km, as was the case for the 1974 data shown in Fig.3-14. Similar aspect sensitivity has also been reported by Röttger et al. (1979) using the SOUSY radar and from 2-3 MHz partial reflection studies by Vincent and Belrose (1978) and Hocking (1979). Fig.3-16 shows the ratio of the mean power in the vertical and off-vertical antennas versus height. In calculating this ratio, the echo power ratio was multiplied by the noise power ratio of the vertical to off-vertical antennas in order to compensate the gain difference in two antennas. The ratio was not plotted at heights where the average signal-to-noise ratio in one or both of the two antennas fell below 0.1. The echo power ratio shows a marked difference between above and below about 75 km. Despite a substantial day-to-day variation, the ratio below 75 km is generally as high as 5-15, while it becomes nearly unity above around 75 km. The ratio is slightly larger than unity on November 14 at heights above 80 km.

The contrast of the aspect sensitivity between above and below 75 km gives an important clue as to turbulence structures responsible for the scattering. Weak Fresnel or diffuse reflections, which occurs from sharp gradients in the electron density over distances of the order of one wavelength, or 6 m, seems to play major role in the echo power from the lower mesosphere. These diffuse reflections either could be from very thin layers of at least 1 km horizontal extent, possibly occurring at the nonturbulent-turbulent interfaces that are implied in the model used by Rastogi and Bowhill (1976c) to explain the mesospheric scattering

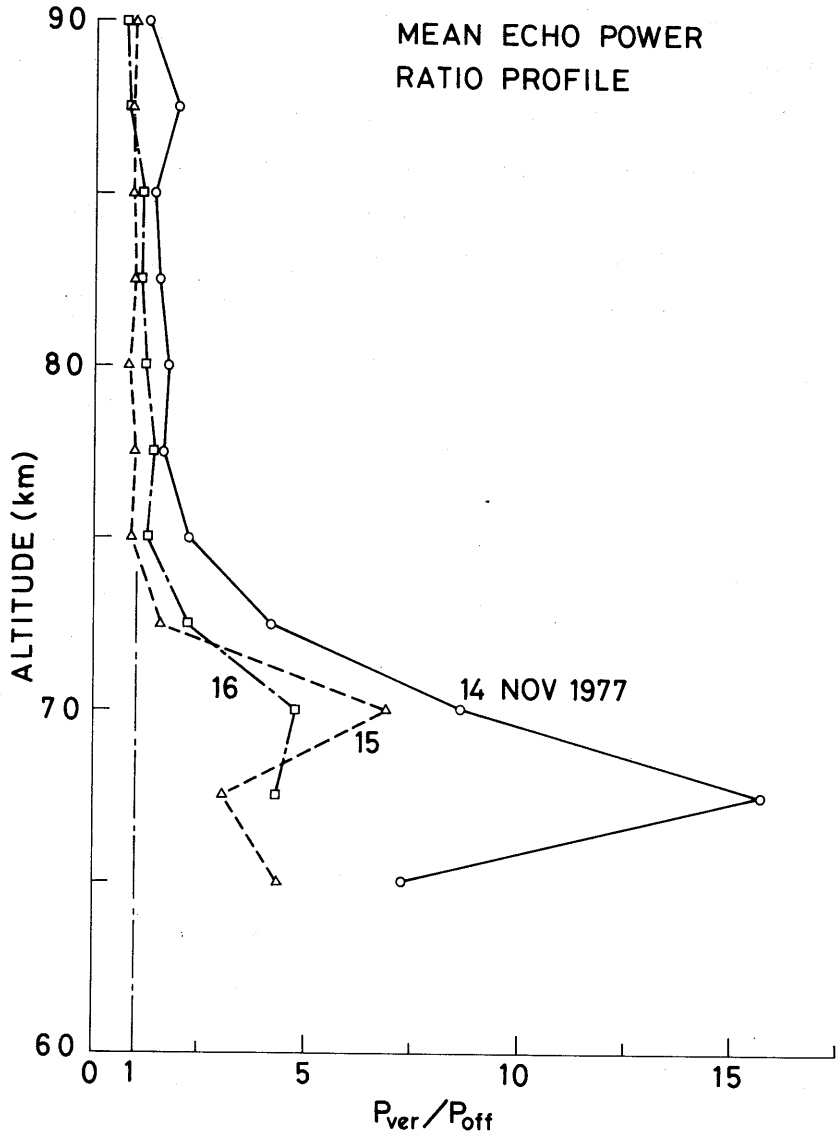

Fig.3-16 Mean echo power ratio of the vertical to off-vertical antenna beam directions versus height. No value is plotted if the average signal-to-noise ratio fell below 0.1 in one or both of the beam directions. Averaging is done over the same periods as in Fig.3-15.

at VHF frequencies, or could be from smaller irregularities which is elongated by about a factor of 5 in the horizontal direction over the vertical direction. Each of these mechanisms has been invoked to explain partial reflection observations at much lower frequencies (Belrose, 1970; Vincent, 1973). The isotropic scattering observed above about 75 km seems to indicate the increasing importance of the molecular viscosity with height to the turbulent eddies of 3-m scale size.

The signal correlation time also offers an important measure of the turbulence. First, we have to specify the mechanism which gives the largest contribution to the observed signal correlation time. There are three possible factors which may dominate the correlation time:

1. The lifetime of scatterers. As for the mesospheric scattering, the direct source of the scattering is thought to be the irregularities in electron density. Since the mean lifetime of the electrons at mesospheric heights is the order of 10 s (Rastogi and Bowhill, 1976b), it cannot explain the observed correlation time of the order of 1 s. An exception is the correlation time of the spikelike echoes which can be well explained by the lifetime of the underdense meteor trails as discussed before.

2. The time required for a scatterer to pass through the antenna beam. A point target which moves together with the background wind of 50 m s^{-1} takes about 24 s to traverse the antenna beam of the Jicamarca radar at the height of 70 km. This is also a too slow mechanism.

3. Temporal or spatial fluctuations of the line-of-sight velocity of scatterers. The r.m.s. fluctuation of 1.5 m s^{-1} in the scatterers distributed in the observed volume can explain the signal correlation time of 1 s. The velocity fluctuation of this order does not seem to be hard to achieve, since large scale vortices in a turbulent layer contain most of the kinetic energy supplied from the background shear flow (Tennekes and Lumley, 1972) and a shear of

10 m $s^{-1}km^{-1}$ can supply a momentum of 10 m s^{-1} per unit mass when the thickness of the layer is 1 km. Although part of this momentum is consumed by the work done against buoyancy, a considerable fraction is supplied into turbulence. The fraction of energy put into each degree of freedom amounts to 1/4 of the produced energy under the critical shear condition (Lilly et al., 1974). Thus the temporal or spatial velocity fluctuation alone can explain the observed signal correlation time.

The contribution of the temporal fluctuation can indirectly be examined by changing the length of the time window used to calculate each power spectrum. The shortest period over which power spectra can be determined without suffering from significant statistical fluctuation seems to be about 7 s, which is sufficiently longer than the observed signal correlation time. Fig.3-17 shows the correlation time and the spectral width obtained in the vertical and off-vertical antennas versus length of the time window used to calculate power spectra. The results are given for two heights, 75 and 77.5 km, where signal-to-noise ratios are sufficiently large. At these heights, the echo power shows virtually no aspect sensitivity, as shown in Fig.3-16.

Two features are worth noting in Fig.3-17. First, the spectral width increases with increasing length of the time window. The width varies about 20 % in the period range considered. This variation suggests that the length of the time window should be considered in discussing the spectral width. This effect can be explained as follows (e.g., Nathanson, 1969). An instantaneous spectrum with a slow shift of the center frequency would result in the observed spectral width which is the sum of the inherent width and the amount of frequency shift due to the slow bulk motion. The slow bulk motion necessary to explain the observed increase in the spectral width is roughly consistent with the short period (5-15 min) velocity oscillations of amplitude of 1 m s^{-1} that are always observed at mesospheric heights over Jicamarca.

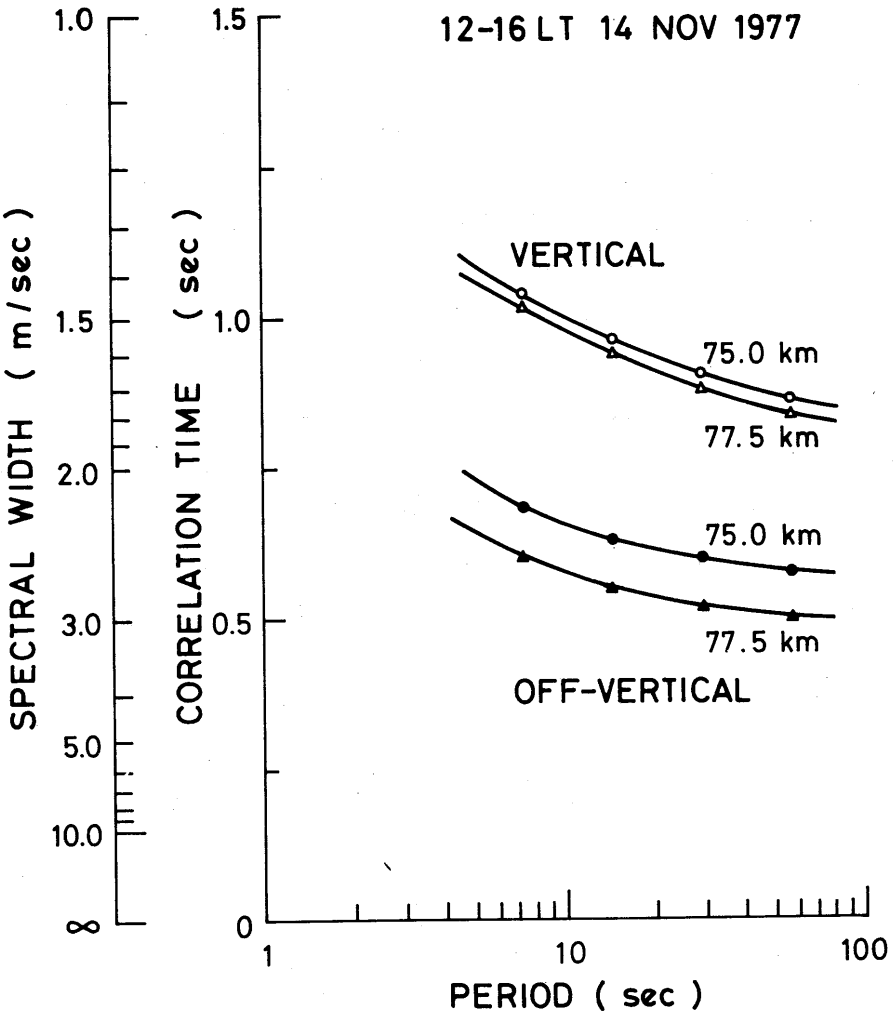

Fig.3-17 Signal correlation time and spectral width versus periods used to calculate power spectra at 75 and 77.5 km, where the signal-to-noise ratio are fairly large. Each curve is an average value over 1200-1600 LT on November 14, 1977. The spectral width is given by the equivalent r.m.s. velocity fluctuations in meters per second.

Second, the spectral width in the off-vertical direction is about 1.5 times larger than the width in the vertical direction. This difference can be well explained by the shear broadening effect. When an antenna beam is looking a turbulent layer obliquely under the presence of a background shear, the scatterers near the upper and the lower boundary give different Doppler shifts, according to the difference in background flow above and below the layer, thus contribute to the broadening of the observed spectra. A scattering layer 1 km thick in the presence of a 10 m $s^{-1}km^{-1}$ vertical shear of the horizontal wind can explain the observed difference in the spectral width.

The mean signal correlation time inferred from the 30-s periods of data by the manner described in Section 3.2 is given versus height for the vertical and off-vertical directions in Fig.3-18. Data were not used in the average if their signal-to-noise ratio fell below 0.2, and no value was plotted in the figure at heights where the number of available data was less than 10 % of the total number of data. A more strict threshold was used for the signal correlation time than the echo power, since estimates of signal correlation time have larger statistical fluctuations than the echo power. Fig.3-18 shows a general tendency that the signal correlation time decreases monotonically with increasing height. The mean value inferred is 1-1.5 s at the 65-70 km region, whereas it is of the order of 0.5 s at 85 km. Meteor trail echoes that have signal correlation times of the order of 0.1-0.2 s may influence the correlation time above 85 km. The decrease in signal correlation time corresponds to the increase in spectral width which indicates the magnitude of the line-of-sight velocity fluctuations. This increase in velocity fluctuations with height seems to be consistent with studies of turbulence by Zimmerman and Murphy (1977) and roughly parallels the height variation of molecular diffusion. Similar height variation is also observed by the 54-MHz SOUSY radar (Röttger et al., 1979). They reported that narrow structures, i.e.,

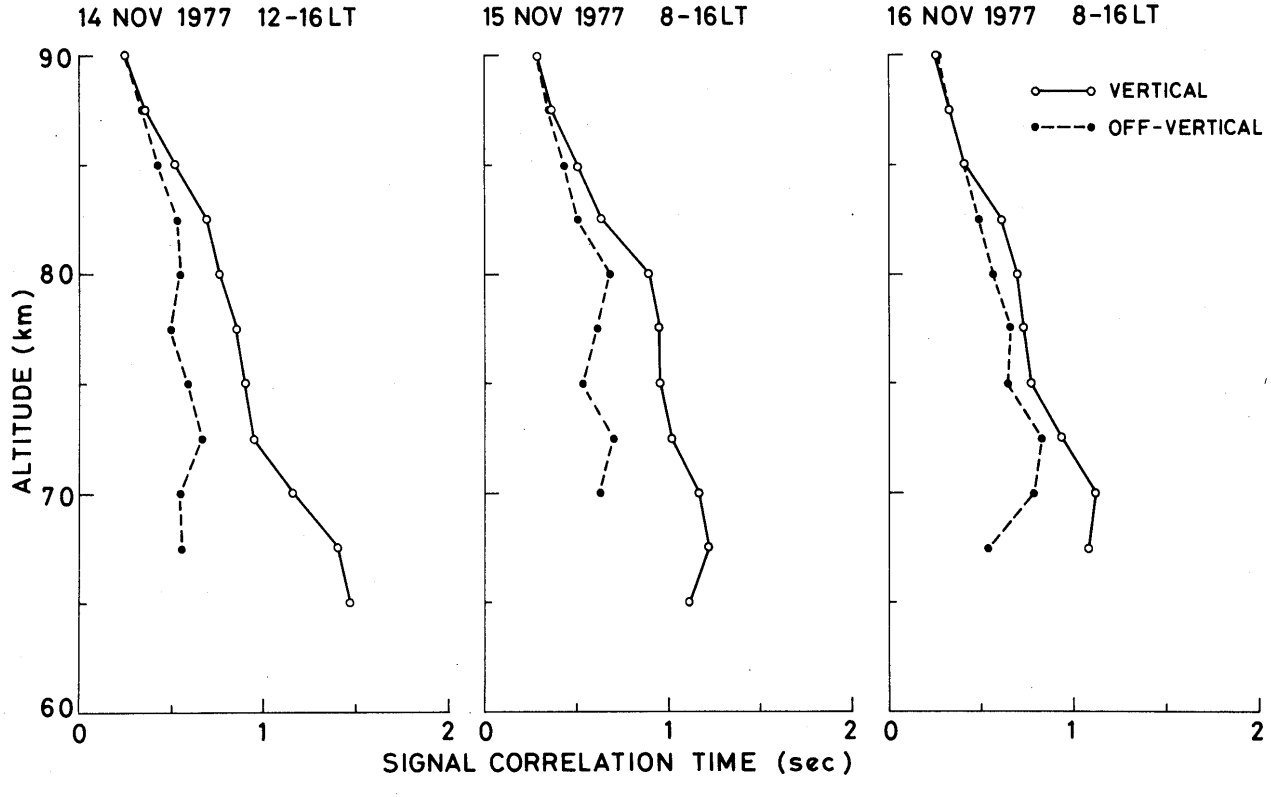

Fig.3-18 Mean signal correlation time versus height obtained in each daytime period on November 14-16, 1977. The solid and broken curves are for the vertical and the off-vertical antenna beam directions, respectively.

blobs and sheets, predominantly occur at lower heights, while thick and diffusive layers occur at higher region, concluding that the thicker structures are associated with a larger spectral width. The fact that no aspect sensitivity was found in the echo power above 75 km, is also consistent with the predominance of thicker and more diffusive turbulence structure there. Another feature worth mentioning in Fig.3-18 is the difference of the signal correlation time between the two antenna beam directions. The ratio of the vertical to off-vertical values is 1.2-2.0 at 70 km, approaching unity with increasing height. This variation is possibly due to the decreasing contribution of the shear broadening effect as the inherent width of the spectra becomes larger.

Rastogi and Bowhill (1976c) reported a clear positive correlation between echo power and signal correlation time at a height of 70 km. On the other hand, a negative correlation between the echo power and the signal correlation time was found by Harper and Woodman (1977), who observed a sudden decrease of the signal correlation time accompanied by a strong burst of the echo power at 75 km.

In the present observations, both types of correlation were found, each in a different height range. Fig.3-19 shows a temporal variation of the echo power together with the signal correlation time at 0700-1200 LT on November 16, 1977. At the lower height, especially at 70 km, the positive correlation prevails. On the other hand, negative correlation is frequently observed at higher region. For example, the temporal variation of echo power is opposite to that of the signal correlation time in the period of 0930-1100 LT at 77.5 and 80 km.

In order to derive a general sense of correlation between the echo power and signal correlation time, all data available at each height are divided into 15 groups according to signal correlation time. Then the mean echo power in each group was computed, giving the graphs shown in Fig.3-20. All of the signal correlation time

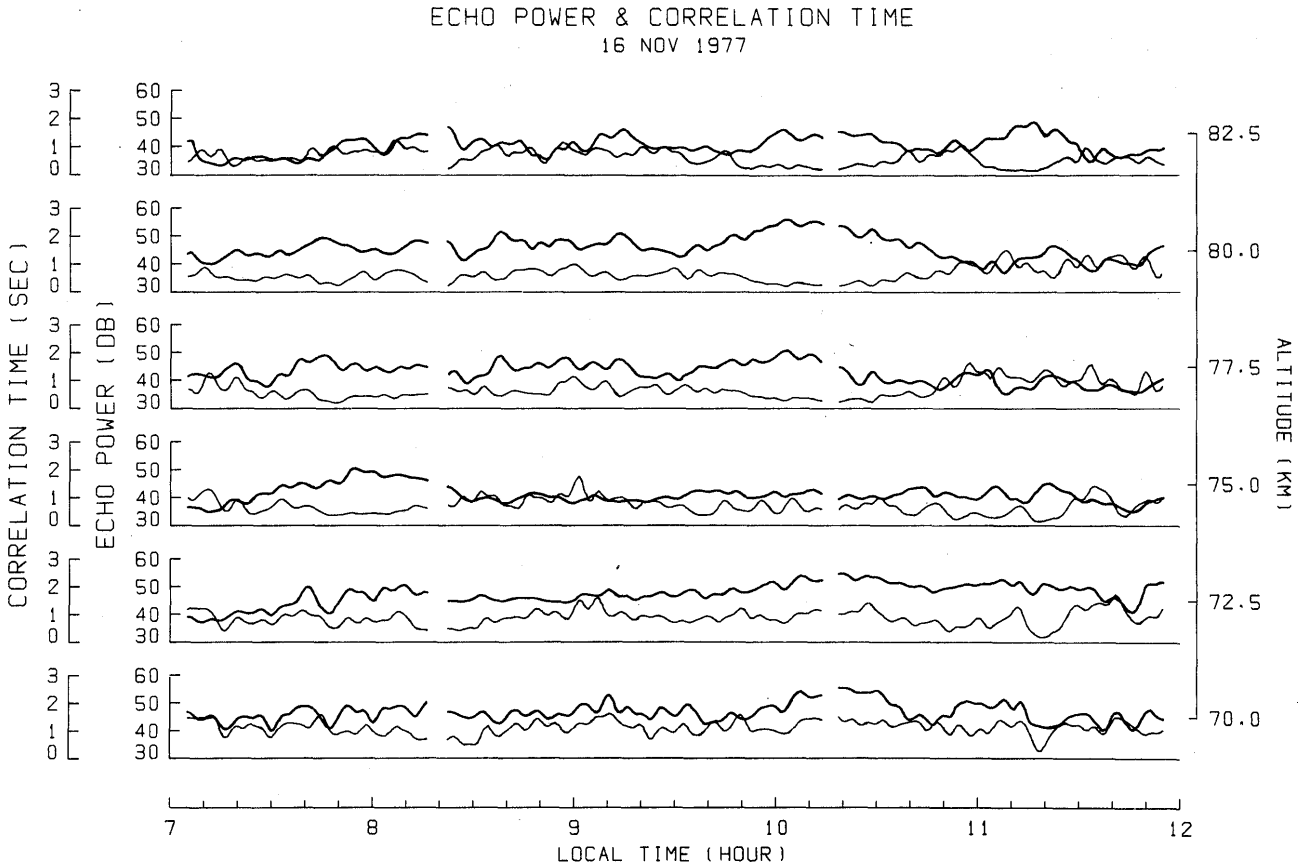

Fig.3-19 A typical temporal variation of the echo power (thick line) and signal correlation time (thin line) at 0700-1200 LT on November 16, 1977.

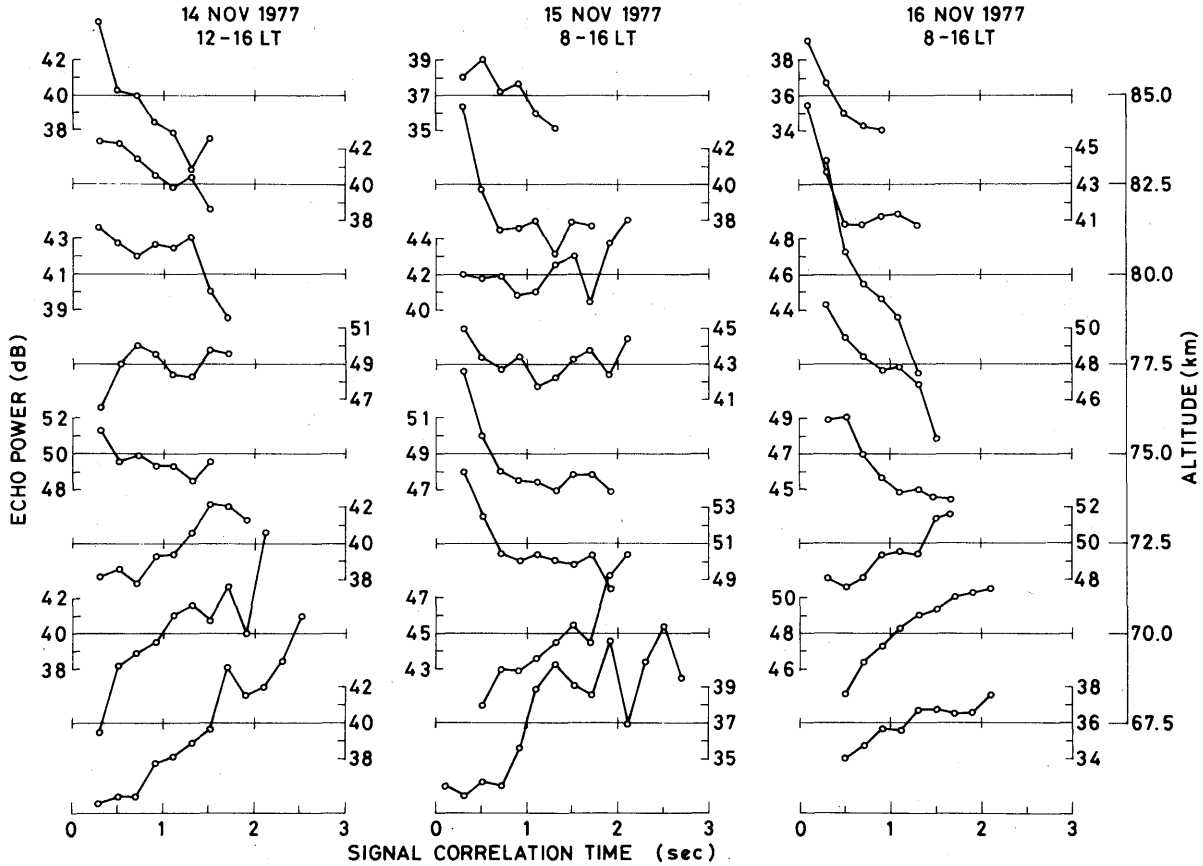

Fig.3-20 Height variation of a relationship between the echo power and signal correlation time. Each curve is an average value for each daytime period shown at the top of the diagram. See text for details.

data used in this calculation are based on the 30-s spectra with signal-to-noise ratio higher than 0.2. Only intervals in which at least 10 data points are contained are plotted.

The most apparent feature in the figure is that the general sense of correlation between the echo power and the signal correlation time reverses from positive to negative with increasing height. The reversal generally occurs around 75 km, although individual data show a considerable scatter there. The standard deviation of individual data around the mean values is fairly large, their correlation coefficient being less than 0.5 in most cases. Despite this limitation, the general sense of correlation seems to be significant, since the data of 3 independent days show quite similar height variations. We should note that the height of the reversal coincides with the height where the aspect sensitivity in the echo power vanishes. The negative correlation above about 75 km means that more intense echo power is associated with stronger velocity fluctuations. Rastogi and Bowhill (1976b) argued that the scattering cross section is independent of the intensity of turbulence in the inertial subrange but depends strongly on the intensity in the viscous subrange. Thus the observations appear to be consistent with an idea that Jicamarca's wavelength falls in the viscous subrange of turbulence above about 75 km.

The mean echo power decreases above 75 km, until about 85 km where it reaches roughly the incoherent scatter level expected from the electron density of 2.5×10^3 cm^{-3}. The signal correlation time is also the order predicted by the theoretical calculation for the incoherent scatter at that height (Fukuyama and Kofman, 1980). Thus the turbulent enhanced electron density fluctuations seem to be highly damped above 85 km, although the signal power still fluctuates occasionally in a way which suggests nonthermal echoes. However, Miller et al. (1978) and Czechowsky et al. (1979) have observed strong thick scattering layers above 85 km at the Illinois and SOUSY radars, respectively.

Below 75 km, on the other hand, the increase in signal correlation time is observed to occur along with increased echo power. Rastogi and Bowhill (1976c) showed that the positive correlation could be explained if stronger turbulence were occurring in narrower layers. The turbulent layers had to be of the order of a few tens of meters thick so that a finite range of wavenumber could contribute to the scattering.

3.7 SUMMARY AND CONCLUSIONS

Two sets of mesospheric observations made with the Jicamarca VHF radar have been presented. The signal characteristics were first examined, which in general confirmed previous observations and supported the theory that the scattering occurs from the electron density fluctuations due to atmospheric turbulence. The observed shapes of the signal auto-correlation functions and the echo power spectra are found to be well represented by the first three spectral moments.

The Doppler shift of the signals was used to study the mesospheric dynamics of various time scales. The mean zonal wind velocity was compared with the meteorological rocket observation, and a good agreement was found between the two. A long period waves with 2-5 day period with comparable amplitude with diurnal tidal winds were found, suggesting the importance of planetary waves in the mesosphere. Short period sinusoidal oscillations were discussed in terms of horizontally propagating internal gravity waves, which has a frequency close to that of the Brunt-Väisälä oscillation.

The echo power generally shows its maximum around 70-80 km, and there is appreciable day-to-day variation in its vertical structure. A strong aspect sensitivity was found in the echo power below about 75 km, where the vertical echo power becomes 5-10 times larger than the off-vertical echo power. Signal correlation time decreases with

height from 1-1.5 s at 70 km to about 0.5 s at 85 km. It was shown that the observed correlation time can be well explained in terms of the temporal or spatial fluctuations of the velocity in scatterers.

The relation between echo power and signal correlation time showed a marked difference below and above about 75 km. Above that height, the echo power and the signal correlation time showed a negative correlation, suggesting that the turbulence in that region is in the viscous subrange at the scale size probed by the Jicamarca VHF radar. Below about 75 km, on the other hand, the correlation becomes positive, which can be explained by postulating that stronger turbulence occurs in a narrower region, as suggested by Rastogi and Bowhill (1976c).

CHAPTER 4

TECHNICAL CONSIDERATIONS ON THE ARECIBO UHF RADAR OBSERVATIONS

4.1 THE ARECIBO UHF RADAR SYSTEM

The Arecibo 430 MHz radar is one of main facilities of the Arecibo Observatory of the National Astronomy and Ionosphere Center of the U.S.A. It is located in a limestone valley among mountains 15 km south of Arecibo, Puerto Rico (18.35°N, 66.75°W). Fig.4-1 shows the aerial view of the Arecibo Observatory.

As was the case for the Jicamarca VHF radar, the Arecibo UHF radar was designed initially as an incoherent scatter radar oriented to the ionospheric study, corresponding to the proposal by W.E.Gordon (Gordon, 1958; Gordon and LaLonde, 1961), and completed in November, 1963. After the upgrading took place in 1974 (LaLonde, 1974), the capability of the antenna was extended to cover the frequency of up to 4830 MHz, greatly improving its performance as a radio telescope. A S-band planetary radar system operating at 2380 MHz was also installed at the same time. These different systems share the same reflector surface with different primary feed for each frequency band. The 430 MHz system has been used to investigate the stratosphere since 1974 (Aso et al., 1977), and the mesosphere since 1977 (Harper, 1978). A stratospheric experiment using 2380 MHz system was also carried out in 1978 (Woodman, 1980b). However, only the stratospheric observations using the 430 MHz system is discussed in this thesis. The details of the antenna is presented by LaLonde (1974), and the 430 MHz system by Woodman (1980a). The following descriptions owe also to the technical data sheets provided by the Arecibo Observatory (National Astronomy and Ionosphere Center, 1979).

The antenna consists of a 305-m fixed spherical reflector with a 30-m line feed designed to illuminate the full aperture at 430 MHz.

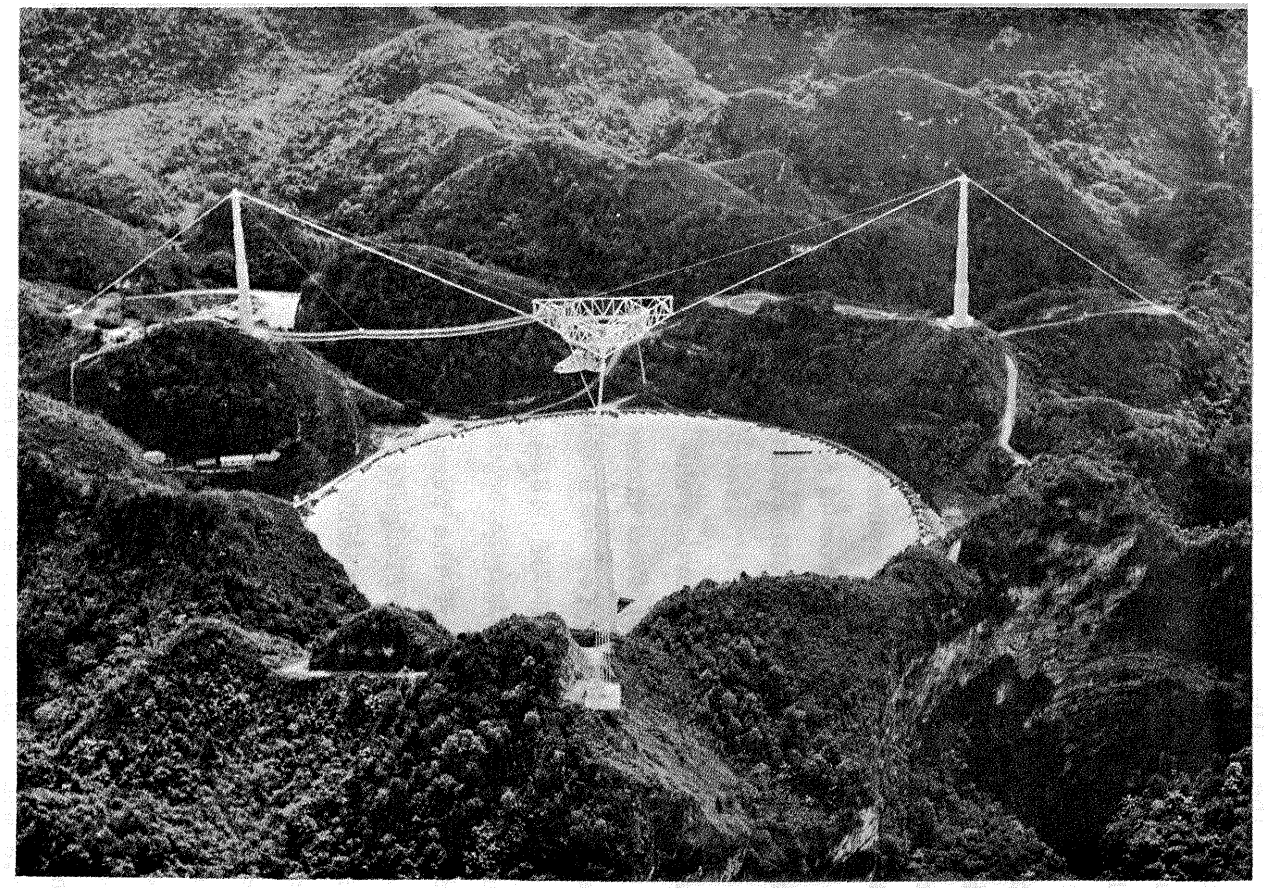

Fig.4-1 An aerial view of the Arecibo Observatory, Puerto Rico (courtesy of the Arecibo Observatory, National Astronomy and Ionosphere Center).

The combination of a spherical reflector with a movable line feed, instead of a fixed parabolic surface and a point feed, allows a limited steerability to the antenna system without sacrificing the performance. The line feed is made of a slitted cylindrical waveguide, tapered to adjust the phase velocity inside the feed so that the radiated wave has a plane phase front in space.

The reflector surface is made of 38,778 perfolated aluminum panels with approximate dimensions of 1 by 2 m. These panels are supported from 3/8-inch cables and stabilized by a system of 1/4-inch prestressed cables which are tied down to concrete anchors on the ground beneath the surface. The accuracy of the surface is 3.2 mm r.m.s. to the perfect sphere. The distance between the surface and the ground varies from a few to about 10 m depending on the position. The radius of curvature is 265 m, and the surface covers about 70° of the sphere.

The structure which supports the primary feeds is suspended about 150 m above the ground from three concrete towers with five 3.25-inch steel bridge cables for each tower. The top of the three towers have the same level of 184 m above the bottom of the reflector surface. The structure is tied down to the ground in order to cancel the heat sag of the structure due to daily or annual temperature variation. The triangular platform shown in Fig.4-1 supports a circular set of rails with a nominal diameter of 37 m. A bowstring truss rotates underside of the rails, allowing a complete azimuth coverage to the line feeds. The line feeds for various frequency bands, including the one for 430 MHz, are mounted beneath either of two carriage houses, which move along rails underside the truss. The motion of carriage houses provides zenith angle coverage of 0-20°. The slew speeds of the carriage houses are $23.5^{\circ}min^{-1}$ for azimuth and $1.8^{\circ}min^{-1}$ for zenith angle directions.

The reference frequency for the 430 MHz system is provided by a rubidium vapor oscillator. Pulse width, IPP, and pulse codes for the pulse compression, are generated by the synchronous programmable

sequencer (SPS), which is controlled by the Harris /4 computer. The details of the pulse compression technique will be given in the following section. The SPS can either 'recirculate' the pulse pattern stored on its own memory, or can fetch the pattern from the main memory of the host through a direct-memory-access line.

The final amplifier of the transmitter consists of two 4-cavity klystrons combined in a 3-dB waveguide coupler. The klystron beam currents are cut off between pulses to avoid generation of radio noise during reception. The RF drive commences 10 μs after starting beam current. The beam current is also controlled by the SPS. The nominal peak and average output power of the transmitter is 2.5 MW and 150 kW, respectively. Power is fed to the line feed through 460 m of WR2100 waveguide, one rotary joint which allows the rotation of the bowstring truss, one linear joint which allows the motion of the carriage house, and the polarization determining turnstile junction. The waveguide loss is estimated as 1.25 dB. The transmitter has an approximate bandwidth of 1 MHz, which determines the bandwidth of the whole 430 MHz system.

The receiver front-end is a parametric amplifier with a noise temperature of 120 K. Received signals are then converted into the IF of 30 MHz, further amplified, filtered with a 1 MHz bandwidth Gaussian filter, and coherently detected. The cosine and sine outputs of the detector is digitized and auto-correlated with the transmitter pulse code by the digital planetary decoder (Woodman, 1980a). It consists of four real cross-correlating channels, each of which is capable of performing 256 operations corresponding to 256 consecutive lags per microsecond. Only two channels are used in the atmospheric radar observations.

The decoded signal is partially integrated in the buffer of the planetary decoder, then transferred to the Harris /4 computer. The data is immediately transferred into the array processor Floating Point AP-120B, in which all of the remaining on-line processing is performed. It consists of a further coherent integration,

computation of the frequency power spectra by the multi-channel FFT algorithm, and the incoherent integration. The resulted spectra are stored on magnetic tapes for the off-line processing. While the array processor is performing these tasks, the host computer can be used for quick-look of the processed data in a TSS mode.

Table 4-1 summarizes characteristics of the Arecibo UHF radar.

4.2 PULSE COMPRESSION TECHNIQUE FOR THE STRATOSPHERIC OBSERVATIONS

As shown in the previous section, the transmitter of the Arecibo UHF radar has a bandwidth of about 1 MHz in contrast with that of about 40 kHz for the Jicamarca VHF radar. This fairly wide bandwidth allows a transmitter pulse of as short as 1 μs, which corresponds to a height resolution of 150 m. However, the signal-to-noise ratio is proportional to the scattering volume, which is the product of the antenna beam width and the pulse width. In order to satisfy these conflicting requirements of the height resolution and the signal-to-noise ratio simultaneously, various pulse compression techniques have been developed (e.g., Skolnik, 1980).

The basic idea of the pulse compression is to widen the bandwidth of a long pulse by modulating the carrier frequency of pulse on transmission, and to process the received signal in a matched filter that compresses the long pulse to a duration 1/B, where B is the bandwidth of the modulated pulse. The matched filter can be realized by taking a cross-correlation of the received signal with the transmitted pulse pattern. Although any kind of modulation can be used, the binary phase coding is the most convenient scheme for the coherent middle atmospheric radars, because the coding and decoding can be done in a digital form, thus requiring no special hardware for the modulation and demodulation.

Performance of a given code can be examined by taking the impulse response of the coded pulse. It is equivalent to take the

Table 4-1 Characteristics of the Arecibo UHF radar

Location	: Arecibo, Puerto Rico (18.35°N, 66.75°W)
Frequency	: 430 MHz
Antenna	
configuration	: fixed spherical reflector with a movable 30-m line feed
aperture	: 73000 m^2 (305 m in diameter)
beamwidth	: 0.13°
on-axis gain	: 62.7 dB
on-axis efficiency	: 0.70
polarization	: circular (right and left)
beam direction	: 0-20° zenith angle
slew speed	: 23.5°min^{-1} (azimuth) 1.8°min^{-1} (zenith)
Transmitter	
final amplifier	: two 4-cavity klystrons
peak power	: 2.5 MW (nominal)
average power	: 150 kW (nominal)
bandwidth	: ~ 1 MHz
TR/ATR switches	: tungsten spark gaps
Receiver	
front end	: parametric amplifier
noise temperature	: 120 K
bandwidth	: 10 MHz
IF	: 30 MHz
A/D converter	: 12 bit × 4 channel
Computer	: Harris /4 with Floating Point AP-120B array processor

auto-correlation function of the pulse pattern. Since the maximum power and the width of compressed pulse are determined by the length of the pulse and the available bandwidth, respectively, the largest point of interest is level of undesired responses of the auto-correlation function at non-zero time delays. They are called the 'time sidelobes' by their similarity to sidelobes in antenna pattern. For the binary phase codes, the optimum series known as Barker codes exist for several length of the code up to 13 bit (Barker, 1953). A N-bit Barker code has the property that the amplitude of time sidelobes is always 1/N of the amplitude at the peak. It corresponds to the sidelobe suppression ratio of 22.3 dB for 13-bit Barker code. Beyond 13 bit, a series of optimum codes, of which the sidelobe level is at most 2/N, exist up to 28 bit (Gray and Farley, 1973; Lindner, 1975). The maximum sidelobe suppression ratio for the 28-bit code is 22.9 dB.

As far as a single pulse is concerned, no better sequence is likely to exist for a moderate length of the code. However, if the signal correlation time is sufficiently longer than 1 IPP, or in other words, if the coherent integration is applicable, it is possible to obtain a better, or even infinite sidelobe suppression ratio by combining two or more pulse codes. The complementary series (Golay, 1961) is a pair of pulse codes that have time sidelobes of the same amplitude with opposite signs. Thus the sum of the auto-correlation functions of these two series is zero for all time delays except at the origin.

Formally, this property is expressed as follows: Let a_i and b_i the pair of a binary complementary series of length N, where a_i and b_i takes values of +1 or -1 for i = 1,...,N, and 0 for other i's. The above property is written as

$$A_j + B_j = \begin{cases} 2N & (j = 0) \\ 0 & (j \neq 0) \end{cases} \qquad (4.1)$$

where

$$A_j = \sum_{i=1}^{N-j} a_i \, a_{i+j}$$

$$B_j = \sum_{i=1}^{N-j} b_i \, b_{i+j}$$

are the auto-correlation functions. The complementary series has an useful feature that longer series can be synthesized from a given pair. Consider a new pair of length 2N defined by

$$\begin{aligned} c_i &= a_i + b_{i-N} \\ d_i &= a_i + b_{i-N} \end{aligned} \tag{4.2}$$

Their auto-correlation functions become

$$\begin{aligned} C_j &= \sum_{i=1}^{2N-j} (a_i + b_{i-N})(a_{i+j} + b_{i+j-N}) \\ &= A_j + B_j + \sum_{i=1}^{2N-j} (a_i b_{i+j-N} + a_{i+j} b_{i-N}) \\ D_j &= A_j + B_j - \sum_{i=1}^{2N-j} (a_i b_{i+j-N} + a_{i+j} b_{i-N}) \end{aligned} \tag{4.3}$$

Clearly,

$$C_j + D_j = 2(A_j + B_j) = \begin{cases} 4N & (j = 0) \\ 0 & (j \neq 0) \end{cases} \tag{4.4}$$

Thus c_i and d_i constitute a complementary series of length 2N.

Since a pair of two sequences +1,+1 and +1,-1 is a complementary pair of length 2, complementary series of any power of 2 can be synthesized by this procedure. Also an independent series of length 10 is found by Golay (1961), allowing any length of 10×2^n.

Apparently, the complementary pulse code has an ideal property for the middle atmospheric radar observations. It was first applied to the stratospheric observations using the Arecibo UHF radar by Woodman (1980a), and to the mesospheric observations using the SOUSY VHF radar by Schmidt et al. (1979). Fig.4-2 shows the pulse

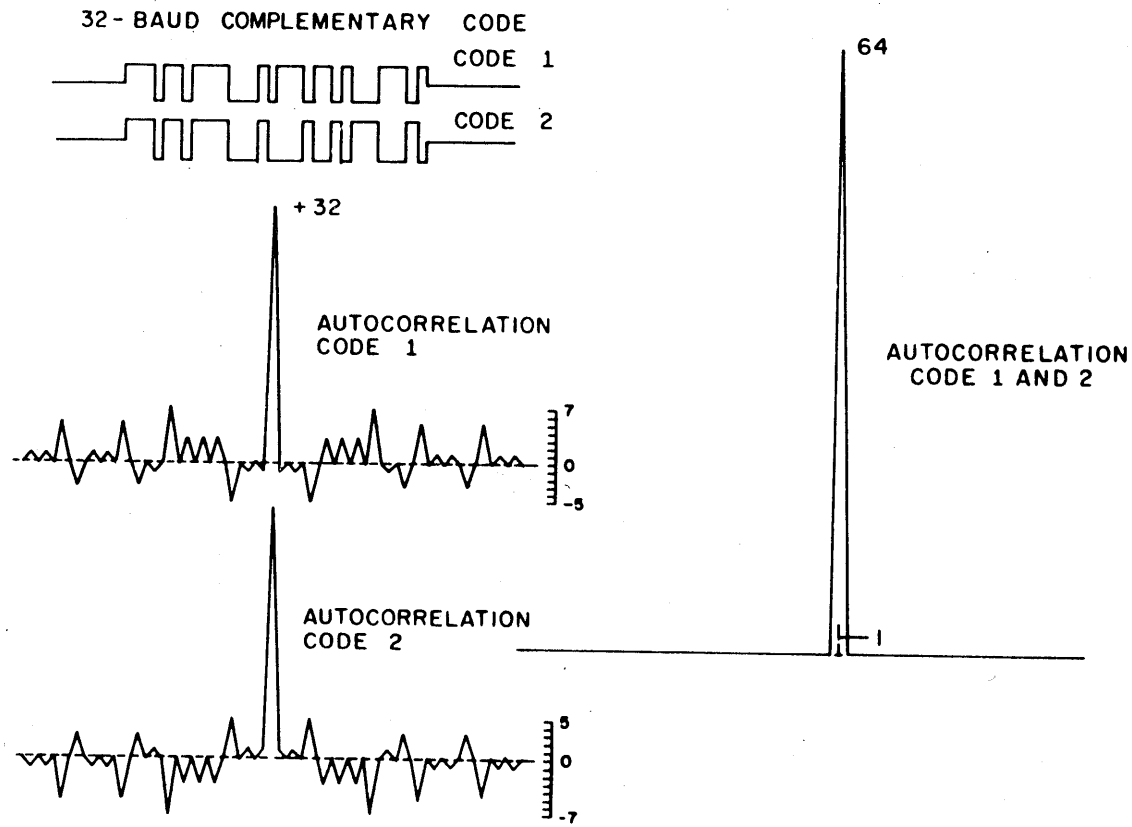

Fig.4-2 The 32-bit complementary code sequence and its individual and summed auto-correlation functions (after Woodman, 1980a).

patterns and auto-correlation functions of the 32-bit complementary code. The sum of the two auto-correlation functions is shown on the right.

Although the theoretical time sidelobe is zero for the sum, finite time sidelobe remains in the practical application. The situation of the impulse response used in the above discussion is realized by a point target with a sufficiently large scattering section. Fig.4-3 shows such case where the target is most likely a large ship on the Atlantic Ocean seen by an antenna sidelobe, judged from its trajectory in range-Doppler domain. Fig.4-3 displays the spectral echo power versus time delay for a Doppler frequency shift where the spectrum takes its maximum. The pulse scheme used was a 32-bit complementary code with the basic pulse width of 1 μs. The figure shows time sidelobes of a few to about 10 dB higher than the background noise level for the range of ±32 μs, which is the length of the code, around the peak. The sidelobe suppression ratio is 25-30 dB. A small peak at time delay of +4 μs may be the double-bounced echo from the suspended platform structure, or the reflections inside the waveguide.

The cause of the time sidelobes is not yet fully identified, but there are two possibilities. One is the incomplete cancellation of time sidelobes due to a phase change of scattered signals over one IPP. It was pointed out by Wakasugi (1981) that a slight phase change due to a line-of-sight velocity of 5 m s^{-1} deteriorates the sidelobe suppression ratio to about 30 dB for a frequency of 400 MHz and an IPP of 1 ms. However, if the observed time sidelobes are due to this incomplete cancellation alone, the sidelobe pattern should be proportional to that of the auto-correlation function of a single code of the complementary pair shown in Fig.4-2. Since there is no such indication in the sidelobe pattern in Fig.4-3, it cannot fully explain the observed time sidelobes.

The other possibility is non-linearities in the transmitter, like an overshoot or ringing occurs only at the leading and trailing

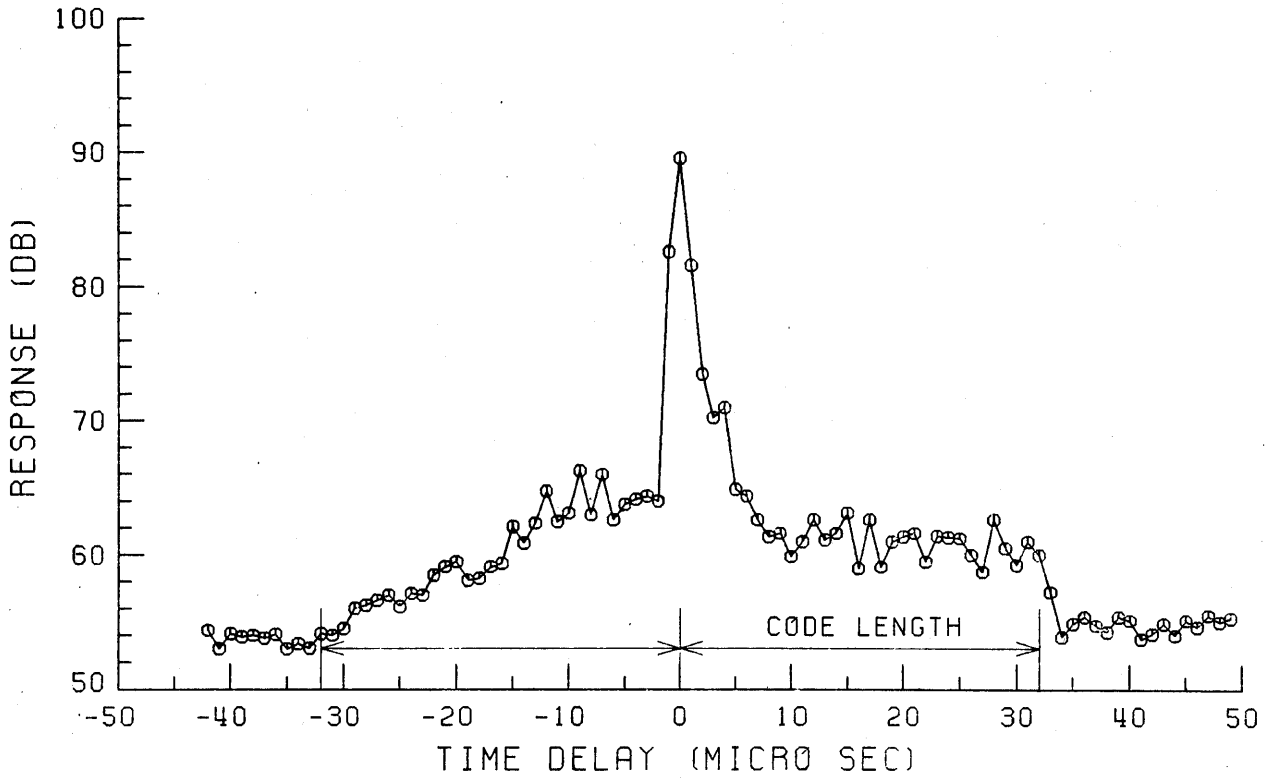

Fig.4-3 Measured response of the 32-bit complementary codes versus time delay.

edge of the entire pulse. Normal overshoot or ringing due to a band limitation cannot be the cause because the pulse compression is a linear operation, thus the effect of band-limiting the transmitted pulse is equivalent to band-limit the compressed pulse, which should be independent from the length of the code (R.F.Woodman, private communication, 1979). It is likely that cutting off the klystron beam current while RF pulse is absent is contributing to this non-linearity.

4.3 SPECTRAL PARAMETER ESTIMATION

The spectral parameter estimation procedure applied to the stratospheric data taken with the Arecibo UHF radar is principally the same as that applied to the Jicamarca mesosphere data described in Chapter 2. However, the presence of very strong ground clutter echoes complicates the situation to some extent. As is imagined from the structure of the primary line feed of the Arecibo UHF radar, it radiates a considerable amount of energy to the horizontal direction. Since the level of the primary feed is higher than surrounding mountains, echoes from southern mountains of within a range of about 25 km directly enter the feed. Sea clutters from the Atlantic Ocean, though much weaker than the mountain echoes, are also observed at even longer ranges.

The echo power of the ground clutter is a few to several orders of magnitude larger than the desired atmospheric echoes. The clutter component shows a weak, but still considerable, fading in time. This fading is probably due to rustling of trees on mountain surface. The spectral width of clutter from wooded terrain under wind velocity of 5 m s^{-1}, for example, is of the order of 4 cm s^{-1} in velocity unit for the frequency of 3-30 GHz (Nathanson, 1969), being independent of frequency in this range. If the same order of width can be expected at 430 MHz, it seems to be sufficient to

explain the observed fading.

The finite width of the clutter component made it impossible to use the simple moment method to derive the spectral parameters. The problem is aggravated by the fact that the finite length of the time window used in the FFT operation produces an spectral spill-over of the clutter contribution over the entire frequency window. In the followings, the nature of this spill-over is examined first. Then, as a solution of these problems, a non-linear parameter estimation technique is described. This method utilizes a theoretical curve-fitting procedure using parameters which specify the shape of the clutter along with the three desired parameters for the atmospheric echoes. The theoretical functions are first distorted in the same fashion as the data are distorted by the system and data processing procedures. They are then compared with data and parameters are adjusted until a best fit is obtained.

In the real-time data processing, each consecutive 32 sampled data points are Fourier-transformed using FFT algorithm, squared, and then incoherently integrated over 100 times. This method of averaged periodgram is widely used to estimate the power spectrum of a long time series because of its high speed and minimum computer memory requirements. It is seldom realized, however, that this averaged periodgram does not converge to the true power spectrum, but gives a systematically distorted spectrum.

Let $f(t)$ be a random process characterized by its frequency power spectrum $F(\omega)$, to which corresponds an auto-correlation function $\rho(\tau)$. We will determine the effect of data processing in $F(\omega)$ through the effects on its transform, $\rho(\tau)$, because this effect is clearer in the time domain than in the frequency domain.

Consider a sampled series

$$f_N(j) = f(j\Delta) \tag{4.5}$$

where Δ is the sampling interval, and j an integer index. We

truncate this series to obtain N points, which corresponds to applying a rectangular weight to $f_N(j)$.

$$\bar{f}_N(j) = f_N(j)W_N(j) \tag{4.6}$$

where

$$W_N(j) = \begin{cases} 1 & (1 \leq j \leq N) \\ 0 & (j < 0,\ j > N) \end{cases}$$

Applying a Fourier transform and squaring the results corresponds to auto-correlating $\bar{f}_N(j)$ in time. Thus,

$$\begin{aligned} \bar{\rho}_N(k) &= \langle \bar{f}_N^*(j)\bar{f}_N(j+k) \rangle \\ &= \rho_N(k)\langle W_N(j)W_N(j+k) \rangle \\ &= \begin{cases} \rho_N(k)(N-k)/N & (0 \leq k \leq N) \\ \rho_N(k)(N+k)/N & (-N \leq k < 0) \\ 0 & (k < -N,\ k > N) \end{cases} \end{aligned} \tag{4.7}$$

where $\rho_N(k)$ is a sampled series of $\rho(\tau)$ at interval Δ, and $\bar{\rho}_N(k)$ is an auto-correlation function taking only the effect of truncation into account. This effect is equivalent to multiply $\rho_N(k)$ by a triangular weight, i.e., the auto-correlation function of $W_N(j)$. Fig.4-4 a) and b) show examples of untruncated and weighted Gaussian auto-correlation functions, respectively. Two cases are shown corresponding to long (left) and short (right) correlation times compared to the length of data. They represent typical situations for fading clutter and stratospheric echo, respectively. The length of data window was chosen on the basis of the signal correlation time of the stratospheric echoes. This caused a severe truncation of the ground clutter contribution which has a much longer correlation time than the signal.

Besides the triangular weight effect, we automatically use a sampling rate of $1/\Delta$ in the frequency domain when using a FFT

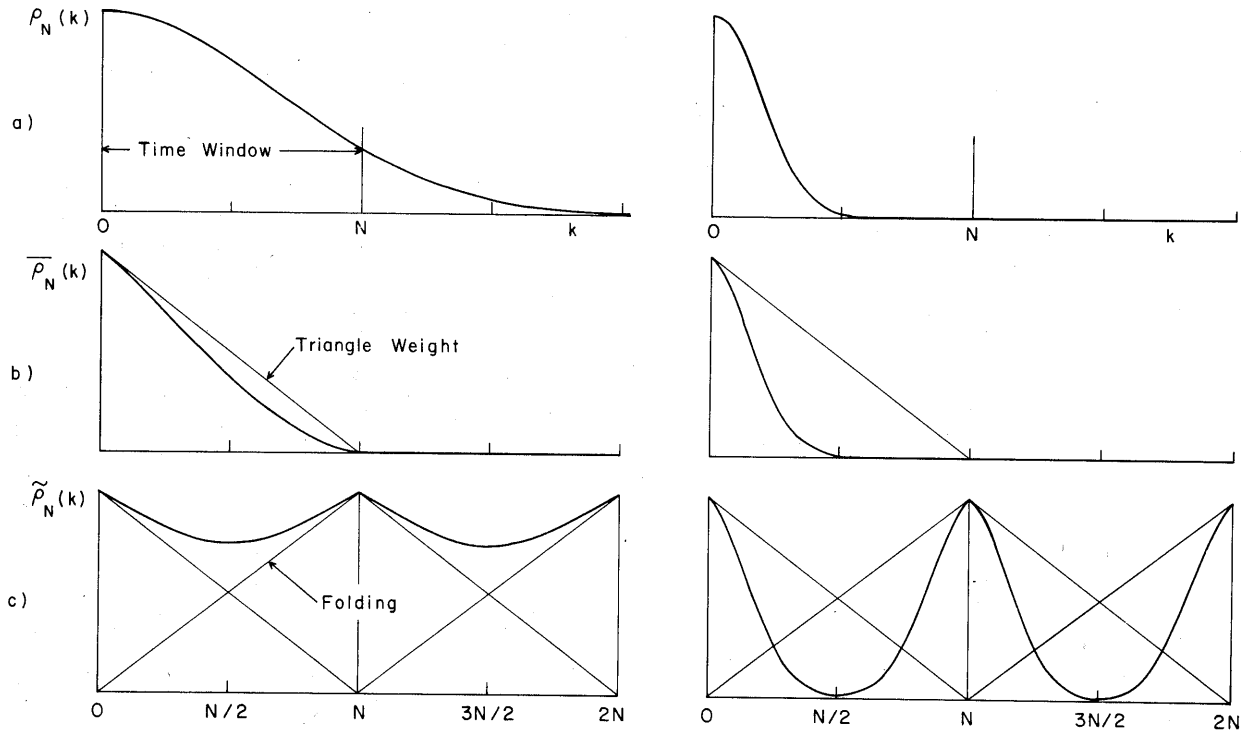

Fig.4-4 Effect of processing distortion on the auto-correlation function caused by the periodgram operation using a FFT algorithm for two cases where correlation time is longer (left) and shorter (right) than the length of data.

algorithm, which causes an additional problem. The sampling in frequency corresponds to convolving $\overline{\rho}_N(k)$ with a series of delta functions of interval $N\Delta$, thus producing an overlapping periodicity in the auto-correlation function, since the entire length of the triangular weights, $2N\Delta$, is twice longer than the interval. We get finally,

$$\tilde{\rho}_N(k) = \rho_N(k)(N-k)/N + \rho_N(k-N)k/N \qquad (0 \leq k < N) \tag{4.8}$$

which is periodic outside this range with period N.

Fig.4-4 c) shows the effect of this convolution which has the same effect as folding b) at the N/2 point and adding the folded part to the first half. Note that this folding affects only when the auto-correlation function has non-zero response beyond N points. This effect is the counterpart of the Nyquist's sampling theorem in the time domain.

Fig.4-5 shows these effect in the frequency domain for the case of long correlation time shown in Fig.4-4. The solid line and dots correspond to Fig.4-4 a) and c), respectively. We can easily see that, even when the true power spectrum has a very narrow shape, the FFT algorithm described above has the effect of spilling high frequency components over the entire frequency range. The high frequency components come from the discontinuity at the apex as well as the base of the triangular weighting function.

Although this small amount of spill over is not a serious problem for most applications, this has a large effect for the present case where the clutter contribution is 10-50 dB stronger than the desired component.

It is worth noting that in the case of non-fading clutter, i.e. when the auto-correlation function is constant versus time delay, the effect of truncation and folding cancels each other, and the distorted auto-correlation is also constant versus time delay. Thus, non-fading ground clutter affects only the center frequency

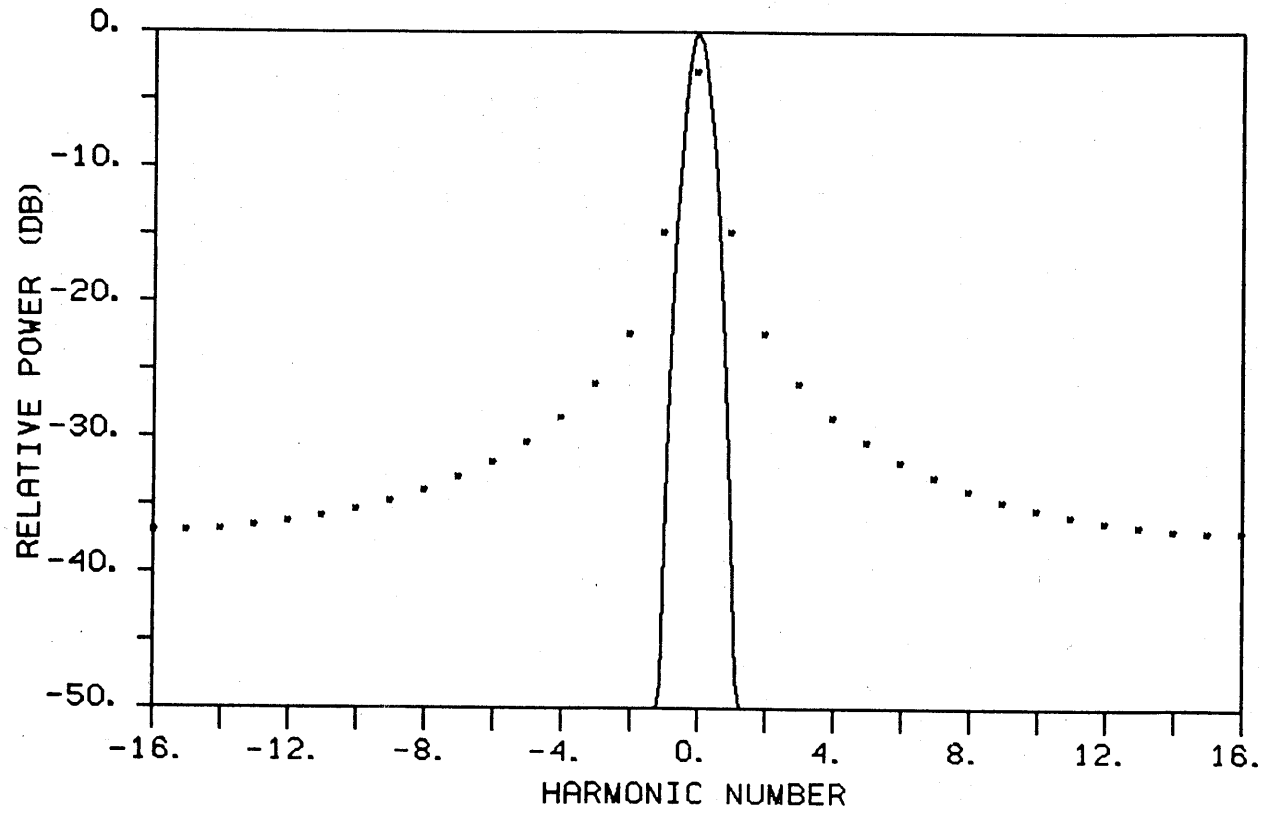

Fig.4-5 Effect of the processing distortion on the frequency power spectrum. The solid line shows the original spectrum and the dotted line shows the distorted spectrum.

with no spill over effect.

As we have seen, the existence of a very strong fading clutter under the effect of systematic distortion due to data processing makes it difficult to estimate the desired spectral parameters from the data. Therefore, it becomes quite important to estimate the spectral parameters of not only the signal component, but also the fading clutter component. Here we consider the application of a non-linear curve fitting technique to this problem.

The outline is as follows. First, we assume the theoretical function shape of the power spectral components of ground clutter and the desired echo. Second, we distort them in the same fashion as described above. Then we compare this theoretically generated power spectrum with the observed one in least-squares manner to determine the optimum set of parameters. In reality, fitting is done in the time domain since the distortion is easier to apply in the time domain than in the frequency domain. Distortion involves only a multiplication and folding in the time domain, but a lengthy convolution in the frequency domain.

By applying the processing distortion to the theoretical auto-correlation function, we can take this effect into account, so that the estimated parameters are free from processing biases. Another advantage of the theoretical curve fitting is that we can obtain a better frequency resolution than the sampling interval in frequency. In fact we can obtain spectral width estimates as narrow as necessary, including single frequency spectral components like the non-fading component of the clutter. This is an advantage which is normally associated with the Maximum Entropy Method (MEM, Smylie et al., 1975). Our approach is, however, better than the MEM for the present case, since we can use the knowledge about the nature of the signals, rather than assuming complete ignorance, which is the basis of the MEM.

In the present case, we can safely assume that the auto-correlation function of the clutter can be approximated by the first

few terms in a Taylor series expansion, since the correlation time is much longer than the size of the time window. Also, since our main purpose is to get the first three spectral moments of the signal, we can assume a Gaussian with a linear phase for the signal component. This assumption is supported by the quality of fitting as shown later.

The curve fitting technique used to compare the theoretical and observed auto-correlation functions is a general technique known as the non-linear least-squares fitting procedure (e.g., Bard, 1974). The principle is to minimize the variance

$$v(\vec{P}) = \sum_{k=1}^{N} \{\tilde{\rho}_N(k;\vec{P}) - R_N(k)\}^2 \qquad (4.9)$$

under certain conditions. Here R_N and $\tilde{\rho}_N$ are observed and distorted theoretical auto-correlation functions, respectively. $\vec{P}$ is the parameter vector which contains the following elements; the unfading clutter power, three even coefficients in the Taylor series expansion of the fading component of the clutter auto-correlation functions, and the first three spectral moments which define the Gaussian signal auto-correlation function. In addition, a slight Doppler shift for the fading component was found necessary to account for small statistical fluctuations in the estimate. Furthermore, a second Gaussian peak is introduced at certain heights to take care of undesired peaks produced by ocean clutter and time sidelobe contamination from lower heights.

The necessary condition for Eq.(4.9) to be minimized are

$$\sum_{k=1}^{N} \{\tilde{\rho}_N(k;\vec{P}) - R_N(k)\} \frac{\partial \tilde{\rho}_N}{\partial P_j} = 0 \qquad (i = 1, \cdots, M) \qquad (4.10)$$

where M is the number of parameters. Equation (4.10) is non-linear in terms of $\vec{P}$, therefore difficult (if not impossible) to solve directly. However, it can be approximately solved by expanding $\tilde{\rho}_N$ around some initial value of $\vec{P}_o$ and taking up to the first order

term.

$$\tilde{\rho}_N(k;\vec{P}_o+\delta\vec{P}) \simeq \tilde{\rho}_N(k;\vec{P}_o) + \sum_{j=1}^{M} \delta P_j \frac{\partial\tilde{\rho}_N}{\partial P_j} \tag{4.11}$$

By substituting (4.11) into (4.10) we obtain

$$\overleftrightarrow{A}\cdot\delta\vec{P} = \vec{C} \tag{4.12}$$

where $\overleftrightarrow{A}$ and $\vec{C}$ are a matrix and a vector, respectively, defined as

$$A_{ij} = \sum_{k=1}^{N} \frac{\partial\tilde{\rho}_N}{\partial P_i}\cdot\frac{\partial\tilde{\rho}_N}{\partial P_j}$$

$$C_j = \sum_{k=1}^{N} \{R_N(k) - \tilde{\rho}_N(k;\vec{P}_o) \frac{\partial\tilde{\rho}_N}{\partial P_j}$$

Equation (4.12) can be solved for $\delta\vec{P}$ as

$$\delta\vec{P} = \overleftrightarrow{A}^{-1}\cdot\vec{C} \tag{4.13}$$

This procedure is iterated by replacing $\vec{P}_o$ by $\vec{P}_o + \delta\vec{P}$, until $\vec{P}$ converges to some value, or $v(\vec{P})$ in Eq.(4.9) becomes small enough.

Eq.(4.10), however, has in general more than one solution, out of which only one is desirable. This ambiguity is solved by giving a proper initial guess of the parameters, and by setting constraints on parameters to prevent physically meaningless values like negative power or width. Additional constraints are set using the knowledge that the spectrum of clutter is always very narrow and almost symmetrical.

The initial set of $\vec{P}_o$ is obtained as follows: The unfading component of clutter is estimated from the dc value of the data which is evaluated and recorded on real time separately. The fading clutter power and its width are estimated assuming no signal power in the observed auto-correlation function by the moment method. The

function shape of the fading clutter is set to be Gaussian, although it is let free in the fitting. The signal power, Doppler shift, and width of the desired signal component are estimated from the asymmetric part of the observed power spectrum, taking advantage of the fact that the clutter component is almost symmetrical. It has been found by experience that the above procedure provides a sufficiently good guess for the fitting procedure to converge to the right answer.

Fig.4-6 shows some examples illustrating the quality of the fitting procedure. They are displayed in the frequency domain for convenience. The dots are the observed spectral points, the thick line is the fitted curve, and the thin line shows the desired signal contribution to the spectrum. The abscissa expresses both the radial velocity (15° off zenith) and zonal velocity.

The spectrum of 10.1 km illustrates a common situation at lower height ranges. Here the power spectrum frequently shows a multi-humped shape, which is due to the time sidelobe of the complementary code corresponding to very strong echoes at lower levels. The desired peak is discriminated from undesired ones based on the continuity of the wind velocity with height and time. Another Gaussian with a linear phase is added to the theoretical function to compensate this effect when fitting is not good without it. The spectra at 14.3 and 17.9 km shows two examples where the desired signal component is strong. The aliasing seen at 14.3 km due to a strong zonal wind causes no problem in fitting, since its effect is automatically taken care in the time domain. The spectrum at 24.3 km is an example of a very weak signal, in which the signal-to-clutter ratio is about -50 dB. It is possible to get a good fit even for a worse signal-to-clutter ratio, provided that the Doppler shift of the signal echo is not too small, and if a good initial guess is given.

At higher regions, a second and usually weak echo with a constant Doppler shift versus height is observed. It is probably

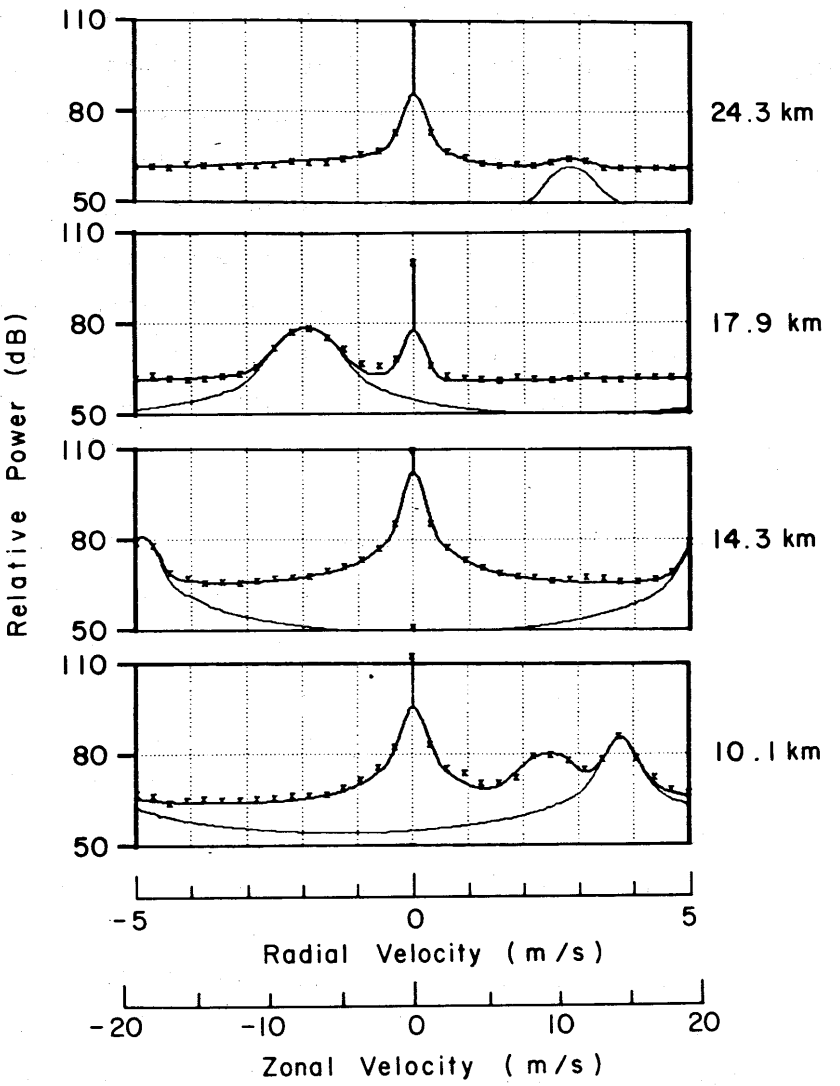

Fig.4-6 Examples of theoretical curves fitted to data at four different heights. The dotted, thick, and thin lines denote the data, fitted spectra, and fitted signal components, respectively. The vertical line at zero Doppler shift shows the unfading clutter component.

echoes from ocean waves with constant phase velocity. The extra Gaussian function, which is used to compensate the time sidelobe echoes at lower heights, is used to fit this component.

Fig.4-7 shows an example of the power spectra before and after processing. It is displayed in the form of contours of equal power density in a logarithmic scale and as a function of Doppler velocity and height. Contours are drawn every 3 dB starting slightly above the minimum detectable level. The contours for the spectra after processing are reproduced using the three spectral moments. A uniform gradient of 2 dB km^{-1} is subtracted from the processed spectra to reduce the number of contours at low heights. The antenna beam was tilted 15° from zenith toward the east. The abscissa is scaled in zonal wind velocity assuming no vertical velocity.

It is evident from the figure that the technique works successfully in discriminating from the undesired spectral components, except for those cases where the signal echo power is weak and the Doppler shift of the echo is small.

Fig.4-7 b) was reproduced here only to illustrate the performance of the fitting procedure. In practice, it is less laborious and more appropriate to obtain only the profiles of each parameter since the spectral profiles are already parameterized in the process of fitting. Fig.4-8 shows the height profiles of echo power, zonal wind velocity, and spectral width of the spectra shown in Fig.4-7. Since the spectra at those heights where echo power is weaker than the neighboring heights are possibly affected by the time sidelobes of the code, the velocity and spectral width are plotted only at heights where the echo power shows local maximum. The thin continuous line in Fig.4-8 b) shows the zonal wind measured by a meteorological balloon launched from the San Juan airport, about 80 km away from the radar site, 4 hours before the radar measurement. The wind velocities measured by the radar and by the balloon show a very good agreement in spite of the fairly large time

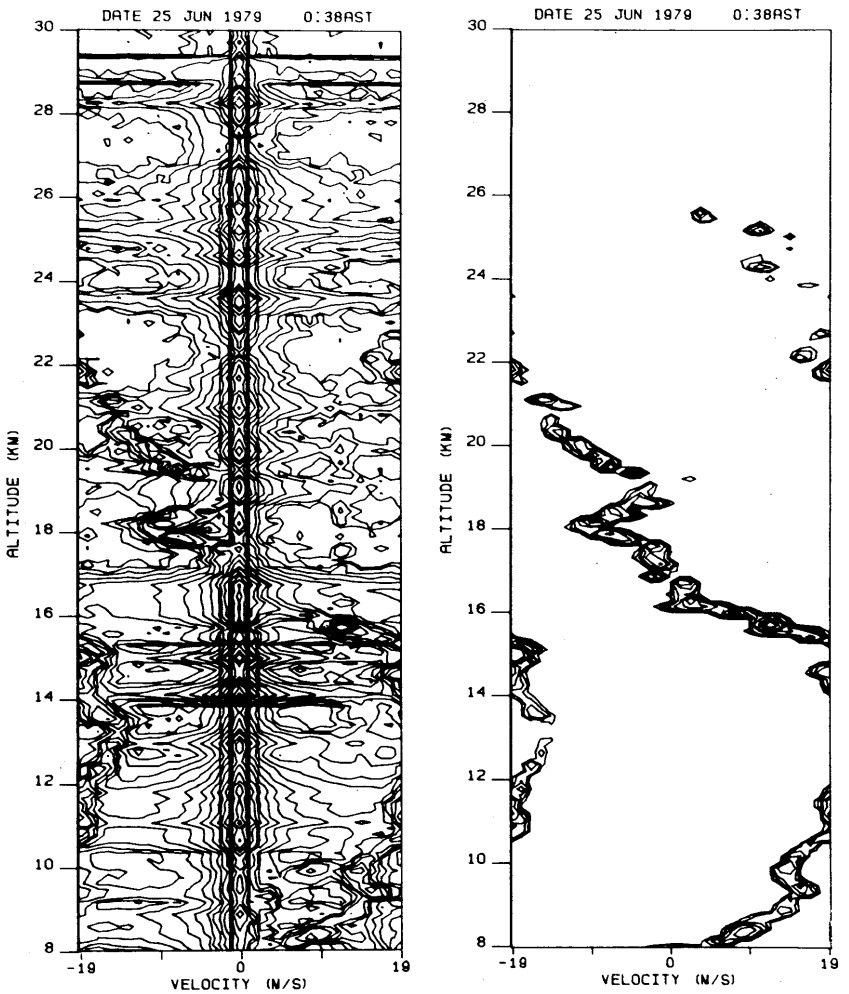

Fig.4-7 Contour plots of equal spectral power density versus height and Doppler velocity. a) is the data before processing, and b) is the estimated signal component. Contours are drawn every 3 dB. The spectra at 10-16 km and above 22 km are aliased because of strong zonal winds.

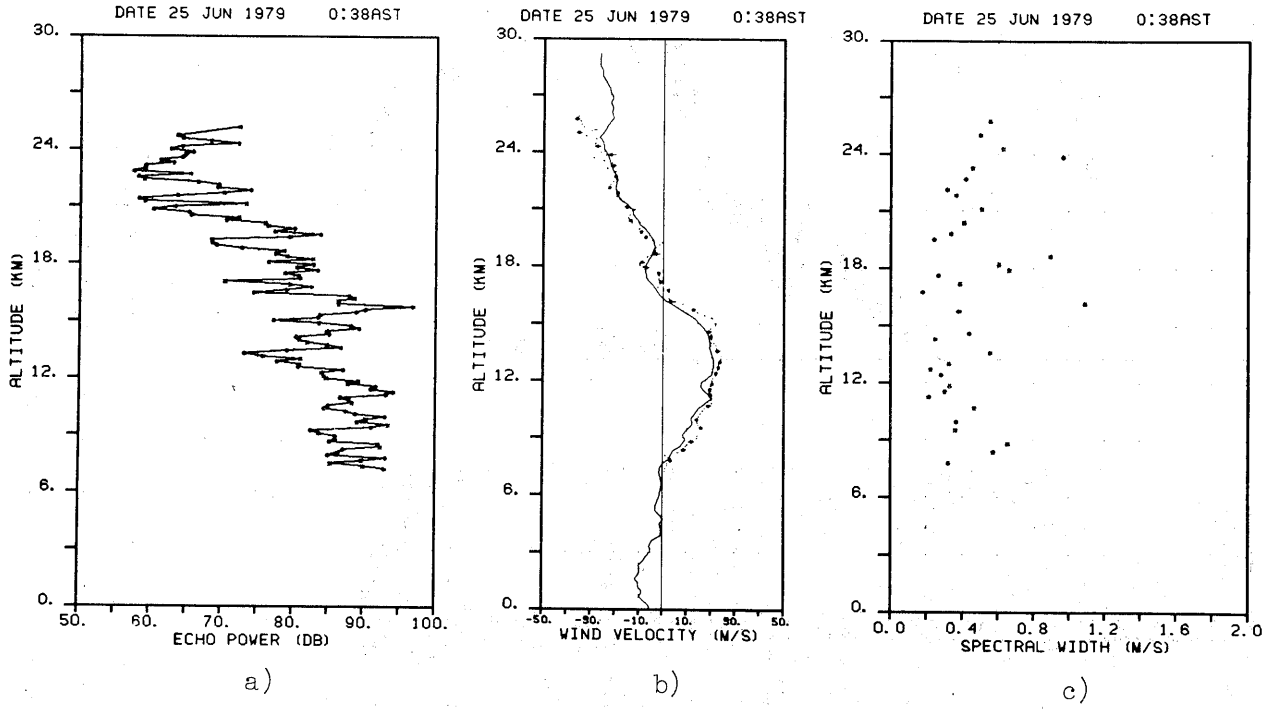

Fig.4-8 Height profiles of a) the echo power, b) zonal wind velocity, and c) spectral width obtained by the non-linear fitting. The velocity and width are plotted only at the heights where the echo power takes local maxima. The continuous line in the velocity plot is the zonal wind profile observed by a rawinsonde launched at 2000 LT on June 24, 1979.

and space differences.

4.4 TECHNICAL LIMITATIONS AND PROBLEMS

As we have seen in the previous section, presence of the strong fading clutter caused troublesome contamination to the observed spectra. In spite of the general success of the non-linear parameter estimation procedure, desired echoes cannot be discriminated from the fading clutter when the signal-to-clutter ratio is low and the Doppler shift of the signal is small. Thus the maximum observable height is usually limited by the signal-to-clutter ratio rather than the signal-to-noise ratio. It also makes the vertical observation very hard because the Doppler shift at the vertical direction is much smaller than that in the oblique directions.

Although the presence of such a strong clutter is particular to the Arecibo UHF radar due to its unique antenna configuration, it suggests the importance of suppressing low elevation sidelobes in the tropospheric and stratospheric observations. As for the Arecibo radar, it is planned to construct a cylindrical shielding net around the reflector which covers the horizontal direction from the primary line feed (R.F.Woodman, private communication, 1980).

Another cause of the spectral contamination noted in the previous section was the secondary peak in the power spectra at lower height ranges due to the time sidelobes of the complementary pulse code. The effect of the time sidelobe to other height becomes larger when the height variation of the echo power is large. Average decay rate of the echo power versus height is the order of 2 dB km^{-1} for the stratospheric heights as shown in Fig.4-7 and in the following chapter. This decay rate means a difference of 9.6 dB in echo power over the height range corresponds to the length of the code. Thus a sidelobe suppression ratio of about 30 dB is required

in order to obtain a signal-to-'ghost' ratio of 20 dB. This decay rate of the echo power should be considered in a design of a pulse compression code with a finite time sidelobe, because a longer code with the same sidelobe suppression ratio as a shorter code gives a worse signal-to-ghost ratio. Thus the optimum length of a code depends on whether the background noise is larger than the time sidelobe echo or not. For example, a single pulse of 1 or 2 μs width gives a better quality of data than the 32-bit complementary code if only the troposphere is to be observed (Larsen et al., 1980).

It should be noted, however, that the large time sidelobes of below about 10 km are mainly due to the fact that the decoding is not perfect at these heights since the receiver is cut off below about 5 km, and a complete decoding requires samples of 32 μs, or 4.8 km, around the height of interest.

A serious, but hardly improvable limitation on the Arecibo radar is the system of mechanical beam steering. It takes about 4 min to change the azimuth direction by 90°, and about 10 min to change the zenith direction by 15°. Also, the transmitter should be stopped while the zenith direction is being changed in order to prevent arking at the linear junction between the bowstring truss and the carriage house. This speed is sufficient for the vector wind measurements of the tidal or planetary waves which have time scales of larger than an hour. However, an electrical beam scanning or a multi-beam configuration is necessary to study the propagation of short period gravity waves, which involves a phase difference of the order of 1 min at different antenna positions as discussed in Section 3.5.

CHAPTER 5

STRATOSPHERIC OBSERVATIONS BY THE ARECIBO UHF RADAR

5.1 INTRODUCTION

The stratosphere has been probed extensively by several coherent VHF radars as Jicamarca (Peru), Sunset and Platteville (Colorado), SOUSY (West Germany), and Poker Flat (Alaska) radars. Although the scattering mechanism of stratospheric echoes observed by these VHF radars is thought to be identical to that of CAT echoes observed by microwave weather radars, the VHF radars have an advantage of higher sensitivity than microwave radars because the turbulence energy spectrum has a negative frequency dependence as discussed in Chapter 1.

As for the comparison of sensitivity in stratospheric observations with VHF and UHF, the situation is somewhat different from the comparison between the VHF and microwave radars because both frequencies probe different scales in the same inertia subrange of turbulence at stratospheric heights. The volume reflectivity due to turbulent scatter increases with the 1/3rd power of frequency (Tatarskii, 1971), while the galactic background noise temperature falls with approximately -2 to -2.5th power of frequency. Since the system sensitivity depends only on the output power and the effective area of the antenna for the case of volume scattering as shown in Eq.(1.13), a UHF radar system has much higher signal-to-noise ratio than a VHF radar system with the same output power and aperture.

Other advantages of using Arecibo UHF radar in observing the stratosphere exist in the very good height resolution and in the fact that the stratosphere falls in a near field of the antenna. The latter point becomes important in quantitative arguments of the observed spectral width. The sphericity of the wave front in the

antenna far field causes a broadening of spectra in the presence of a background flow. This broadening results in an extra source of error in estimating the true spectral width due to stratospheric turbulence (e.g., Wakasugi, 1981).

In this chapter, we examine the data obtained by a series of high-resolution observations carried out in 1979-1980 using the Arecibo UHF radar. The data are processed in the manner described in Section 4.3 to give the first three spectral moments. After a brief description of the observational parameters, a few interesting phenomena found in the wind velocity are presented, which demonstrate the importance of a high-resolution observation. Next, the nature of the stratospheric turbulence is examined in terms of the echo power and the spectral width, and the relations between different spectral parameters. Lastly, an attempt is made on estimations of turbulence parameters as the energy dissipation rate and the effective eddy viscosity from the observed width of spectra.

5.2 OBSERVATIONS

The data presented in this chapter is part of a series of data taken since 1977, when the experimental technique described in the previous chapter was first employed (Woodman, 1980a). The length of data sets in this series varies from a few hours to a few days depending on the availability of facilities, which is shared by various atmospheric and astronomical experiments. Mainly three data sets which cover the longest duration are discussed here. They are taken on June 25-26 and October 10-13, 1979, and on January 22-23, 1980.

Basic pulse scheme is common to all of data sets. Transmitter pulses of 2.5 MW peak output power (nominal) are coded by 32-bit complementary codes with the subpulse width of 1 μs, and sent at the IPP of 0.73 ms. Received signal is sampled at 256 heights at 150 m

intervals starting from the ground level. However, the receiver was cut off below about the height of 5 km in order to protect it from saturation due to very strong ground echoes from near ranges. The upper limit of the height where reliable data can be obtained varies day to day between 20-30 km.

Sampled data were coherently integrated over every 48 IPP's after decoding to give a time series of 35 ms interval. Power spectra were evaluated from this time series using 32-point multi-channel FFT algorithm. Incoherent integration time of the spectra was originally chosen to be 2 min, but changed to 1 min when observation was aimed at short period phenomena.

Various attempts were made on the choice of antenna beam directions depending on observational purposes under the limitation of slow slew speed of the antenna beam. In the observations on June 25-26 and October 10-13, 1979, the antenna beam was pointed alternately toward the east and north directions at a fixed zenith angle. In the June experiment, the east and north directions are observed for about 1 hour and 6 min, respectively, before the antenna beam was moved. The different duration at the two directions were employed, because the zonal wind was predominating over the meridional wind at that period and thus seemed more interesting. In the October experiment, on the other hand, the zonal and meridional wind showed similar magnitudes, so that the antenna direction was switched in every 1 hour. These two data sets are suitable for the study of long period waves since the two horizontal wind components are obtained with time resolutions of 1-2 hour.

In the observation of January 22-23, 1980, the antenna position was fixed in the eastward direction in order to study short period temporal variations in more details, which is difficult when the antenna direction is switched frequently. The incoherent integration time of 1 min was used in this observation.

The zenith angle was set to 7.5-15.0° depending on the magnitude

of the prevailing horizontal wind velocity. When the horizontal wind is large, a small zenith angle was used so that the line-of-sight velocity does not suffer from the aliasing effect largely. When the horizontal wind is small, on the other hand, a large angle was used in order to obtain a better frequency separation between the desired echoes and the ground clutter echoes.

The observational parameters are summarized in Table 5-1.

5.3 WINDS AND WAVES

Fig.5-1 shows vertical profiles of wind velocity measured every 2 minutes. Profiles are plotted side-by-side spaced according to their time of observation. The velocity scale for the individual profiles is the same as the averaged profile on the left. Blank parts of each profile indicate poor quality of data points due to bad signal-to-noise, or signal-to-clutter ratio. The antenna beam direction was switched between the eastward and northward every one hour. The time scales are measured from the beginning of each figure, and differs by about 80 min between the upper and lower figures.

The most apparent feature in these profiles is the consistency of wind velocity in time. This is especially true of the wavy structure at 15-18 km which remains unchanged throughout the observation. This structure has an apparent vertical wavelength of about 1.5 km and an amplitude of about 5 m s^{-1}. Fig.5-2 shows 10 hour mean profiles of the zonal and meridional wind components. The phase difference between the two components indicates that the direction of flow associated with this structure rotates clockwise when traced upwards.

Although these features seem to be similar to those of diurnal tidal winds, which are reported in Fukao et al. (1981a), this structure is distinguished from tidal oscillations by inspecting the

Table 5-1 Observational parameters of the stratospheric experiments using the Arecibo UHF radar

Date	: June 25-26, 1979
	October 10-13, 1979
	January 22-23, 1980
Antenna beam directions	: east or north directions
	with 7.5-15.0° zenith angle
Pulse scheme	: 32-bit complementary codes
Pulse width	: 32 μs
Subpulse width	: 1 μs
IPP	: 0.73 ms
Sampled heights	: 0-36.3 km (0.15 km interval)
Height resolution	: 0.15 km
Coherent integration	: 35 ms

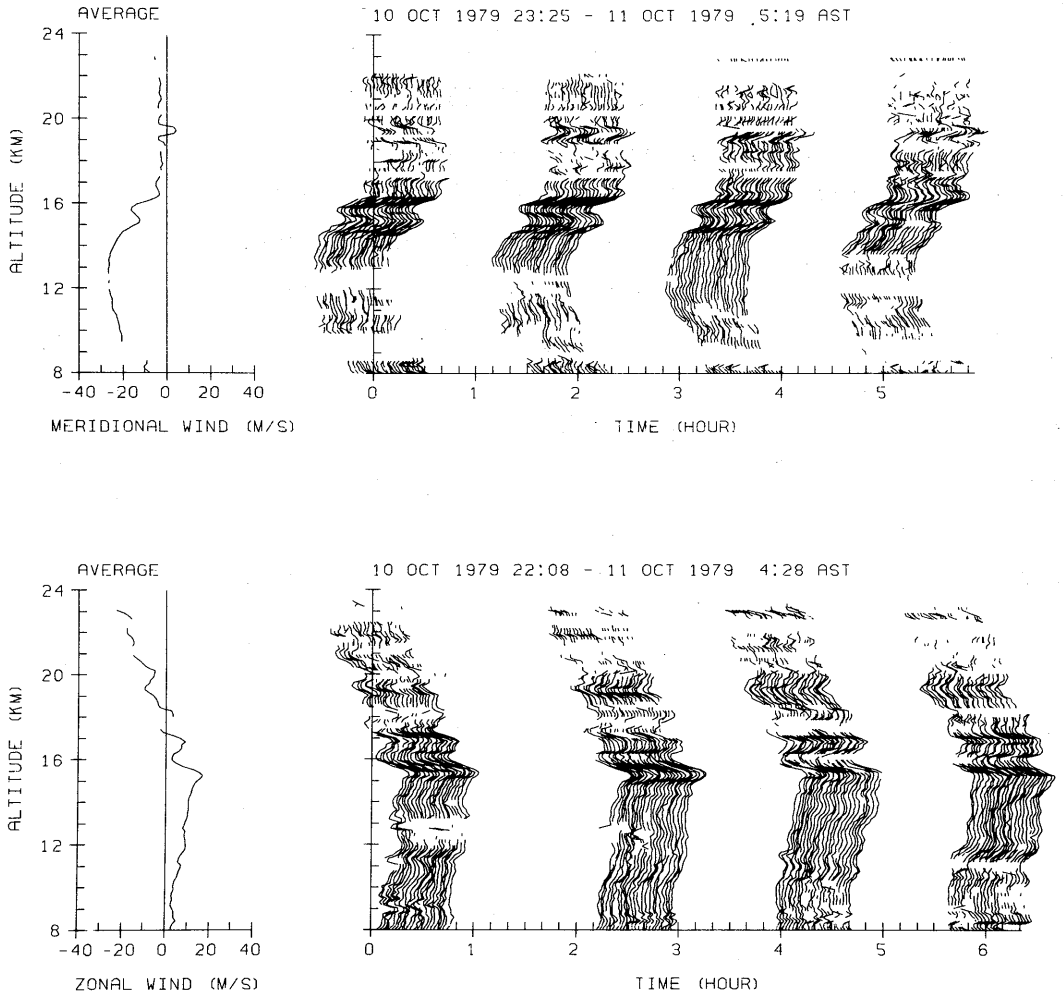

Fig.5-1 Zonal and meridional wind velocity versus height and time. Height profiles are plotted side-by-side spaced according to the observed time. The time scale is measured from the beginning of each figure.

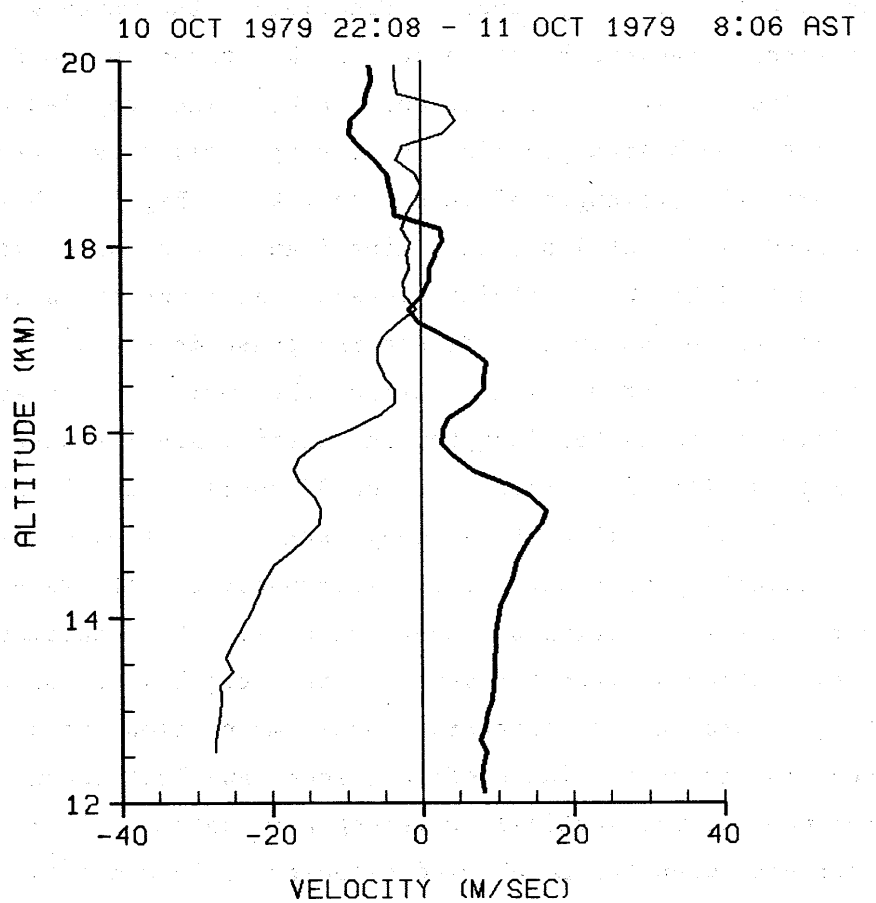

Fig.5-2 10 hour average height profile of the zonal (thick line) and the meridional (thin line) wind components. Directions are positive eastward and northward, respectively.

long term temporal behavior. Weinstein et al. (1966), and more recently Cadet and Teitelbaum (1979) observed similar mesoscale structure in the lower stratosphere by successive balloon experiments and discussed it in terms of quasi-inertial oscillations and quasi-inertial gravity waves. Especially the waves with very short vertical wavelength of about 1 km found by Cadet and Teitelbaum looks quite similar to our case. They applied a high-pass filter to each wind profile to pick up only those structures with the vertical wavelength of less than 2 km. Fig.5-3 shows one-hour averaged wind profiles (thin lines) and those after low-pass filtering with 3 km cutoff (thick lines). Although the structures in the 14-17 km region show a descending phase in time, it changes only about 180° in 48 hours indicating the period to be about 96 hours. This period is too long for an inertial gravity wave, since the inertial oscillation period is about 38 hours at the latitude of Arecibo (18.35°N). Thus this wavy structure is more likely an equatorial planetary wave such as a mixed-Rossby gravity wave. The very short apparent vertical wavelength may be explained by a Doppler shift which shorten the vertical wavelength when the wave is propagating through an eastward zonal mean flow than if it propagated in the zero wind profile (Cadet and Teitelbaum, 1979). The difference of the vertical wavelength amounts to 1.5-3 km for the present case when the zonal wind velocity is 5-10 m s^{-1}.

Corresponding wavy structure can be seen in the temperature data of the same period. Fig.5-4 shows 4 temperature and the Brunt-Väisälä frequency profiles obtained from the rawinsonde observations at San Juan, Puerto Rico (80 km east of Arecibo). Symbols denote data points and lines are deduced by the spline interpolation. The line of 10 October above 18 km is dubious because of sparse sampling points. The wavy structure is more pronounced in the profile of the Brunt-Väisälä frequency. The vertical wavelength changes from about 1.5 to 2.0 km, and agrees well with that of the velocity structure. The amplitude in temperature is 1-2 K, which agrees with the typical

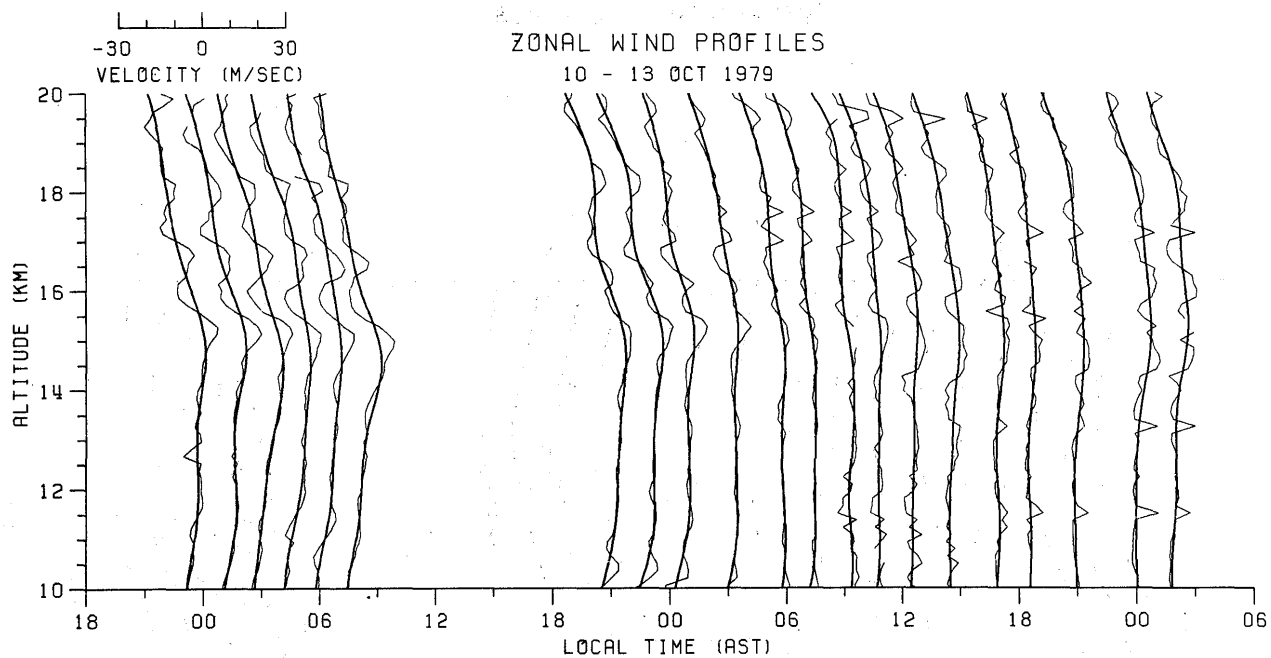

a)

Fig.5-3 One hour averaged a) zonal and b) meridional wind profiles (thin lines) and smoothed profiles with a 3 km cutoff filter (thick lines) over 54 hours.

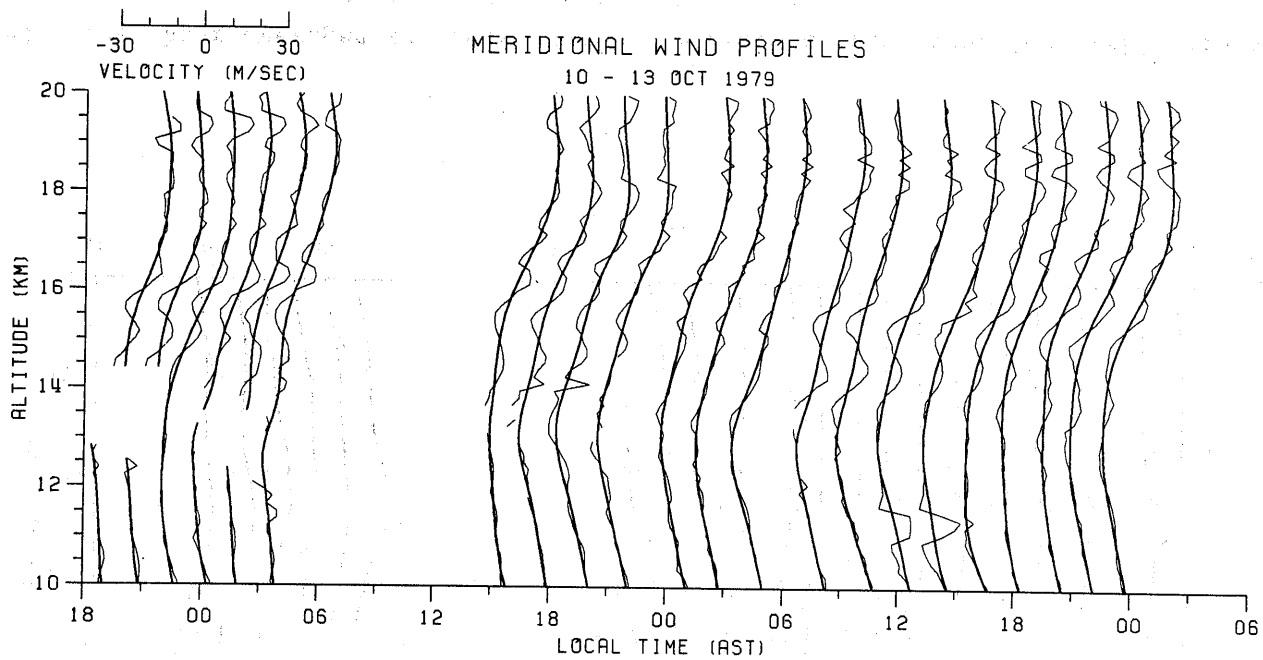

b)

Fig.5-3 (continued)

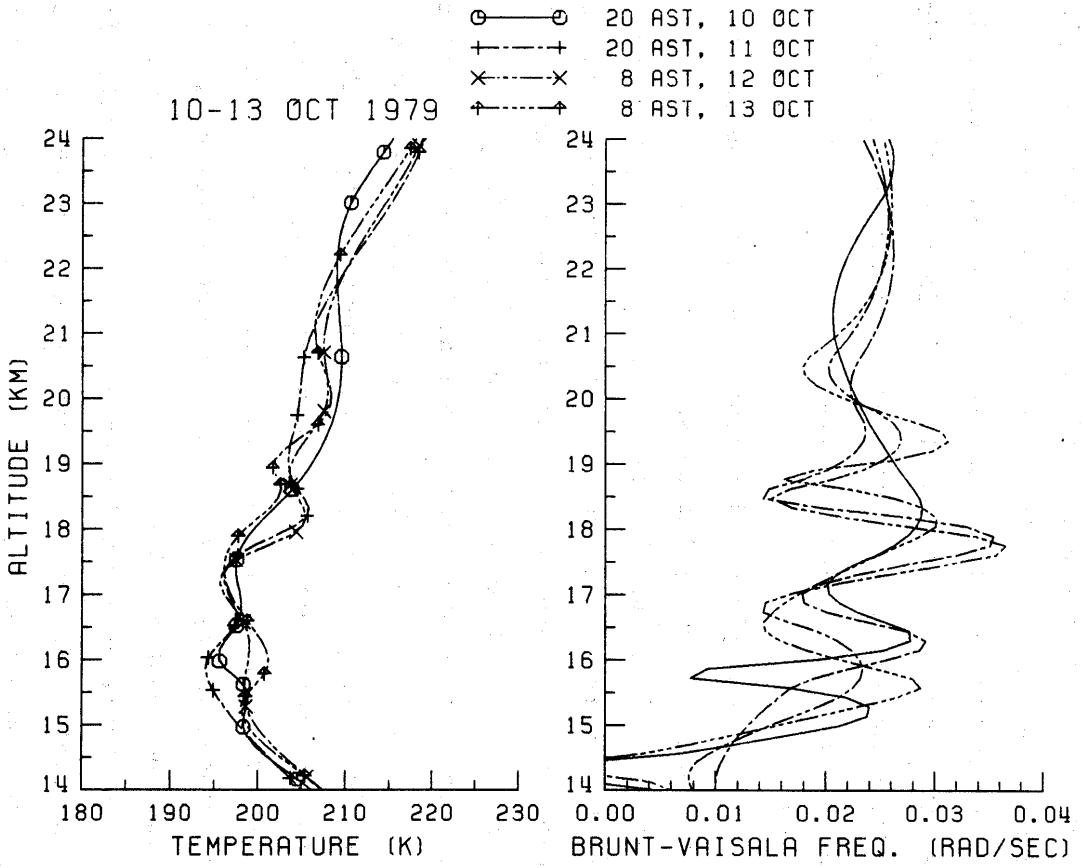

Fig.5-4 Temperature and the Brunt-Väisälä frequency obtained from 4 rawinsonde flights at San Juan, Puerto Rico. Symbols denote data points and lines are deduced by the spline interpolation.

value of the equatorial mixed-Rossby gravity wave (e.g., Holton, 1975). The phase of temperature maxima seems, on the other hand, to coincide with the eastward velocity maxima, roughly 90° apart from the theoretical relation for the mixed-Rossby gravity mode, which predicts the coincidence of temperature maxima with the northward velocity maxima. It is of course difficult to determine the phase accurately from the given intervals of the temperature data.

Although smaller in amplitude compared to the height variation, there also exist substantial temporal variations in the observed velocity. One important mode is the solar diurnal tide, which is reported separately (Fukao et al., 1981a), and the other is the gravity wave mode.

Fig.5-5 shows an example of low-passed velocity time series at 12-16 km height range. The system measures the radial component of the wind velocity, from which the horizontal component can be estimated if the vertical component is much smaller than the horizontal component. However, it is not the case for short period waves with frequencies close to the Brunt-Väisälä frequency. In Fig.5-5, both the horizontal and the radial velocity scales are shown on the top of the figure. The horizontal scale corresponds to assume no vertical wind. A pronounced periodicity of about 25 minutes exists over the entire plotted height range for about two hours. A cross correlation analysis revealed less than two minutes of phase difference, if any, over 4 km of height difference. This good phase coherency suggests that this wave is propagating almost horizontally. The horizontal wavelength of this wave estimated from the dispersion relation for an isothermal atmosphere (Hines, 1960) is about 300 km. Such a pure sinusoidal wave is, however, a rare example of a gravity wave which persists for such a long period during our observations.

On the other hand, similar purely sinusoidal oscillations (or waves) with short periods are frequently observed. Fig.5-6 is an example of a very short period oscillation (about 3 minutes in this

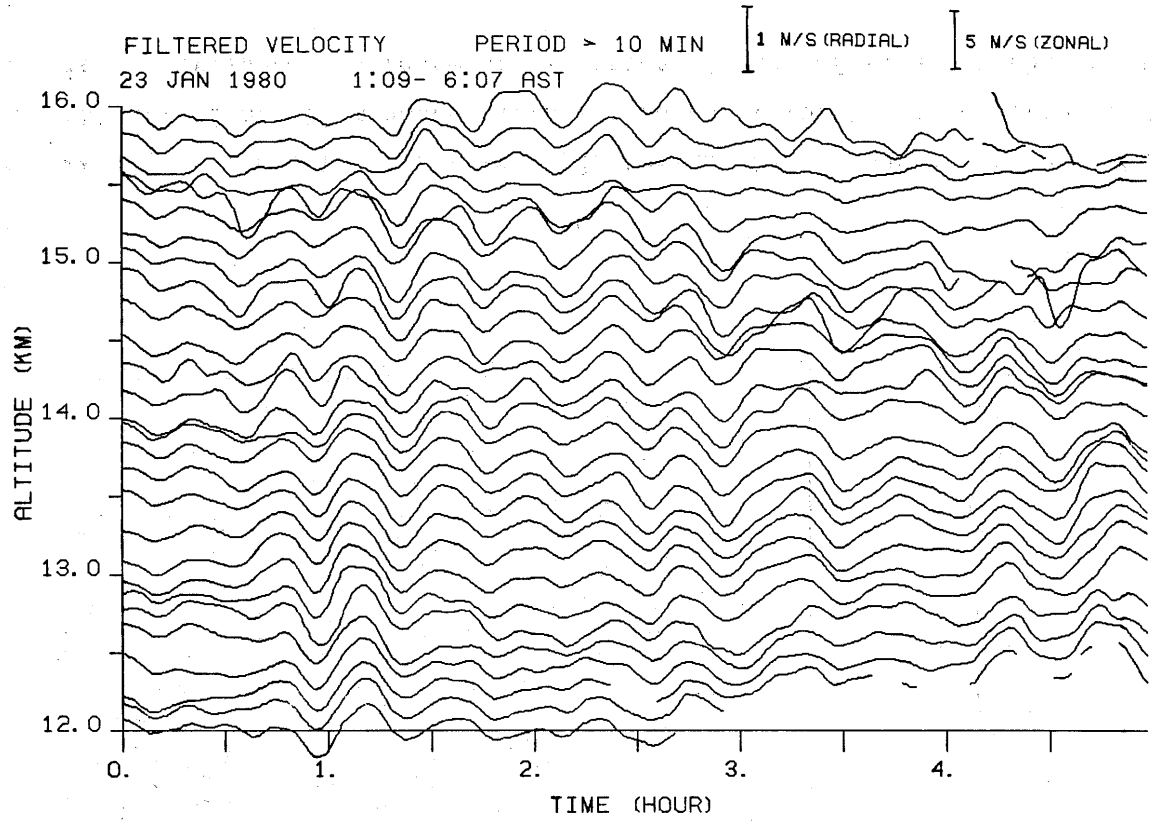

Fig.5-5 Temporal variation of the wind velocity at 28 heights of 12-16 km. The time series was filtered by a low-pass filter of a cutoff period of 10 minutes. The antenna was pointed 10° from zenith in the zonal plane.

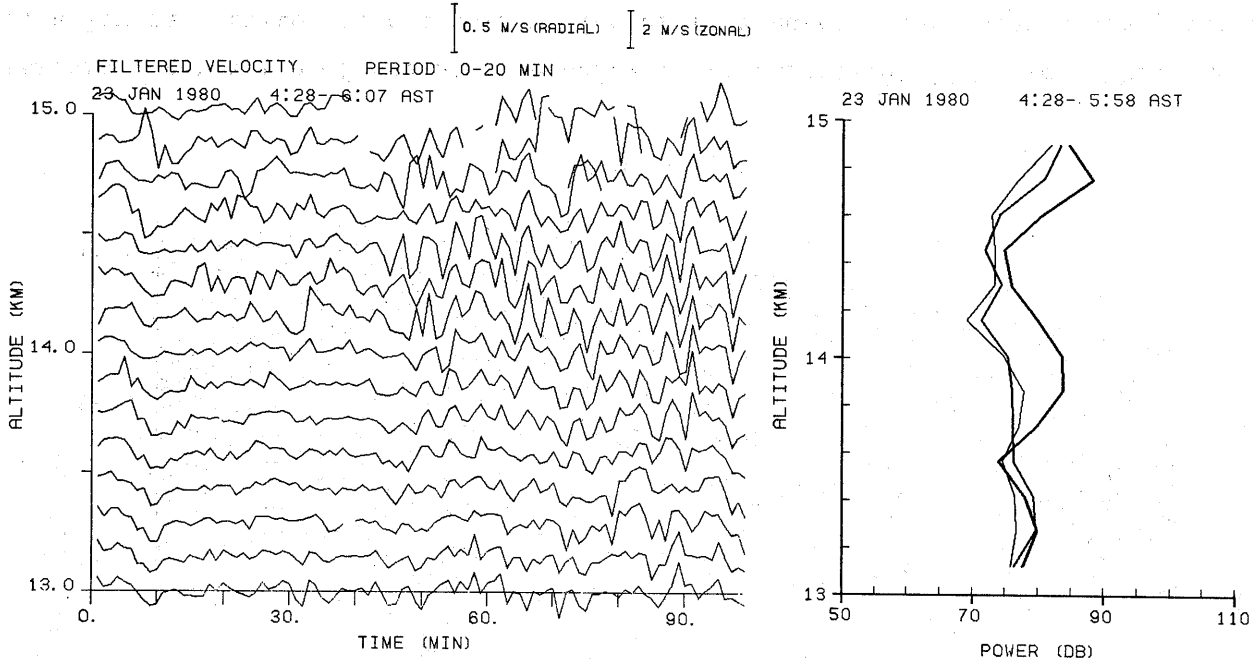

Fig.5-6 Same as Fig.5-5, but for a different filtering (0-20 minutes high-pass filter), and for a different height and time. 30 minutes average echo power for the same period is plotted on the right. Three lines correspond to consecutive three blocks of time in the increasing order of thickness.

case). Shown on the right of the figure are three height profiles of the echo power averaged over 30 minutes each. The third one, which corresponds to 60-90 minutes on the time scale on the left, is 2-8 dB larger than the other two, showing a good coincidence between the amplitude of the oscillation. Similar oscillations of 4-8 minutes period have been observed in lower height regions by other radars, and are discussed in terms of the Kelvin-Helmholtz instability (VanZandt et al., 1979, and Klostermeyer and Rüster, 1980). Klostermeyer and Rüster found a good agreement between the height variation of observed amplitude and phase of the oscillation and the theoretical calculation. The characteristic feature of their results is the amplitude minimum and the rapid phase change around the central height where the background wind shear exceeds the critical shear condition.

In our case, on the other hand, the strongest shear is observed around 15 km height, and no clear oscillation of similar period can be found above that height. Also, there can be seen no appreciable phase variation with height. Our result may be explained that the rapid change in the atmospheric stability above and below the tropopause height, which is about 15.5 km in this case, possibly damped the upper half of the oscillation.

It is of course dangerous to make too many assertions on the nature of these short period oscillations from our limited information. Simultaneous observation at different points in space will help our understanding on the mechanism of these waves and oscillations.

5.4 STRATOSPHERIC TURBULENCE

An example of a height profile of the scattered echo power was given in Fig.4-8 a). The large fluctuation of the power with height indicate that scatterers are not distributed uniformly, but rather

concentrated in discrete layers. The power decreases a few to ten dB at adjascent heights around most maxima. Since the height samples are spaced at the nominal height resolution of 150 m, this sharp decrease in power around peaks means that most layers are thinner than 150 m.

Much better height resolution is required to observe microstructures of the layer directly. However, the sharp minima in power between strong layers indicate that this height resolution is sufficient to separate individual turbulent layers. Average vertical separation between layers is a few to several hundred meters.

Fig.5-7 shows a height-time variation of the echo power in an 8-level shade plot. The dynamic range from white to black corresponds to 32 dB. The antenna beam was pointed east and north at 15° zenith angle alternately at one hour interval. A fairly good continuity between the power in these two directions indicates the uniformity of turbulent layers over 3-10 km in the horizontal direction.

A descending layer which starts from 13 km at around 19 AST in Fig.5-7 is a typical example of turbulent layers in the troposphere. This movement seems to indicate the passage of a solitary gravity wave propagating its energy upward (Titheridge, 1971). It is important to note that these thin layers show vertical motions because the slowly sweeping motion of a turbulent layer increases its effective diffusivity several times more than a fixed layer with the same thickness (Woodman et al., 1980). The scattering layers in the stratosphere (above 16 km) are more stable than those in the troposphere. The layers stay at almost the same height, sometimes for several hours. Since the layers should be moving at the speed of the mean flow, this continuity in time means the horizontal extent of these layers is the order of 100 km. It is surprising that even such layers have a thickness of 150 m or less. This stationarity is, however, consistent with the observed stability of the vertical shear structure of the horizontal velocity (Sato and

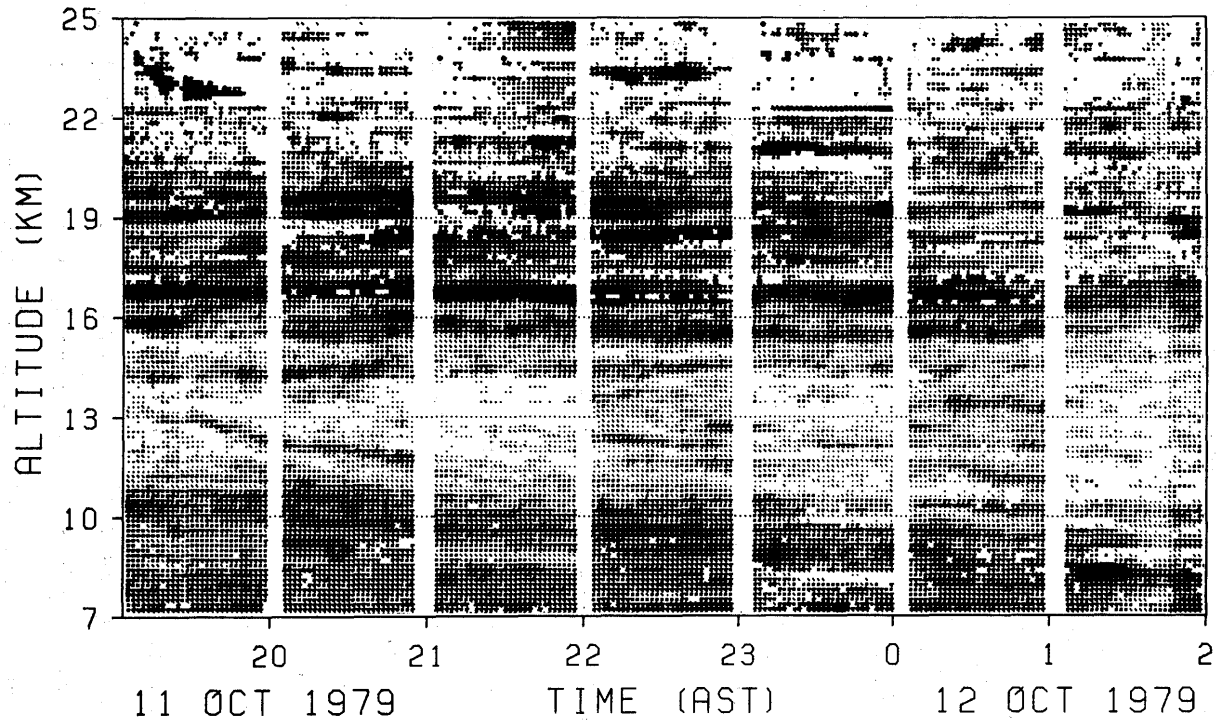

Fig.5-7 8-level height-time shade plot of the echo power. The dynamic range is 32 dB. Missing points due to poor quality of data are left white.

Woodman, 1981a).

There is a good correlation among the echo power, the vertical shear of horizontal velocity, and the spectral width of echoes. Fig.5-8 shows 10 hour average height profiles of these three parameters. The shear is determined by a central finite difference over 300 m. Two thin lines around the thick line indicate the standard deviation from the mean. Although the total velocity vector should be used for this comparison, only the E-W component is shown since only one component can be measured at a time, and the E-W component is dominating over the N-S component in this case. Three large peaks at 15-17 km in the power profile clearly have corresponding peaks in the shear and the width profiles. The correspondence among the shear and the other two profiles becomes worse above 18 km probably due to the smaller number of available data points in this height region. Resemblance between the power and width profiles is very good throughout the observed height range.

This positive correlation among these three parameters can be easily interpreted by an intuitive model; when the vertical shear of the horizontal velocity becomes large, the flow becomes more unstable, and the turbulence dissipates more energy into the scale size observed by the 430 MHz radar. The spectral width also becomes large since it reflects the line-of-sight component of the velocity distribution of the turbulence. The shear broadening may also contribute to this correlation as discussed later.

In fact, the Richardson number calculated at the two strongest peaks at 15.5 and 17 km using balloon temperature data is slightly lower than 1.0, showing that these layers are in a subcritical state on the average. This fact is consistent with the persistence of the strong echo at these heights throughout the experiment.

The existence of a strong angular dependence in the received echo power has been found by VHF radars, and are discussed in terms of the Fresnel reflection from the zenith direction (see the review

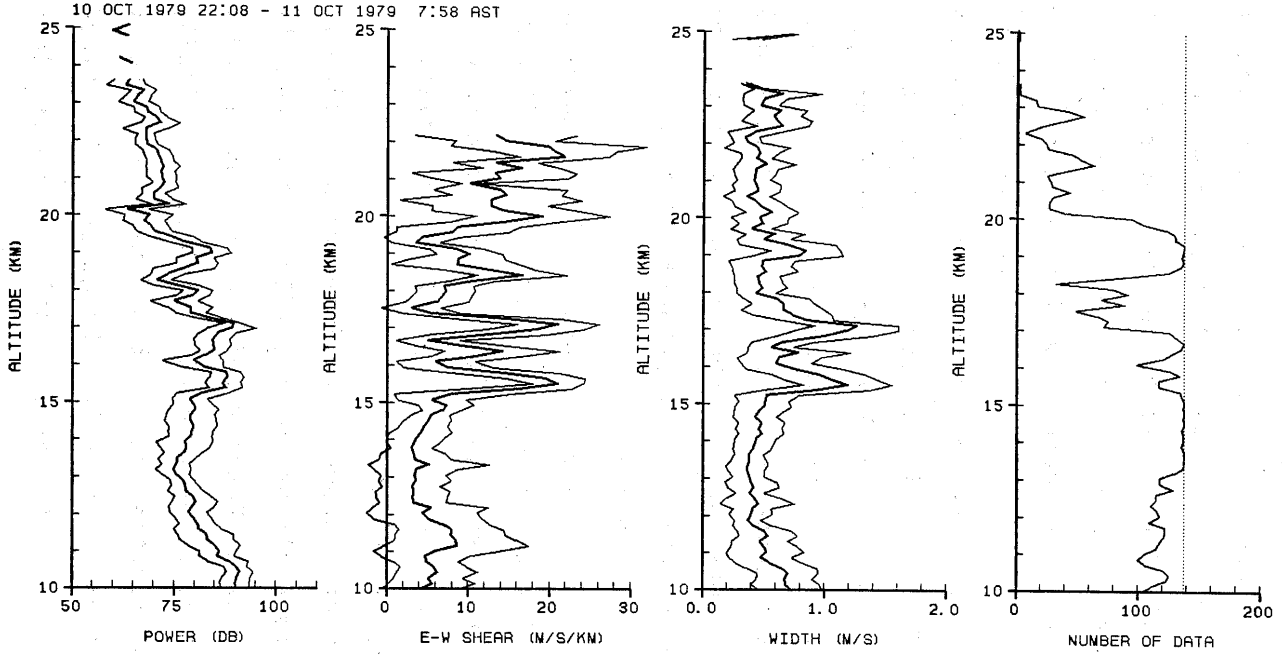

Fig.5-8 10 hour mean echo power, E-W component of the wind shear, and the spectral width versus height. The number of good data points used in the average are plotted on the right. The dashed line in the figure shows the total number of data points. Two thin lines around the thick line in each profile indicate the standard deviation from the mean.

by Balsley and Gage, 1980). Similar anisotropy is found at UHF frequency by Fukao et al. (1981b) with the aid of a special program dedicated to the observation of the zenith direction. To examine the angular dependence of observed parameters at the frequency of UHF in more detail, we made a short experiment changing the zenith angle between zero and 15°. Fig.5-9 shows the echo power, the spectral width, and the line-of-sight velocity versus zenith angle. Each point is an average of 3 minutes and 14-19 km height range in which the zonal velocity decreases from 30 to 10 m s^{-1}. The zenith angle was changed from 15° toward zero, then back to 12.5°. Open circles show data taken on the way toward zenith, and black circles show the reverse. This experiment took about 70 minutes. The data in the zenith direction are not used since the stratospheric echo having almost no radial velocity component can not be discriminated from the strong ground clutter contribution. The data at 1° zenith angle are also suspicious for the same reason although plotted in the figure. The echo power is compensated for the dependence of antenna efficiency on zenith angle.

The echo power seems to show no appreciable angular dependence in the 2.5-15° zenith angle range. This result combined with the former experiment (Fukao et al., 1981b) leads to a conclusion that the specular reflection occurs only when the mirror reflection condition is strictly satisfied.

The spectral width shows an interesting linear angular dependence. It can be explained most easily by the shear broadening effect. The difference in Doppler shift of the upper and the lower boundary of the turbulent layer moving with the vertically sheared background flow contributes to a broadening of the echo power spectrum when the antenna is pointing obliquely. This broadening is proportional to the sine of the zenith angle, which is almost linear within 15°. If we assume this angular dependence is caused by shear broadening effect alone, we can then estimate the zonal velocity difference over the turbulent layer to be about 1.2 m s^{-1} from the

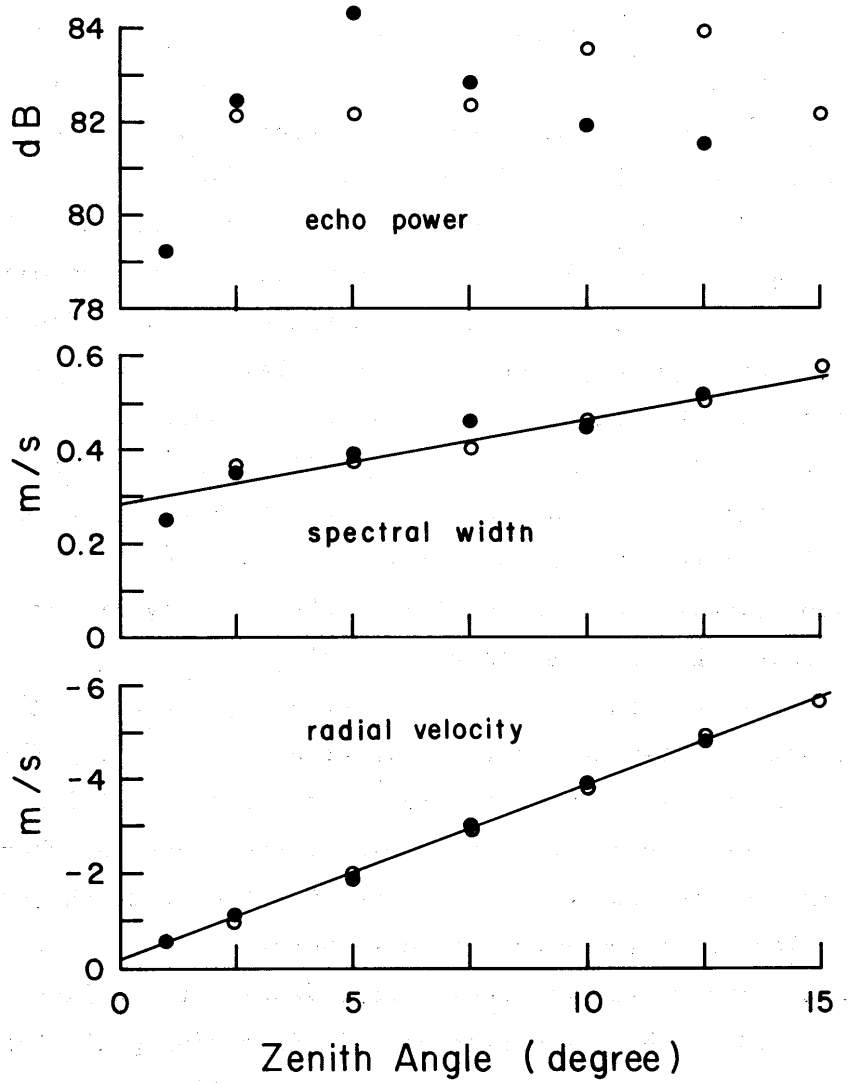

Fig.5-9 The echo power, the spectral width, and the radial velocity versus zenith angle. The zenith angle was changed from 15° to zero (open circles), then back to 12.5° (black circles) spending about 70 minutes.

gradient of the fitted straight line. If we take the meridional velocity difference over the layer, which is not observed, to be the same as that of zonal, we can estimate the vector velocity difference over the layer to be about 1.7 m s^{-1}. Postulating that the local background shear is critical around the turbulent layer, it becomes about 40 m $s^{-1}km^{-1}$ around the tropopause height. We can thus estimate the thickness of the layer to be about 40 m.

There is another way to estimate the thickness of the layer (Woodman and Guillén, 1974). By extrapolating the straight line toward zero zenith angle, we obtain the true spectral width of about 0.3 m s^{-1} in the line-of-sight velocity scale. This velocity can be interpreted as the random velocity of turbulence caused by the shearing instability. Assuming that all of the available energy supplied by the background shear goes to the kinetic energy except the loss due to the work done against the buoyancy, we can evaluate the random velocity to be about 1/7 of the velocity difference over the layer under the critical shear condition.

Applying this method to the present data, we can estimate the vector velocity difference over the layer as 2.1 m s^{-1}. This value is in a good agreement with the former estimate of 1.7 m s^{-1}, and leads to an estimate of the thickness of the layer of about 50 m. These estimates are also consistent with the fact that the thickness is usually less than 150 m as mentioned before.

A good linear zenith angle dependence of the line-of-sight velocity supports the assumption used in determining the horizontal velocity that the vertical velocity is very small on the average.

5.5 EFFECTS OF STRATOSPHERIC TURBULENCE ON THE VERTICAL TRANSPORT

The most fundamental characteristic of the stratosphere is its high static stability based on the positive temperature gradient in this height region. The transport of momentum, the heat, or

material proceeds much slower in the stratosphere than in basically unstable troposphere. Therefore the transport phenomena in the stratosphere had not been paid much attention for long, partly due to sparse observations. Its importance was realized only after the possibility was pointed out on destruction of the ozone layer due to stratospheric flights of supersonic airplanes or to artificially released chemicals (Molina and Rowland, 1974).

Two mechanisms have been postulated which may dominate the vertical transport in the stratosphere (e.g., Woodman, 1980c): the global scale quasi-horizontal motions, and the three dimensional turbulence (Gudiksen et al., 1968). Since the total amount of the vertical transport is estimated from the diffusion of radio actives (e.g., Reed and German, 1965), the role of the turbulence can be clarified by evaluating the eddy diffusivity due to the stratospheric turbulence.

The eddy diffusivity due to the stratospheric turbulence has been estimated using aircraft (Lilly et al., 1974), balloon (Cadet, 1977), and coherent radar observations. As for the radar observations, the estimates are derived from the echo power with the aid of balloon temperature data (Gage et al., 1980), and from the occurrence frequency and measured thickness of the turbulent layers (Woodman et al., 1980). These different estimates resulted in a fairly wide range of the values and different conclusion on the importance of the stratospheric turbulence on the vertical transport phenomena. We will examine here an alternative way based on the observed width of the power spectra. A similar attempt was made for the mesospheric observation (Cunnold, 1975) interpreting the spectral width in terms of the eddy diffusivity.

The three dimensional wavenumber spectrum of the kinetic energy of turbulence in the inertial subrange is given by

$$S(k) = \alpha\varepsilon^{2/3}k^{-5/3} \qquad (5.1)$$

where a is the Kolmogoroff's constant of about 1.6, and ε is the energy dissipation rate per unit mass and time. S(k) integrated from k_o to k_i is the kinetic energy of the turbulence per unit mass measurable by a radar, where k_i is the radar Bragg wavenumber and k_o is the wavenumber associated with the largest vortex in a turbulent layer. Since k_i is 18 rad m^{-1} for the radar frequency of 430 MHz, and k_o is 0.1 - 1 rad m^{-1} for the thickness of the layer discussed before, thus $k_i >> k_o$. The standard deviation of the echo power spectra can be interpreted as the representative velocity of turbulence, if the shear broadening effect is removed from the spectra. We may then write the energy per unit mass as

$$\int_{k_o}^{k_i} S(k)dk = \frac{3}{2}\sigma^2$$

and thus we obtain

$$\begin{aligned}\varepsilon &= a^{-3/2}\sigma^3/(k_o^{-2/3}-k_i^{-2/3})^{3/2} \\ &\simeq a^{-3/2}\sigma^3 k_o \end{aligned} \qquad (5.2)$$

where σ is the one side 1/e echo power spectral width, which is 0.6 times the usual half power spectral width. We should note that spectral parameters in the radar observations are mean values over the volume determined by the antenna beam width and the height resolution weighted by the echo power. The true average in a height sample is obtained by multiplying (5.2) by the fraction of the turbulence in a height resolution. We may use the ratio of the size of the largest vortex in a turbulent layer and the height resolution as a crude estimate of this factor, when the echo power of the height exceeds the detectable threshold. We simply put the factor zero when the echo power is below the threshold. For turbulence we obtain

$$\overline{\varepsilon} \simeq (2\pi/k_o)/\Delta h \cdot \varepsilon$$

$$= 2\pi a^{-3/2}\sigma^3/\Delta h \qquad (5.3)$$

where $\bar{\varepsilon}$ denotes the mean energy dissipation rate in a height resolution Δh. Eq. (5.3) shows that the energy dissipation rate is directly connected to the spectral width. The eddy thermal diffusivity is given by (Lilly et al., 1974)

$$K_h = \varepsilon/3N^2 \qquad (5.4)$$

where N is the Brunt-Väisälä frequency.

Fig.5-10 shows one hour mean profiles of the energy dissipation rate, Brunt-Väisälä frequency, and the eddy thermal diffusivity versus height. Since the Brunt-Väisälä frequency was obtained from seven rawinsonde measurements and interpolated to the day of the radar observation, it should be interpreted as a model. The variance in a month is, however, within 50 % around the interpolated value. Resulted eddy diffusivity shows a clear maximum of about 1 m^2s^{-1} around 16 km, the tropopause height. The average eddy diffusivity in the higher troposphere and the lower stratosphere are about 0.3 and 0.1 m^2s^{-1}, respectively. These values of the energy dissipation rate and its peak at the tropopause height are in a general agreement with the Sunset VHF radar observations (Gage et al., 1980). The eddy diffusivity is about an order of magnitude larger than those reported in Lilly et al. (1974), but agrees well with the mean value given by Woodman et al. (1980). It supports the importance of the stratospheric turbulence in the vertical transport phenomena.

This method of estimating turbulence parameters cannot be directly applied to data of other periods, since the shear broadening effect cannot be separated from the true spectral width when the antenna beam direction is fixed. However, we can derive turbulence parameters from these data if we assume the shear broadening effect is constant throughout the observation period and

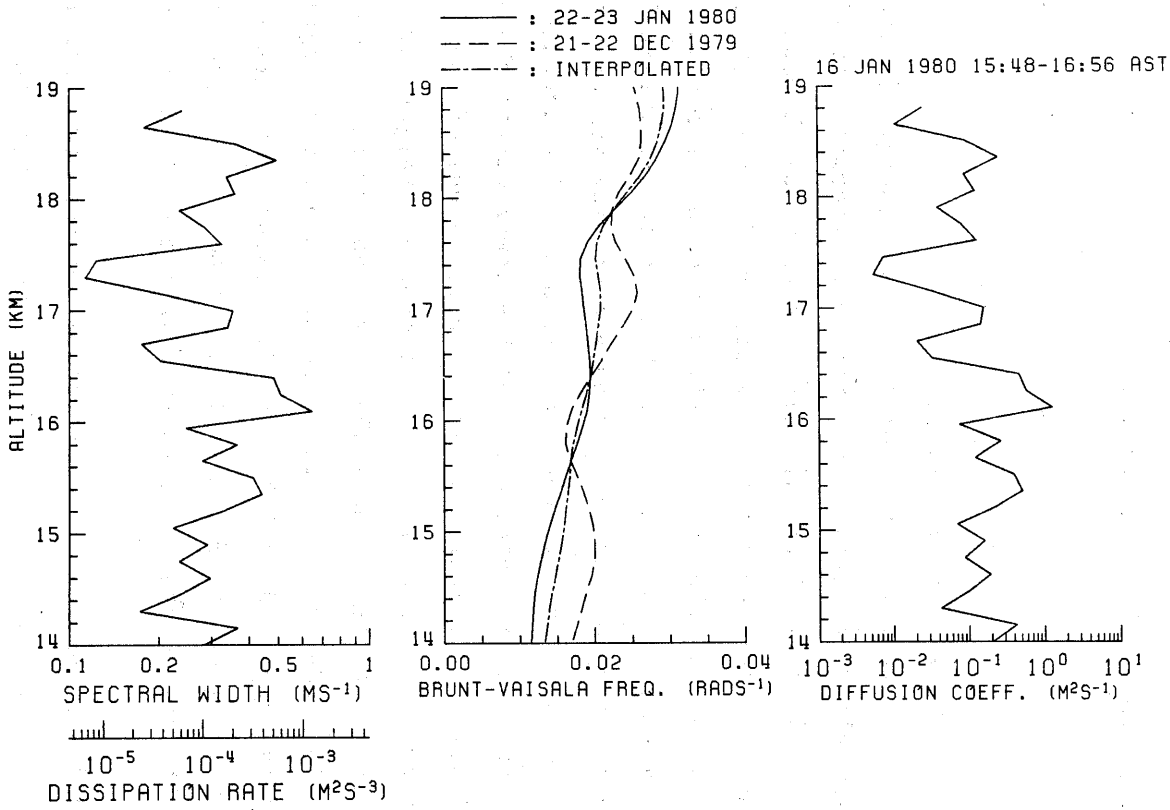

Fig.5-10 One hour mean profiles of the energy dissipation rate, the Brunt-Väisälä frequency, and the eddy thermal diffusivity.

depends only on the zenith angle of the antenna beam direction. It is equivalent to postulate the velocity difference above and below the turbulent layer is constant. Since the validity of this assumption is to be judged by future observations, absolute values obtained from this assumption should be interpreted with care.

Fig.5-11 shows the energy dissipation rate for October 10-13, 1979 versus time and height in a form of a contour map. Since the antenna beam was switched every 1 hour between the east and the north directions at the zenith angle of 10°, results for the two antenna beam directions are given separately. The contours are drawn at 10 dB intervals through the hourly mean values obtained every two hours. No smoothing was applied to the height direction. Blank parts of the figure indicate either the observation was absent due to troubles in the system, or the quality of data is poor. The average value over this period is plotted versus height on the right of the figure.

In the troposphere of below 15 km, the energy dissipation rate shows height or temporal variations of more than three orders of magnitude. A fairly large difference between the eastward and the northward antenna directions seems to indicate the spatial inhomogeneity is large at these heights. The structures become stratified above about 15 km, large values being concentrated in narrow layers. Also the difference between the two antenna positions becomes smaller as is clear in the height variation of the average value. The agreement, however, becomes worse again above about 20 km, where the average values shows a difference of a factor of 2-4. The assumption of the constant shear broadening may be responsible for this discrepancy because the observed width itself becomes smaller with increasing height.

Fig.5-12 shows temperature and the Brunt-Väisälä frequency deduced from 6 rawinsonde flights during this period. Curves are obtained by a spline interpolation between the observed points. The thick line shows the mean value of the 6 flights. The mean value of

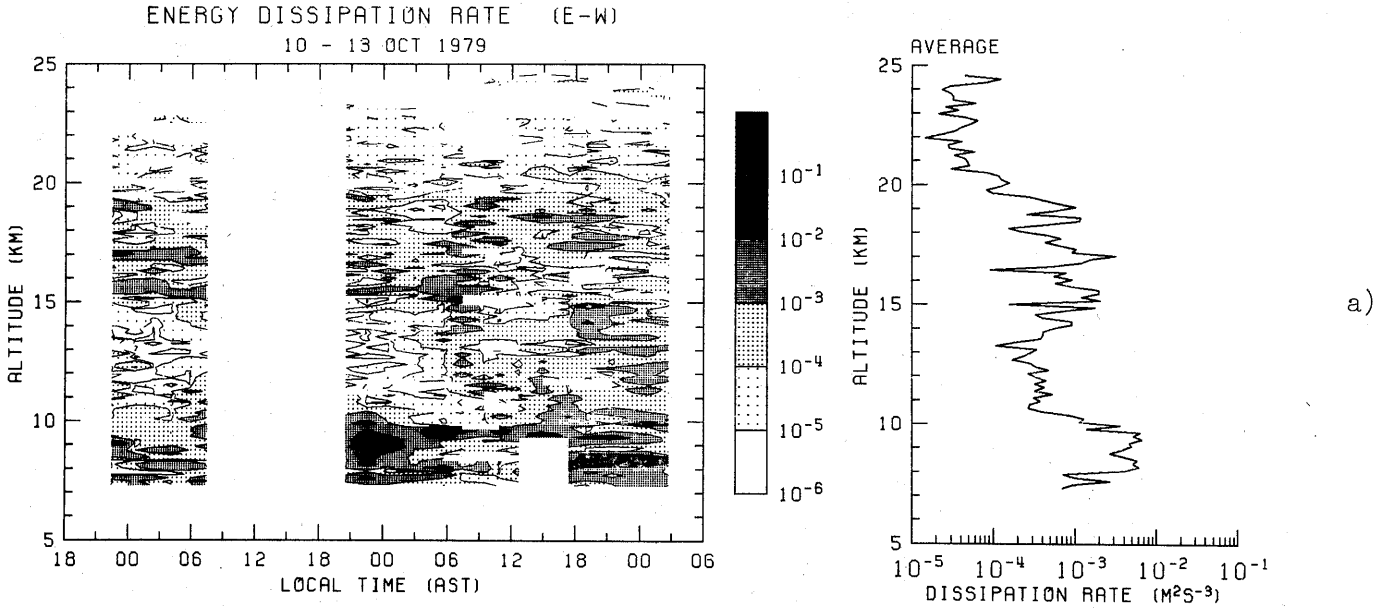

Fig.5-11 Contour diagrams of the energy dissipation rate versus time and height at a) the east and b) the north antenna beam directions on October 10-13, 1979. Contours are drawn at 10 dB intervals. Blank parts denote either the observation is absent, or the quality of data is poor. The height profile of the average over the entire period is plotted on the right.

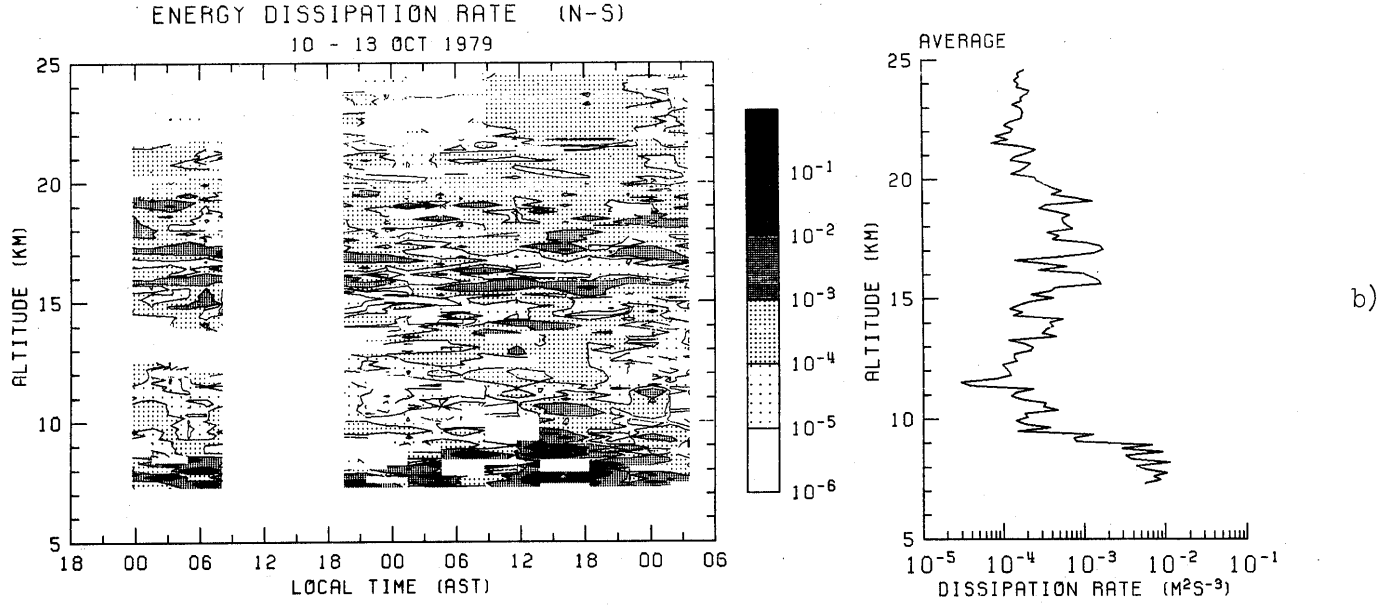

Fig.5-11 (continued)

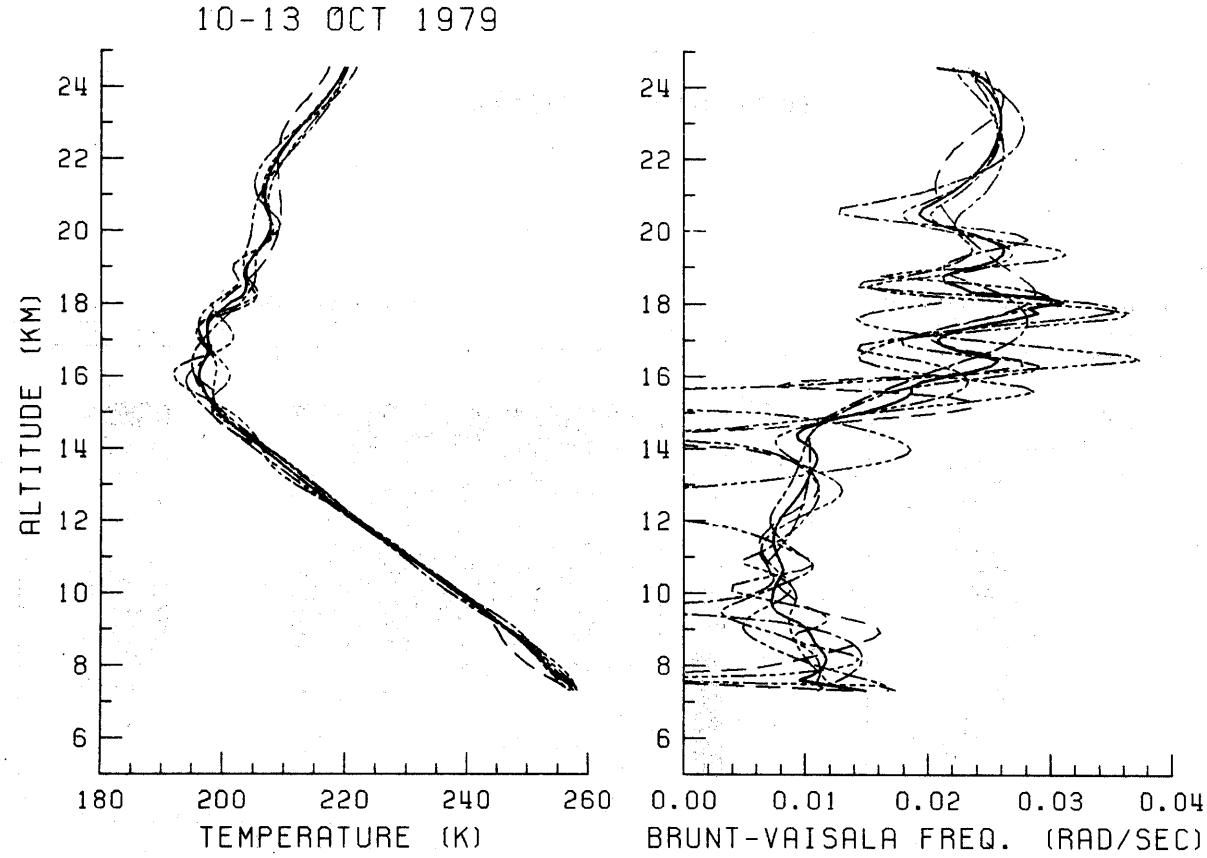

Fig.5-12 Temperature and the Brunt-Väisälä frequency obtained from 6 rawinsonde flights on October 10-13, 1979 launched from San Juan, Puerto Rico. Lines are deduced by a spline interpolation between the given data points.

the Brunt-Väisälä frequency was used in evaluating the eddy diffusivity, because the fluctuations in the original profiles seem to be fairly large and no appreciable trend can be found over three days. Fig.5-13 is a similar contour map as Fig.5-11, but for the eddy diffusivity. The basic feature of Fig.5-13 is the same as that of Fig.5-11 since the height variation of the Brunt-Väisälä frequency is smoother than the variations of the energy dissipation rate. The mean decay rate of the eddy diffusivity versus height is 1-1.5 dB km^{-1} for this period.

The advantage of this method of estimating the turbulence parameters is that instantaneous values of the energy dissipation rate can be deduced from the radar data alone. Though the eddy diffusivity depends on temperature through the Brunt-Väisälä frequency, it seems fairly stable to allow the interpolation between balloon observations. The disadvantage may be that a very accurate value of the spectral width is required since the parameters depends on its cube. The assumption used in determining the fraction of the turbulence in a height sample may add the error of a factor of 2 or so. If a radar with a lower frequency or a smaller aperture than the Arecibo 430 MHz radar is to be used for this purpose, a correction is needed for an additional broadening of the echo power spectra due to the sphericity of the wave front in the far field of the antenna.

5.6 SUMMARY AND CONCLUSIONS

Some interesting results found in a series of high-resolution stratospheric observations using the Arecibo UHF radar have been presented. As for the wind velocity, a stable wavy vertical structure and purely sinusoidal short period oscillations are discussed. The former is a good example to show the importance of a high height resolution, since the associated vertical wavelength is

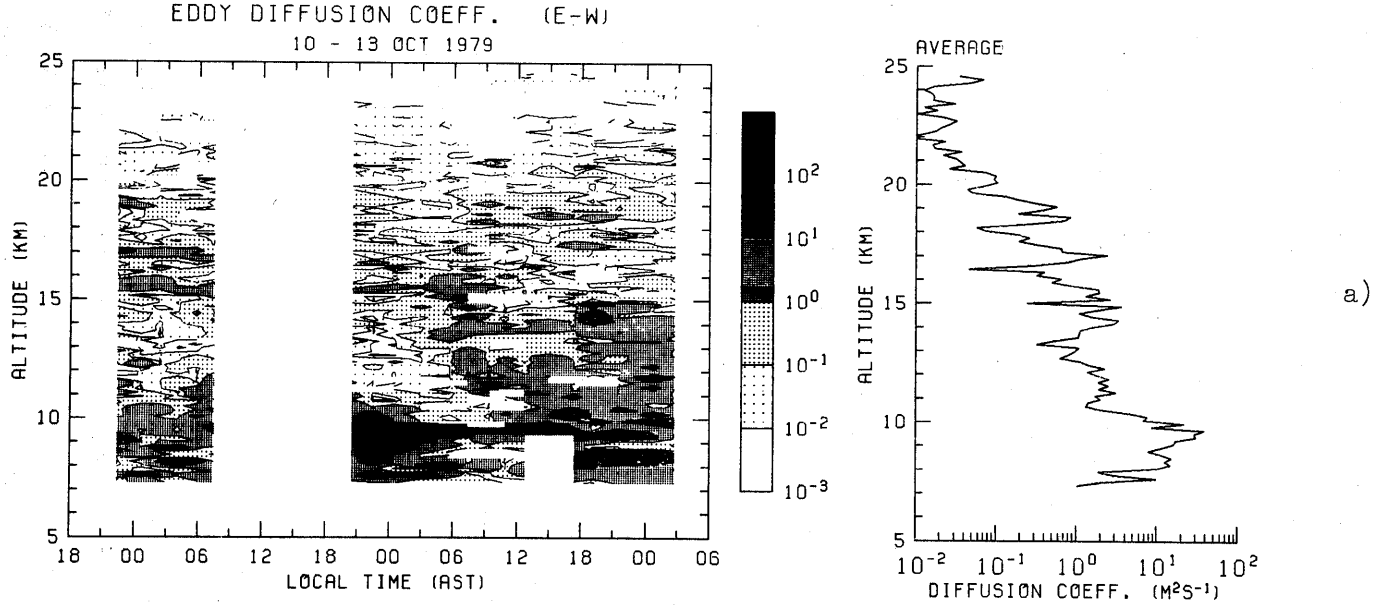

Fig.5-13 Same as Fig.5-11, but for the eddy diffusivity.

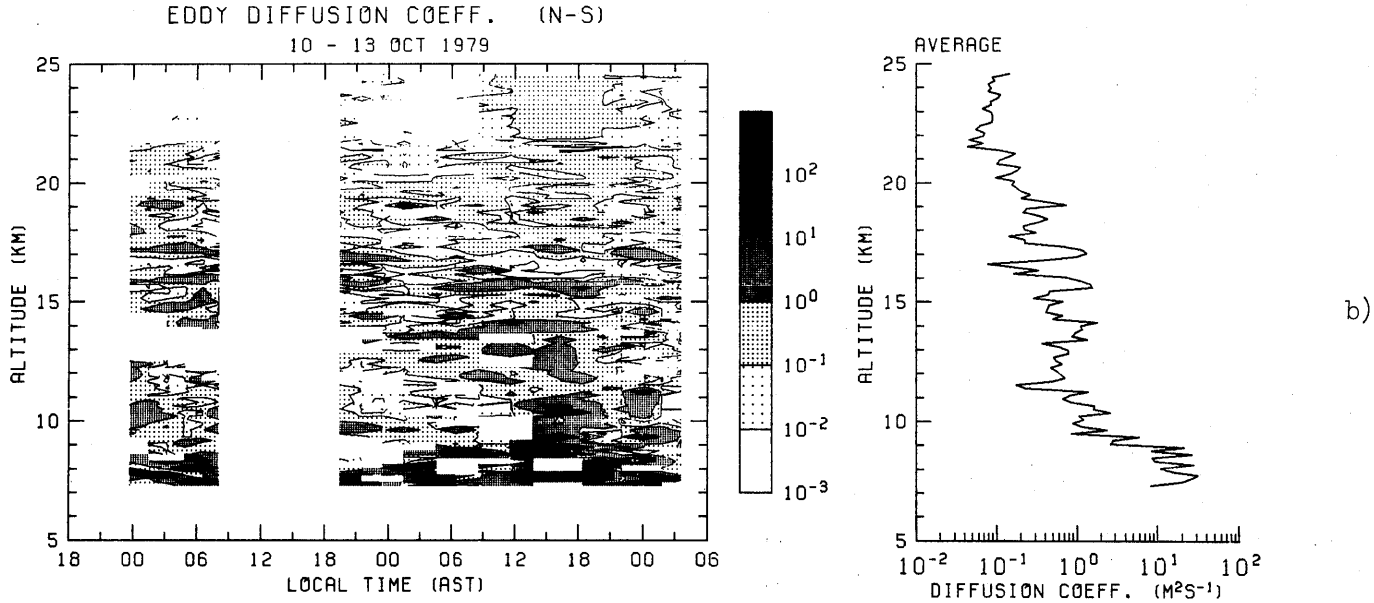

Fig.5-13 (continued)

very short. The latter demonstrated the importance of high time resolution in the study of dynamics of gravity waves.

The turbulent layers were found to appear as many discrete layers separated by a few to several hundred meters. The thickness of the layers was usually less than the height resolution of 150 m, and estimated to be about 50 m on average from the results of a zenith angle swinging experiment. Descending layers are observed in the troposphere, but the layers are very stable in the stratosphere. The horizontal extent of the layer was estimated to be of the order of 100 km.

Observed echo power showed a good correlation with the vertical shear of the horizontal velocity, and with the spectral width of the echo as shown in Fig.5-8, which can be understood by considering an intuitive model of the turbulent layer.

The turbulent energy dissipation rate and the effective eddy thermal diffusivity were evaluated based on the observed spectral width of the echo power spectra. A good agreement was found with other radar investigations of these parameters, showing the importance of the stratospheric turbulence on the vertical transport phenomena.

CHAPTER 6
MU RADAR DESIGN CONCEPTS

6.1 THE MU RADAR PROJECT

The capability and associated technical limitations of large VHF and UHF radars of Jicamarca and Arecibo for the middle atmospheric study have been examined. A similar kind of coherent VHF radar is now under design in Japan (Fukao et al., 1980a). It is a monostatic pulse radar of 1 MW peak output power with a Yagi array antenna of about 10000 m^2 area. It is planned to be located in a national forest of Shigaraki, Shiga (34.85°N, 136.10°E). This radar is named the Middle and Upper atmosphere radar (MU radar or MUR for short) because its principal target is the atmospheric dynamics of 10-300 km height range. Fig.6-1 is an artist's conception of the MU radar.

The operational frequency is planned to be 46.5 MHz with a bandwidth of 1 MHz. The choice of this frequency was based on the compromise between the requirements for high sensitivities in stratospheric and mesospheric observations. As we have seen in Chapter 3, coherent scatter from mesospheric turbulence can be detected only with frequencies of about 50 MHz or lower due to the high-frequency cutoff of the turbulence energy spectrum. Observations of weak incoherent scatter from the mesosphere requires a system as large as that of Arecibo UHF radar, even with which the signal-to-noise ratio is very low. In the stratosphere, on the other hand, the signal-to-noise ratio increases rapidly with increasing frequency as shown in Chapter 4. Therefore, frequencies of around 50 MHz are appropriate for both stratospheric and mesospheric observations.

In designing the system, much attention was paid for the fast steerability of the antenna beam since the vector wind measurement

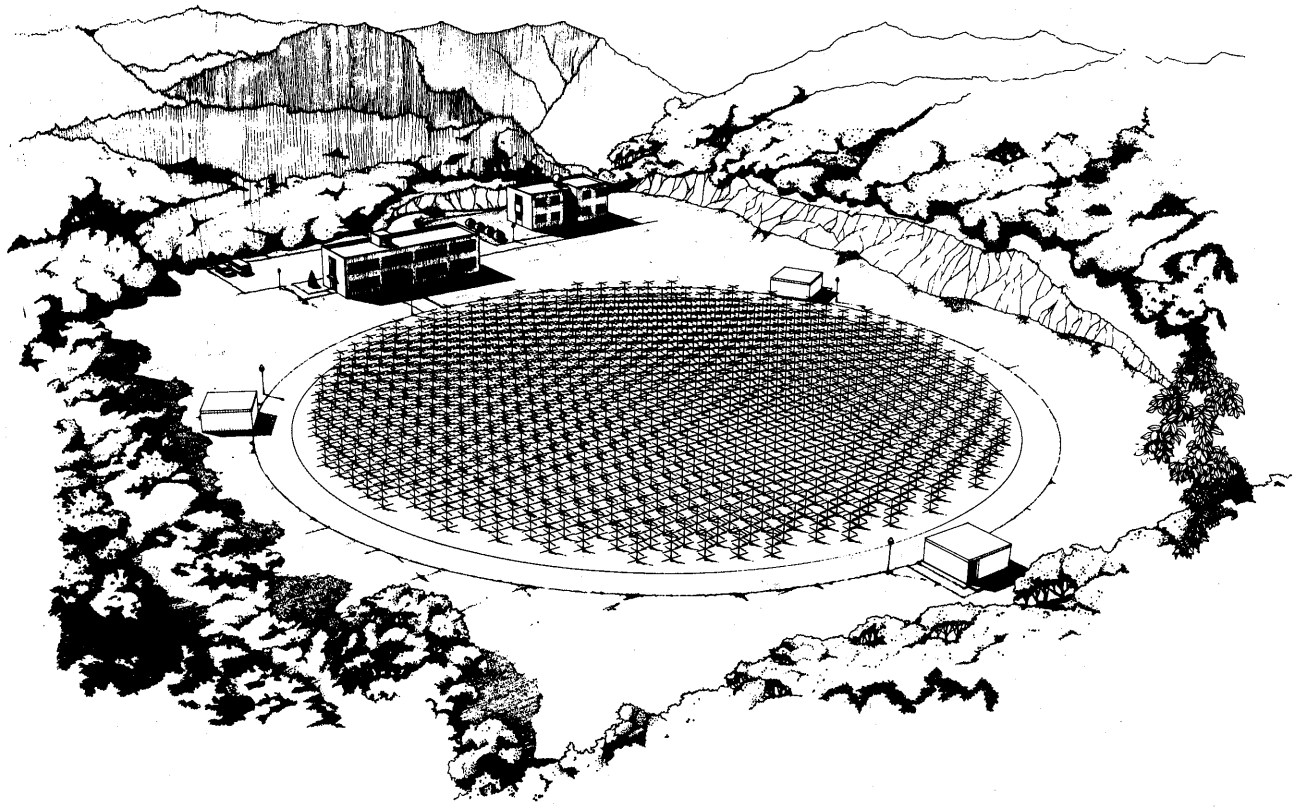

Fig.6-1 An artist's conception of the MU radar.

with a high temporal resolution is essential to the understanding of short period dynamics as indicated in the results of Chapters 3 and 5. Also, the advantage of the fast beam switching method over the multi-beam technique was demonstrated in Section 2.4.

A wide scan range is another important requirement for the antenna performance. Combined with the fast beam steerability, it allows a three-dimensional study of the wind field and the turbulence structure, which have not yet been performed at the middle atmospheric heights by any of the existing coherent VHF or UHF radars.

From a technical viewpoint, suppression of the ground clutter contaminations entering low elevation sidelobes of the antenna is an important requirement as shown in Sections 4.3 and 4.4. Thus the low elevation sidelobe levels must be kept as low as possible. This requirement is also important in preventing interference to the environments.

These scientific and technical requirements concerns most deeply with the design of the antenna system and its control circuits. As for the latter, it has already been shown that necessary performances can be realized by a combination of existing techniques (Fukao et al., 1980a). The design of the antenna system, on the other hand, contains more unknown factors as we see later. Here we briefly examine the control circuit design first, and then discuss the design of the antenna in detail. In the MU radar system, a very accurate phase control of each array element is necessary in order to achieve a low antenna sidelobe level. This accurate and fast phase shifting is performed by a unique configuration of the active phased array, which is usually employed at much higher frequencies.

Contrary to conventional large coherent VHF radars which utilize a high-power transmitter with a power-dividing network, the MU radar has low-power solid state transmitter for each antenna element. Thus the phase shifting can be performed at a low-power level using delicate electronic devices. The phase shifter consists of a

directional coupler with a 90° phase difference, and two 8-bit digitally controlled attenuators operate on orthogonal components. The outputs of the attenuators are combined to give a desired phase angle with an increment of 0.45°. This flexible design also allows to divide the array into subarrays, which is necessary when a spaced-antenna-drift technique is applied as discussed in Section 2.4. Subarrays can be used for other purposes as multi-beam meteor radar to study nighttime mesosphere.

Each antenna array element is driven by a transmitter-receiver (TR) module. A TR module consists of a solid-state transmitter, a receiver preamplifier, a TR switch, and the digital phase shifter. Also the frequency conversion between RF and IF of 3 MHz is done inside the TR module. The signal is transferred between the TR module and the control building at the IF. This frequency conversion prevents instabilities of the amplifier due to possible leakage of output power into the input signal.

An antenna element consists of two orthogonally crossed Yagi's both pointed toward zenith. Thus linear or circular polarizations of any sense can be synthesized by switching the connection between the TR module and the elements. The crossed Yagi was chosen as the array element for its simple configuration and easiness in obtaining various polarizations compared to other kind of antennas as the helical or short backfire antennas.

The phase shifting of TR modules is controlled by a network of microprocessors. The time delay between signals radiated from different elements is at most 0.17 s even when the antenna beam is directed 30° from zenith, thus can be neglected compared to the shortest pulse width of 2 μs. Bit patterns of the digital attenuators are stored in the ROM of the processor and transferred to each digital attenuators according to commands from the radar controller, which controls the entire network. Fig.6-2 shows a general block diagram of the MU radar system (after Fukao et al., 1980a).

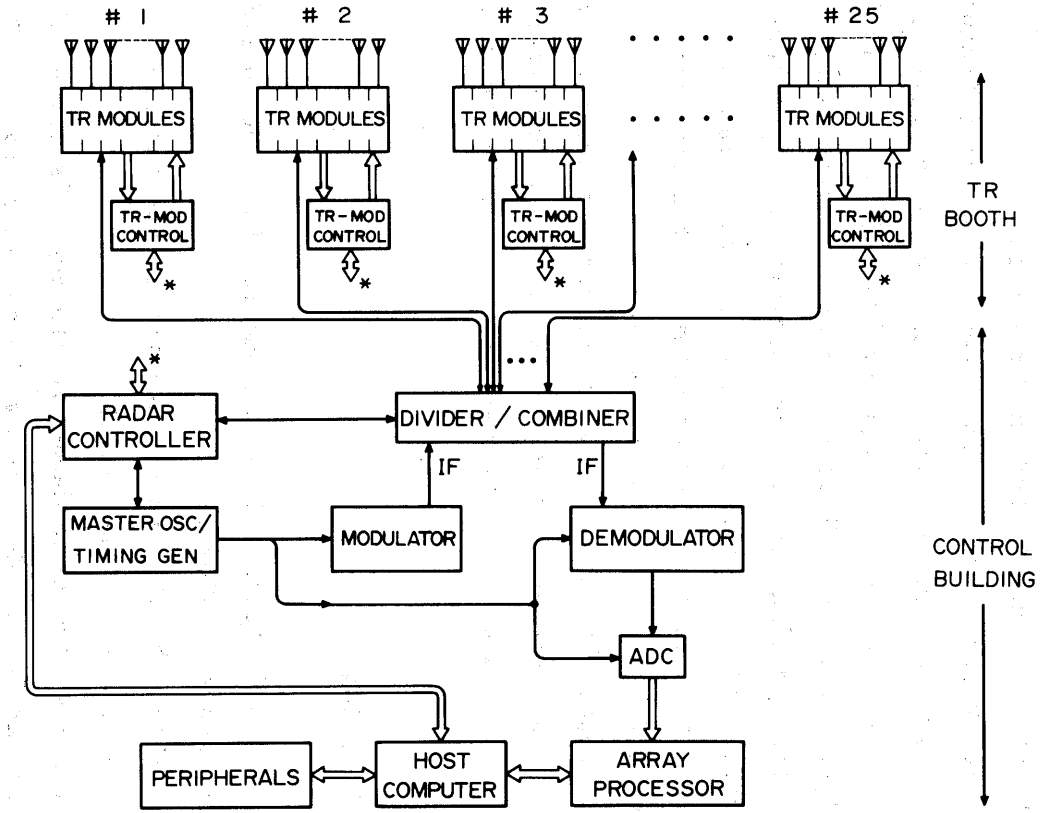

Fig.6-2 General block diagram of the MU radar system. Asterisks show that the radar controller and TR module controllers are logically connected. TR modules and TR module controllers are housed in TR booths built by the antenna area. Other parts of the system are set in the control building (after Fukao et al., 1980a).

Pulse width and IPP are determined by the programmed radar controller. The transmitter pulse can be compressed by any kind of binary phase code discussed in Section 4.2. Received signals are coherently detected, demodulated, and digitized at a sampling rate of up to 1 MHz. On-line processing is performed by an array processor under supervision of the host computer. The planned basic parameters of the MU radar are listed in Table 6-1.

By this control system, the antenna beam can be, in principle, pointed to any desired direction within a sufficiently short time. The remaining problem is to realize required low sidelobe levels for a desired main lobe direction. There are three important factors to be considered: the grating lobe, the positional and electrical errors in elements, and the mutual coupling between elements. The first two factors are related to the arrangement of array elements, and the third one affects the design of the element.

In the followings, theoretical investigations are presented for the antenna array and element design, that are made in order to satisfy the scientific and technical requirements for the MU radar.

6.2 ANTENNA ARRAY DESIGN

The scientific and technical requirements for the MU radar antenna are summarized as follows;

1. Antenna beam should be able to be pointed in any desired up to 20°, and preferably 30° around the zenith.
2. Sidelobes at a low elevation whose zenith angle is larger than 70° should be kept at least 40 dB below the mainlobe level. This condition must be satisfied even when the antenna beam is tilted to the limit specified above.
3. The gain of the antenna should be maximized and level of sidelobes near the mainlobe should be kept as low as possible under the conditions 1 and 2.

Table 6-1 Planned basic parameters of the MU radar

Location	: Shigaraki, Shiga, Japan (34.85°N, 136.10°E)
Frequency	: 46.5 MHz
Antenna	
configuration	: circular array of 475 crossed Yagi antennas
aperture	: 8330 m^2 (103 m in diameter)
beamwidth	: 3.6°
on-axis gain	: 34.0 dB
polarizations	: linear or circular
beam directions	: 0-30° zenith angle
Transmitter	
power amplifier	: 475 solid-state amplifiers
peak power	: 1 MW min
average power	: 50 kW min
bandwidth	: 1 MHz
TR switch	: PIN diodes with a directional coupler
Receiver	
bandwidth	: 1 MHz
dynamic range	: 70 dB min
IF	: 3 MHz
A/D converter	: 12 bit × 4 channel

In addition, in order to minimize the complexity in construction and maintenance, it is desired that these conditions are satisfied by a simplest possible configuration, namely, by a geometrically symmetric and periodic arrangement of elements with a uniform excitation. The requirement for a uniform excitation agrees with the condition of the maximum gain. Thus only the case of equally spaced elements with a uniform excitation is discussed here.

Consider a planar array of N elements arranged in x-y plane of the coordinate system shown in Fig.6-3. The radiation field of the array in a far field is given by (e.g., Steinberg, 1975)

$$F(\theta_x,\theta_y) = \sum_{n=1}^{N} F_{En}\exp\{jk(x_n\cos\theta_x + y_n\cos\theta_y)\} \tag{6.1}$$

where $k = 2\pi/\lambda$ is the wavenumber, λ is the wavelength, and F_{En} denotes the directivity of each element. If all elements are identical except a uniform phase progression, and if the elements are arranged in a general triangular grid shown in Fig.6-4, Eq.(6.1) can be rewritten as

$$F(\theta_x,\theta_y) = F_E \sum_{n=-\infty}^{\infty}\sum_{m=-\infty}^{\infty} W_{mn}\exp\{jk(na+mc)(\cos\theta_x-\cos\theta_{xo}) + jkmb(\cos\theta_y-\cos\theta_{yo})\} \tag{6.2}$$

where θ_{xo} and θ_{yo} show the direction in which the radiation from all elements adds in phase, and a, b, and c, are intervals between elements. W_{mn} is 1 for N elements and 0 for others. The summation and F_E in Eq.(6.2) are referred to as the array factor and the element factor, respectively.

The array factor in Eq.(6.2) takes maxima at the direction

$$\begin{aligned}\theta_x &= \cos^{-1}(\cos\theta_{xo} + \lambda n/a)\\ \theta_y &= \cos^{-1}(\cos\theta_{yo} + \lambda m/b - \lambda cn/ab)\end{aligned} \tag{6.3}$$

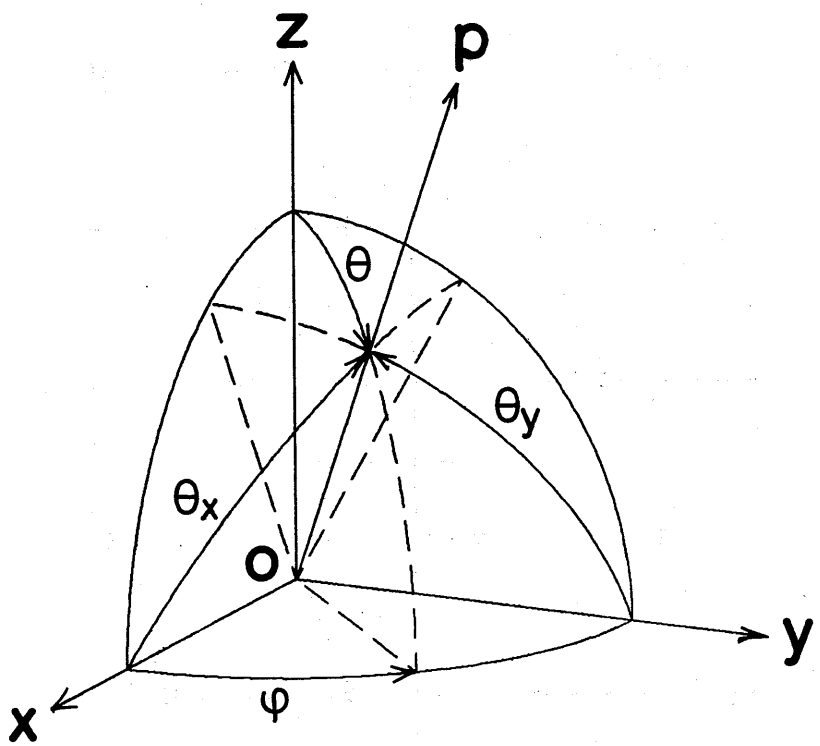

Fig.6-3 Coordinate system used in this chapter. Array elements are arranged on x-y plane.

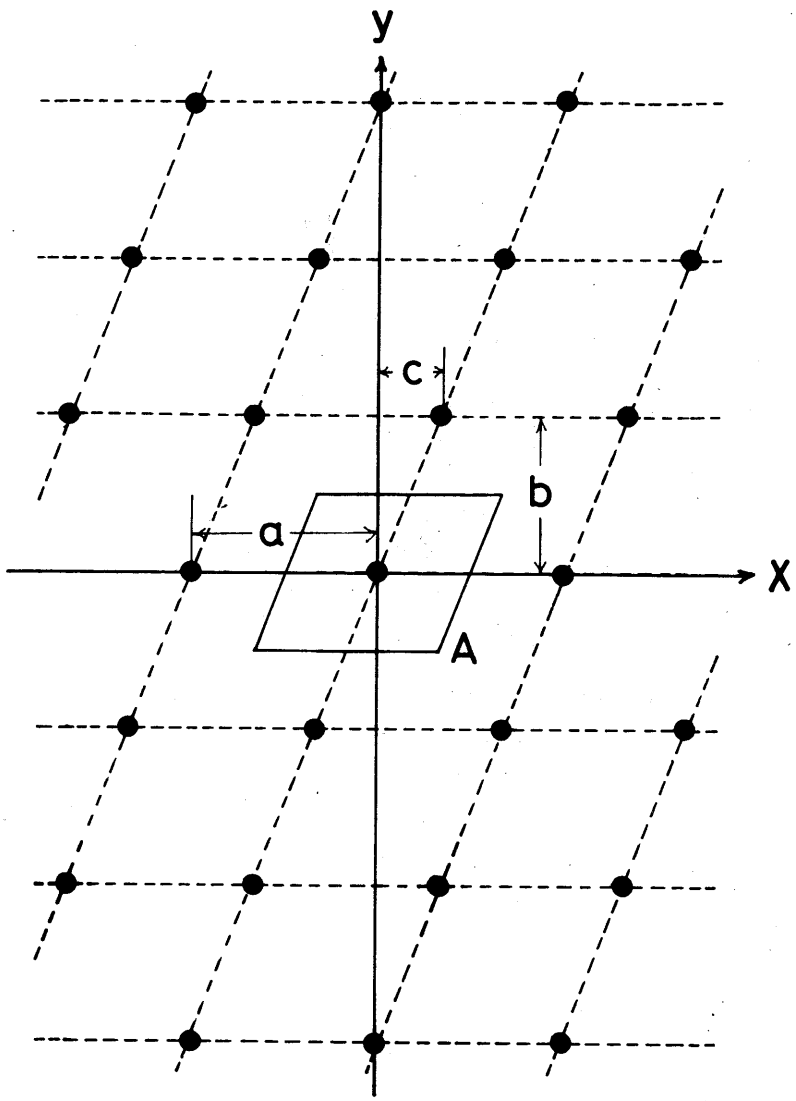

Fig.6-4 General triangular arrangement of array elements (dots) on the antenna plane. The area A denotes the element unit cell.

where n = m = 0 corresponds to the desire mainlobe, while others are to the undesired grating lobes if such combinations of n and m fall in the defined range of the arccosine function. The condition for which no grating lobe appears in any direction for a given zenith angle of the mainlobe is obtained by a geometrical consideration as

$$\max\{b,\ a/2,\ a/(1+c^2/b^2)^{1/2}\} < \lambda/(1+\sin\theta) \qquad (6.4)$$

where θ is the zenith angle, and $-a/2 < c \leq a/2$. The left hand side of this equation means to take the maximum term in the bracket. This condition sets the upper limit to element spacings. The lower limit is given by the size of elements, which is of the order of a half wavelength.

Choice of the element spacing is closely related to the antenna gain of the array element. In order to maximize the gain of the array, the effective area A_E of an isolated element should be equal or larger than the physical area ab of the element unit cell. Otherwise, the total gain of the array is limited by the number of elements N times the element gain G_E, which is related to A_E by

$$G_E = \frac{4\pi A_E}{\lambda^2} \qquad (6.5)$$

When A_E is larger than ab, it is reduced to below ab by the mutual coupling effect between antenna elements as shown later.

In the MU radar project, it is desired to keep the number of elements as small as possible in order to improve the reliability and to reduce the total cost of transmitters which are attached to each antenna element. Therefore it is planned to use Yagi antennas as elements of the MU radar antenna array because of their relatively large effective area. In the following computations of this section, an empirical element pattern for a 4-element Yagi antenna shown in Fig.6-5 is used as the element pattern in Eq.(6.2). A more detailed consideration is given for the array element in the

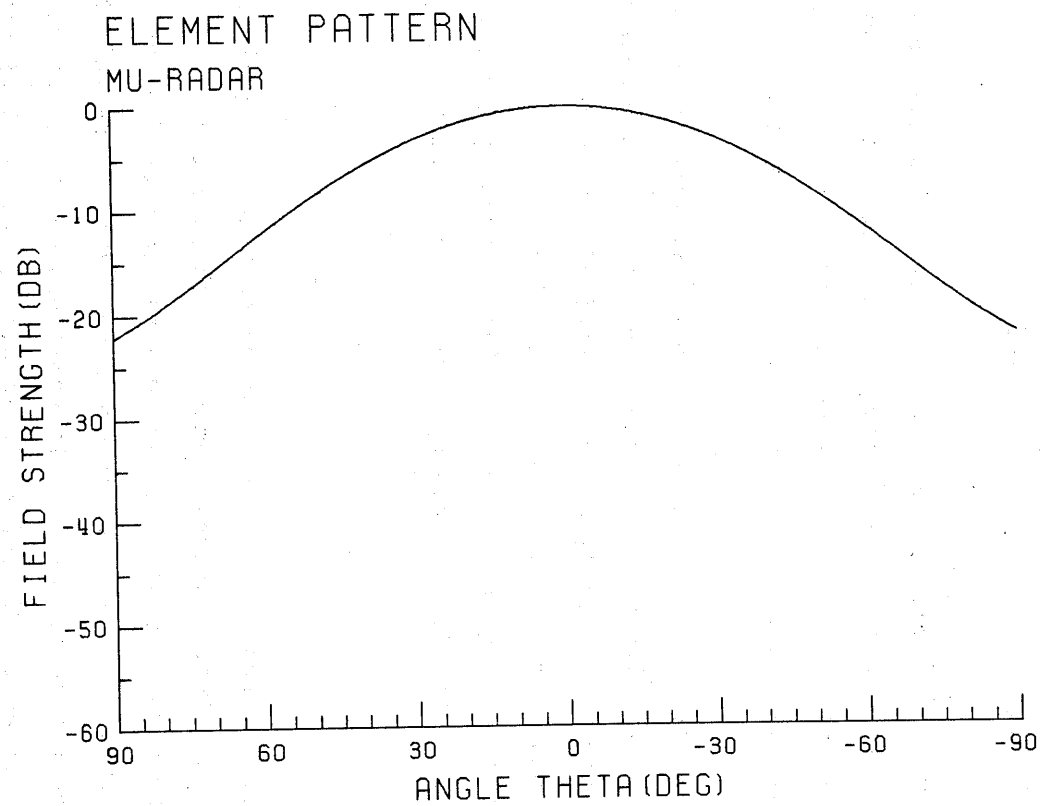

Fig.6-5 Empirical radiation pattern of a 4-element Yagi antenna.

following sections.

Fig.6-6 shows the arrangement of elements and computed radiation patterns of the original plan for the MU radar antenna (Fukao et al., 1980a). The solid and dashed curves show the pattern in the directions A and B, respectively, indicated on the arrangement by arrows. The ordinate is given in the unit of relative field strength normalized by that of a system with the effective area of 10000 m^2 and the same power density as the MU radar. Antenna elements are arranged to form a rectangular grid of (2/3) intervals. Its physical dimension is 103 m × 103 m. Deletion of elements at four corners is made in order to reduce sidelobe levels. The highest sidelobe is 16.0 dB below the mainlobe level compared to that of 13.6 dB for the square array. Low elevation sidelobes satisfy the required conditions when the antenna beam is pointed to zenith. However, Eq.(6.4) indicates that this arrangement gives a grating lobe when the antenna beam is tilted 30° from zenith. Fig.6-7 illustrates this aspect by three radiation patterns with the antenna beam tilted 0°, 15°, and 30° from zenith. The large sidelobe around -90° is the grating lobe which is suppressed only by the element directivity.

It is known that a triangular arrangement gives wider scan range than a rectangular arrangement with the same element density (Sharp, 1961). In order to increase the scan range of the antenna beam, the left hand side of Eq.(6.4) is to be decreased. Under the restriction that the area of the element unit cell S = ab is constant, the problem reduces to a problem of finding the minimum of a function

$$f(a) = \max\{S/a,\ a/2,\ a/(1+a^2c^2/S^2)^{1/2}\} \qquad (6.6)$$

Clearly, the third term takes its minimum value for the maximum value of c, which is a/2. Thus

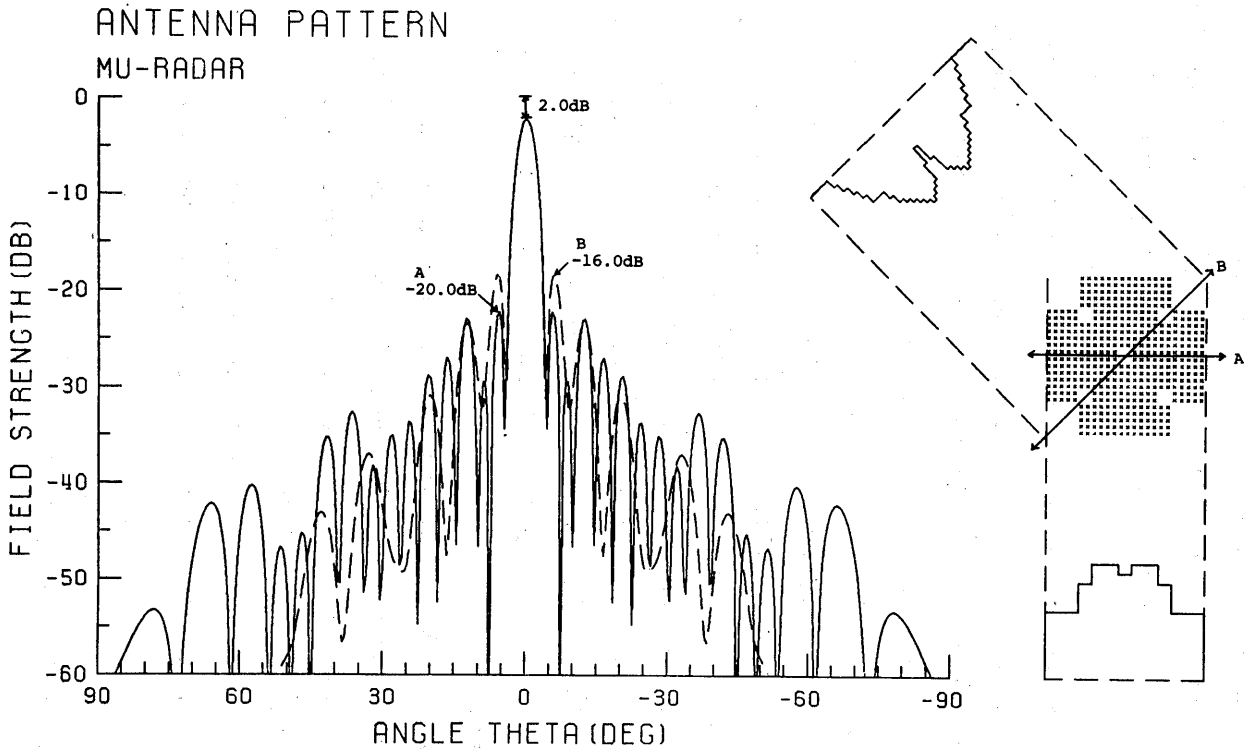

Fig.6-6 Arrangement of array elements (right) and computed radiation patterns of the original plan (left). Solid and dashed curves show radiation patterns computed in directions A and B, respectively, shown on the right. Current distributions projected on each directions are also shown above and below the figure of arrangement. Ordinate is normalized to the gain of a system with the effective area of 10000 m^2 and the same power density as the MU radar. First sidelobe levels written in the figure are relative to the main lobe level.

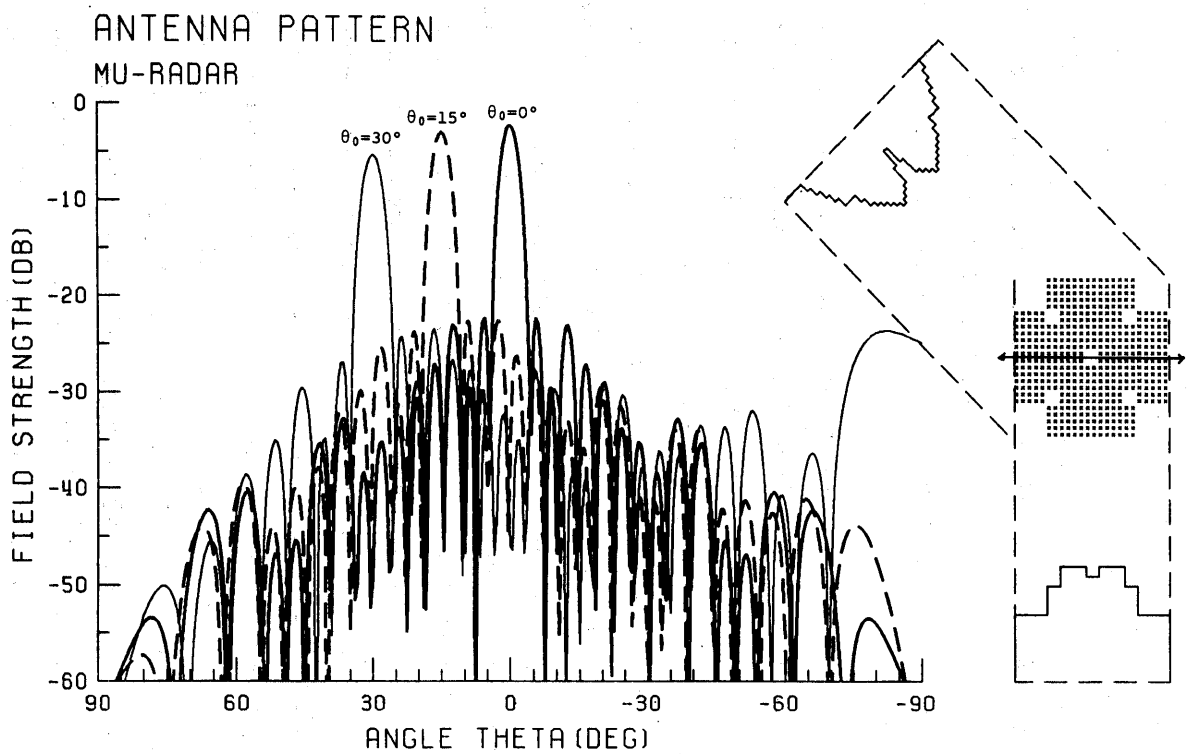

Fig.6-7 Same as Fig.6-6, but for tilted antenna beam directions.

$$f(a) = \max\{S/a,\ a/2,\ 2Sa/(4S^2+a^4)^{1/2}\} \qquad (6.7)$$

Eq.(6.7) takes its minimum value $(3/4)^{1/4}S^{1/2}$ for $a = (4/3)^{1/4}S^{1/2}$ and $12^{1/4}S^{1/2}$, for which $b = (3^{1/2}/2)a$ and $(1/12^{1/2})a$, respectively. These solutions correspond to grids of equilateral triangles with one of their sides along the x and y axis, respectively. Therefore, the optimum arrangement of the antenna elements which allows the widest beam scan range is the grid of equilateral triangles. For an element intervals of 0.7λ, which gives roughly equal element density as the arrangement of Fig.6-6, the grating lobe appears at the zenith angle of 40.5°.

Another point worth improving in the radiation patterns of Fig.6-6 is the unbalanced sidelobe levels in azimuthal direction. Fairly high sidelobes exist in the direction A corresponding to sharp discontinuities in the projected current distribution in this direction. A smoother and more balanced current distributions for all directions are obtained by changing the shape of the array to a circle, though it is not proved to be the optimum shape.

Fig.6-8 shows the element arrangement and the radiation pattern of a circular array with a equilateral triangular grid arrangement. The diameter of the array is 103 m and elements are spaced at 0.7λ intervals. As is expected, sidelobe levels are reduced and better balanced than those of Fig.6-6. The highest sidelobe level is 17.5 dB below the mainlobe. Fig.6-9 shows the radiation patterns when the antenna beam is tilted toward the direction in which the grating lobe appears first. In contrast to Fig.6-6, low elevation sidelobes are kept more than 40 dB below the mainlobe even when the antenna beam is tilted 30° from zenith. Fig.6-10 shows a stereographic radiation pattern of the improved MU radar antenna. It demonstrates that the sidelobes are distributed symmetrically and uniformly without outstanding peak for any particular direction.

In the above computations, all of the elements have been assumed to be placed exactly on the grid points on a perfect plane, and

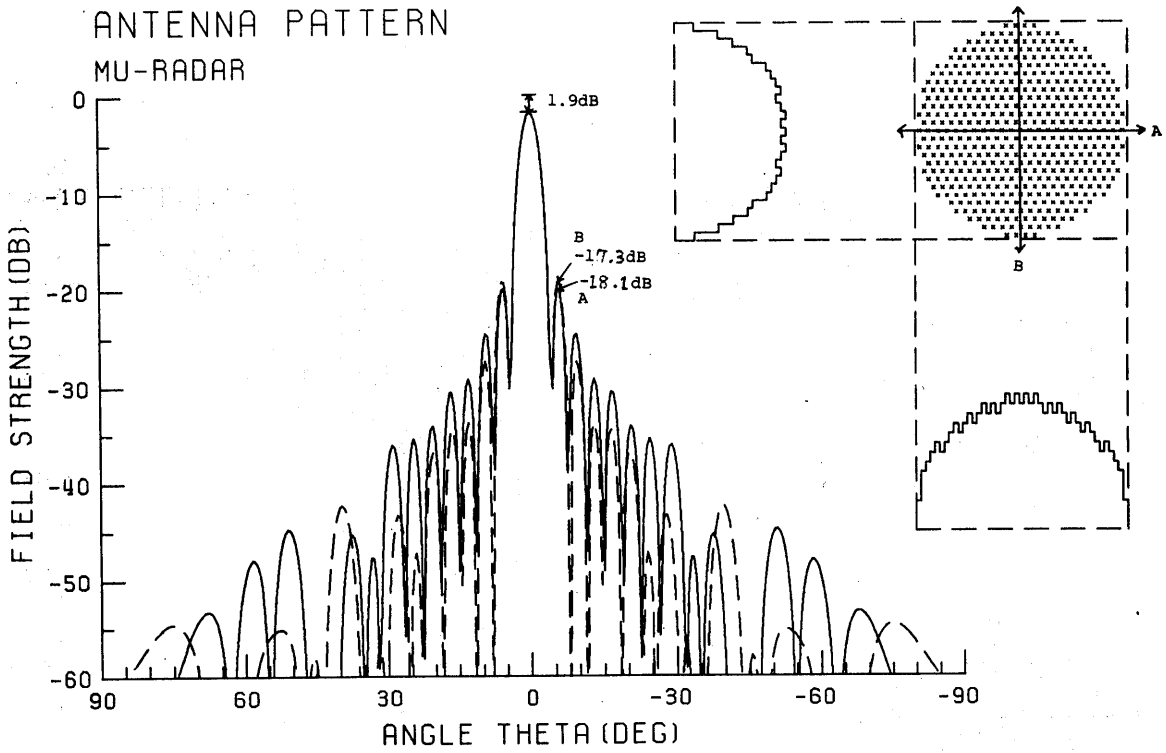

Fig.6-8 Arrangement of array elements (right) and computed radiation patterns of the improved array.

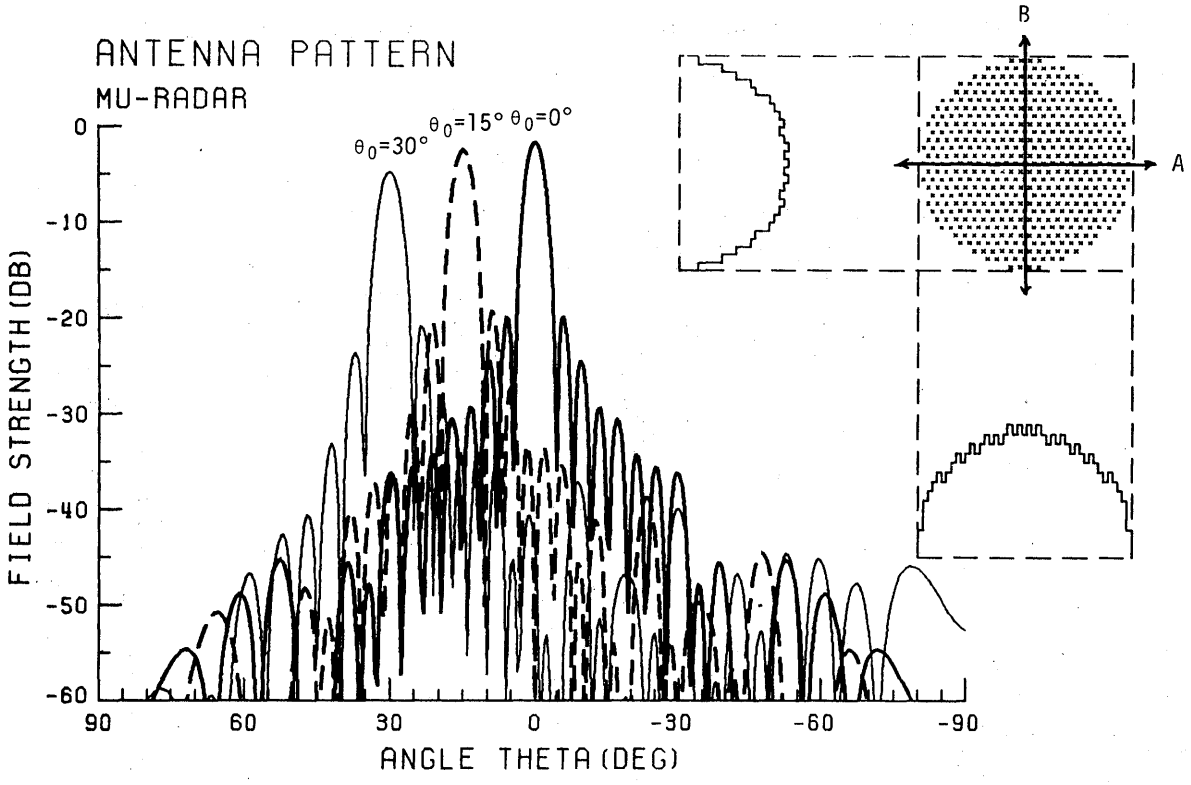

Fig.6-9 Same as Fig.6-8, but for tilted antenna beam directions.

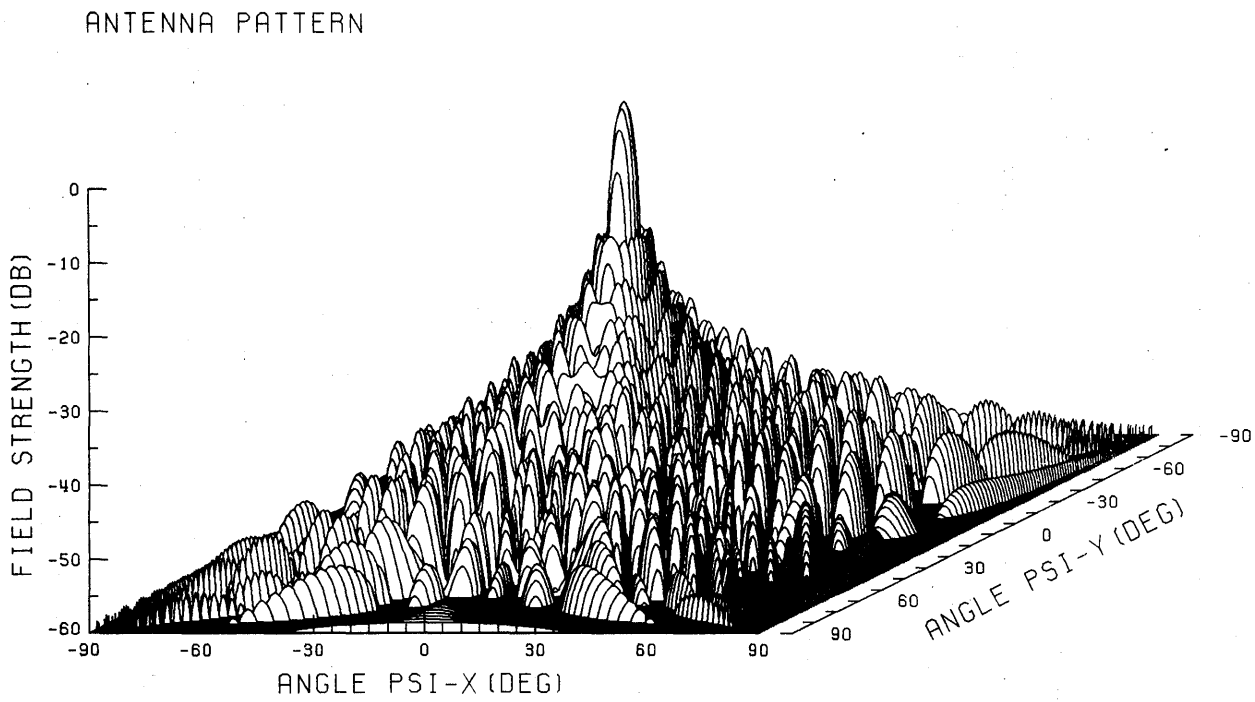

Fig.6-10 Stereographic radiation pattern of the improved MU radar antenna array. The antenna beam is pointed toward zenith.

excited with the same amplitude and desired phase with a perfect accuracy. However, the actual positioning of elements is subject to errors in construction. Also the amplitude and phase of each element may have errors due to fluctuations in individual transmitters. It is thus important to examine the effect of these errors on the antenna pattern and determine the tolerance for these errors.

First, consider the effect of these errors on a linear array of N isotropic elements for simplicity (e.g., Steinberg, 1975). The normalized radiation pattern in the existence of positional error x_n is given as

$$F(\theta) = \frac{1}{N}\sum_{n=1}^{N} W_n \exp(j\psi_n)\exp(j\Delta\psi_n) \tag{6.8}$$

where

$$\psi_n = kx_n\sin\theta, \quad \Delta\psi_n = k\Delta x_n\sin\theta$$

and W_n is the weight of each element excitation. When the error is sufficiently small, deviation of the radiation pattern due to the error is expressed as

$$D(\theta) \equiv F(\theta) - F_o(\theta) \simeq \frac{j}{N}\sum_{n=1}^{N} W_n \exp(j\psi_n)\cdot\Delta\psi_n \tag{6.9}$$

where $F_o(\theta)$ is the pattern with no error. If we assume Δx_n to be a random variable with zero mean and the standard deviation σ, the r.m.s. value of $D(\theta)$ is obtained as

$$\begin{aligned} D_{rms}^2(\theta) &= \frac{1}{N^2}\sum_{m=1}^{N}\sum_{n=1}^{N} W_m W_n \langle\Delta\psi_m\Delta\psi_n\rangle \exp\{j(\psi_m-\psi_n)\} \\ &= \Big(\sum_{n=1}^{N} W_n^2/N^2\Big)k^2\sigma^2\sin^2\theta \end{aligned} \tag{6.10}$$

For the case of uniform excitation, Eq.(6.10) reduces to

$$D_{rms}(\theta) = N^{-1/2} k\sigma \sin\theta \tag{6.11}$$

Note that for the mainlobe,

$$D(0) = \frac{j}{N} \sum_{n=1}^{N} \Delta\psi_n = 0 \tag{6.12}$$

which means that the mainlobe is not affected by small random errors. For a sidelobe of level S_o, the expected level in the presence of such error is

$$S = S_o + N^{-1/2} k\sigma \sin\theta \tag{6.13}$$

Fig.6-11 displays it for $N = 475$ and $\theta = 90^\circ$. Note that these sidelobe levels do not contain the element factor, so that further suppression can be expected if the antenna element has low sidelobe levels.

Eq.(6.8) shows that the effect of phase error is equivalent to that of the position error simply by regarding $\Delta\psi_n$ as the phase error. The amplitude error can be treated by the same manner by replacing W_n in Eq.(6.8) by $W_{no}(1 + \Delta\psi_n)$. The r.m.s. position error of 10 cm is equivalent to 5.8° of phase error and 0.83 dB of amplitude error. Fig.6-12 shows the result of a numerical simulation with random position errors. Sidelobe levels shown in this figure agree well with those expected from Fig.6-10 combined with the element pattern shown in Fig.6-5. They suggest that the tolerance for the random position error is about 30 cm r.m.s. according to the basis of 40 dB sidelobe suppression. It corresponds to the tolerance for the phase error of about 17° and the amplitude error of about 2 dB. If all of these errors exist simultaneously, the tolerance for each kind of error decreases. If they are random and independent from each other, which seems to be a fair assumption, the r.m.s. tolerance for position, phase, and

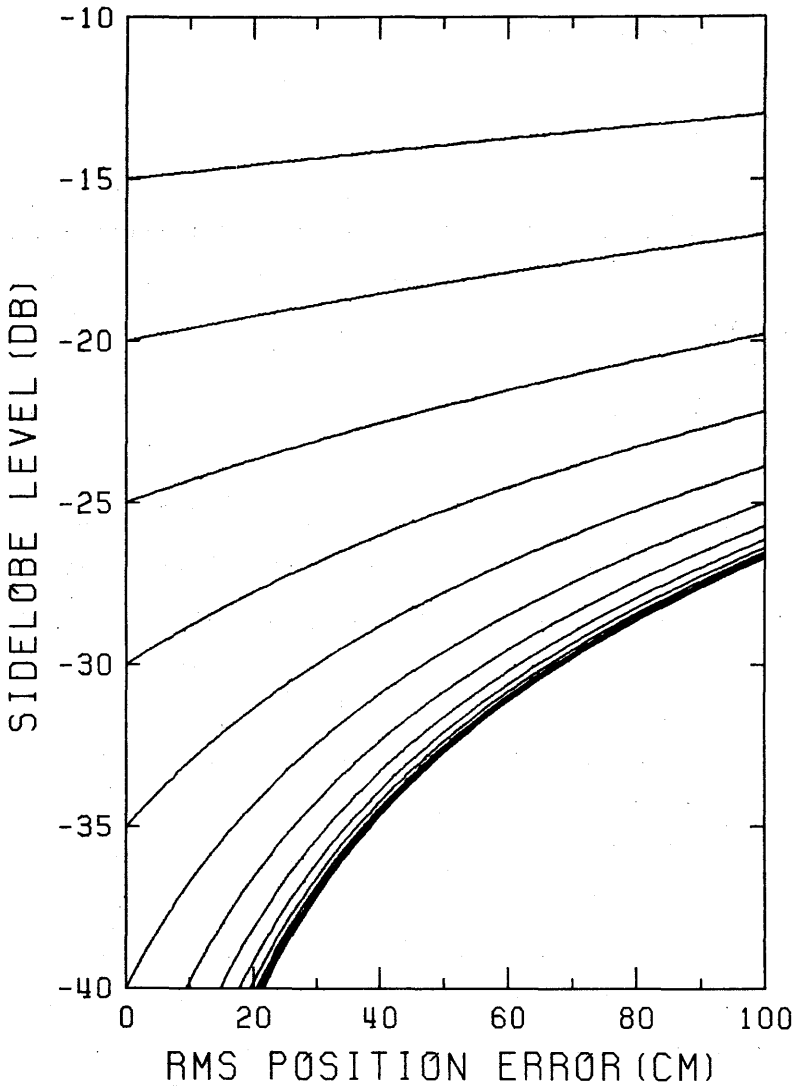

Fig.6-11 Effect of random position errors on sidelobe levels of the array factor. The abscissa is r.m.s. position error in centimeters. Lines are drawn at 5 dB intervals of sidelobe level of the error-free pattern.

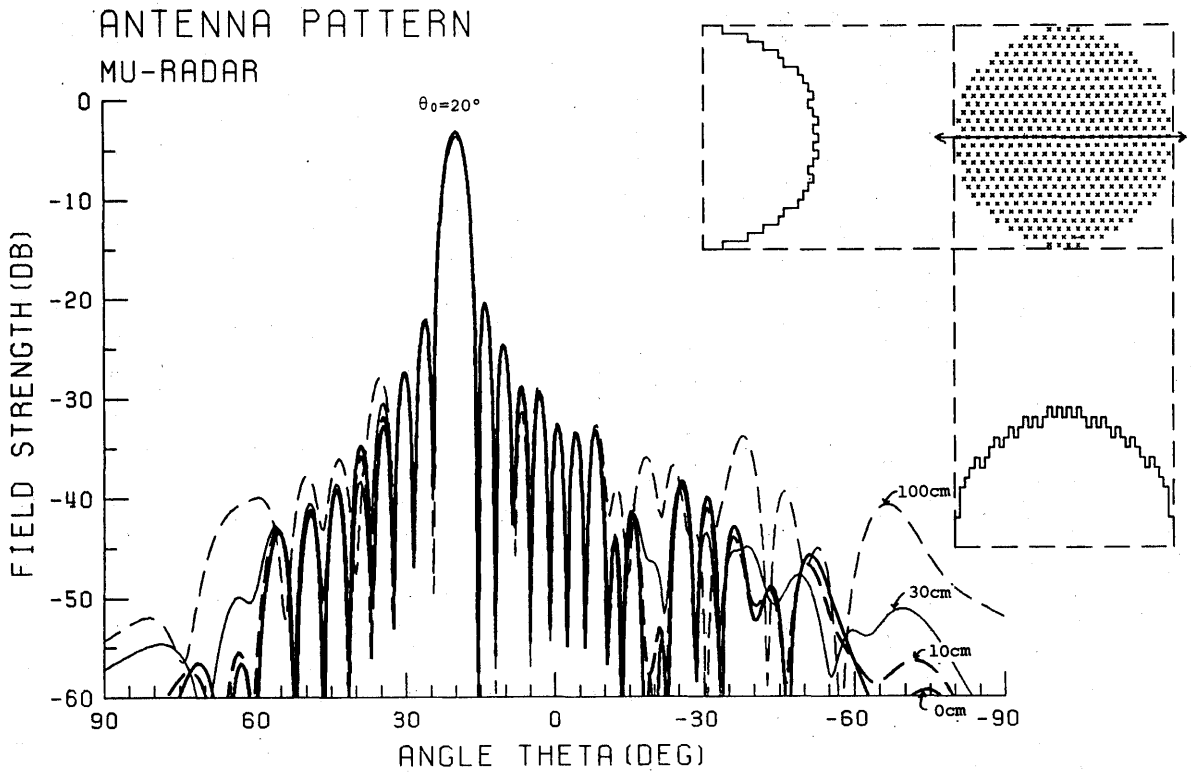

Fig.6-12 Effect of random position errors on the radiation patterns for r.m.s. error of 0, 10, 30, and 100 cm. The antenna beam is tilted 20° from zenith.

amplitude errors are about 17 cm, 10°, and 1.3 dB, respectively.

6.3 EFFECTS OF THE MUTUAL COUPLING ON ANTENNA ELEMENT PROPERTIES

In the previous section, discussion was focused on the antenna array design, and a simple empirical pattern was used for the array element in computations. Fairly abundant knowledges and data have been accumulated on the design of Yagi antenna because of its wide commercial use. However, its radiation pattern as well as the input impedance is modified by the mutual coupling effect between elements when it is used in a large array. Accurate treatment of the mutual coupling effect is a difficult task even for a small array of a few tens of dipoles (e.g., King et al., 1968).

Here we consider a simplified situation of infinite array of crossed Yagi antennas on a perfectly conducting ground plane. Radiation impedance and element pattern have been investigated for an infinite array of dipoles (Stark, 1966), crossed dipoles (Shibagaki and Tokumaru, 1979), Yagi antennas (Tokumaru and Tagura, 1980), and crossed Yagi antennas (Hojo et al., 1981). In these treatments, all elements are assumed to have equal current distribution. The current distribution is expanded into spatial Fourier series, and Maxwell's equation is solved for each component to give the relation between the current and the electric field. The self and mutual impedances of subelements can then be evaluated according to the induced electro-motive force (EMF) method. The active impedance of the element and the radiation pattern is obtained in turn from the impedance matrix.

However, the EMF method often shows an error of a few tens of percents in the antenna impedance because of its simple assumption that the current distribution along elements is represented by single sinusoid. In order to obtain more accurate values, a

modified method called the improved circuit theory (ICT; Inagaki, 1969) is often used in designing Yagi antennas. In ICT, the current distribution is expressed by a linear combination of two or more functions in contrast to a sinusoid in the EMF method. It was shown that a combination of two functions gives an antenna impedance and a current distribution which agree with those obtained by experiments with an error of about 5 % or less (Inagaki, 1969). We apply the ICT here to the case of an infinite array.

The current is assumed to flow in a sheet of width d uniformly in lateral direction, and approximated by a linear combination of following two functions. For a crossed Yagi antenna of N subelements, they are given as

$$K_{\ell}^{p1} = \frac{I_{\ell}^{p1}}{d} \cdot \frac{\sin\{k(r_{\ell}-|p|)\}}{\sin(kr_{\ell})}$$

$$K_{\ell}^{p2} = \frac{I_{\ell}^{p2}}{d} \cdot \frac{1-\cos\{k(r_{\ell}-|p|)\}}{1-\cos(kr_{\ell})} \qquad (p = x,y;\ \ell = 1,\cdots,N) \tag{6.14}$$

where I_{ℓ} is the current at the center of each subelement of length $2r_{\ell}$, the first superscript p indicates the direction of subelement alignment, and the second superscript (1 or 2) distinguishes the two current distributions.

These current distributions mean that the shape of subelements is assumed to be an infinitely thin strip. Although such a shape is not realistic, it is known that the effect of cross sectional shape of the antenna subelement is represented by its effective radius alone (Uda and Mushiake, 1954). Thus a thin strip of width d is equivalent to a cylinder of radius d/4.48, which is the effective radius of the strip. Eq.(6.14) is expanded into spatial Fourier components for the triangular element arrangement shown in Fig.6-4 as follows (see Appendix):

$$K^{x1}_{\ell mn} = \frac{I^{x1}_{\ell}}{ab} \cdot \frac{\sin(h_{mn}d/2)}{h_{mn}d/2} \cdot \frac{2k}{\sin(kr_{\ell})} \cdot \frac{\cos(\beta_m r_{\ell})-\cos(kr_{\ell})}{k^2-\beta_m^2} \qquad (6.15)$$

$$K^{x2}_{\ell mn} = \frac{I^{x2}_{\ell}}{ab} \cdot \frac{\sin(h_{mn}d/2)}{h_{mn}d/2} \cdot \frac{2}{1-\cos(kr_{\ell})} \cdot$$

$$\cdot\left\{\frac{\beta_m \sin(\beta_m r_{\ell})-k\sin(kr_{\ell})}{k^2-\beta_m^2} + \frac{\sin(\beta_m r_{\ell})}{\beta_m}\right\}$$

$$(\ell = 1,\cdots,N;\ m,n = \{-\infty, \infty\})$$

where β_m and h_{mn} are wavenumbers in x and y directions, respectively, and given by

$$\beta_m = k\cos\theta_x + 2\pi m/a$$
$$h_{mn} = k\cos\theta_y + 2\pi n/b - 2\pi mc/ab$$

Only the expansions for the x-aligned elements are shown in the above. The expressions for y-aligned elements are obtained by interchanging x and y, and h_{mn} and β_m in Eq.(6.15), and also in the following equations.

From Maxwell's equation for the spatial Fourier components, and from the boundary conditions on subelements, Fourier components of the electric fields are obtained (Stark, 1966). Again for the x-aligned elements,

$$E^{xi}_{x\ell mn} = \frac{1}{2}\eta_o \frac{\beta_m^2-k^2}{k\gamma_{mn}} K^{xi}_{\ell mn}$$

$$E^{xi}_{y\ell mn} = \frac{1}{2}\eta_o \frac{\beta_m h_{mn}}{k\gamma_{mn}} K^{xi}_{\ell mn} \qquad (i = 1,2) \qquad (6.16)$$

where η_o is the characteristic impedance of free space (=376.73 Ω),

the first subscript denotes the direction of the electric field, and

$$\gamma_{mn} = (k^2-\beta_m{}^2-h_{mn}{}^2)^{1/2}$$

The mutual impedance between current distributions i and j (i,j = 1,2) on subelements s and t (s,t = 1,...,N), respectively, is given by

$$Z_{st}^{pqij} = \frac{2}{I_s^{pi*} I_t^{qj}} \iint_A \frac{\vec{K}_s^{pi*} \cdot \vec{E}_t^{qj}}{2} \, dxdy \qquad (p,q = x,y;\ i,j = 1,2) \tag{6.17}$$

where A denotes the unit cell that an element occupies, and the asterisk indicates the complex conjugate. By substituting Eq.(6.16) into Eq.(6.17) and using the fact that only products of terms having the same wavenumber contribute to the integral, we obtain

$$\begin{aligned} Z_{st}^{xxij} &= -\frac{ab}{2}\eta_o \sum_{m=-\infty}^{\infty}\sum_{n=-\infty}^{\infty} \frac{\beta_m{}^2-k^2}{k\gamma_{mn}} \cdot \frac{K_{smn}^{xi*} K_{tmn}^{xj}}{I_s^{xi*} I_t^{xj}} \\ &\quad \cdot\{\exp(-j\gamma_{mn}|t_s-t_t|)-\exp(-j\gamma_{mn}|t_s+t_t|)\} \\ Z_{st}^{xyij} &= -\frac{ab}{2}\eta_o \sum_{m=-\infty}^{\infty}\sum_{n=-\infty}^{\infty} \frac{\beta_m\, h_{mn}}{k\gamma_{mn}} \cdot \frac{K_{smn}^{xi*} K_{tmn}^{yj}}{I_s^{xi*} I_t^{yj}} \\ &\quad \cdot\{\exp(-j\gamma_{mn}|t_s-t_t|)-\exp(-j\gamma_{mn}|t_s+t_t|)\} \end{aligned} \tag{6.18}$$

where t_ℓ (ℓ = 1,...,N) is the height of subelements. Currents on each subelement can be obtained by solving the simultaneous equations

$$\begin{aligned} &\overleftrightarrow{Z} \cdot \vec{I} = \vec{V} \\ &\vec{V} = \vec{V}_o - Z_g \vec{I} \end{aligned} \tag{6.19}$$

where $\overleftrightarrow{Z}$ is the 4N × 4N impedance matrix, $\vec{I}$ and $\vec{V}$ are 4N-element current and voltage vectors, $\vec{V}_o$ and Z_g (= 50 Ω) are the given voltage vector and impedance of the power supply seen from the

antenna input terminal, respectively. The factor 4 accounts for the crossed elements and the two current distributions. The actual current on each element is obtained by adding two terms for the two current distributions. The input impedance is given by the ratio of voltage and the current at the feed point of the element. The input impedance obtained here is referred to as the active impedance because it is measured in the presence of all other elements excited by the identical power supply.

From the current distributions, the element pattern can be computed as

$$\begin{aligned} F_{Ex}(\theta) &= 2j \sum_{i=1}^{2} \sum_{\ell=1}^{N} f_{\ell}^{i}(\theta_x) I_{\ell}^{xi} \sin(kt_{\ell}\cos\theta) \\ F_{Ey}(\theta) &= 2j \sum_{i=1}^{2} \sum_{\ell=1}^{N} f_{\ell}^{i}(\theta_y) I_{\ell}^{yi} \sin(kt_{\ell}\cos\theta) \end{aligned} \tag{6.20}$$

where $f_{\ell}^{i}(\theta)$ denotes the contribution of each current distribution to the radiation pattern of each subelement, and given by

$$\begin{aligned} f_{\ell}^{1}(\theta_p) &= \frac{j\eta_o}{2\pi} \cdot \frac{\cos(kr_{\ell}\cos\theta_p) - \cos(kr_{\ell})}{\sin(kr_{\ell})\sin\theta_p} \\ f_{\ell}^{2}(\theta_p) &= \frac{j\eta_o}{2\pi} \cdot \frac{\sin(kr_{\ell}\cos\theta_p) - \cos\theta_p \sin(kr_{\ell})}{\{1-\cos(kr_{\ell})\}\sin\theta_p \cos\theta_p} \qquad (p = x,y) \end{aligned} \tag{6.21}$$

Fig.6-14 shows an example of computed active impedance and radiation pattern versus zenith angle for an array of 4-subelement Yagi antennas shown in Fig.6-13. The radiator of the Yagi antenna is folded in order to cancel the unbalanced current on the radiator. This folding also works as an impedance transformer, and the input impedance of the antenna becomes 4 times that of an antenna without folding (Mushiake, 1954). It is assumed throughout this chapter that another impedance transformer which reduces the input impedance to 1/4 is inserted between the antenna and feed line. The effect of

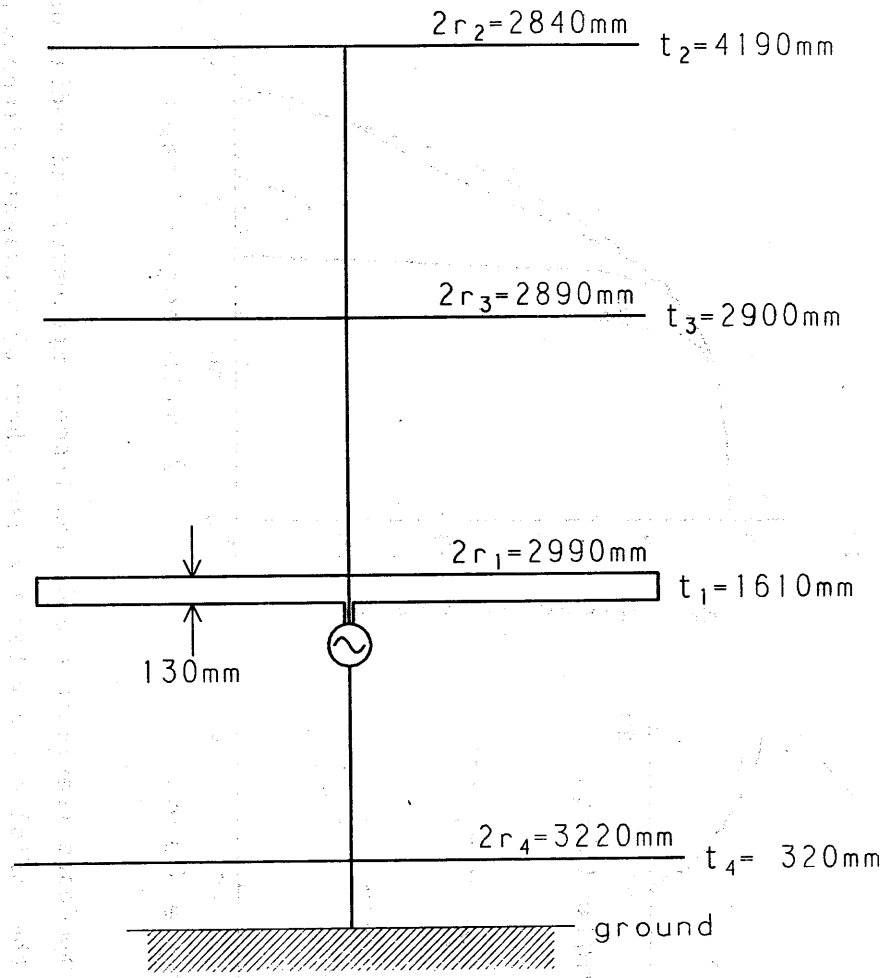

Fig.6-13 Dimensions of the 4-subelement Yagi antenna used as the example in the computations of Section 6.3. r_ℓ and t_ℓ (ℓ = 1,2,3,4) are the half-length and height of each subelement, respectively.

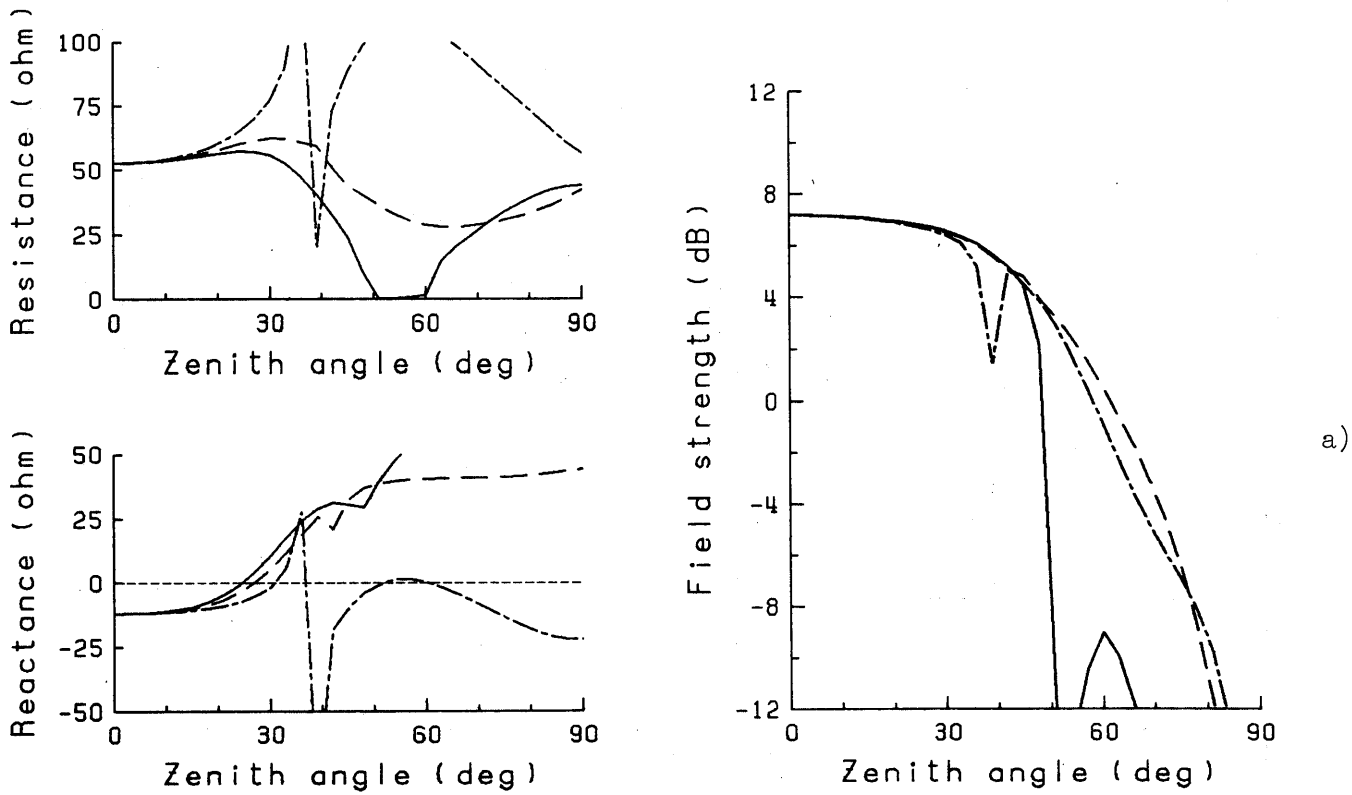

Fig.6-14 Computed active impedance (resistance and reactance components) and radiation pattern of the 4-subelement Yagi in the infinite array for the case where a) x-aligned elements and b) y-aligned elements are excited. Solid and dashed curves, and chain are for the directions of $\phi = 0^\circ$ (x-z plane), 45°, and 90° (y-z plane), respectively. The field strength is normalized to the radiation field of an isotropic antenna matched to the feed line.

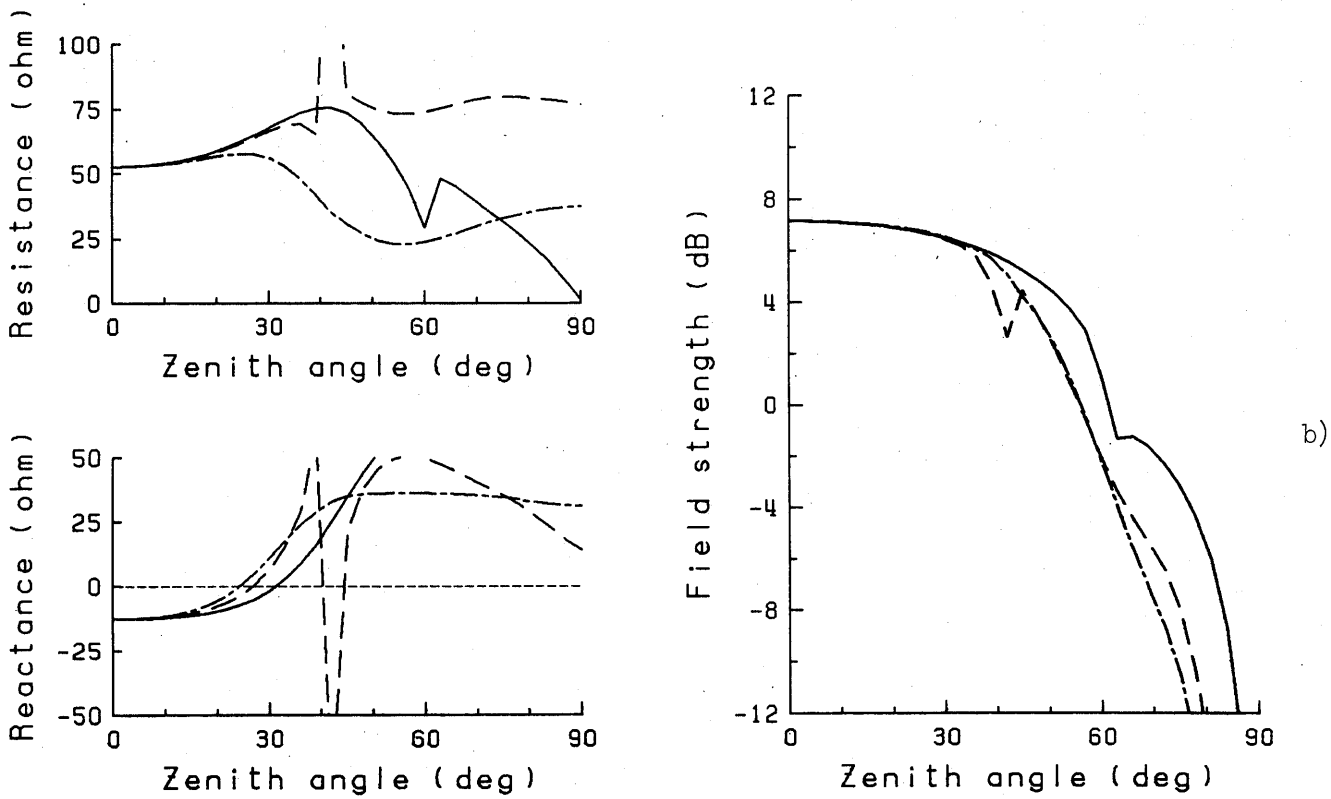

Fig.6-14 (continued)

folding is taken into account by using the geometrical mean distance of the cross section of the folded subelement as its effective radius.

Fig.6-14 a) is for the case that x-aligned elements are excited, and b) is for y-aligned-element excitation. The elements aligned to the other direction are assumed to be terminated by the feed line impedance of 50 Ω. The case of exciting both elements can be thought as the superposition of these two cases. Solid and dashed curves, and chain in Fig.6-14 denote the impedance and patterns for $\phi = 0^\circ$ (x-z plane), 45°, and 90° (y-z plane), respectively. The radiation pattern is normalized to the radiation field of an isotropic antenna matched to the feed line impedance. Fig.6-15 shows the radiation pattern of the same Yagi antenna in an isolated situation computed by the ICT. The input impedance is 60.8 + j17.0 Ω. The steep decay of the radiation pattern toward 90° zenith angle is mainly due to the presence of the mirror image by the conducting ground plane.

Comparison of Fig.6-14 and 6-15 shows the effect of the mutual coupling clearly. First, element gain reduced from 10.70 dB to 7.18 dB by the mutual coupling effect. It demonstrates that the effective areas of the adjascent elements have overlapping regions, and are limited by the physical area of the element unit cell, which corresponds to a gain of 7.24 dB. The slight difference between the theoretical upper limit and the computed gain is probably due to mismatching of the element with the feed line. The mutual coupling effect on active impedance appears mainly as the decrease of the reactance component of about 30 Ω.

Second, sudden change of the active impedance and associated sharp dip exist in the array element characteristics. Especially those at about 40° and 60° zenith angles correspond to the appearance of grating lobes, which change the matching condition of the element drastically.

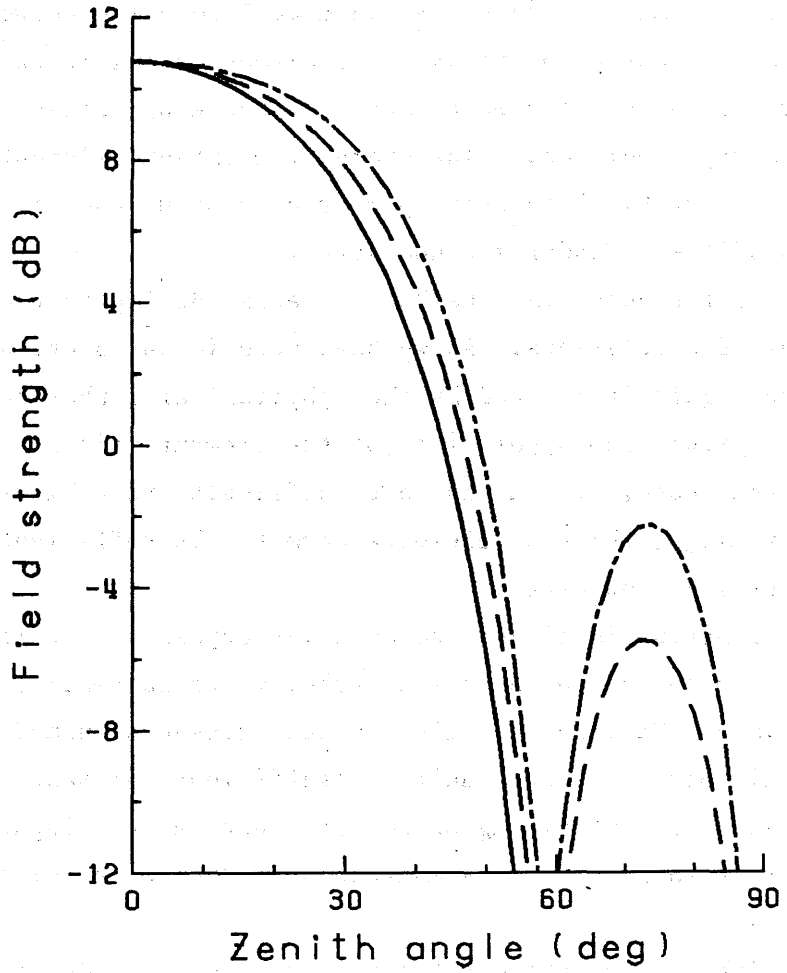

Fig.6-15 Computed radiation pattern of the isolated Yagi antenna used as the array element in Fig.6-14. Solid and dashed curves, and chain are for the directions of ϕ = 0° (x-z plane), 45°, and 90° (y-z plane), respectively.

6.4 ANTENNA ELEMENT DESIGN

We have examined effects of the mutual coupling between antenna elements on element properties. The element gain, input impedance, and the radiation pattern were found to change appreciably under the infinite array condition. Therefore, the antenna element should be designed to exhibit its best performance when used in the actual condition of the MU radar antenna array.

The first problem in the Yagi antenna design is the choice of the number of subelements. As we have seen in the previous section, the element gain is limited by the physical area that each element occupies. Since the upper limit of the element gain is 7.24 dB for the present case, which is not difficult to achieve with a 3-subelement Yagi, three subelements seem to be sufficient as far as the element gain concerns.

From constructional and economical viewpoints, it is of course desirable to choose the number of subelements as small as possible. Two-subelement Yagi and single dipole, however, turned out to be impractical because of their insufficient element gain and difficulties in controlling parameters such as the input impedance and the front-to-back ratio simultaneously due to the smaller number of freedom.

The high front-to-back ratio is required in order to avoid the effect of the variation in the reflectivity of the ground plane. It is costly to maintain a reflecting wire mesh as that used at Jicamarca, because the high humidity in Japan brings a serious problem of corrosion.

Therefore, the practical choice depends on whether a 3-subelement Yagi with sufficient performances can be found or not. If not, then we have to employ more costly Yagi's with a larger number of subelements.

In designing a 3-subelement Yagi antenna, parameters to be

determined are the length of 3 subelements, spacings between subelements, and their diameters. Since the diameters do not affect the element properties largely if they are not too small, we fix the diameters of all subelements to 2.17 cm, to which a commercial steel pipe is available.

In order to satisfy the requirements for high gain and high front-to-back ratio, we look for the element which shows the highest gain in the absence of the ground plane in an infinite array. It was found by experience that the properties of an element optimized in the presence of the ground plane is affected largely by the variation in the reflectivity of the ground. Since the amount of energy available from the power supply is kept constant in the computation, radiations to undesired directions and the reflection at the feed point become very small when the maximum gain is obtained as shown later.

The procedure for finding the optimum element dimensions consists of two steps: 1) Compute element gain in the infinite array using the ICT, changing the length and spacings of subelements at a given increment, and find out the combination which gives the highest gain. 2) Optimize the length and spacings using a gradient search method around the values obtained in the first step.

In the first step, the increment of parameters should be chosen small enough so that any maximum or minimum of the gain is not missed. We can use empirical knowledges on Yagi antennas such as that the length of radiator should be equal or shorter than the half-wavelength, and that the length of director and reflector should be shorter and longer than that of the radiator, respectively. The sizes examined are: 0.44-0.50 λ at 0.02 λ interval for the length of radiator r_1, 0.80-0.95 r_1 at 0.05 r_1 interval for the length of director r_2, 1.05-1.20 r_1 at 0.05 r_1 interval for the length of reflector r_3, and 0.14-0.22 λ at 0.02 λ interval for the spacings between subelements. These values give 1600 combinations of 3-subelement Yagi's.

The procedure used in the second step is the one known as the Newton-Raphson method (e.g., Bard, 1974). The optimization problem is reduced to a problem of maximizing the objective function $f(\vec{P})$. $\vec{P}$ is the parameter vector which contains length and spacing of each subelement as variables.

The necessary condition for $f(\vec{P})$ to take a maximum is given by

$$g_i(\vec{P}) \equiv \frac{\partial f}{\partial P_i} = 0 \qquad (i = 1,2,\cdots,M) \tag{6.22}$$

where M is the number of parameters. If a proper initial guess $\vec{P}_o$ is given for $\vec{P}$, Eq.(6.22) can be approximately expressed in terms of the first order Taylor series expansion as

$$g_i(\vec{P}) \simeq g_i(\vec{P}_o) + \sum_{j=1}^{M} \delta P_j \frac{\partial g_i}{\partial P_j} = 0 \tag{6.23}$$

Eq.(6.23) can be solved for $\delta\vec{P}$ as

$$\delta\vec{P} = -\overleftrightarrow{G}^{-1} \cdot \vec{g}(\vec{P}_o) \tag{6.24}$$

where

$$G_{ij} \equiv \frac{\partial g_i}{\partial P_j} = \frac{\partial^2 f}{\partial P_i \partial P_j}$$

Thus

$$\vec{P} = \vec{P}_o - \overleftrightarrow{G}^{-1} \cdot \vec{g}(\vec{P}_o) \tag{6.25}$$

This procedure is iterated until a sufficiently good value is obtained or $f(\vec{P})$ converges to some value. Note that this procedure may converge to any stationary point, not necessarily to a maximum. In order that a given point is a maximum, G_{ii} $(i = 1,2,...M)$ must be negative. This condition is monitored in each iteration, and different direction is searched by reducing the number of parameters

if it is not satisfied. The best combination obtained in the first step was used as the initial guess of the parameters.

After the procedure converged, a few iterations were appended including the perfectly conducting ground plane in the computation. The modification in the element dimensions by these additional iterations was very small because the properties of the optimized element are hardly affected by the ground plane as we see later. Fig.6-16 illustrates dimensions of the 3-subelement Yagi antenna thus optimized.

Fig.6-17 shows the active impedance and radiation pattern of this Yagi antenna versus zenith angle in the infinite array. The element gain at the zenith direction coincides the theoretical limit of 7.24 dB. It is worth mentioning that the active impedance was automatically adjusted close to 50 Ω, providing an excellent matching to the feed line. The impedance matching is kept well even when the beam direction is tilted by 30° from zenith, and the voltage standing wave ratio (VSWR) is always below 1.3 within this zenith angle range.

The front-to-back ratio in the absence of the ground plane is higher than 30 dB. In consequence, the element gain varies only by about 0.02 dB when the ground plane is removed, and the active impedance by about 2 Ω. These results indicate that the reflector of the Yagi antenna is blocking most of the downward radiated power.

We have so far discussed the element properties at a point frequency. Since the MU radar uses a bandwidth of 1 MHz, the performance of the antenna should be examined over this bandwidth. Fig.6-18 shows the active impedance, VSWR, and the radiation field strength at the zenith direction versus frequency. The solid and dashed lines are for the x-aligned- and y-aligned-element excitations, respectively. As shown in the figure, the frequency response of the element is fairly flat, and VSWR is kept below 1.15 within the bandwidth of 1 MHz.

Fig.6-19 shows the computed radiation pattern of the MU radar

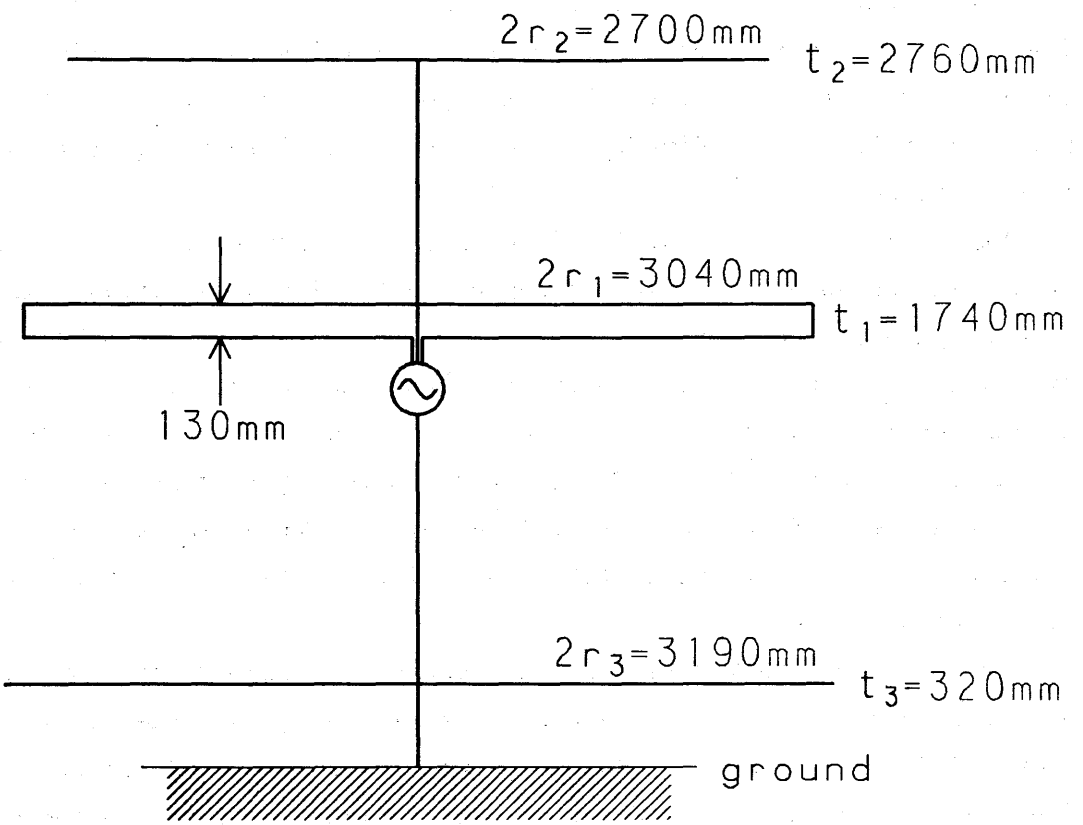

Fig.6-16 Dimensions of the optimized 3-subelement Yagi antenna. r_ℓ and t_ℓ (ℓ = 1,2,3) are the half-length and height of each subelement, respectively.

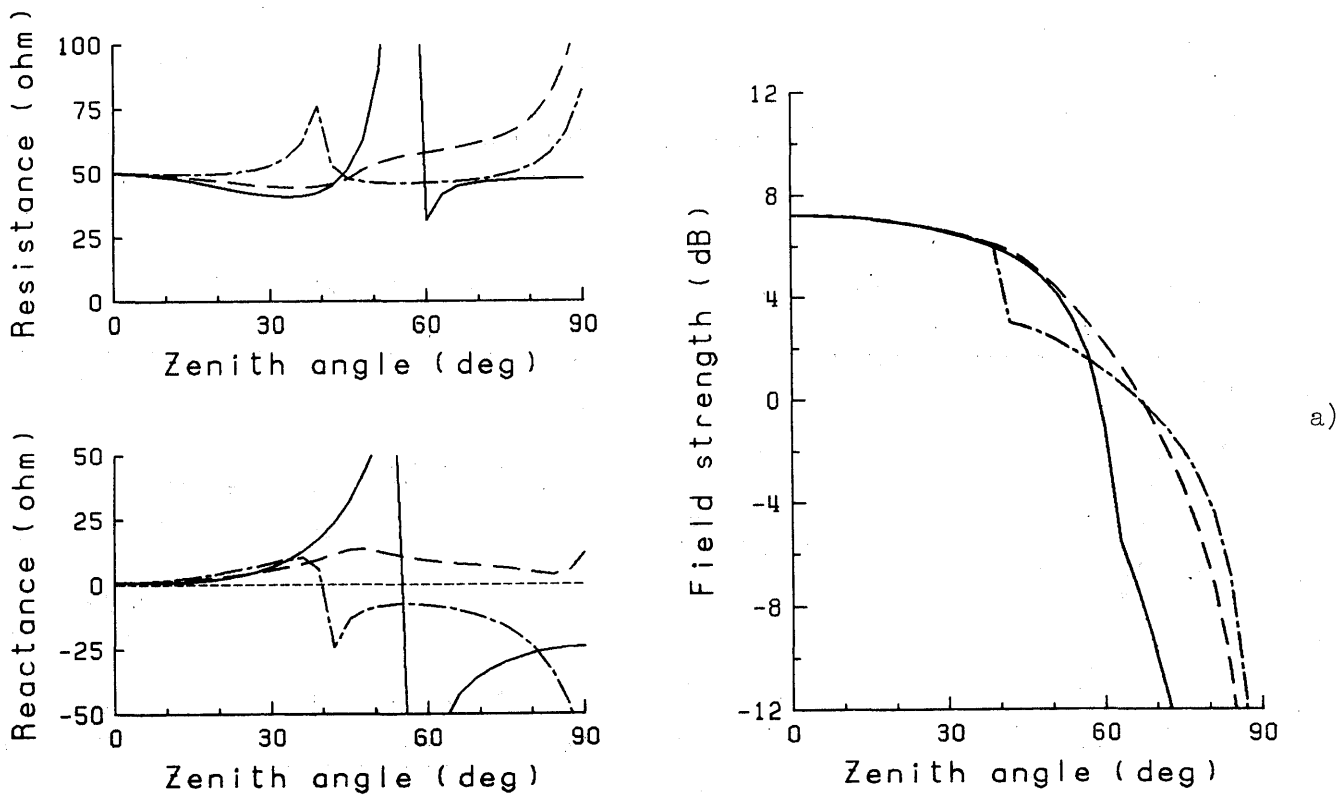

Fig.6-17 Computed active impedance (resistance and reactance components) and radiation pattern of the optimized 3-subelement Yagi in the infinite array for the case where a) x-aligned elements and b) y-aligned elements are excited. Solid and dashed curves, and chain are for the directions of $\phi = 0^\circ$ (x-z plane), 45°, and 90° (y-z plane), respectively.

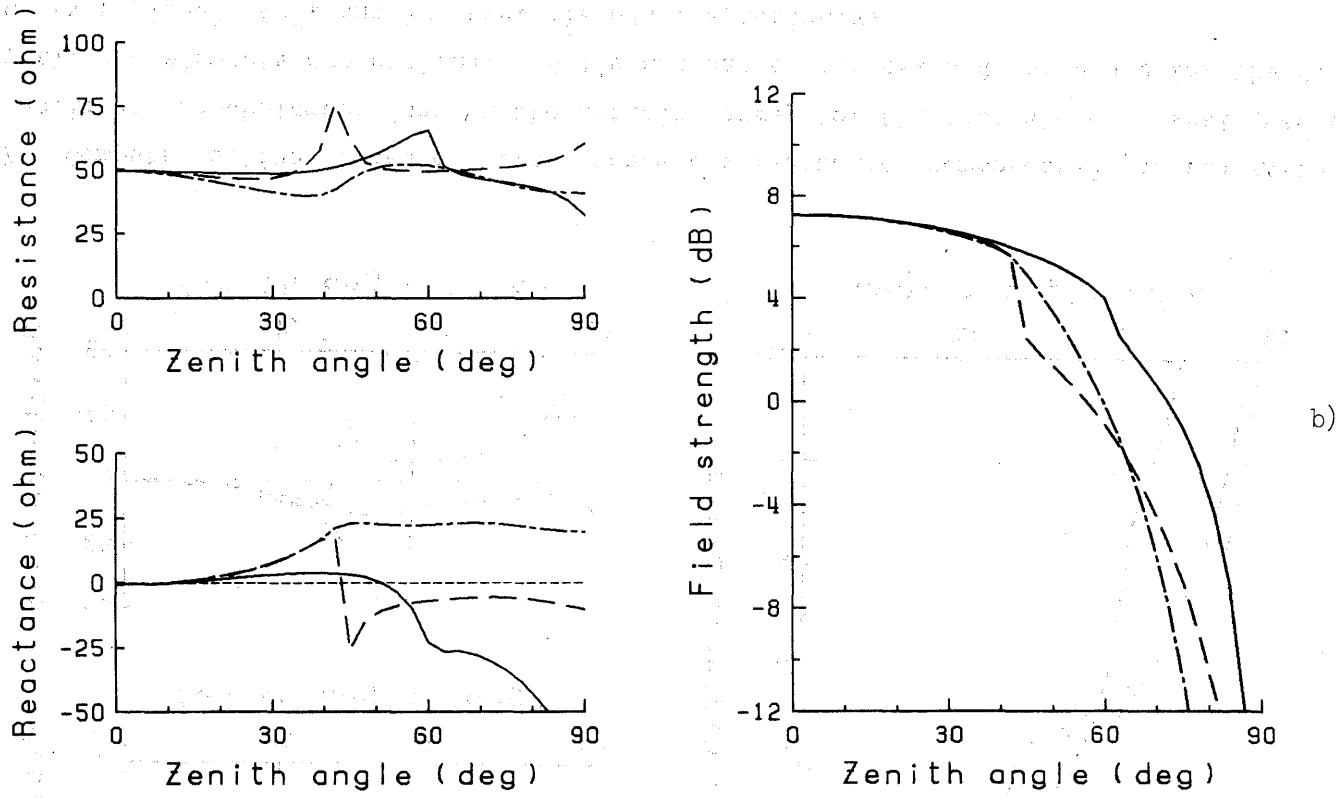

Fig.6-17 (continued)

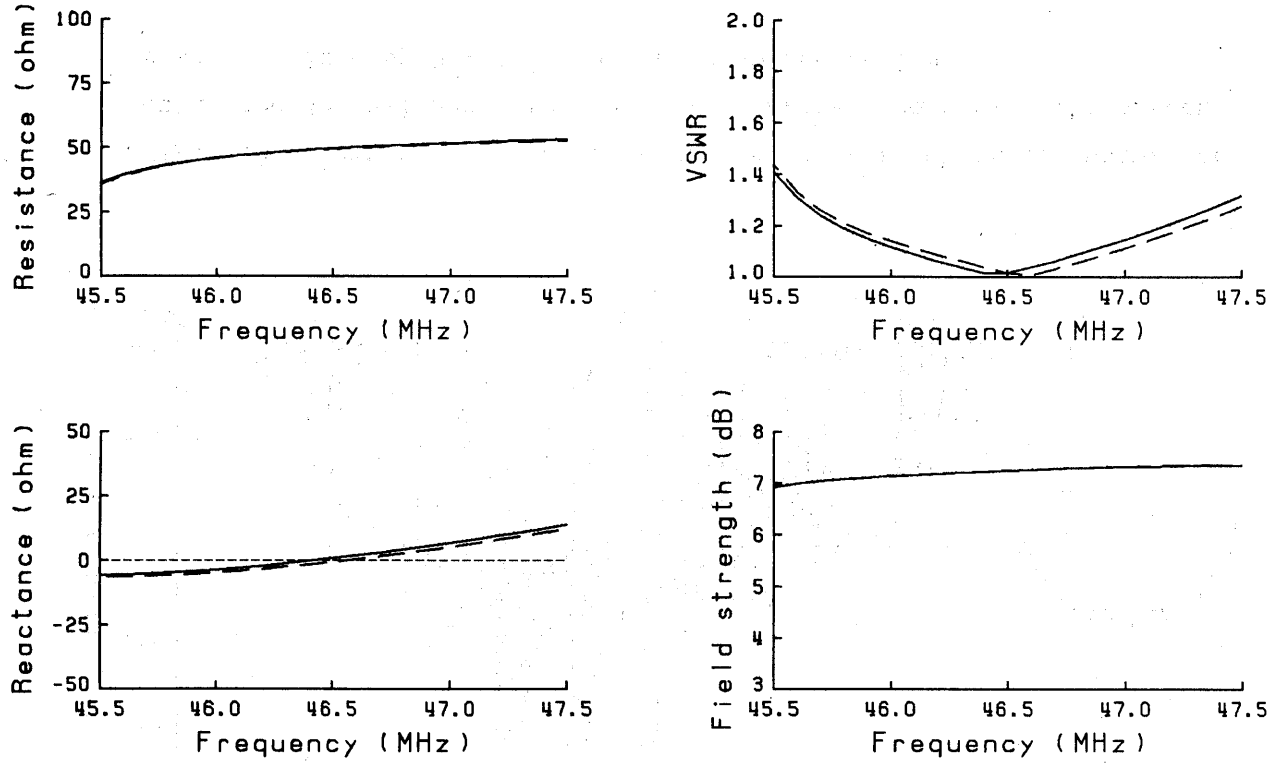

Fig.6-18 Computed active impedance, VSWR, and the radiation field strength of the optimized 3-subelement Yagi in the infinite array versus frequency. The frequency band of the MU radar is 46.0-47.0 MHz. Solid and dashed lines are for the x-aligned and y-aligned elements excitations, respectively.

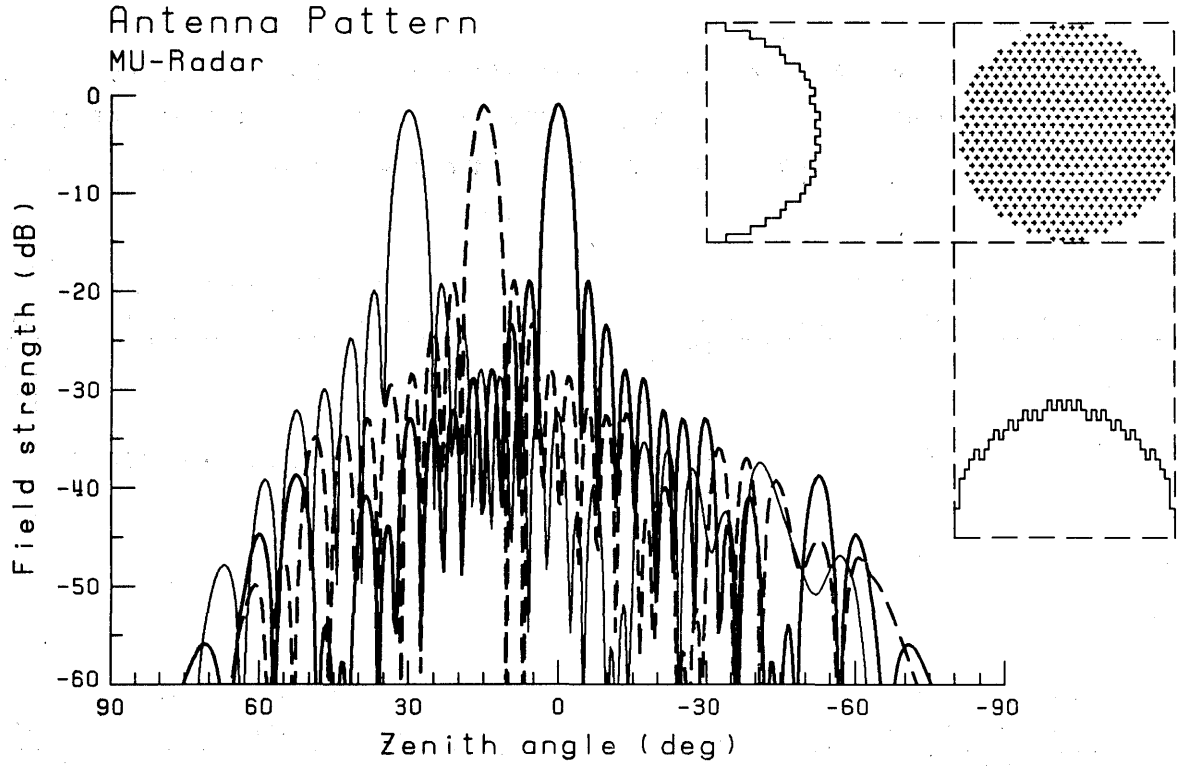

Fig.6-19 Computed radiation patterns of the MU radar using the optimized 3-subelement crossed Yagi as array elements. The antenna beam is tilted by 0°, 15°, and 30° from the zenith.

antenna using the optimized 3-subelement Yagi as array elements, instead of the empirical element pattern used in Figs.6-8 to 12. The main conclusions on the antenna beam steerability and low elevation sidelobe suppression derived from these figures are confirmed by the more realistic computation of Fig.6-19.

6.5 EDGE EFFECT OF THE FINITE ARRAY

In the previous section, the array element design was presented for the infinite array. However, elements near the edge of the real array suffer different mutual coupling effect from those of the elements in an infinite array. The mutual coupling in finite arrays has been extensively studied mainly for dipole antenna arrays (e.g., Oliner and Malech, 1966), and it was found that properties of elements on the edge or the corner of the array often differ largely from those of the center element.

This edge effect is best understood by solving the current distributions on each subelement of 475 crossed Yagi's as unknowns. Unfortunately, however, the amount of computer memory required to perform this computation far exceeds the available amount.

Therefore, we examine here a smaller array of 91 Yagi's arranged hexagonally. We also neglect the mutual coupling between orthogonal elements, which is zero in the E- and H-plane, and much smaller than the mutual coupling between parallel elements in other directions. These simplifications reduce the required computer memory size to about 1/100, or to 1.1 MBytes, which is feasible.

All elements are assumed to be separately excited by equal power through feedlines. The current on each subelement is calculated using ICT by solving the simultaneous equations for the current distributions. Fig.6-20 shows the computed active impedance and the radiation pattern of the optimized 3-subelement Yagi in the infinite array similar to those shown in Fig.6-17, but neglecting the mutual

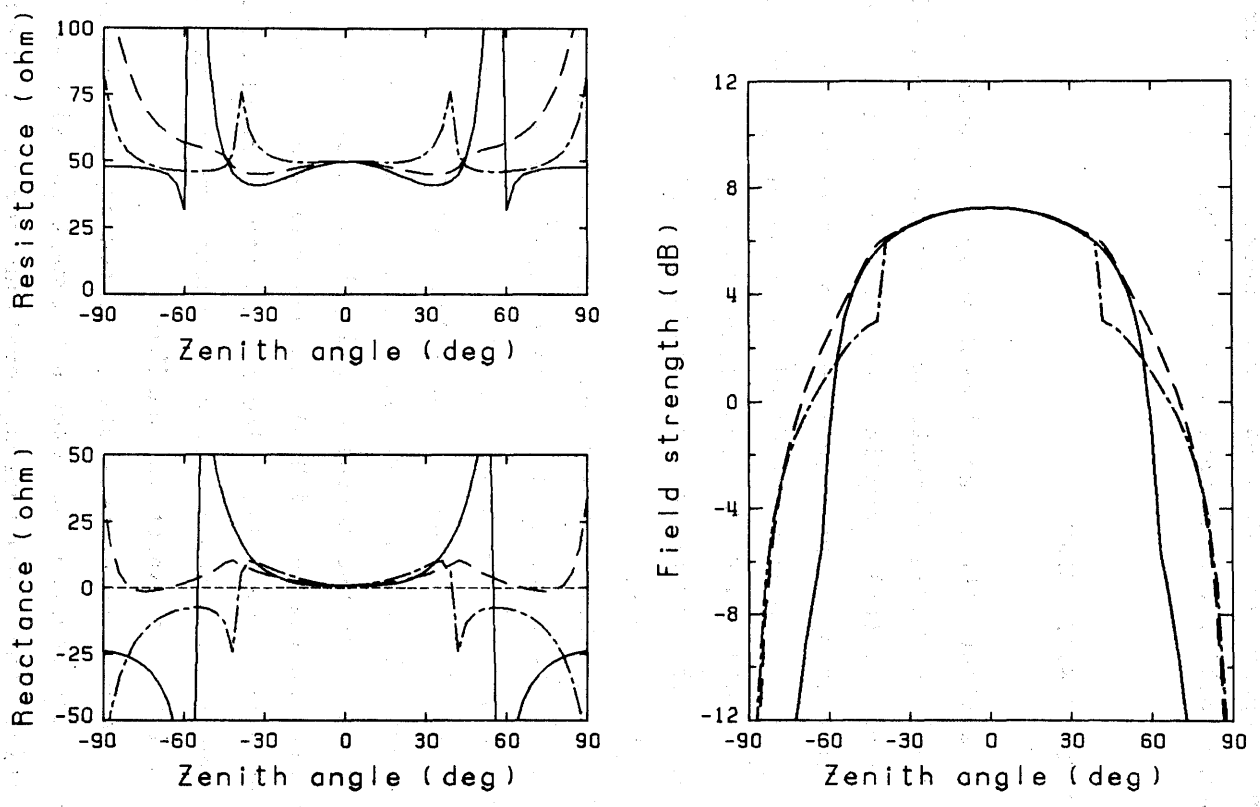

Fig.6-20 Computed active impedance (resistance and reactance components) and radiation pattern of the optimized 3-subelement Yagi in the infinite array for the case where x-aligned elements are excited. The mutual coupling between orthogonal elements is neglected. Solid and dashed curves, and chain are for the directions of ϕ = 0° (x-z plane), 45°, and 90° (y-z plane), respectively.

coupling between orthogonal elements. Zenith angle is varied from -90° to 90° in order to compare with following results where asymmetric patterns appear. Only the case of exciting x-aligned elements is discussed here for simplicity. Comparison of Figs.6-17 and 20 shows that the difference due to neglecting the mutual coupling between orthogonal elements is indeed small.

Fig.6-21 shows the arrangement of the 91 elements. In the followings, the properties of the eight elements encircled in the figure are discussed in order to examine the edge effect of the finite array. Although the choice of these eight elements is arbitrary, tendencies shown below are common to all elements which have the same distance as these elements from the center of the array.

The array element patterns of the eight elements are shown in Fig.6-22. The elements are in the order of approaching from edge to the center of the array with increasing number. The most clear feature in Fig.6-22 is the asymmetric pattern of Element No. 1 and 3. The largest deviation of the field strength of Element No. 1 from that shown in Fig.6-20 within 30° zenith angle amounts to 1.2 dB. This asymmetry is apparently caused by the fact that Element No. 1 and 3 have surrounding elements only on one side of the element. The asymmetry in the radiation pattern decreases rapidly with approaching toward the center of the array. The deviation of the patterns from that of the same element in the infinite array is less than 0.3 dB within 30° zenith angle range for all elements except Element No. 1 and 3.

A quite similar feature can be seen in the active impedance of these elements shown in Fig.6-23. The active impedance of Element No. 1 and 3 show a zenith angle asymmetry of about 10 Ω, while it is less than 5 Ω for other elements. Thus it can be concluded that the edge effect is considerable in the outermost elements, while it is not serious for other elements.

Although the edge effect cannot be neglected for the outermost

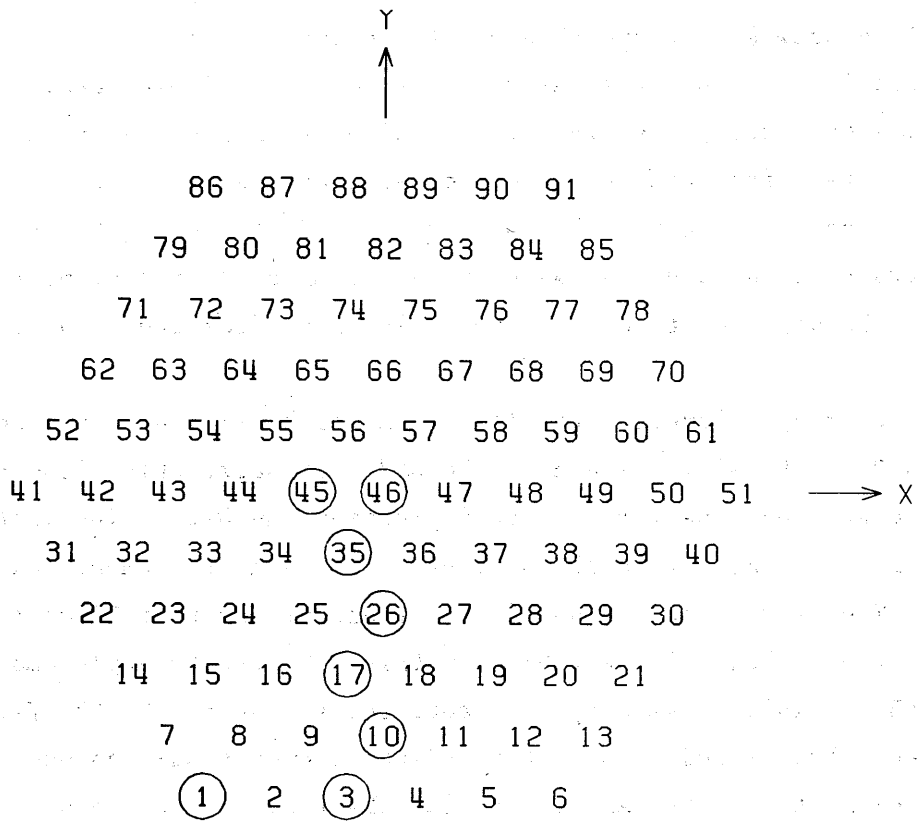

Fig.6-21 Arrangement of the 91 elements. The properties of the eight encircled elements are discussed.

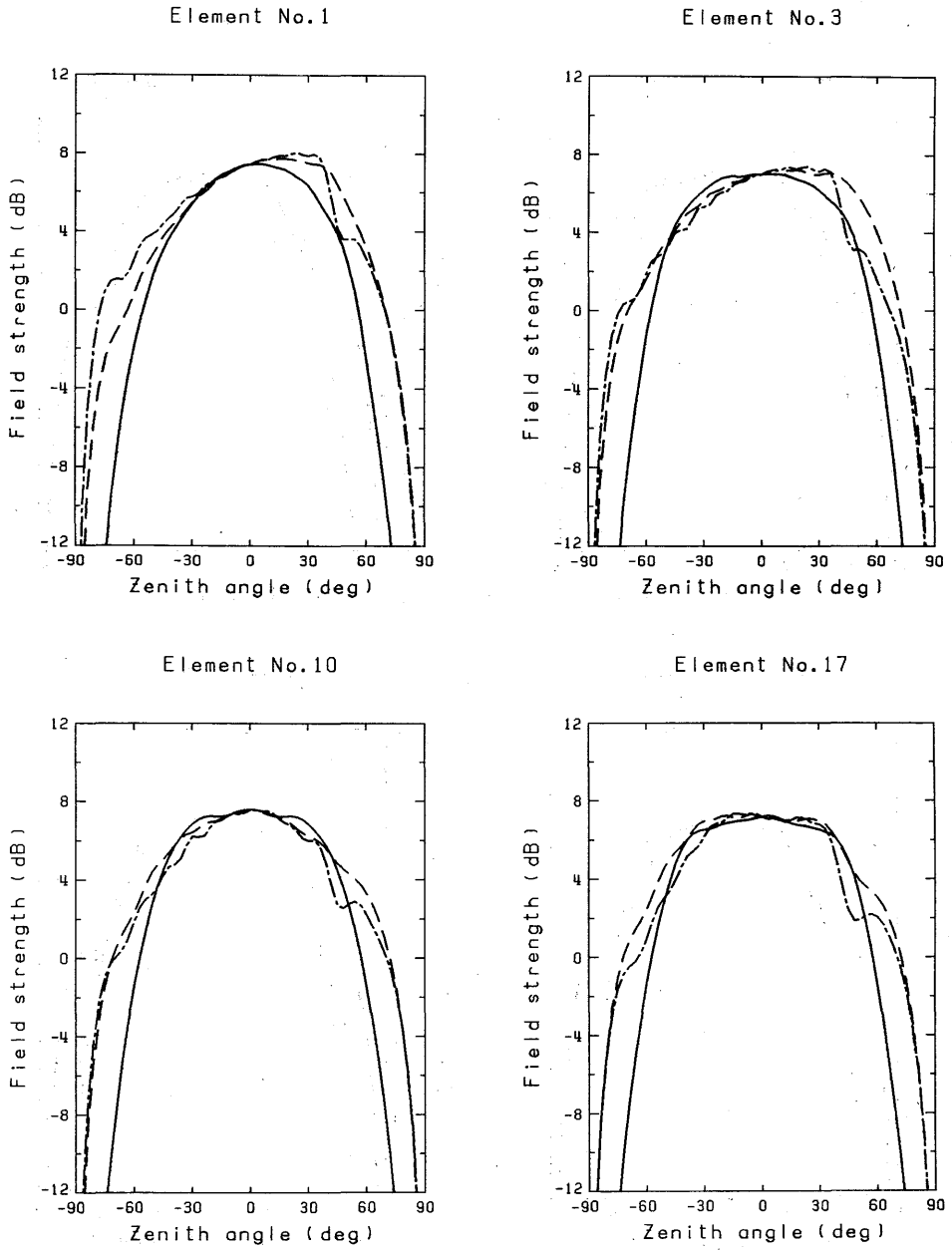

Fig.6-22 Radiation pattern of the eight elements encircled in Fig.6-21. Solid and dashed curves, and chain are for the directions of $\phi = 0^\circ$ (x-z plane), 45°, and 90° (y-z plane), respectively.

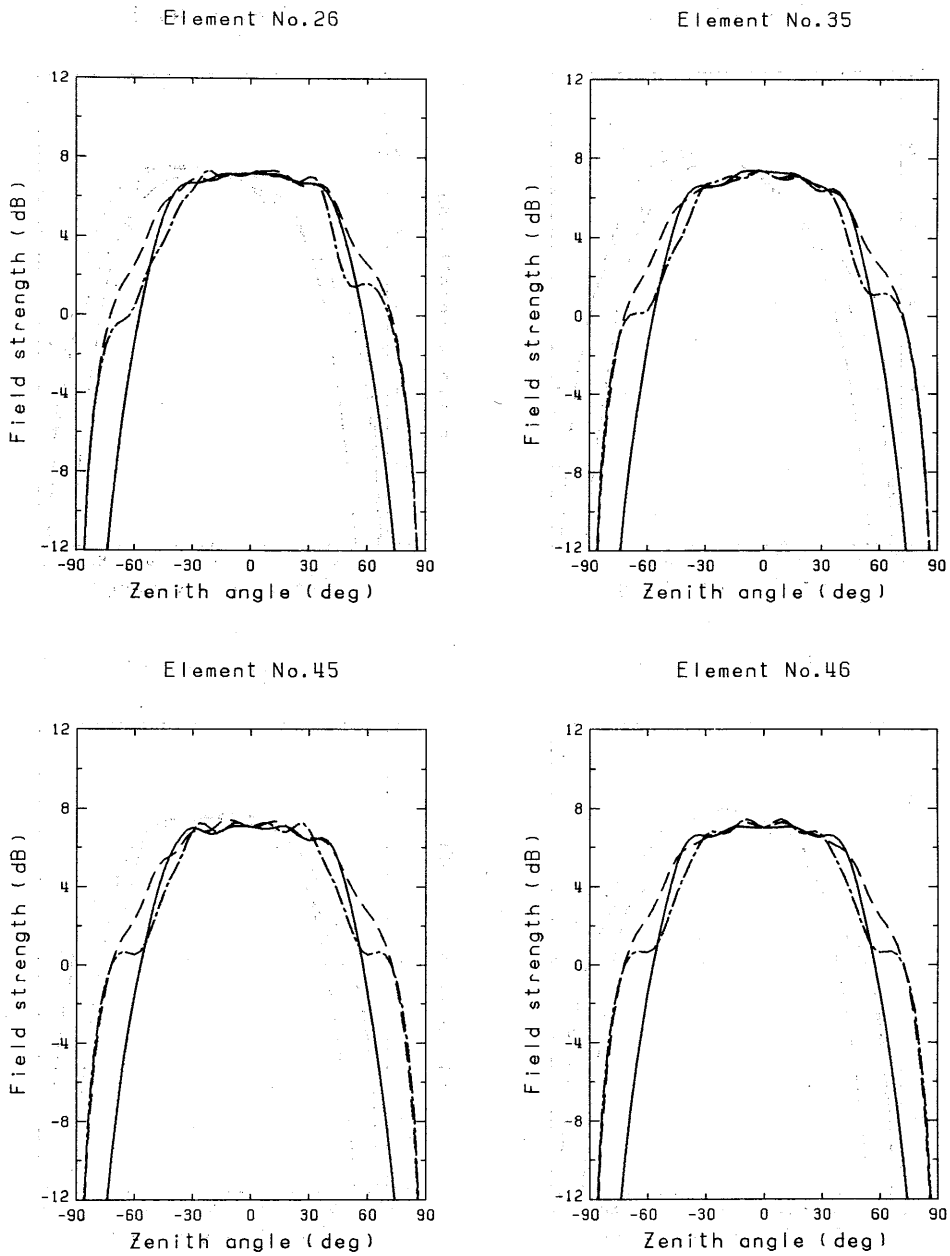

Fig.6-22 (continued)

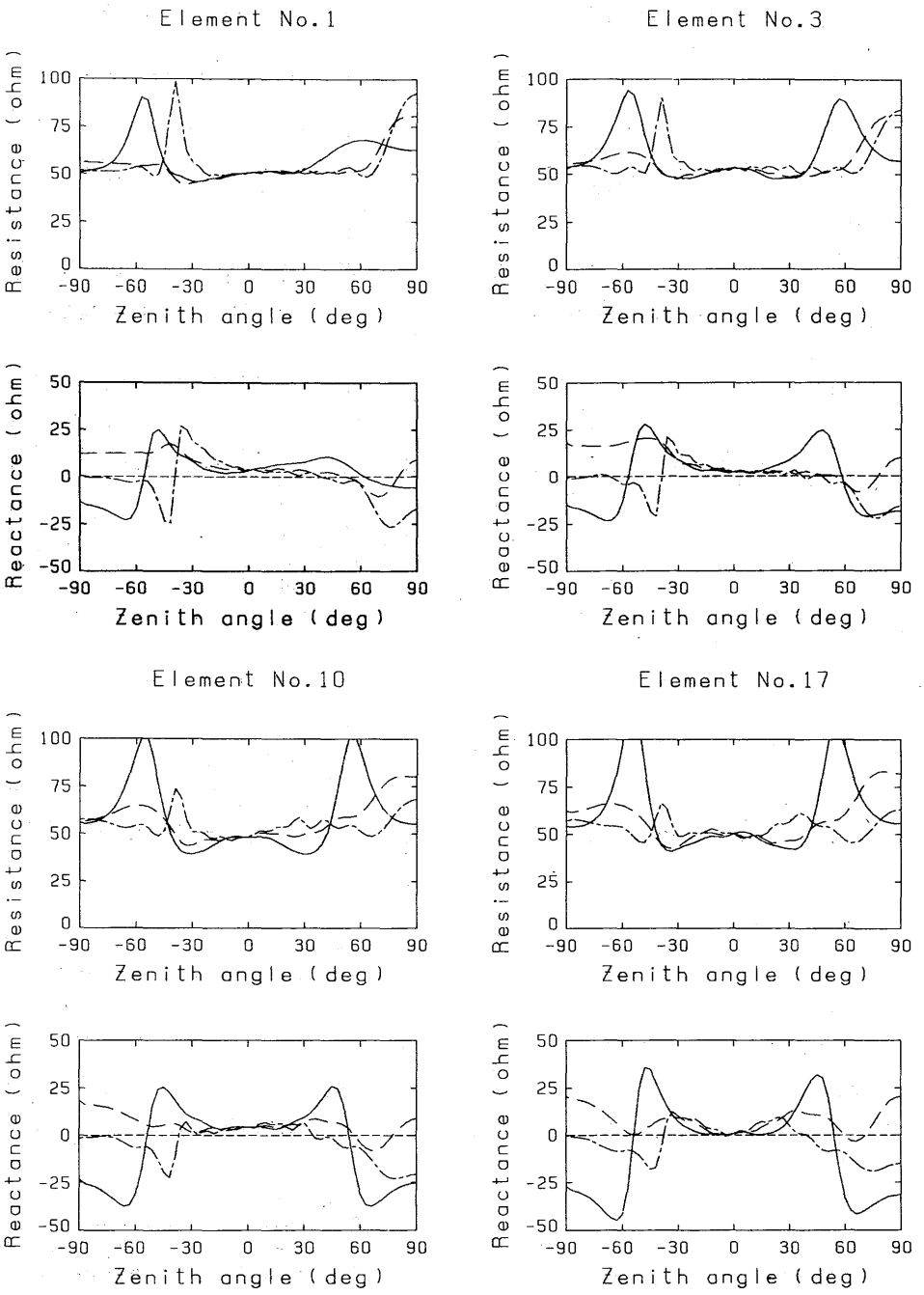

Fig.6-23 Active impedance of the eight elements encircled in Fig.6-21. Solid and dashed curves, and chain are for the directions of ϕ = 0° (x-z plane), 45°, and 90° (y-z plane), respectively.

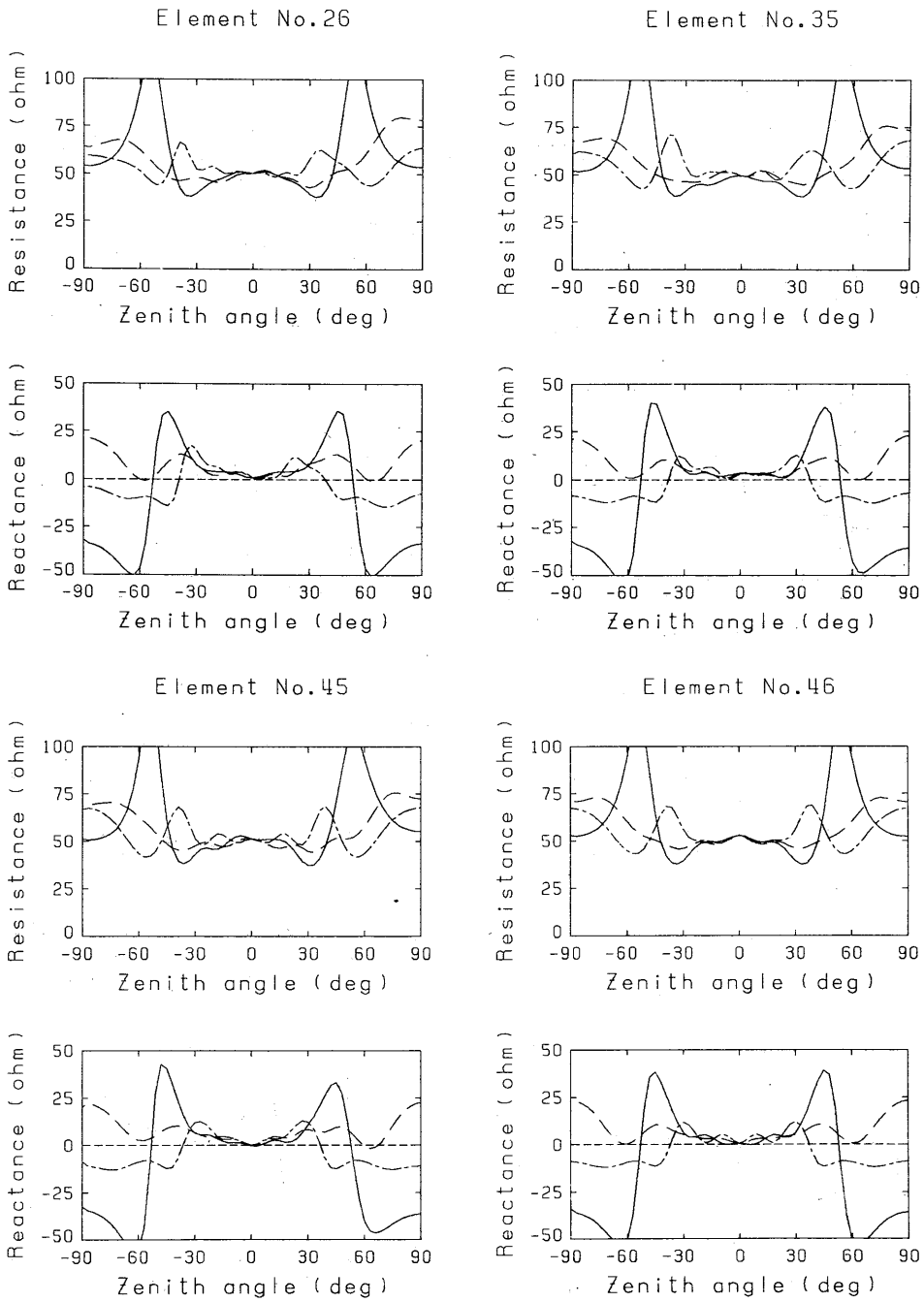

Fig.6-23 (continued)

elements themselves, it does not seem to affect the properties of the entire array of the MU radar largely, since the deviations of the field strength of the elements on the edge are at most 1.2 dB, and the number of the edge elements is only about 1/6 of the total number of elements, 475.

6.6 SUMMARY AND CONCLUSIONS

Design concepts for the MU radar antenna have been presented. The outline of the MU radar project and scientific and technical requirements for the MU radar antenna performance were described first.

The antenna array design was examined based on numerical computations of the radiation pattern. The original plan for element arrangement gave an acceptable performance when the antenna beam is pointed to the zenith, but it was shown to have a fairly limited scan range of about 20° due to grating lobes. An improved element arrangement of a circular array with the equilateral triangular grid, which has an optimum property for grating lobe suppression, was then proposed. The antenna beam scan range was extended to 30° zenith angle by this arrangement.

Relating to the antenna element design, effects of mutual coupling between array elements were examined for the infinite array of crossed Yagi antennas. An example of theoretical computation showed that the mutual coupling effect changes the input impedance of a Yagi antenna by about 30 Ω, and reduced its gain more than 3 dB.

A 3-subelement Yagi was designed to exhibit its best performance in the infinite array condition. It showed the highest possible element gain of 7.24 dB, a very high front-to-back ratio, and an excellent matching to the feed line impedance. Its properties showed little deterioration over the scan range of 30°, and over the

frequency bandwidth of 1 MHz. The edge effect of the finite array was examined for a smaller array of 91 elements, and it was found to be not serious except for the outermost elements.

CHAPTER 7
CONCLUDING REMARKS

Considerations have been made on coherent radar systems and measurements of the middle atmosphere using them. The systems and observational capabilities of two of the most powerful coherent radars of Jicamarca and Arecibo were examined, and then some design concepts were given for the proposed MU radar of Japan based on these examinations.

General introduction was first presented on characteristic features of the middle atmosphere and the scattering of radio waves from the atmospheric turbulence of this region. The outline of previous coherent radar studies of the middle atmosphere were briefly reviewed.

The Jicamarca VHF radar system and basic observational techniques for the middle atmosphere were described in Chapter 2. A few problems and limitations associated with the Jicamarca radar system were discussed. Effects of a limited height resolution were investigated in some detail since it may dominate the quality of observed physical parameters. A numerical simulation showed that the height resolution of the Jicamarca VHF radar is not sufficient for detailed study of the stratospheric dynamics.

In Chapter 3, results of two continuous mesospheric observations by the Jicamarca VHF radar were presented. The general characteristics of the mesospheric echo supported the theory that scattering occurs mainly from the electron density fluctuations due to atmospheric turbulence. The mean zonal wind was compared with that measured by meteorological rocket observations, and a good agreement was obtained. Short period waves were discussed in terms of propagating internal gravity waves. Presence of long period waves with 2-5 day period suggested the importance of planetary scale waves at mesospheric heights. A strong aspect sensitivity was

found below about 75 km, which disappears above that height. The correlation between echo power and signal correlation time reverses its sign also around 75 km, suggesting a clear difference in turbulence structure above and below that height.

The Arecibo UHF radar system and observational techniques developed for stratospheric studies were discussed in Chapter 4. The theory of complementary pulse coding scheme was described, and its performance was examined under the real situation of stratospheric observations. A non-linear parameter estimation procedure was applied to the observed spectra in order to eliminate contaminations due to very strong fading clutters. It was found to work successfully except when the echo power is weak and the Doppler shift of the echo is small.

In Chapter 5, physical parameters deduced from a series of high-resolution stratospheric observations by the Arecibo UHF radar were discussed. A stable wavy structure with very short vertical wavelength was found in the horizontal wind velocity, which demonstrates the importance of a high height resolution. Short period oscillations, on the other hand, showed the importance of a high time resolution. The stratospheric turbulent layers were usually found to be thinner than the height resolution of 150 m, and estimated to be of the order of 50 m on average by a beam swinging experiment. Horizontal extent of scattering layers were estimated to be of the order of 100 km. Observed echo power showed a good correlation with the vertical shear of the horizontal wind, and with the spectral width of echoes, which can be explained by a simple model of the turbulent layer. An attempt was made to evaluate turbulent eddy diffusivity based on the observed spectral width. The results agreed well with other radar investigations, supporting the importance of the stratospheric turbulence on the vertical transport phenomena.

Based on the considerations on the capability and limitations of the Jicamarca and Arecibo radars given in Chapters 2-5, design

concepts for the MU radar were discussed in Chapter 6. Scientific and technical requirements for the MU radar system clarified in preceding chapters were summarized first. It was shown that most important remaining problems in satisfying these requirements exist in the antenna design. As for the antenna array design, a modification of element arrangement to the circular array with a equilateral triangular grid was proposed. The antenna beam scan range was extended by about 10° in zenith angle by this modification. The mutual coupling effect between array elements was examined relating to the element design. An example of theoretical computation assuming an infinite array showed that the mutual coupling effect changes the input impedance of a Yagi antenna by about 30Ω, and reduces its gain more than 3 dB. Dimensions of the Yagi antenna was designed for an infinite array using an optimization procedure. A 3-subelement Yagi was found to have the maximum gain, excellent front-to-back ratio, and a fine impedance matching, which shows little deterioration even when the beam is steered by 30° from the zenith. The edge effect of the finite array was examined, and was found to be not serious except for the outermost elements of the array.

APPENDIX

SPATIAL FOURIER COMPONENTS OF THE CURRENT DISTRIBUTIONS IN AN INFINITE ANTENNA ARRAY

The positional vector of a grid point in an infinite array shown in Fig.6-4 is expressed as

$$\vec{r}_{st} = s\vec{d}_1 + t\vec{d}_2 \qquad (s,t = \{-\infty, \infty\}) \qquad \text{(A-1)}$$

where

$$\vec{d}_1 = (a,0), \quad \vec{d}_2 = (c,b)$$

Any function which is periodic along this grid can be expanded into spatial Fourier series with basis wavenumber vectors $\vec{h}_1$ and $\vec{h}_2$ which are perpendicular to $\vec{d}_1$ and $\vec{d}_2$, and have amplitudes equal to the reciprocal of grid intervals along them, respectively (Brillouin, 1953). The spatial wavenumber vector for a harmonic is thus given by

$$\vec{k}_{mn} = m\vec{h}_1 + n\vec{h}_2 \qquad (m,n = \{-\infty, \infty\}) \qquad \text{(A-2)}$$

where

$$\vec{h}_1 = (1/a,-c/ab), \quad \vec{h}_2 = (0,1/b)$$

The current distribution function K is expanded as

$$K(\vec{r}) = \sum_{m=-\infty}^{\infty} \sum_{n=-\infty}^{\infty} K_{mn} \exp(-j\vec{k}_{mn} \cdot \vec{r}) \qquad \text{(A-3)}$$

When the antenna beam is tilted by θ_x and θ_y from x- and y-axis, respectively, K becomes

$$K(\vec{r}) = K_o(\vec{r})\exp\{jk(x\cos\theta_x + y\cos\theta_y)\} \qquad \text{(A-4)}$$

where K_o is the current distribution in the absence of the phasing, and k is the wavenumber in free space.

Using Eqs.(A-2) and (A-3), (A-4) reduces to

$$K(\vec{r}) = \sum_{m=-\infty}^{\infty} \sum_{n=-\infty}^{\infty} K_{mn}\exp\{-j(\beta_m x + h_{mn} y)\} \qquad \text{(A-5)}$$

where

$$\beta_m = k\cos\theta_x + 2\pi m/a$$
$$h_{mn} = k\cos\theta_y + 2\pi n/b - 2\pi mc/ab$$

The Fourier coefficients K_{mn} are obtained by

$$K_{mn} = \frac{1}{ab} \iint_A K\exp\{j(\beta_m x + h_{mn} y)\}\, dxdy \qquad \text{(A-6)}$$

where A denotes the unit cell that an antenna element occupies. Eq.(6.15) is obtained by substituting current distributions given by Eq.(6.14) into (A-6).

REFERENCES

Aso, T., S.Kato, and R.M.Harper, Arecibo middle atmosphere experiment, Geophys. Res. Lett., 4, 10-12, 1977.

Balsley, B.B., and K.S.Gage, The MST radar technique: Potential for middle atmospheric studies, Pure Appl. Geophys., 118, 452-493, 1980.

Bard, Y., Nonlinear Parameter Estimation, 265pp., Academic Press, New York, 1974.

Barker, R.H., Group synchronizing of binary systems, in Communications Theory, W.Jackson, Ed., 273-287, Academic Press, New York, 1953.

Belmont, A.D., D.G.Dartt, and G.d.Nastrom, Periodic variations in stratospheric zonal wind from 20 to 65 km, at 80°N to 70°S, Quart. J. Roy. Meteorol. Soc., 100, 203-211, 1974.

Belrose, J.S., Radio wave probing of the ionosphere by the partial reflection of radio waves (from heights below 100 km), J. Atmos. Terr. Phys., 32, 567-596, 1970.

Booker, H.G., and W.E.Gordon, Theory of radio scattering in the troposphere, Proc. IEEE, 38, 401-412, 1950.

Bowles, K.L., Lima radar observatory, NBS Rep. 7208, 55pp., U.S. Dep. of Commer. Nat. Bur. of Stand., Boulder, Colo., 1961.

Briggs, B.H., Radar observations of atmospheric winds and turbulence: a comparison of techniques, J. Atmos. Terr. Phys., 42, 823-833, 1980.

Brillouin, L., Wave Propagation in Periodic Structures, 255pp., Dover, New York, 1953.

Cadet, D., Energy dissipation within intermittent clear air turbulence patches, J. Atmos. Sci., 34, 137-142, 1977.

Cadet, D., and H.Teitelbaum, Observational evidences of inertia-gravity waves in the tropical stratosphere, J. Atmos. Sci., 36, 892-907, 1979.

Crane, R.K., A review of radar observations of turbulence in the lower stratosphere, Radio Sci., 15, 177-193, 1980.

Cunnold, D.M., Vertical transport coefficients in the mesosphere obtained from radar observations, J. Atmos. Sci., 32, 2191-2199, 1975.

Czechowsky, P., R.Rüster, and G.Schmidt, Variations of mesospheric structures at different seasons, Geophys. Res. Lett., 6, 459-462, 1979.

Dutton, J.A., Clear-air turbulence, and atmospheric science, Rev. Geophys. Space Phys., 9, 613-657, 1971.

Ecklund, W.L., D.A.Carter, and K.S.Gage, Sounding of the lower atmosphere with a portable 50 MHz coherent radar, J. Geophys. Res., 82, 4969-4971, 1977.

Ecklund, W.L., D.A.Carter, and B.B.Balsley, Continuous measurements of upper atmospheric winds and turbulence using a VHF Doppler radar: Preliminary results, J. Atmos. Terr. Phys., 41, 983-994, 1979.

Evans, J.V., High-power radar studies of the ionosphere, Proc. IEEE, 63, 1636-1650, 1975.

Farley, D.T., Multi-pulse incoherent-scatter correlation function measurements, Radio Sci., 4, 935-953, 1969.

Farley, D.T., B.B.Balsley, W.E.Swartz, and C.LaHoz, Winds aloft in the tropics measured by the Arecibo radar, J. Appl. Meteor., 18, 227-230, 1979.

Fejer, J.A., Scattering of radio waves by an ionized gas in thermal equilibrium, Can. J. Phys., 38, 1114-1133, 1960.

Fleisch, D.A., Stratospheric scattering of radio waves and the Jicamarca radio telescope, M.S. thesis, Rice Univ., Houston, Tex., 1976.

Forbes, J.M., The equatorial electrojet, Rev. Geophys. Space Phys., 19, 469-504, 1981.

Friend, A.W., Theory and practice of tropospheric sounding by radar, Proc. IRE, 37, 116-138, 1949.

Fukao, S., S.Kato, S.Yokoi, R.M.Harper, R.F.Woodman, and W.E.Gordon, One full-day radar measurement of lower stratospheric winds over

Jicamarca, J. Atmos. Terr. Phys., 40, 1331-1337, 1978.

Fukao, S., T.Sato, S.Kato, R.M.Harper, R.F.Woodman, and W.E.Gordon, Mesospheric winds and waves over Jicamarca on May 23-24, 1974, J. Geophys. Res., 84, 4379-4386, 1979.

Fukao, S., S.Kato, T.Aso, M.Sasada, and T.Makihira, Middle and upper atmosphere radar (MUR) under design in Japan, Radio Sci., 15, 225-231, 1980a.

Fukao, S., K.Wakasugi, and S.Kato, Radar measurement of short period atmospheric waves and related scattering properties at the altitude of 13-25 km over Jicamarca, Radio Sci., 15, 431-438, 1980b.

Fukao, S., T.Sato, R.M.Harper, and S.Kato, Radio wave scattering from the tropical mesosphere observed with the Jicamarca radar, Radio Sci., 15, 447-457, 1980c.

Fukao, S., T.Sato, I.Hirota, and S.Kato, A preliminary radar observation of long-period waves in the tropical mesosphere over Jicamarca, J. Geophys. Res., 85, 1955-1957, 1980d.

Fukao, S., T.Sato, N.Yamasaki, R.M.Harper, and S.Kato, Radar measurement of tidal winds at stratospheric heights over Arecibo, J. Atmos. Sci., 37, 2540-2544, 1980e.

Fukao, S., T.Sato, Y.Maekawa, S.Kato, and R.F.Woodman, Tidal vector wind measurement at stratospheric heights over Arecibo, in preparation, 1981a.

Fukao, S., T.Sato, N.Yamasaki, R.M.Harper, and S.Kato, Vertical sounding of the lower stratosphere by the Arecibo radar, in preparation, 1981b.

Fukuyama, K., and W.Kofman, Incoherent scattering of an electromagnetic wave in the mesosphere: A theoretical consideration, J. Geomag. Geoelectr., 32, 67-81, 1980.

Gage, K.S., and B.B.Balsley, Doppler radar probing of the clear atmosphere, Bull. Amer. Meteorol. Soc., 59, 1074-1093, 1978.

Gage, K.S., and J.L.Green, Evidence for specular reflection from monostatic VHF radar observations of the stratosphere, Radio

Sci., 13, 991-1001, 1978.

Gage, K.S., and J.L.Green, Tropopause detection by partial specular reflection using VHF radar, Science, 203, 1238-1240, 1979.

Gage, K.S., J.L.Green, and T.E.VanZandt, Use of Doppler radar for the measurement of atmospheric turbulence parameters from the intensity of clear-air echoes, Radio Sci., 15, 407-416, 1980.

Golay, M.J.E., Complementary series, IRE Trans., IT-6, 400-408, 1961.

Gordon, W.E., Incoherent scattering of radio waves by free electrons with applications to space exploration by radar, Proc. IRE, 46, 1824-1829, 1958.

Gordon, W.E., and L.M.LaLonde, The design and capabilities of an ionospheric radar probe, IRE Trans., AP-9, 17-22, 1961.

Gossard, E.E. and W.H.Hooke, Waves in the Atmosphere, 456pp., Elsevier, Amsterdam, 1975.

Gray, R.W., and D.T.Farley, Theory of incoherent-scatter measurements using compressed pulses, Radio Sci., 8, 123-131, 1973.

Green, J.L., K.S.Gage, and T.E.VanZandt, Atmospheric measurements by VHF pulsed Doppler radar, IEEE Trans., GE-17, 262-280, 1979.

Groves, G.V., Annual and semi-annual zonal wind components and corresponding temperature and density variations, 60-130 km, Planet. Space Sci., 20, 2099, 2112, 1972.

Gudiksen, P.H., A.W.Fairhale, and R.J.Reed, Roles of mean meridional circulation and eddy diffusion in the transport of trace substance in the lower stratosphere, J. Geophys. Res., 73, 4461-4473, 1968.

Harper, R.M., Preliminary measurements of the ion component of the incoherent scatter spectrum in the 70-90 km region over Arecibo, Geophys. Res. Lett., 5, 784-786, 1978.

Harper, R.M., and W.E.Gordon, A review of radar studies of the middle atmosphere, Radio Sci., 15, 195-211, 1980.

Harper, R.M., and R.F.Woodman, Preliminary multiheight radar

observations of waves and winds in the mesosphere over Jicamarca, J. Atmos. Terr. Phys., 39, 959-963, 1977.

Hines, C.O., Internal atmospheric gravity waves at ionospheric heights, Can. J. Phys., 38, 1441-1481, 1960.

Hirota, I., Equatorial waves in the upper stratosphere and mesosphere in relation to the semiannual oscillation of the zonal wind, J. Atmos. Sci., 35, 714-722, 1978.

Hocking, W.K., Angular and temporal characteristics of partial reflections from the D region of the ionosphere, J. Geophys. Res., 84, 845-851, 1979.

Hojo, H., T.Sato, S.Fukao, I.Kimura, and S.Tokumaru, Radiation characteristics of the MU radar phased array of crossed Yagi antenna elements (in Japanese), Tech. Rep. IECE, AP81-52, 1981.

Holton, J.R., The Dynamic Meteorology of the Stratosphere and Mesosphere, 216pp., Amer. Meteor. Soc., Boston, Mass., 1975.

Inagaki, N., An improved circuit theory of a multielement antenna, IEEE Trans., AP-17, 120-124, 1969.

Kato, S., Dynamics of the Upper Atmosphere, 233pp., D. Reidel, Dordrecht, Netherlands, 1980.

King, R.W.P., R.B.Mack, and S.S.Sandler, Arrays of Cylindrical Dipoles, 494pp., Cambridge Univ. Press, London, 1968.

Klostermeyer, J., and R.Rüster, Radar observation and model computation of a jet stream-generated Kelvin-Helmholtz instability, J. Geophys. Res., 85, 2841-2846, 1980.

Lalonde, L.M., The upgraded Arecibo Observatory, Science, 186, 213-218, 1974.

Larsen, M.F., W.E.Swartz, and R.F.Woodman, Radar observations of the development of tropical thunderstorm and convection cells using the Arecibo radar, Proc. 19th Conf. on Radar Meteor., 585-587, Miami, Fla., 1980.

Lilly, D.K., D.E.Waco, and S.I.Adelfang, Stratospheric mixing estimated from high-altitude turbulence measurements, J. Appl. Meteor., 13, 488-493, 1974.

Lindner, J., Binary sequences up to length 40 with best possible autocorrelation function, Elec. Lett., 11, 507, 1975.

Mechtly, E.A., S.A.Bowhill, and L.G.Smith, Changes of lower ionosphere electron concentrations with solar activity, J. Atmos. Terr. Phys., 34, 1899-1907, 1972.

Miles, J.W., On the stability of heterogeneous shear flows, J. Fluid Mech., 10, 496-508, 1961.

Miller, K.L., S.A.Bowhill, K.P.Gibbs, and I.D.Countryman, First measurements of mesospheric vertical velocities by VHF radar at temperate latitudes, Geophys. Res. Lett., 5, 939-942, 1978.

Molina, M.J., and F.S.Rowland, Stratospheric sink for chlorofluoromethanes: chlorine atom-catalysed destruction of ozone, Nature, 249, 810-812, 1974.

Mushiake, Y., An exact step-up impedance-ratio chart of a folded antenna, IRE Trans., AP-2, 163, 1954.

Nathanson, F.E., Radar Design Principles, 626pp., McGraw-Hill, New York, 1969.

National Astronomy and Ionosphere Center, The users manual for the Arecibo Observatory, 30pp., Ithaca, New York, 1979.

Nowak, R., An integrated meteor radar system for wind and density measurements in the upper atmosphere, Rep. SU-SEL-046, 135pp., Stanford Electron. Lab., Stanford, Calif., 1967.

Ochs, G.R., The large 50 Mc/s dipole array at Jicamarca radar observatory, NBS Rep. 8772, 61pp., U.S. Dep. of Commer. Nat. Bur. of Stand. Boulder, Colo., 1965.

Oliner, A.A., and R.G.Malech, Mutual coupling in finite scanning arrays, in Microwave Scanning Antennas, R.C.Hansen, Ed., pp.337-392, Academic Press, New York, 1966.

Ottersten, H., Atmospheric structure and radar backscattering in clear air, Radio Sci., 4, 1179-1193, 1969.

Probert-Jones, J.R., The radar equation in meteorology, Quart. J. Roy. Met. Soc., 88, 485-495, 1962.

Rastogi, P.K., and S.A.Bowhill, Remote sensing of the mesosphere

using the Jicamarca incoherent-scatter radar, Aeronomy Rep. 68, 241pp., Univ. of Illinois, Urbana, Ill., 1975.

Rastogi, P.K., and S.A.Bowhill, Gravity waves in the equatorial mesosphere, J. Atmos. Terr. Phys., 38, 51-60, 1976a.

Rastogi, P.K., and S.A.Bowhill, Scattering of radio waves from the mesosphere-1. Theory and observations, J. Atmos. Terr. Phys., 38, 399-411, 1976b.

Rastogi, P.K., and S.A.Bowhill, Scattering of radio waves from the mesosphere-2. Evidence for intermittent mesospheric turbulence, J. Atmos. Terr. Phys., 38, 449-462, 1976c.

Rastogi, P.K., and R.F.Woodman, Mesospheric studies using the Jicamarca incoherent-scatter radar, J. Atmos. Terr. Phys., 36, 1217-1231, 1974.

Ratcliffe, J.A. (Ed.), Physics of the Upper Atmosphere, Academic Press, New York, 1960.

Reed, R.J., and K.E.German, A contribution to the problem of stratospheric diffusion by large-scale mixing, Mon. Weather Rev., 93, 313-321, 1965.

Röttger, J., Structure and dynamics of the stratosphere and mesosphere revealed by VHF radar investigations, Pure Appl. Geophys., 118, 494-527, 1980.

Röttger, J., Investigations of lower and middle atmosphere dynamics with spaced antenna drifts radars, J. Atmos. Terr. Phys., 43, 277-292, 1981.

Röttger, J., and C.H.Liu, Partial reflection and scattering of VHF radar signals from the clear atmosphere, Geophys. Res. Lett., 5, 357-360, 1978.

Röttger, J., and G.Schmidt, High resolution VHF radar soundings of the troposphere and stratosphere, IEEE Trans., GE-17, 182-189, 1979.

Röttger, J., P.K.Rastogi, and R.F.Woodman, High-resolution VHF radar observations of turbulence structures in the mesosphere, Geophys. Res. Lett., 6, 617-620, 1979.

Rüster, R., and P.Czechowsky, VHF radar measurements during a jetstream passage, Radio Sci., 15, 363-369, 1980.

Sato, T., and S.Fukao, Altitude smearing due to instrumental resolution in MST radar measurements, accepted for publication in Geophys. Res. Lett., 1981.

Sato, T., and R.F.Woodman, Spectral parameter estimation of CAT radar echoes in the presence of fading clutter, Proc. 19th Conf. on Radar Meteor., Miami, Fla., 1980.

Sato, T., and R.F.Woodman, High-altitude resolution observations of the stratospheric winds and waves by the Arecibo 430 MHz radar, submitted to J. Atmos. Sci., 1981a.

Sato, T., and R.F.Woodman, High-altitude resolution observations of the stratospheric turbulent layers by the Arecibo 430 MHz radar, submitted to J. Atmos. Sci., 1981b.

Schmidt, G., R.Rüster, and P.Czechowsky, Complementary code and digital filtering for detection of weak VHF radar signals from the mesosphere, IEEE Trans., GE-17, 154-161, 1979.

Sharp, E.D., A triangular arrangement of planar-array elements that reduces the number needed, IRE Trans., AP-9, 126-129, 1961.

Shibagaki, T., and S.Tokumaru, Circularly polarized crossed-dipole phased arrays (in Japanese), Trans. IECE, 62-B, 237-244, 1979.

Singleton, R.C., An algorithm for computing the mixed radix fast Fourier transform, IEEE Trans., AU-17, 93-103, 1969.

Skolnik, M.I., Introduction to Radar Systems, 581pp., McGraw-Hill, New York, 1980.

Smylie, D.E., G.K.C.Clark, and T.J.Ulrych, Maximum entropy spectral analysis and auto-regressive decomposition, Rev. Geophys. Space Phys., 13, 183-200, 1975.

Stark, L., Radiation impedance of a dipole in an infinite planar phased array, Radio Sci., 1, 361-377, 1966.

Steinberg, B.D., Principles of Aperture and Array System Design, 356pp., John Wiley & Sons, New York, 1975.

Tatarskii, V.I., The Effects of the Turbulent Atmosphere on Wave

Propagation, 472pp., U.S. Dep. of Commer., 1971.

Tennekes, H., and J.L.Lumley, A first course in turbulence, 300pp., MIT Press, Cambridge, Mass., 1972.

Titheridge, J.E., Nonperiodic irregularities in the ionosphere, J. Geophys. Res., 76, 6955-6960, 1971.

Tokumaru, S., and T.Tagura, Dipole phased arrays with parasitic directors (in Japanese), Tech. Rep. IECE, AP80-23, 1980.

Uda, S., and Y.Mushiake, Yagi-Uda antenna, Res. Inst. of Elec. Comm., Tohoku Univ., Sendai, 1954.

U.S. Department of Commerce, High altitude meteorological data, Rep. 11, NOAA Nat. Clim. Center, Asheville, N.C., 1974.

VanZandt, T.E., J.L.Green, K.S.Gage, and W.L.Clark, Vertical profiles of refractivity turbulence structure constant: Comparison of observations by the Sunset radar with a new theoretical model, Radio Sci., 13, 819-829, 1978.

VanZandt, T.E., J.L.Green, W.L.Clark, and J.R.Grant, Buoyancy waves in the troposphere: Doppler radar observations and a theoretical model, Geophys. Res. Lett., 6, 429-432, 1979.

Vincent, R.A., The interpretation of some observations of radio waves scattered from the lower ionosphere, Aust. J. Phys., 26, 815-827, 1973.

Vincent, R.A., and J.S.Belrose, The angular distribution of radio waves partially reflected from the lower atmosphere, J. Atmos. Terr. Phys., 40, 35-47, 1978.

Wakasugi, K., MST radar technique for remote sensing of the middle atmosphere, Ph. D. thesis, Kyoto Univ., Kyoto, 1981.

Wait, J.R., Electromagnetic waves in stratified media, 608pp., Pergamon Press, London, 1970.

Weinstein, A.I., E.R.Reiter, and J.R.Scoggins, Mesoscale structure of 11-20 km winds, J. Appl. Meteor., 5, 49-57, 1966.

Woodman, R.F., High altitude-resolution stratospheric measurement with the Arecibo 430-MHz radar, Radio Sci., 15, 417-422, 1980a.

Woodman, R.F., High altitude-resolution stratospheric measurements

with the Arecibo 2380-MHz radar, Radio Sci., 15, 423-430, 1980b.

Woodman, R.F., Turbulence in the middle atmosphere: A review, Proc. 6th Int. Symp. on Equat. Aeronomy, Aguadilla, Puerto Rico, 1980c.

Woodman, R.F., and A.Guillén, Radar observations of winds and turbulence in the stratosphere and mesosphere, J. Atmos. Sci., 31, 493-505, 1974.

Woodman, R.F., P.K.Rastogi, and T.Sato, Evaluation of effective eddy diffusive coefficients using radar observations of turbulence in the stratosphere, Proc. Int. Symp. on Middle Atmos. Dynam. Trans., Urbana, Ill., 1980.

Zimmerman, S.P., and E.A.Murphy, Stratospheric and mesospheric turbulence, in Dynamical and Chemical Coupling Between the Neutral and Ionized Atmosphere, B.Grandal and J.A.Holtet, Ed., pp.35-47, D.Reidel, Dordrecht, Netherlands, 1977.